High-Fidelity Simulation of Dynamic Stall on Helicopter Rotors

A thesis accepted by the Faculty of
Aerospace Engineering and Geodesy of the University of Stuttgart
in partial fulfillment of the requirements for the degree of
Doctor of Engineering Sciences (Dr.-Ing.)

by
Johannes Letzgus
born in Tübingen

Main-referee: Prof. Dr.-Ing. Ewald Krämer
Co-referee: Dr. habil. Anthony D. Gardner

Date of defense: 10.02.2021

Institute of Aerodynamics and Gas Dynamics
University of Stuttgart
2021

Acknowledgments

First and foremost, many thanks to my doctoral advisor Prof. Ewald Krämer for providing a great working environment, and for the helpful feedback I received in many challenging and fruitful discussions. I also thank Tony Gardner for his role as examiner for the PhD defense, and for the excellent cooperation and support not only during our joint DFG project.

A special thanks goes to Manuel Keßler for his kind guidance and mentorship over the years. He always offered good advice and wisdom, often enough beyond technical matters, that is, about life, the universe and everything.

Thanks also to Pascal Weihing for the countless nerve-wrecking but also fun hours we spent working together on the numerics, for being my CFD go-to guy, and for proofreading the manuscript. To Christopher Fuhrer for the nice lunch breaks that cleared my mind, and also for proofreading. To Daniel Cornel for patiently answering all my computer science questions.

I also thank all my colleagues at IAG for all the valuable discussions and for giving me a good time. Likewise, thanks to the colleagues at DLR Göttingen for the productive cooperation and sharing their outstanding experimental data and experience. Thanks also to Airbus Helicopters, in particular to Alexander Klein, for providing technical support and real-world expertise.

Many thanks to my wife Patricia for always having my back and reminding me to get things done.

And finally, I gratefully acknowledge the funding by the Deutsche Forschungsgemeinschaft[1] and the German Federal Ministry of Economics and Energy[2], as well as the computing resources provided by the High-Performance Computing Center Stuttgart[3].

Filderstadt, April 2021
Johannes Letzgus

[1] Grant *Untersuchung der dreidimensionalen dynamischen Strömungsablösung an Rotorblättern*
[2] Federal research project *LuFo V-2 CHARME*
[3] Project *HELISIM*

Contents

Abstract

In the present thesis, high-fidelity computational fluid dynamics (CFD) simulations of helicopter rotors are carried out to investigate the complex unsteady flow phenomenon of dynamic stall, which occurs on helicopter rotors during high-speed forward or maneuvering flight. It is associated with leading-edge vortex shedding and massive flow separation leading to severe overshoots in aerodynamic and structural loads that might compromise the structural integrity of the rotor and, thus, limit the flight envelope. The simulations are based on two novel experimental test cases, namely a model rotor with high cyclic pitch control in low axial inflow operated in the rotor test facility (RTG) at DLR Göttingen, and a highly-loaded, high-speed turn flight of the Bluecopter demonstrator helicopter. Unsteady Reynolds-averaged Navier-Stokes (URANS) and delayed detached-eddy simulations (DDES) are carried out using the flow solver FLOWer, which additionally is loosely coupled with the structural dynamics code CAMRAD II in the helicopter case.

First, a validation of the numerical methods is conducted based on the experimental model-rotor RTG case, which shows that the onset of dynamic stall and the associated peak values of lift and pitching-moment overshoot agree well in overall. In the case of rotor dynamic stall, an unprecedented comparison of instantaneous particle image velocimetry (PIV) and CFD results reveals that after stall onset, only the DDES captures the chaotic nature of separated flow and exhibits small-scale vortical structures that correlate nicely with the measurement. Also, using URANS, a noticeable dependency of the results on the turbulence models and flow solver specifics is observed. However, the DDES suffers from the numerical artifact of modeled-stress depletion leading to grid-induced separation. Therefore, several improvements to the so-called boundary-layer shielding, by others and self-developed, are thoroughly investigated for both dynamic stall cases and found to eliminate the issue. Also, an advanced, shear-layer-adaptive filter width is successfully applied to the large-eddy simulation (LES) mode of the DDES that promotes a more realistic development of flow instabilities in separated shear layers. The cycle-to-cycle variations of the RTG measurements are analyzed by a flow-feature-based cycle clustering and it shows that they are mostly limited to small variations of the point in time of dynamic stall onset.

Concerning the turn flight simulation of the Bluecopter demonstrator, the three-degree-of-freedom trim of an isolated rotor yields main rotor control angles that agree very well with the flight-test measurements. A comparison of computed and in-flight-measured pitch-link loads shows a good correlation regarding the overall trends and a significant improvement over a lower-order analysis. It shows that the additional inclusion of the hub cap and fuselage on CFD side further improves the agreement. However, the pitch-link-load amplitudes are still underpredicted. Furthermore, the flow field is found to be highly unsteady and complex throughout a large portion of the azimuth, exhibiting strong separation and multiple dynamic stall events that are partly triggered by blade-vortex interaction. These findings are phenomenologically very similar to other experimental and numerical dynamic stall investigations that considered different rotor geometries and flight conditions.

Kurzfassung

In der vorliegenden Arbeit werden hochaufgelöste CFD- (computational fluid dynamics) Simulationen von Hubschrauberrotoren durchgeführt, um das komplexe instationäre Strömungsphänomen der dynamischen Strömungsablösung (Dynamic Stall) zu untersuchen, das bei Hubschraubern im schnellen Vorwärts- oder Manöverflug auftritt. Es ist mit der Bildung und Ablösung eines Vorderkantenwirbels und massiver Strömungsablösung am Rotorblatt verbunden, was zu einer starken Überhöhung der aerodynamischen und strukturellen Lasten führt, was wiederum die strukturelle Integrität des Rotors beeinträchtigen kann und somit den Flugbereich einschränkt. Die Simulationen basieren auf zwei neuartigen experimentellen Untersuchungen, nämlich einem Modellrotor, der mit hoher zyklischer Einstellwinkeländerung bei geringer axialer Anströmung im Rotorteststand (RTG) des DLR Göttingen betrieben wird und einem hochbelasteten, schnellen Kurvenflug des Bluecopter-Hubschraubers. URANS- (unsteady Reynolds-averaged Navier-Stokes) und Delayed-Detached-Eddy-Simulationen (DDES) werden mit dem Strömungslöser FLOWer durchgeführt, der im Hubschrauberfall auch schwach mit dem Strukturdynamik-Programm CAMRAD II gekoppelt ist.

Zunächst wird eine Validierung der numerischen Methoden anhand des RTG-Modellrotor-Testfalls durchgeführt, die zeigt, dass der Beginn der dynamischen Strömungsablösung und die damit verbundenen Maximalwerte der Auftriebs- und Nickmomentenüberhöhung insgesamt gut mit der Messung übereinstimmen. Ein in diesem Zusammenhang noch nie dagewesener Vergleich von PIV- (Particle Image Velocimetry) und CFD-Ergebnissen zeigt jedoch, dass nach Beginn des Strömungsabrisses nur die DDES die chaotische Natur der abgelösten Strömung abbildet und kleinskalige Wirbelstrukturen aufweist, die sehr gut mit der Messung korrelieren. Auch wird bei Verwendung von URANS eine merkliche Abhängigkeit der Ergebnisse von den Turbulenzmodellen und den Feinheiten des Strömungslösers ersichtlich. Allerdings leidet die DDES unter dem numerischen Artefakt der nicht ausreichend modellierten turbulenten Schubspannungen, was zu gitterinduzierter Ablösung führt. Daher werden verschiedene verfügbare und selbst entwickelte Verbesserungen der sogenannten Grenzschichtabschirmung für beide Dynamic-Stall-Fälle gründlich untersucht und als geeignet zur Lösung des Problems identifiziert. Außerdem wird eine fortschrittliche, scherschichtadaptive Filterweite, die eine realistischere Entwicklung von Strömungsinstabilitäten in abgelösten Scherschichten ermöglicht, erfolgreich auf den Large-Eddy-Simulation (LES)-Modus der DDES angewandt.

Die Zyklus-zu-Zyklus-Schwankungen der RTG-Messungen werden mithilfe einer strömungsbasierten Cluster-Bildung analysiert, wobei sich zeigt, dass diese meist auf kleinere Variationen des Zeitpunkts der dynamischen Strömungsablösung beschränkt sind.

Die Kurvenflugsimulation des Bluecopter Demonstrators betreffend liefert die Drei-Freiheitsgrad-Trimmung eines isolierten Rotors Hauptrotor-Steuerwinkel, die sehr gut mit den Messungen aus dem Flugversuch übereinstimmen. Es wird klar, dass die zusätzliche Berücksichtigung der Rotorkopfabdeckung sowie der Zelle in CFD die Übereinstimmung weiter verbessert. Ein Vergleich von berechneten und im Flug gemessenen Steuerstangenlasten zeigt eine gute Korrelation hinsichtlich der allgemeinen Tendenzen und eine signifikante Verbesserung gegenüber einer Analyse mit vereinfachtem Verfahren, allerdings werden die Maximalwerte unterschätzt. Es zeigt sich zudem, dass das Strömungsfeld über einen großen Teil des Azimuts hochgradig instationär und komplex ist und es zu starker Strömungsablösung und mehreren Dynamic-Stall-Ereignissen kommt, die teilweise durch Blatt-Wirbel-Interaktion ausgelöst werden. Diese Ergebnisse sind phänomenologisch sehr ähnlich zu anderen experimentellen und numerischen Dynamic-Stall-Untersuchungen, die mit anderen Rotoren und unter anderen Flugbedingungen durchgeführt wurden.

Notation

Latin letters

A	Rotor disk area (m^2), $A = \pi R^2$
A	Matrix for POD decomposition
a	Speed of sound ($^{\mathrm{m}}/_{\mathrm{s}}$)
a_1	Constant of Menter-SST turbulence model
$\vec{b}$	Line vector of WNFA
C_3	Constant of ZDES19
C_d	Drag coefficient of airfoil, $C_d = {}^{D}/_{(1/2\,\rho_\infty\,u_\infty^2\,c)}$
C_{d1}, C_{d2}	Constants of delay function of DDES
C_{DES}	Constant of DES
C_L	Integral rotor blade lift coefficient, $C_L = {}^{L}/_{\left(\rho_\infty\,(\Omega\,R)^2\pi R^2\right)}$
C_l	Lift coefficient of airfoil, $C_l = {}^{L}/_{(1/2\,\rho_\infty\,u_\infty^2\,c)}$
$C_l\,M^2$	Sectional lift coefficient of rotor blade, $C_l\,M^2 = {}^{L}/_{(1/2\,\rho_\infty\,a_\infty^2\,c)}$
C_M	Integral rotor blade moment coefficient, $C_M = {}^{M}/_{\left(\rho_\infty\,(\Omega\,R)^2\pi R^3\right)}$
C_m	Moment coefficient of airfoil, $C_m = {}^{M}/_{(1/2\,\rho_\infty\,u_\infty^2\,c\,l)}$
$C_m\,M^2$	Sectional moment coefficient of rotor blade, $C_m\,M^2 = {}^{M}/_{(1/2\,\rho_\infty\,a_\infty^2\,c^2)}$
$C_p\,M^2$	Rotor pressure coefficient, $C_p\,M^2 = {}^{(p-p_\infty)}/_{\left(1/2\,\rho_\infty a^2\right)}$
C_T	Rotor thrust coefficient, $C_T = {}^{T}/_{\left(\rho_\infty\,(\Omega\,R)^2\,\pi R^2\right)}$
$C_z\,M^2$	Sectional thrust coefficient of rotor blade, $C_z\,M^2 = {}^{T}/_{(1/2\,\rho_\infty\,a_\infty^2\,c)}$
CV	Coefficient of variation, $\mathrm{CV} = {}^{\sigma}/_{\mu}$
c	Chord length (m)
D	Drag (N)
D	Sectional drag force ($^{\mathrm{N}}/_{\mathrm{m}}$)
d_w	Wall distance (m)
$d_{w\Omega}$	Wall distance of final shielding of WNFA (m)
dS	Boundary of control volume (m^2)
$\vec{F}_C$, $\vec{F}_V$	Vector of conservative and viscous fluxes
F_{SH}	Stock-Haase diagnostic function ($^{\mathrm{m}}/_{\mathrm{s}}$)
f	Rotor rotational frequency (Hz)
f_{3dturb}	Function to detect 3D turbulence of BDES
f_b	Grid-based near-wall shielding part of IDDES
f_{BL}	Boundary-layer shielding part of BDES

f_{CV}	Diagnostic function based on CV of WNFA
f_d	Boundary-layer shielding function of DDES
f_{d_w}	Wall-distance-based weighting function of WNFA
f_{inv}	Function for inviscid regions of BDES
f_{P2}	Second shielding function of ZDES19
f_R	Inhibition function of ZDES19
f_{sep}	Flag for flow separation of VIADES and WNFA
f_{SL}	Function for separated shear layers of BDES
f_δ	Final shielding function of WNFA
H	Shape factor, $H = {}^{\delta^*}/_{\theta}$
L	Lift (N)
L	Sectional lift force (${}^{\mathrm{N}}/_{\mathrm{m}}$)
L	Length scale (m)
l	Reference length (m)
M	Mach number
M	Pitching moment (Nm)
N_b	Number of rotor blades
n	Wall-normal coordinate (m)
$\vec{n}$	Wall-normal vector
$P(i)$, P_S, P_E	Points on wall-normal vorticity profile of WNFA
p	Pressure (Pa)
$\vec{p}$	Auxiliary vector of WNFA
$\vec{Q}$	Vector of source terms
q	Dynamic pressure (Pa)
R	Rotor radius (m)
r	Radial distance (m)
r_d	Delay function of DDES
r_{ZDES}	Delay function of ZDES19
Re	Reynolds number
S	Velocity gradient invariant of strain rate (${}^{1}/_{\mathrm{s}}$)
S	Matrix of mode energy of POD
s	Grid cell spacing (m)
s, $\vec{s}$	Minimum distance of WNFA
$\vec{s}$	Spanwise vector of VIADES
T	Thrust (N)
T	Oscillation or rotation period (s)
t	Time (s)
t	Threshold value for boundary-layer shielding
U	Matrix of spatial eigenmodes of POD
u, $\vec{u}$	Velocity (${}^{\mathrm{m}}/_{\mathrm{s}}$)
u_{PoMA}	Projected velocity of WNFA (${}^{\mathrm{m}}/_{\mathrm{s}}$)

u_{ps}	Pseudo velocity from vorticity integration of VIADES ($^{\mathrm{m}}/_{\mathrm{s}}$)
V^T	Matrix of time coefficients of POD
$\vec{W}$	Vector of conservative variables
x, y, z	chordwise, spanwise, normal direction (m)
$y+$	Non-dimensional wall distance

Greek letters

α	Angle of attack ($^\circ$)
γ	Isentropic exponent
Δ	Difference
Δ	Filter width (m)
Δ_{max}	Filter width based on maximum cell edge length (m)
Δ_{SLA}	Filter width based on shear-layer adaptive method (m)
δ	Boundary-layer thickness (m)
δ^*	Displacement thickness (m)
ϵ	Threshold value for Stock-Haase criterion
θ	Blade pitch angle ($^\circ$)
θ	Momentum thickness (m)
κ	von Kármán constant
$\kappa^{(4)}$	Dissipation coefficient of JST scheme
λ_2	Criterion for vortex identification ($^1/_{\mathrm{s}^2}$)
μ	Dynamic viscosity ($^{\mathrm{kg}}/_{\mathrm{m\,s}}$)
μ	Rotor advance ratio, $\mu = {}^{u_\infty}/_{\Omega R}$
μ	Mean value
μ_t	Dynamic eddy viscosity ($^{\mathrm{kg}}/_{\mathrm{m\,s}}$)
ν	Kinematic viscosity ($^{\mathrm{m}^2}/_{\mathrm{s}}$), $\nu = {}^{\mu}/_{\rho}$
ν_t	Kinematic eddy viscosity ($^{\mathrm{m}^2}/_{\mathrm{s}}$), $\nu_t = {}^{\mu_t}/_{\rho}$
ρ	Density ($^{\mathrm{kg}}/_{\mathrm{m}^3}$)
σ	Rotor solidity, $\sigma = {}^{N_b\,c}/_{\pi R}$
σ	Standard deviation
φ	Phase angle ($^\circ$)
ψ	Azimuthal angle ($^\circ$)
Ω	Rotor rotational frequency ($^1/_{\mathrm{s}}$)
Ω	Control volume (m^3)
Ω	Vorticity magnitude ($^1/_{\mathrm{s}}$)
Ω_s, Ω_{n+u}	Spanwise, wall-normal plus streamwise vorticity component ($^1/_{\mathrm{s}}$)
$\vec{\omega}$	Vorticity vector ($^1/_{\mathrm{s}}$)

Subscripts

0	Index of cell at wall of WNFA
e	At boundary-layer edge
i	Index of cell of wall-normal "pillar" of WNFA
MA	Moving average
MI	Monotonically increasing
ss	Static stall
tip	At rotor blade tip
∞	At far field

Abbreviations

AL	Aerodynamic loads
BC	Boundary condition
BDES	Bernoulli-based detached-eddy simulation
BL	Boundary layer
BVI	Blade-vortex interaction
CA	Control angles
CL	Cluster
CFD	Computational fluid dynamics
CSD	Computational structural dynamics
DES	Detached-eddy simulation
DES97	Original DES formulation from 1997
DDES	Delayed detached-eddy simulation
DNS	Direct numerical simulation
DS	Dynamic stall
DSV	Dynamic stall vortex
EL	Extraction location of wall-normal boundary-layer data
FFT	Fast Fourier transform
FT	Flight test
HLRS	High Performance Computing Center Stuttgart
IAG	Institute of Aerodynamics and Gas Dynamics, University of Stuttgart
IDDES	Improved delayed detached-eddy simulation
JST	Jameson-Schmidt-Turkel
LE	Leading edge
LES	Large-eddy simulation
M	Million
p2p	Peak to peak
PIV	Particle image velocimetry
PL	Pitch-link loads

POD	Proper orthogonal decomposition
RANS	Reynolds-averaged Navier Stokes
RSM	Reynolds-stress model
RTG	Rotor test facility Göttingen
SA	Spalart-Allmaras
SL	Shear layer
SL	Structural loads
SM	Stall map
SST	Shear stress transport
TE	Trailing edge
URANS	Unsteady Reynolds-averaged Navier Stokes
VIADES	Vorticity-integrated algebraic DES
WNFA	Wall-normal flow analysis shielding
WT	Wind tunnel
ZDES	Zonal detached-eddy simulation

1 Introduction

The unique ability of rotorcraft to take-off and land vertically or hover in midair has made them indispensable, for example, to emergency medical or search and rescue services, law enforcement authorities or extraordinary transportation of passengers and cargo. Over decades, continuous research and development has led to decreases in fuel consumption and noise emission or improvements in overall performance, yet, the flight envelope of rotorcraft is primarily bounded by rotor aerodynamics, which is in conflict with the constant urge to fly faster or carry more payload. Especially with conventional helicopters, a limiting factor in high-speed flight is the significant increase in drag and, consequently, power consumption due to compressibility effects on the advancing side of the rotor disk. Another major factor is the occurrence of flow separation on the retreating side, leading to a breakdown of the aerodynamic performance of the rotor blade, which is called stall [1].

This flow separation is a natural consequence of the interaction of rotor aerodynamics and flight mechanics. Due to the superposition of rotational velocity and freestream velocity, a rotor blade experiences a higher inflow velocity on the advancing side than on the retreating side, which would cause, if not balanced, a dissymmetry in lift and a roll-over of the helicopter. Of course, this is not the case in actuality, where a combination of dynamic rotor blade movements and controlled changes in blade pitch angles lead to higher effective angles of attack on the retreating side that compensate for the flow velocity deficits. However, as airspeed or rotor blade loading increases, the angles of attack must also increase to provide the required lift and, eventually, they exceed a so-called critical angle at which the flow separates from the rotor blade surface [1].

This flow separation is subject to a highly unsteady situation, as the effective angles of attack permanently and quickly change throughout a rotor revolution and, in fact, the critical angle is exceeded only temporarily for a short period of time. Under that condition, the flow process fundamentally differs from conventional separation: As the angle of attack is rapidly increased beyond the point where the flow would normally separate, a vortex evolves at the leading edge of the rotor blade that is associated with even more lift. Eventually, the vortex detaches and convects downstream, moving the center of pressure to the aft, which causes an overshoot in nose-down pitching moment. When the vortex passes the trailing edge and is shed

into the wake, the lift breaks down and the flow remains completely separated until the angle of attack is substantially reduced again [2]. It is precisely this process, known as dynamic stall, that is the main topic of the present thesis.

For a classification of the flight conditions associated with this phenomenon, rotor blade loadings measured on a flight test of a UH-60A helicopter [4, 3] at different advance ratios μ, which can be assumed here to be proportional to airspeed, are shown in Fig. 1.1. Three distinct cases are marked in which severe dynamic stall was reported, namely a fast high-altitude level flight, a high-g pull-up maneuver and a high-speed diving turn. It is apparent that the dynamic stall region is found at a combination of high airspeed and high blade loading, which is, of course, related to the aforementioned rotor aerodynamics. In general, the dynamic stall cases not only lie beyond the lift stall boundary that was experimentally identified by McHugh [5] on a model rotor based on steady rotor performance (Fig. 1.1), they are also associated with large structural and control loads and vibrations that severely exceed the levels reported in standard flight conditions and, consequently, limit the flight envelope of a helicopter [6, 1].

Of course, it is of great interest to know and predict these limits, both for the save operation and enhancement of helicopters. As flight tests come with immense cost and efforts and possible risks, as one inherently operates in edge cases, computational fluid dynamics (CFD) methods come into focus. Furthermore, the natural strengths of CFD, that is, having access to the entire flow field and being able to vary parameters relatively easily, open the possibility to investigate the flow physics of dynamic stall in greater detail. This is where the present thesis aims to contribute.

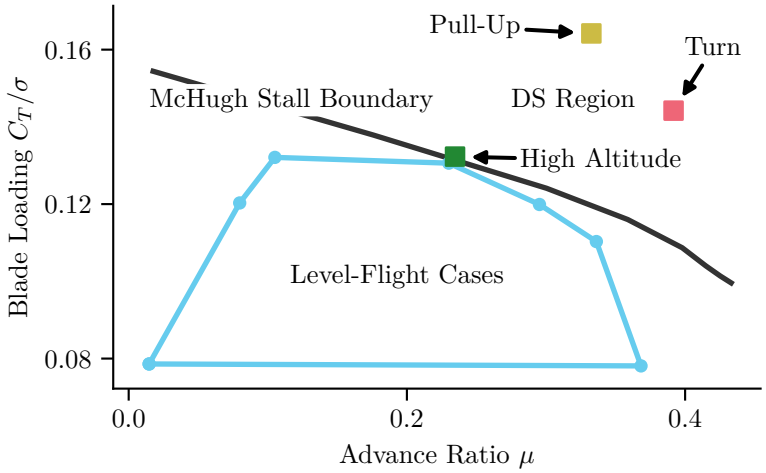

Figure 1.1: Classification of flight conditions associated with dynamic stall based on UH-60A flight-test measurements with selected dynamic stall cases. Adapted from Kufeld and Bousman [3].

1.1 State of the Art

Considering the importance of dynamic stall to rotorcraft, its complexity, and the fact that it has been known for decades, it comes as no surprise that there is an overwhelming number of research studies on the subject. Besides, as dynamic stall basically occurs on any lifting surface that experiences a rapid and critical change in the inflow angle, it is observed and investigated not only on rotor blades of helicopters but also on those of wind turbines, on fixed-wing aircraft during extreme maneuvers, on turbine blades or even on the wings of insects [7]. However, the following survey of existing experimental and numerical research is not supposed to be complete but gives an overview and focuses on fundamental works or important studies that are most relevant to the topic of the present thesis.

1.1.1 Experimental Investigation of Dynamic Stall

In the late 1930s, the early days of rotorcraft, Bailey and Gustafson [8] managed to take photographs of tufts mounted on the rotor blade of an autogiro that was in forward flight. By analyzing the orientation of the tufts in post-processing, they identified stalled and reversed flow in the inboard section of the retreating side, as predicted by the theory of asymmetrical relative inflow. As rotorcraft became heavier, faster and more agile, dynamic stall was encountered, that is, pitch-link loads and torsional moments suddenly and drastically increase on the retreating side, where large angles of attack occur in high-speed and maneuvering flight [9].

A first step to experimentally investigate the phenomenon in detail was to create a much simpler setup that reproduces the flow conditions, under which dynamic stall was believed to occur on a rotor. The solution was to sinusoidally oscillate an airfoil in a wind tunnel with Reynolds and Mach numbers and pitching motions corresponding to selected radial stations of a rotor. Without blade deformation or finite wing effects and especially without rotation, the latest measuring techniques like pressure transducers, hot-wire anemometers and smoke visualizations could be applied and countless variations of flow conditions, pitching motions and airfoils could be tested. Especially the works of Carr et al. [10, 7] and McCroskey [2] provide a comprehensive analysis of dynamic stall on pitching airfoils and define the fundamental process of moment and lift stall with a large overshoot in nose-down pitching moment and lift caused by the formation and convection of a leading-edge vortex.

To this day, experiments of pitching airfoils are carried out to provide a reliable database for CFD validations [11], compare the dynamic stall performance of different airfoil designs [12], reveal the dynamic stall development with high-resolution particle image velocimetry (PIV) [13, 14], study aerodynamic damping and stall flutter [15] or investigate advanced flow scenarios like reverse-flow dynamic stall [16].

The next step to better recreate the flow conditions of a real rotor blade in a controllable wind tunnel environment is to use pitching finite wings, which allows pressure-driven spanwise flow and the formation of a tip vortex. As known from fixed wings, having a tip vortex leads to lower effective angles of attack, thus, in the vicinity of the wing tip, dynamic stall was found to be delayed and weakened [17]. Furthermore, Schreck and Helin [18] showed that in this case the initially rather two-dimensional leading-edge vortex is substantially deformed since its formation and convection is slowed down near the tip. Comprehensive studies of pitching finite wings were also conducted by Piziali [19], Le Pape [11] and Merz et al. [20], who used unsteady pressure measurements, high-speed PIV and laser Doppler anemometry to give insight into the chaotic nature of separated flow and to generate valuable data for CFD validation. Recently, Lütke et al. [21] investigated a pitching finite wing version of the advanced rotor blade tip of one of the rotor blades simulated in the present work, and observed a flow-stabilizing effect of the forward-backward sweep.

Despite the great challenges for measurement techniques, researchers simultaneously began to investigate dynamic stall on model or full-scale rotors operated in wind tunnels to capture the effects of rotation and non-uniform relative inflow. Already in the early 1970s, McCroskey and Fisher [22] found that on a model CH-47C rotor under forward flight conditions, dynamic stall appeared as a series of events occurring over a large portion of the rotor azimuth, questioning the theoretical models of the time. Since 1988, a rotor test rig [23] was being developed at ONERA's large S1MA wind tunnel, featuring the so-called 7A rotor (Fig. 1.2a), a quarter-scale model of a Super Puma rotor. With this setup, various forward flight cases including light and deep dynamic stall were conducted. Lately, the measured surface pressures and sectional loads were used by many CFD researchers [24, 25, 26, 27, 28, 29] for extensive validation, as discussed later in Section 1.1.4. The same rotor was also used in a large international wind tunnel measuring campaign called GOAHEAD, this time including a modified NH90 fuselage and a Bo105 tail rotor [30]. Mulleners et al. [31] gathered PIV data at three spanwise slices on the retreating side and identified a stretched dynamic stall vortex that was parallel to the leading edge at mid-span and interacted with the blade-tip vortex further outboard. In contrast to pitching airfoil studies, the vortex was found to be spatially very compact and close to the blade surface, supposedly due to a stabilizing effect of the rotation. This was confirmed by Raghav and Komerath [32, 33] applying PIV to another rotor test rig. They


(a) 7A Rotor


(b) UH-60A Rotor


(c) UH-60A Helicopter

Figure 1.2: Setups of famous experiments of rotor dynamic stall. (a) Courtesy of ONERA [24] (b), (c) Courtesy of NASA [34, 4].

also showed that the overshoots in loads are noticeably weaker in phase-averaged data due cycle-to-cycle variations. In the US, a comprehensive test campaign was carried out using a full-scale UH-60A rotor (Fig. 1.2b) with extensive state-of-the-art instrumentation of rotor blades, hub and wind tunnel [34]. By slowing down the rotational frequency of the rotor, high advance ratios were reached, leading to reverse flow on large parts of the retreating side that causes intensive dynamic stall on the lower side of the rotor blade [35]. Similar phenomena were also observed by Berry and Chopra [36], who conducted wind tunnel measurements of a slowed Mach-scale rotor at advance ratios well beyond one (this typically applies only to high-speed compound rotorcraft) to create datasets for the validation of predictive tools. A novel approach [37] was taken at DLR Göttingen, where a model rotor is operated in a low axial inflow to reduce the ground effect and recirculation. Their comprehensive state-of-the-art measurements of the rotor blade flow during various dynamic stall conditions provide insight into the three-dimensionality of dynamic stall and were used by researchers for corresponding CFD investigations [38, 39, 40, 41] – including the present work, see Chapter 5. Currently, new measurements are ongoing [42] using an innovative double-swept rotor blade tip, which is also used on the Bluecopter helicopter that is investigated in Chapter 7.

Published flight-test measurements of dynamic stall are very rare, presumably due to the immense efforts and costs, safety concerns or confidentiality reasons. In 1989, Isaacs and Harrison [43] studied retreating blade stall and flutter measured on an experimental rotor blade that was mounted on a Lynx helicopter. They proposed that the dynamic stall could be amplified by blade-vortex interaction and flow displacements caused by the fuselage. Then, extensive data, including surface pressures and blade and pitch-link loads, were gathered in a UH-60A flight-test campaign (Fig. 1.2c) by NASA and US Army [4]. Bousman [6] thoroughly examined the captured dynamic stall cases and found, among others, similarities to airfoil dynamic stall regarding the basic characteristics, multiple dynamic stall events in one rotor revolution and an outboard propagation of the dynamic stall vortices. He also created rotor maps showing the regions of lift and moment stall and flow

separation on the rotor disk. Kufeld and Bousman [3] then analyzed maneuver flight measurements of the same campaign, confirming the severity of dynamic-stall-induced rotor loads during high-g maneuvers. Over the years, several researchers used the UH-60A flight-test data as basis of their CFD investigations [44, 45, 46, 47, 48], see Section 1.1.4.

1.1.2 Dynamic Stall Control

Since dynamic stall is considered to limit the flight envelope of a helicopter, various attempts were made to reduce and control it. For example, Yu et al. [49] had some success in reducing the pitching-moment overshoot at low Reynolds and Mach numbers by using slatted, deformable or surface-blown pitching airfoils, that, in some way or the other, trap or weaken the dynamic stall vortex. In another concept, pulsed [50] or constant blowing [51] air jets in different variants were used effectively to add momentum to the boundary layer to delay separation and mitigate dynamic stall. Similarly, Post and Corke [52] demonstrated on a pitching airfoil that plasma actuators can also be used to excite the flow and reduce overshoots of loads. A promising concept of passive control was studied by Mai et al. [53] and revisited by Heine et al. [54], who mounted small vortex generators, that is, flat cylinders, at the leading edge of an oscillating rotorcraft airfoil. Using PIV and infrared thermography, they visualized the small-scale streamwise vortices forming at the vortex generators and showed that, by altering the vorticity distribution, the negative effects of dynamic stall can be reduced dramatically. Another idea that well improved the dynamic stall behavior was to use a trailing-edge flap [55], which generates a downforce on the pressure side that counteracts the strong nose-down pitching moment, or a small active or passive spoiler-type flap on the suction side [56], which breaks up the coherent dynamic stall vortex into smaller vortices. Although the studies mentioned here and many more successfully demonstrated the principle of dynamic stall control, there is, as of today, no application to production helicopters.

1.1.3 Lower-Order Modeling of Dynamic Stall

In many applications in research and industry, knowledge of the aerodynamics of lifting surfaces is essential. Often, integral values like lift and drag are required basically instantaneously, for example in flight simulator software or in comprehensive rotorcraft codes like CAMRAD II [57], which may be used for extensive parameter studies. Therefore, experiments or elaborate CFD simulations are not always an option and lower-order models are required. In case of attached flow, for example the

panel or the thin-airfoil method, both based on potential flow theory, yield satisfactory results [1]. However, in case of high angles of attack, when flow separation and dynamic stall occurs, these methods fail, as they are inherently unable to predict highly rotational flow. Therefore, advanced mathematical or empirical modeling is required.

A popular lower-order model was developed at Boeing [58]. To simulate the overshoot in loads and the hysteresis effects, the pitch rate is considered to compute a delayed angle of attack that is then used to obtain the aerodynamic coefficients from experimental static airfoil data, depending on airfoil geometry and Mach number. Another often-used semi-empirical model was proposed by Leishman and Beddoes [59], which considers a leading-edge-vortex or shock-induced-separation criterion based on a Mach-number-dependent critical lift. The so-called ONERA model [60] uses second-order differential equations to approximate lift, drag and pitching moment during dynamic stall, including effects of heave and time-varying inflow. More recently, the effect of leading-edge vortex shedding was incorporated into the unsteady thin-airfoil theory by Ramesh et al. [61], who found an empirical critical leading-edge-suction parameter that defines the onset of stall. By that, they managed to model the growth, convection and shedding of a leading-edge vortex and its inducing effect quite accurately. With increasing physical understanding of dynamic stall, lower-order models also try to capture minor effects like secondary vortex shedding leading to additional load peaks during the downstroke [62]. Also, advances in deep learning or neural networks technology led to a promising new type of reduced-order modeling of unsteady flow [63].

1.1.4 CFD Simulation of Dynamic Stall

The unsteadiness and complexity of dynamic stall and flow separation pose a great challenge to CFD simulations in terms of meshing and computational effort, turbulence modeling and solver stability or convergence. Nevertheless, for many years, numerous attempts have been made to simulate the phenomenon, as already reported in 1988 by Carr [7].

As with the experiments, numerical investigations first focused on pitching airfoils thanks to the significantly reduced complexity. Ekaterinaris and Menter [64] were one of the firsts to carry out two-dimensional unsteady Reynolds-averaged Navier-Stokes (URANS) simulations corresponding to the Piziali data [19]. They compared turbulence models that are still widely in use today, for example the Spalart-Allmaras (SA) [65] and Menter-SST [66] model, and demonstrated the capability to simulate the key characteristics of dynamic stall. However, they also

reported difficulties to predict the point of flow separation or separation at all – a problem that still exists today. A joint European-US study [67] used the same experimental data to compare the elsA and CFL3D codes, but only for static angles of attack. It showed, that grid convergence was not achieved, even with very fine grids at that time, and that boundary conditions could have a major influence. Another joint validation of the flow solvers TAU and elsA was conducted by DLR and ONERA [68]. Based on two-dimensional URANS computations of a pitching OA209 airfoil, they confirmed that a high spatial and temporal resolution is required, that turbulence modeling has a large impact and that the effect of transition modeling is very case-dependent when simulating dynamic stall. Similarly, Klein et al. [69] used the FLOWer code for two- and three-dimensional computations, including Reynolds-stress turbulence modeling (RSM), of pitching airfoils and showed by comparison to experimental data that the three-dimensionality of separated flow must be considered. Zanotti et al. [70] also emphasized the necessity of three-dimensional modeling for simulations of deep dynamic stall. Liggett and Smith [71] went one step further by applying scale-resolving hybrid RANS/large-eddy simulations (LES) to investigate dynamic stall on a pitching VR7 airfoil and demonstrated the importance of temporal convergence to reduce phase-shift errors in load predictions. Today, very high-fidelity CFD simulations of pitching airfoils have become very popular to investigate specific characteristics of dynamic stall. For example, Hodara et al. [72] demonstrated the clear benefits of a hybrid RANS/LES approach (here HRLES [73]) in case of massively separated flow and achieved good agreement with PIV data for a pitching NACA 0012 airfoil in reverse-flow dynamic stall. Also, Visbal and Garmann [74] and Benton and Visbal [75] carried out very high-fidelity, wall-resolved LES of the onset of dynamic stall on a pitching NACA 0012 airfoil at Reynolds numbers up to one million. They showed in great detail the upstream propagation of trailing-edge separation, shear-layer rollup, bursting of a laminar separation bubble, and formation of a coherent dynamic stall vortex at the leading edge.

To account for pressure-driven spanwise flow and tip vortex influences, numerous CFD studies of dynamic stall on pitching finite wings were conducted as well. An important breakthrough was made by Spentzos et al. [76, 77], who provided insight into the flow topology during dynamic stall – with very limited computational resources from a present-day perspective. They visualized a highly three-dimensional Ω-shaped dynamic stall vortex that interacts with the tip vortex, and concluded that two-dimensional and three-dimensional dynamic stall are very similar only at more inboard spanwise stations, and that on a pitching finite wing, the load overshoots are less severe. Furthermore, it showed that the wing planform has only a minor influence on the formation of the dynamic stall vortex and its interaction with the tip vortex. Based on the ONERA OA209 finite wing experiment [11], several CFD investigations were carried out. Costes et al. [78] noted for their URANS simulations that deep

dynamic stall is in fact less critical to simulate, as the leading-edge flow separation is more pronounced. While the main dynamic stall characteristics were matched well, greater discrepancies remained especially in the hysteresis part of the cycle. Then, Kaufmann et al. [79] used the elsA and TAU codes for comparing URANS simulations and conducted grid convergence studies. Although comparable setups were used, the codes yielded large discrepancies for static stall. While the SA turbulence model failed to capture dynamic stall, satisfactory results were achieved using the Menter-SST model. In good agreement with the experiment, they also confirmed the interaction of the dynamic stall vortex with the tip vortex. Jain et al. [80] revisited the case and also obtained good correlations between high-fidelity transitional delayed detached-eddy simulations (DDES) using the flow solvers OVERFLOW and elsA, and the measurements. A similar experiment by Merz et al. [20] was the basis of another TAU URANS investigation by Kaufmann et al. [81] that showed by comparison with two-dimensional simulations that two- and three-dimensional dynamic stall is only very similar at the spanwise station where the leading-edge vortex evolves. However, the resulting aerodynamic loads are similar. Recently, with great computational effort, Visbal and Garmann [82] provided deep insight into the flow mechanisms of dynamic stall with the help of a wall-resolved LES of a pitching finite NACA 0012 wing and confirmed effects seen by URANS and hybrid RANS/LES simulations like the evolution and distortion of an initially Ω-shaped dynamic stall vortex that is restrained at the wing tip.

Minimizing the gap to rotor flows, Gardner and Richter [83] numerically investigated the influence of rotation on dynamic stall on a generic single blade and showed that the induced spanwise flow reduces the severity of lift and moment stall. In the mid-2000s, with ever-increasing computational power and advances in fluid-structure coupling, simulating the phenomenon on real rotors came into reach. A detailed overview of selected state-of-the-art CFD investigations, grouped according to the corresponding experimental test cases, is given in Table 1.1. Within the European GOAHEAD project, rather unsuccessful attempts were made. While Dietz et al. [84] showed in a CFD-only study the difficulties in predicting the edge case of no-stall to stall, Antoniadis et al. [85] reported discrepancies in rotor trim and failed to capture dynamic stall at all, although clearly observed via PIV in the experiment.

Regarding ONERA's 7A-rotor case, several loosely coupled CFD/computational structural dynamics (CSD) simulations of light and deep dynamic stall were carried out by French and US researchers, using different flow and structure solvers and grids ranging from 22 million [24] to 390 million [27] points. In the first study, Ortun et al. [24] emphasized the necessity of a robust trim procedure, for example, by removing the stall from the polars used on CSD side, as well as the importance of including the test rig in CFD. In general, their computed aerodynamic and

Table 1.1: Overview of selected state-of-the-art CFD investigations of rotor dynamic stall.
CA: Control angles, AL: Aerodynamic loads, SL: Structural loads, PL: Pitch-link loads, SM: Stall map.

Case	References	Year	c_T/σ	μ	Codes CFD/CSD	Turbulence Modeling	Used Validation Data				
							CA	AL	SL	PL	SM
GOAHEAD [30]	Dietz et al. [84]	2008	0.096	0.42	FLOWer/HOST	URANS Wilcox k-ω					
(Wind Tunnel)	Antoniadis et al. [85]	2011	?	0.31	FLOWer/HOST	URANS Wilcox k-ω		✓			
					HMB			✓			
7A Rotor [23]	Ortun et al. [24]	2016	0.1	0.3	Helios/RCAS	DES SA	✓	✓	✓		
(Wind Tunnel)					elsA/HOST	URANS Kok-SST	✓	✓	✓		
	Yeo et al. [26]	2016	0.1	0.3	Helios/RCAS	DES SA	✓	✓	✓		
					elsA/HOST	URANS Kok-SST	✓	✓	✓		
	Richez [28]	2017	0.1	0.3	elsA/HOST	URANS Kok-SST	✓	✓			
	Richez [25]	2017	0.095	0.42	elsA/HOST	URANS Kok-SST	✓	✓			
	Grubb et al. [27]	2018	0.095	0.42	FUN3D/RCAS	DDES SA	✓	✓			
					OVERFLOW/RCAS	DDES SA & M-SST	✓	✓			
					elsA/HOST	URANS SA & Kok-SST	✓	✓			
	Castells et al. [29]	2019	0.11	0.315	elsA/HOST	URANS Kok-SST	✓	✓	✓		
UH-60A [4]	Potsdam et al. [44]	2004	0.129	0.24	OVERFLOW/CII	URANS Baldwin-B. & inviscid	✓	✓			✓
(Flight Test)	Sitaraman et al. [86]	2005	0.129	0.24	TURNS/UMARC	URANS SA	✓	✓	✓	✓	
	Datta & Chopra [46]	2006	0.129	0.24	TURNS/UMARC	URANS Baldwin-L. & SA	✓	✓	✓	✓	
	Yeo & Potsdam [87]	2014	0.129	0.24	Helios/RCAS & CII	URANS SA & inviscid	✓	✓	✓	✓	
	Chaderjian [48]	2017	0.129	0.24	OVERFLOW/CII	DDES SA	✓	✓			✓
	Bhagwat et al. [45]	2007	Maneuver		OVERFLOW/RCAS	URANS Baldwin-B. & inviscid	✓	✓	✓	✓	
UH-60A [34]	Yeo & Romander [88]	2012	0.126	0.3	OVERFLOW/CII	URANS SA & inviscid	✓	✓	✓	✓	
(Wind Tunnel)	Potsdam et al. [89]	2012	0.045	0.8	Helios/RCAS	URANS SA & inviscid	✓	✓			

structural loads agree very well with the experiment, which holds true for the other 7A simulations of Table 1.1. Yeo et al. [26], who focused on structural loads, demonstrated the clear improvement of a CFD/CSD approach compared to a comprehensive-only analysis. Then, Richez [28, 25] took a closer look at the global flow field and found different flow separation mechanisms, like trailing- or leading edge and shock-induced separation, occurring over a large portion of the azimuth. He also noticed that blade-vortex interaction (BVI) could trigger dynamic stall. Grubb et al. [27] compared several codes, grids and turbulence models including a laminar-turbulent transition model, but concluded that transition plays only a minor role in deep dynamic stall. They also found that, in their case, modeling the rotor with rigid blades still captures the basic characteristics of dynamic stall. Concerning the turbulence modeling, however, the impact of a detached-eddy simulation (DES) approach remained unclear. Most recently, Castells et al. [29] investigated three dynamic stall cases and confirmed the findings of Richez. They also suggested that the dynamic stall events on the retreating side could cause an elastic deformation in a way that noticeably influences the blade's aerodynamics on the advancing side.

The comprehensive data gathered from the UH-60A flight tests was used by many US researchers to validate various codes, numerical approaches and coupling procedures, focusing on one high-thrust dynamic stall case. The sizes of the CFD grids ranged from as few as 3.3 million [44] to as many as 1.8 billion points [48]. Overall, good agreement regarding measured aerodynamic, structural and pitch-link loads was achieved throughout the studies listed in Table 1.1. Potsdam et al. [44] (later revisited in Yeo and Potsdam [87]) were the first to prove that a loose coupling can be applied to a dynamic stall case, significantly improving the predictions over a lower-order comprehensive analysis. Later, both Sitaraman et al. [86] and Datta and Chopra [46] showed that, by replacing CFD loads with actual measured loads, for the prediction of structural and pitch-link loads deficits in the structural dynamics model are a likely source of error. Recently, Chaderjian [48] presented a detailed analysis of the flow field of the respective case and found that, as for the 7A-rotor case, dynamic stall is triggered by blade-vortex interaction. A different flight condition, namely a high-g pull-up maneuver including dynamic stall events, was comprehensively investigated by Bhagwat et al. [45]. They compared a time-accurate strong to a quasi-steady loose coupling and found very similar aerodynamic and structural loads, which is quite surprising given the highly unsteady maneuver. Furthermore, it showed that the stiffness and damping properties of the pitch links and bearings on the CSD side have a considerable and complex influence on the results.

The sensitivity to stiffness properties was also noticed by Yeo and Romander [88], who used the wind tunnel measurements of the UH-60A rotor for their study. After having computed a widespread speed and thrust sweep corresponding to the experiment, they

pointed out that cases with a massively stalled rotor might require an advanced trim procedure, since changes in collective pitch are basically without effect, questioning trimming for rotor thrust. Potsdam et al. [89] supported that concern in their investigation of a very high-speed case of the same wind tunnel campaign. There, they studied the rather unexplored phenomenon of reverse-flow dynamic stall and reported discrepancies in predicting the point in time and the severeness of dynamic stall, supposedly due to insufficient spatial resolution and poor turbulence modeling.

1.2 Objectives of the Thesis

The provided literature review shows that it is possible to capture key dynamic stall features on airfoils, wings and rotors in accordance with experimental data using common CFD approaches. However, regarding load peak-values, point in time of lift and moment stall and high-frequency fluctuations, some discrepancies remain, on the one hand due to the complexity of the test cases and on the other hand due to known deficiencies of the modeling. Concerning dynamic stall on helicopter rotors in particular, computations are basically restricted to only two cases, namely the UH-60A and 7A rotor.

The overall objective of the present thesis is to investigate two novel, challenging cases of rotor dynamic stall by means of high-fidelity CFD simulations. The first case, in the following denoted *RTG*, is a two-bladed model rotor in low axial inflow, where large cyclic input triggers dynamic stall, and is based on a state-of-the-art experiment recently carried out at DLR in their Rotor Test Facility Göttingen (RTG) [37]. Thanks to time-accurate, full-cycle measurements of surface pressures and PIV, an unprecedented, detailed comparison of experimental and computed flow fields and loads is to be presented, providing deeper insight into the whole dynamic stall process and allowing to validate different URANS and DES approaches. In detail, the effects of spatial and temporal resolution, turbulence modeling and flow solver influences are to be investigated. Furthermore, the large experimental database is to be used to study the cycle-to-cycle variation by means of an innovative clustering concept [90]. Also, due to the relative simplicity of this test case, widespread parameter studies are to be simulated to show the influence of the pitching motion and inflow conditions on three-dimensional rotor dynamic stall and compare the results to the early findings from pitching airfoils [10].

The second test case, in the following denoted *Bluecopter*, is a highly loaded, high-speed turn flight of Airbus Helicopters' demonstrator helicopter named Bluecopter. Compared to the studies mentioned in the literature review (Table 1.1), in the

flight-test case of the present work the rotor blade loading ($^{C_T}/_{\sigma} = 0.145$) is even higher and new challenges are introduced by the high-speed ($\mu = 0.35$) turn flight scenario. This unprecedented flight condition is expected to be very demanding to both the CSD side including the trim procedure and the CFD simulation. Therefore, the capabilities of a loosely coupled FLOWer/CAMRAD II approach to simulate this case are to be assessed and the results regarding control angles and pitch-link loads compared to flight-test measurements – which was performed before only for the UH-60A helicopter. A further goal is to analyze the dynamic stall and flow separation events in detail and to compare them to the other known rotor dynamic stall investigations.

Regarding the reported discrepancies between simulations and experiments, turbulence modeling via standard URANS models, which are applied by most researchers (Table 1.1), is of greater concern. As all of these models are deliberately designed and calibrated for averaged, attached boundary-layer flows, they introduce a high artificial eddy viscosity to the flow field, suppressing flow instabilities, small-scale structures and the chaotic nature that naturally comes with separated flow. Fortunately, many investigations of stalled airfoils or wings [91, 92, 93, 94] proved that results are greatly improved when using hybrid RANS/LES in the form of DES instead of pure URANS. Consequently, DES more and more finds its way into dynamic stall computations [80, 24, 87, 27, 48]. However, new drawbacks and "pitfalls" that come along with DES – most severely modeled-stress depletion leading to grid-induced separation [95, 96] and the so-called gray-area problem [97], see Chapter 3 – have not been investigated or even addressed in the rotorcraft community. Thus, another major objective of the present thesis is to thoroughly assess the applicability and necessity of a high-resolution DES of rotor dynamic stall.

It will turn out that the current state-of-the-art DES method is flawed regarding its transition from RANS to LES, which leads to the aforementioned issue of grid-induced separation. Therefore, several alternative so-called shielding mechanisms (the attached boundary layer must be treated in RANS mode and "shielded" from the LES mode) are to be tested and a novel approach is to be developed that specifically aims at complex helicopter rotor flows. The second major issue of DES, the gray-area problem, is also to be tackled by applying a new shear-layer-adaptive subgrid filter width and investigating its influence on rotor dynamic stall.

The present work has largely been funded by the Deutsche Forschungsgemeinschaft (DFG, German Research Foundation) under grant *Untersuchung der dreidimensionalen dynamischen Strömungsablösung an Rotorblättern* (investigation of three-dimensional dynamic stall on rotor blades) and to some extent by the federal research project *LuFo V-2 CHARME* led by the German Federal Ministry of Economics and Energy.

1.3 Outline

The present thesis is organized as follows: In **Chapter 2**, the fundamentals of airfoil aerodynamics, boundary-layer flow and its separation, helicopter aeromechanics and of dynamic stall are briefly introduced. Then, in **Chapter 3**, a short overview of the numerical CFD methods used in this work, focusing on turbulence modeling by means of detached-eddy simulations, is given. In **Chapter 4**, studies of parameters influencing rotor dynamic stall on the RTG test case are presented. Furthermore, the effects of including a wind tunnel environment in the RTG setup are shown. A comprehensive analysis of high-fidelity CFD simulations of dynamic stall on the RTG test case, that is, on the model rotor in rotor-axial inflow, follows in **Chapter 5**. By comparing loads, surface pressures and flow field snapshots to experimental data including PIV and results of the flow solver TAU, a validation of the URANS and DDES simulations is carried out. Also, the cycle-to-cycle variation observed in the experiment is addressed. Based on the findings of the previous chapter, numerical issues of DDES are confirmed and several improvements – by others and self-developed – regarding the so-called boundary-layer shielding are presented in **Chapter 6**. Here, both rotor dynamic stall cases, that is RTG and Bluecopter, are used for demonstration. Then, the investigation of dynamic stall on the Bluecopter test case, that is, on a highly loaded helicopter rotor in high-speed turn flight, is shown in **Chapter 7**, including a detailed analysis of the complex flow field. In addition, the computational results are compared to flight-test measurements and to observations made in other dynamic stall cases. Finally, in **Chapter 8**, the key findings and conclusions of the present thesis are summarized and future developments suggested.

2 Fundamentals

The present thesis deals with the complex flow phenomenon called dynamic stall. To understand where, when and why dynamic stall occurs on helicopter rotor blades, some fundamentals of airfoil flow and separation as well as helicopter aerodynamics are essential. Also, the basic characteristics of dynamic stall are described that are already known from decades of research.

2.1 Airfoil Aerodynamics

According to Anderson [98], the lift L generated by a given lifting surface, here for the sake of simplicity an airfoil, at a given angle of attack α, depends on physical properties governing the freestream as well as on the size of the lifting surface represented by a reference length like the chord length c. The freestream can be described with the velocity u_∞, the density ρ_∞, the viscosity μ_∞ and the speed of sound a_∞, thus, $L = f(u_\infty, \rho_\infty, \mu_\infty, a_\infty, c)$. A dimensional analysis yields the lift coefficient $C_l = {}^{L}/_{(1/2 \rho_\infty \, u_\infty^2 \, c)}$ or, with using the dynamic pressure q_∞, one has $C_l = {}^{L}/_{(q_\infty \, c)}$. Considering the Reynolds number $\mathrm{Re} = {}^{\rho_\infty \, u_\infty \, c}/_{\mu_\infty}$ and the Mach number $M = {}^{u_\infty}/_{a_\infty}$, the lift coefficient is – for a given airfoil shape and angle of attack – only dependent on the Reynolds and Mach number, so $C_l = f(\mathrm{Re}, M)$. This applies equally to the coefficients of drag C_d and pitching moment C_m.

For a given airfoil shape and a given freestream, the aerodynamic loads are thus only dependent on the angle of attack α, which is defined as the angle between the inflow and the chord. The typical correlation between lift, drag and pitching moment, and static angle of attack is illustrated by the polars in Fig. 2.1. For lower angles of attack, the lift increases basically linearly with an increase in angle of attack, thus this part is referred to as the linear phase or regime. Here, the drag and the slope of the pitching moment change only very little. Eventually, the lift curve starts to flatten and reaches its maximum. Increasing the angle of attack quasi-statically even further leads to a rather abrupt breakdown in lift, a severe increase in negative or nose-down pitching moment and a strong increase in drag. This phenomenon is called stall and it limits the performance of a lifting surface, thus the angle at which it occurs is called the static stall angle α_{ss} or critical angle of attack. The causes of stall are viscous effects that lead to flow separation, as discussed in the next section.

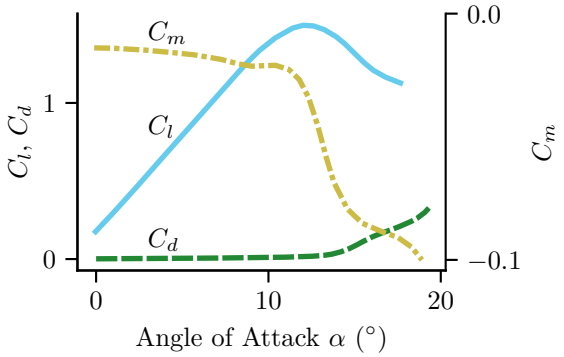

Figure 2.1: Exemplary static polars of coefficients of lift C_l, drag C_d and pitching moment C_m. VR-7 rotor blade airfoil, $M = 0.25$, adapted from McCroskey [2].

2.2 Boundary-Layer Flow and Separation

According to Prandtl's boundary-layer theory [99], the flow of a fluid past a body can conceptually be divided into two regions. The first, outer region covers most parts of the flow field. Here, the flow essentially behaves as if it was inviscid. The second, inner region, called boundary layer, is in the immediate vicinity of the body's surface. In the boundary layer, the inner friction or viscosity of the fluid plays a major role, as it is the source of shear stresses that slow down the fluid until the velocity is zero at the surface, satisfying the no-slip condition. The resulting wall-normal distribution of the velocity is called velocity profile and its shape is dependent on many conditions, for example on the pressure gradient or if the flow is laminar or turbulent. The boundary between the thin inner, viscous and the outer, inviscid region is called boundary-layer edge, and the wall-normal distance from the surface to this edge is called boundary-layer thickness δ. In actuality, of course, there is no distinct "edge" but a continuous transition, consequently, any definition of the boundary-layer thickness is somewhat arbitrary [100]. However, from an engineering point of view, for example to design a turbulence model, some sort of boundary-layer thickness is very useful, compare Section 3.3. Unfortunately, for more complex flows, its determination is non-trivial, as shown in Chapter 6.

In general, on a wing or a rotor blade, the boundary layer evolves from the stagnation point and thickens downstream, following the contour of the airfoil [100, 101]. The basic forces that act on fluid particles in the boundary layer are governed by friction and pressure. In the process of friction, which is caused by viscous and turbulent stresses, some energy of the fluid is dissipated into heat. If there is a positive streamwise pressure gradient, the flow is further slowed down. Such a pressure gradient is typically found at the aft part of a streamlined body or downstream a suction peak and is associated with flow separation, thus, it is also referred to as

an adverse pressure gradient. Eventually, when the flow has lost too much of its energy to "overcome" a positive streamwise pressure gradient, the near-wall flow stops moving in the general direction of the outer flow, comes to a standstill and is pushed backwards or sideways, leading to reverse and spanwise flow. Also, the remaining boundary layer abruptly detaches or separates – coining the name of the phenomenon – from the surface and no longer follows the contour of the body. Strong flow separation is connected with a severe loss of the aerodynamic performance of an airfoil, as shown by the polars in Fig. 2.1. While the massive thickening and deforming of the effective airfoil shape experienced by the flow, compare Fig. 2.2, leads to a strong breakdown in lift, the low pressure that dominates the separation region drastically increases the pressure drag. Furthermore, the separated boundary layer or rather free shear layer is unstable and exhibits Kelvin-Helmholtz instabilities, that is, a breakup or rollup into several large-scale vortical structures that seem to pair together, leading to an unsteady and complex flow field [102].

Commonly, flow separation on the suction side or the associated stall on airfoils is divided into three types [98], based on the location and extent of the separation, as sketched in Fig. 2.2. First, there is trailing-edge separation, where the separation starts at the trailing edge. Typically, with an increase in angle of attack, the separation point moves upstream, which gradually reduces the generated lift. Secondly, complete flow separation can rather suddenly occur at the leading edge, associated with a sharp kink in the load polars. Thirdly, the flow can separate only locally near the leading edge, which leads to a thin "separation bubble" of recirculating flow, but either due to laminar-turbulent transition or due to a favorable pressure gradient, the flow manages to reattach. Since flow separation is always coupled with increased unsteadiness and some sort of chaos, trailing-edge separation or a small separation bubble can eventually transform into complete leading-edge separation, which is especially true for dynamic stall, as reported in literature [1] and also revealed in Chapter 5.

An important aspect of boundary-layer flow affecting separation is the presence of turbulence, that is, chaotic fluctuating motions that transfer momentum from the undisturbed, high-energy outer flow to the near-wall flow that is being slowed down [100, 101]. This becomes apparent when comparing laminar and turbulent

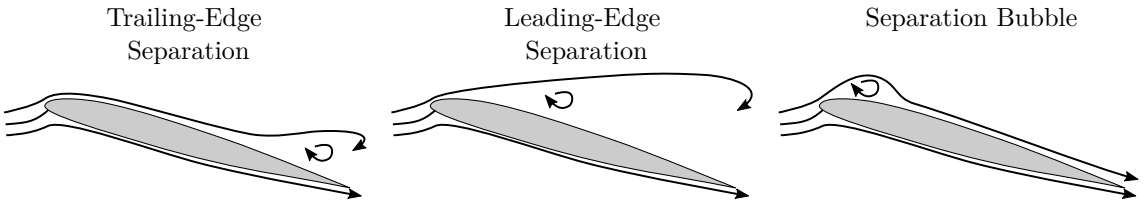

Figure 2.2: Sketch of common types of flow separation or stall on airfoils.

flows regarding their capability to withstand an adverse pressure gradient, which is much greater for a turbulent than for a laminar flow that tends to early separation. Thus, considering the resulting turbulent stresses is also vital in turbulence modeling to prevent premature separation, as discussed in Section 3.3.

2.3 Helicopter Aerodynamics

In conventional helicopters, most of the lift is generated by the main rotor. In accordance with Section 2.1, the lift at a radial station of a rotor blade depends on its local angle of attack α and local dynamic pressure $q \propto u^2$ with u being the local flow speed [1]. As long as the helicopter is in an ideal hover, the dynamic pressure is primarily a function of the radial station defining the rotational velocity, since $u = \Omega\, r$ with Ω being the rotational frequency of the rotor and r the distance from the rotational axis. However, in forward flight, or any translatory movement for that matter, the rotor blade experiences an additional velocity, the freestream velocity u_∞. In detail, on the advancing side a component of that freestream adds to the rotational velocity, and on the retreating side, a component subtracts from it, see Fig. 2.3. Thus, in translatory flight, the relative rotor inflow is highly asymmetric and the flow speed as well as the dynamic pressure experienced by a rotor blade depends on its azimuthal position.

Considering a constant angle of attack at a radial station of a rotor blade, the direct consequence of the asymmetric relative inflow would be that much more lift is generated on the advancing side than on the retreating side, which would lead

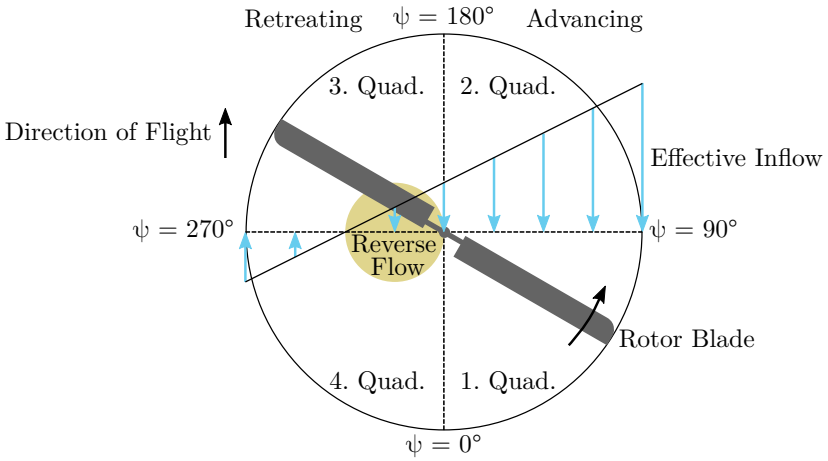

Figure 2.3: Sketch of the asymmetric inflow in forward flight. The rotor disk is divided into advancing side with first and second quadrant and retreating side with third and fourth quadrant. The azimuth ψ is zero when the blade is over the tail.

to an uncontrollably large roll moment. In actuality, this is obviously not the case, since lateral lift balance is, in general, achieved primarily due to the lift-induced blade-flapping mechanism. In short, when the rotor blade flaps up, it experiences a relative downwash that decreases the effective angle of attack and when it flaps down, it is the other way around. Now, in forward flight, the maximum upward flapping velocity is on the advancing side around $\psi = 90°$, where the dynamic pressure is at its maximum. Here, the effective angle of attack is decreased the most by the flapping motion. Conversely, on the retreating side around $\psi = 270°$, the dynamic pressure is at its minimum, but the downward flapping velocity is at its maximum, and, consequently, the effective angle of attack is increased the most. In the end, an equilibrium is reached that balances the lift distribution, as the asymmetry of the dynamic pressure is compensated by changes in angles of attack due to blade flapping [1].

Another mechanism that leads to an azimuthally varying angle of attack is cyclic pitch control. With the swashplate system, it is possible to sinusoidally change the blade pitch angle in a 1/rev variation, which tilts the rotor disk and the direction of the main rotor thrust vector, thus, to steer the helicopter in the horizontal plane. This is especially relevant to maneuvering flight, but cyclic pitch control is also applied in forward flight to counteract the longitudinal and lateral tilt of the rotor disk that is due to blade flapping and coning, respectively [103].

Yet, there are even more factors that locally and significantly alter the effective angles of attack on a rotor blade, for example induced inflow, elastic twist or blade-vortex interaction [6]. In conclusion, on a helicopter rotor, there are multiple mechanisms that lead to an azimuthal, and therefore highly unsteady, change in angle of attack. In challenging flight conditions, this makes the rotor environment, especially on the retreating side, utterly prone to dynamic stall.

2.4 Dynamic Stall

The fundamental knowledge of dynamic stall is mostly based on decades of experimental research on pitching airfoils, especially by Carr et al. [10, 7] and McCroskey [2]. Leishman [1] and Johnson [103] provide comprehensive overviews of this phenomenon, which is described here only in a compact manner, as several more aspects of dynamic stall are also explained throughout the present thesis. In principle, dynamic stall occurs on any lifting surface that experiences a fast change in angle of attack whereby the static stall angle is temporarily exceeded, leading to results that greatly differ from static conditions.

The dynamic stall process is best described by analyzing load and flow field characteristics of a complete cycle of a sinusoidally pitching airfoil, which allows to define certain stages as depicted in Fig. 2.4. Beginning the upstroke at the lower turning point, where the angle of attack is at its minimum, the lift increases linearly with the angle of attack. In this linear regime, lift and pitching moment are comparable to those obtained in static conditions. When the airfoil is pitched beyond its static stall angle, at first the lift continues to increase, thus, stall obviously is delayed (①). According to Leishman [1], this is primarily due to unsteady boundary-layer effects:

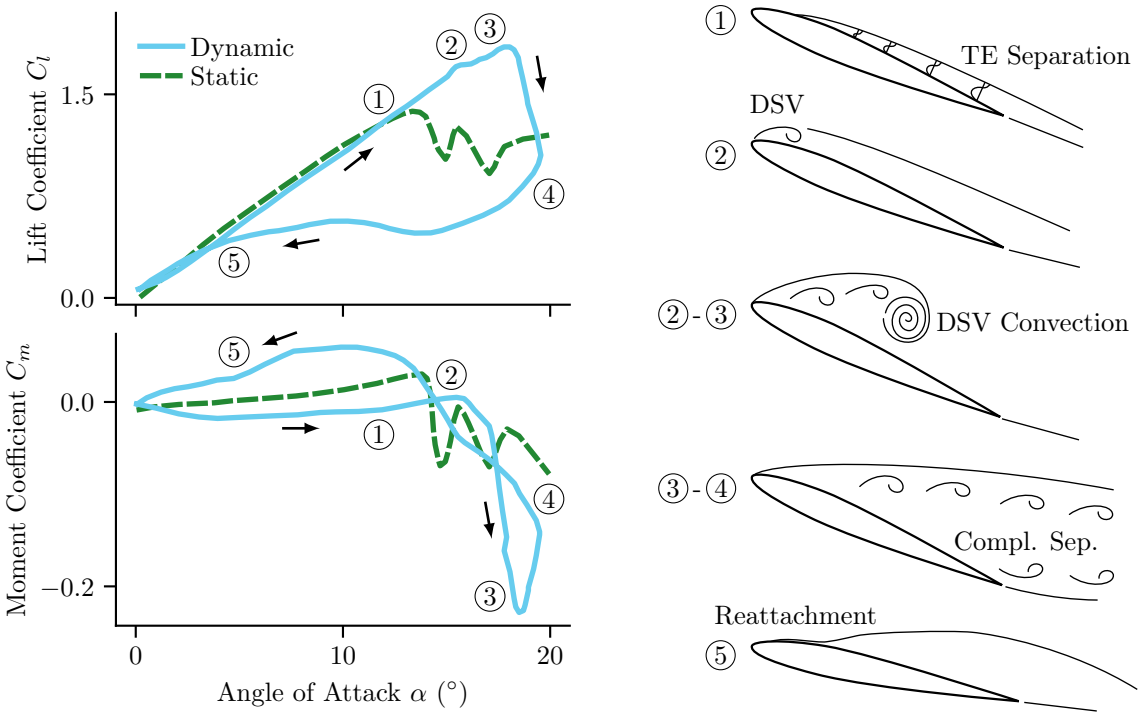

Figure 2.4: Key load and flow field characteristics of dynamic stall on a pitching airfoil including the development and shedding of a leading-edge dynamic stall vortex (DSV), adapted from Leishman [1].

Shallow flow reversal starts to appear at the trailing edge that weakens the suction peak and the adverse pressure gradients at the leading edge. A similar effect results from the upstroke pitching motion that reduces the effective angle of attack. Then, the boundary layer separates near the leading edge and rolls up into a rather coherent dynamic stall vortex (DSV) that generates additional lift exceeding the static maximum by far (②). Eventually, the vortex detaches and convects downstream, which moves the center of pressure to the aft, which in turn causes a dramatic increase in negative or nose-down pitching moment called moment stall (start of stage ②). When the dynamic stall vortex passes the trailing edge and is shed into the wake, lift stall occurs (start of stage ③). Afterwards, the flow is completely separated for some time, which is accompanied by a strong unsteadiness, secondary dynamic stall events and a large hysteresis in the loads (③-④). As the angle of attack is deceasing during the downstroke, the flow starts to reattach at the leading edge. However, it is usually not until a very low angle of attack is reached that the flow is fully attached again (⑤).

Besides these basic characteristics, it is known that the specifics of dynamic stall are to some extent case-dependent and vary, for example, according to the airfoil shape, the pitching motion (frequency, amplitude and mean angle of attack), or the inflow conditions [1], which is also investigated in this work, see Chapter 4. Furthermore, three-dimensional and rotational effects play a role when the phenomenon occurs on pitching wings or rotors, compare Section 1.1.

3 Numerical Methods

In this chapter, the numerical methods are described that are used to carry out high-fidelity CFD computations of dynamic stall using the solver FLOWer. Therefore, some fundamentals of the underlying numerics and solver features are introduced with a focus on DES turbulence modeling. Note that since a coupling of CFD and CSD using CAMRAD II is only applied to the Bluecopter dynamic stall case, the numerical details of that are given in the corresponding Chapter 7.

3.1 Governing Equations

The goal of CFD is to predict fluid motions and the interaction with solid bodies. According to Blazek [104], the derivation of the governing equations, called Navier-Stokes equations, is based on the fundamental conservation laws of mass, momentum and energy. The complete system of the differential equations in integral formulation for a fluid reads

$$\frac{\partial}{\partial t}\int_{\Omega}\vec{W}\,\mathrm{d}\Omega+\oint_{\partial\Omega}(\vec{F_C}-\vec{F_V})\,\mathrm{d}S=\int_{\Omega}\vec{Q}\,\mathrm{d}\Omega. \tag{3.1}$$

The first term with the vector $\vec{W}$, which consists of the unknown conservative variables, represents the variation in time within a finite control volume Ω. The second term on the left-hand side describes the fluxes, that is, the amount of a quantity crossing the boundary $\mathrm{d}S$ of the control volume. While the first part of it is the convective flux vector $\vec{F_C}$ that contains the transport of a quantity via convection, the second part is the viscous flux vector $\vec{F_V}$ that covers diffusion of viscous stresses and heat. Finally, $\vec{Q}$ is a source term representing external volume forces like gravity. Furthermore, two additional equations for the state variables are required, and for this, the ideal gas law is typically applied.

3.2 Turbulence Modeling

Turbulent flow exhibits chaotic movements of fluid that increase the mixing and by that the momentum and energy transfer across layers. The unfiltered simulation of turbulence, called direct numerical simulation (DNS), is only possible for rather simple flows at lower Reynolds numbers up to the order of 10^5, because the computational effort to resolve in space and time even the smallest turbulent structures, which shrink with an increase in the Reynolds number, is immense. Therefore, there is a large variety of methods, called turbulence models, that try to approximate the macroscopic effects of turbulence on reduced levels of complexity and accuracy [104].

The least modeling is applied in large-eddy simulations (LES), where the idea is to directly resolve large, energy-containing flow structures, which primarily promote momentum transfer, and only model the more homogeneous small-scale structures in order to capture dissipative effects. The so-called subgrid-scale modeling can be achieved either by applying an explicit mathematical model like the one of Smagorinsky [105], or by only utilizing the dissipation that is caused by the numerical scheme, which is referred to as an implicit LES. Today, thanks to the ever-increasing computational power, certain aspects of dynamic stall can already be simulated using LES [74, 82].

Way more empiricism-based modeling is introduced by the so-called Reynolds-averaged Navier-Stokes (RANS) approach, where, conceptually, the flow variables are decomposed into a mean and a fluctuating part. Although the governing equations are solved for only the mean values, unsteadiness on length and time scales much larger than those of turbulence, for example forced by the unsteady motion of a body, can be resolved to a certain degree using unsteady RANS (URANS). By applying the Reynolds or rather Favre averaging, an additional term, the Reynolds-stress tensor, emerges that represents the effect of the turbulent fluctuations to the mean flow. However, this new term introduces six more unknowns that need to be addressed for closure, which is where the RANS turbulence models appear [106, 101].

For that purpose, a higher-order approach is the so-called Reynolds-stress modeling (RSM) that approximates the individual components of the Reynolds-stress tensor directly. However, this comes with an increase in modeling and computational effort and reduced numerical robustness, thus, RSM is barely used in complex simulations. Most popular turbulence models, like the transport-equation-based SA [65] or Menter-SST [66] models that are used in the present work, are based on the simpler Boussinesq hypothesis that assumes a linear dependency of the turbulent shear stress on the strain rate. Analogous to the molecular viscosity μ, a turbulent or eddy viscosity μ_t (or $\nu_t = \mu_t/\rho$) is introduced, which is to be computed by the respective turbulence model.

Despite their relative simplicity, RANS turbulence models have proven to give accurate results in many aerodynamic applications they were designed and calibrated for, that is, cases with thin, fully attached boundary-layer flows [106]. Beyond this flow condition, it is well known that more or less all of them have difficulties in predicting the onset of flow separation and the static stall angle of an airfoil correctly. Matyushenko and Garbaruk [107], for example, showed that a simple modification of the a_1 constant of the Menter-SST turbulence model can significantly improve its accuracy in the stall regime, but then, the predicted skin friction with attached flow is wrong, which demonstrates the difficulty of simulating all types of flows with one single turbulence model using universal settings. Moreover, in cases of massive flow separation or strong rotation like in a tip vortex, the Boussinesq hypothesis is invalid, and, consequently, the linear eddy-viscosity models struggle here the most and give results resembling a time-averaged flow field in the best case [104]. As a remedy, Spalart et al. [108] proposed the concept of detached-eddy simulation (DES) that tries to combine the benefits of both RANS (computationally cheap) and LES (resolving larger-scale turbulence). A comprehensive overview of so-called hybrid RANS/LES methods is given by Fröhlich and von Terzi [109].

3.3 Detached-Eddy Simulation

DES and its derivatives are becoming increasingly popular especially to simulate separated flows, since the mean flow approach of RANS is basically inconsistent with the actual flow physics, which are well described in the words of Piziali [19]: "The fundamental nature of the flow about a stalling wing is one of chaos". Thus, the basic idea of DES is to apply RANS only to attached boundary layers and LES to regions of massively separated flow, as illustrated in Fig. 3.1. Spalart et al. [108] addressed that for the SA turbulence model by replacing the RANS length scale L_{RANS}, which is the wall distance d_w for SA, in the destruction term with a new length scale L_{DES97}:

$$L_{\mathrm{DES97}} = \min(L_{\mathrm{RANS}}, C_{\mathrm{DES}}\Delta), \tag{3.2}$$

with a model constant C_{DES} and the filter width Δ, typically the maximum edge length of a respective grid cell (Δ_{max}). Now, near the surface, where the wall distance d_w is assumed to be much smaller than the cell size Δ, the model acts like in the classical RANS formulation, but far off the wall, the new length scale is used that allows the model to behave similarly to the Smagorinsky subgrid-scale model from LES, that is, the eddy viscosity ν_t becomes proportional to the strain rate S and the filter width Δ squared ($\nu_t \propto S\,\Delta^2$).

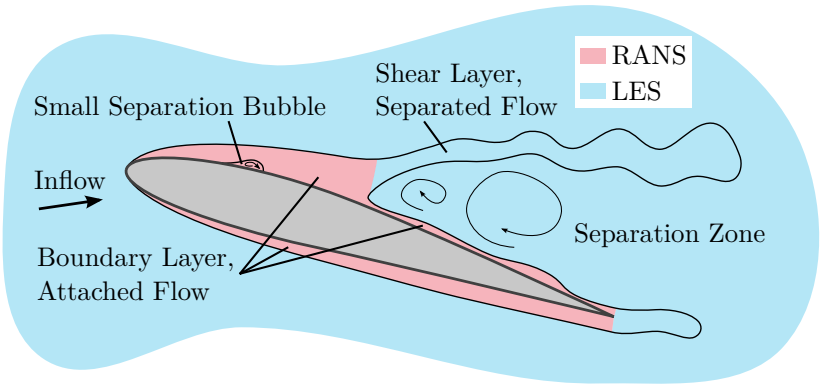

Figure 3.1: Sketch of boundary and shear layers and the respective RANS or LES mode of an airfoil flow featuring a small separation bubble at the leading part and strong flow separation at the aft part of the suction side.

Although this first DES model could proof the concept, the authors already pointed out a major flaw: The switch from RANS to LES mode is completely dependent on the computational grid, which appeared to be a serious problem when grids became finer and finer, resulting in an unintended intrusion of LES into the boundary layer. As a consequence of treating parts of the boundary layer in LES on a typical RANS grid, modeled-stress depletion sets in, that is, the eddy viscosity and by that the modeled transfer of momentum is reduced, which can lead to severe grid-induced separation [95]. This numerical artifact is, in fact, quite comparable to the actual physics of flow separation described in Section 2.2, and therefore hard to recognize if there is no measurement data for confirmation.

Today, the most widely used derivative of the original DES is the delayed detached-eddy simulation (DDES) [96] that uses an advanced mechanism to switch from RANS to LES:

$$\begin{aligned} L_{\mathrm{DDES}} &= L_{\mathrm{RANS}} - f_d \max(0, L_{\mathrm{RANS}} - L_{\mathrm{LES}}), \\ f_d &= 1 - \tanh\left[(C_{d1} \cdot r_d)^{C_{d2}}\right], \\ r_d &= \frac{\nu_t + \nu}{\kappa^2 d_w^2 \sqrt{\frac{\partial u_i}{\partial x_j}\frac{\partial u_i}{\partial x_j}}}. \end{aligned} \tag{3.3}$$

Now, there is the so-called shielding function f_d that controls the RANS/LES interface based on flow properties. Inside the boundary layer, f_d is expected to be zero, returning the RANS length scale. Outside of it, r_d approaches zero, thus, f_d becomes one and the LES length scale is used. The model constants $C_{d1,2}$ are used for fine-tuning of the switching sensitivity and adaption to other underlying RANS models like Menter-SST [110]. Besides DDES, there are several other, less popular derivatives available like the improved delayed detached-eddy simulation (IDDES) [111], which introduces a wall-modeled LES capability for fine enough grids and ambient turbulence in the boundary layer.

Grid-Induced Separation and the Gray-Area Problem

Some years after the publication of DDES, researchers unexpectedly noticed that the already described problem of modeled-stress depletion leading to grid-induced separation still exists [91, 112, 113, 114, 115] despite the additional shielding mechanism. As explained by Weihing [116], there still is a dependency of the RANS/LES switching on the grid due to a coupling of the r_d sensor function and the eddy viscosity: The finer the grid, the more is the outer part of the boundary layer already in LES mode, which leads to a decrease in eddy viscosity ν_t, which in turn reduces r_d and promotes the LES mode even more. In Chapter 6 of the present thesis, it will be confirmed that grid-induced separation also plays a role in the RTG dynamic stall case. So far, the robust prevention of the phenomenon is still in the focus of active research [117, 112, 118, 119], but no generally accepted solution has been found. Several possible approaches, proposed by others and self-developed, are presented and tested in Chapter 6 for both the RTG and Bluecopter dynamic stall case.

Another major conceptual issue of DES, or actually any hybrid RANS/LES method, is the so-called gray-area problem, which was also already forecasted in the original DES publication. As sketched in Fig. 3.1, Spalart et al. [108] envisioned the LES mode to be activated just downstream of the point of separation. Now, at the beginning of the LES region, there is, of course, no seeding of resolved turbulence from the upstream RANS region, as turbulence is completely modeled there. Thus, an ambiguous transition region – or gray area – exists, where there is neither modeled turbulence by RANS nor resolved turbulence by LES. The scale-resolving capability of the LES region at the interface is further hindered due to some eddy viscosity convected from the RANS region, which has a damping effect, and insufficient grid resolution to resolve the initially smaller turbulent structures. As a result, the separated shear layer takes non-physically long to develop Kelvin-Helmholtz instabilities, especially in cases of shallow separation, where macroscopic flow unsteadiness, which could amplify turbulent mixing, is only weak [106]. Besides grid-induced separation, the gray-area problem is very much in the focus of current research [97] with promising concepts that look into injecting synthetic turbulence at the RANS/LES interface or to drastically reduce the eddy viscosity there. Concerning the latter, the approach by Shur et al. [120], implemented into FLOWer by Weihing [116], uses an alternative, shear-layer-adaptive filter width Δ_{SLA}. This filter width aims at unlocking Kelvin-Helmholtz instabilities in the initial part of a shear layer by using local kinematic measures to detect a two-dimensional shear flow and by incorporating the strong anisotropy of near-wall grids. The effect of using Δ_{SLA} on both dynamic stall test cases is investigated in Chapter 6.

3.4 Flow Solver FLOWer

FLOWer is a block-structured, cell-centered finite-volume Navier-Stokes code that was originally developed by DLR [121] and has been enhanced by the Institute of Aerodynamics and Gas Dynamics (IAG) of the University of Stuttgart. During the years, the IAG version of the code was optimized for high-performance computing [122, 123], received state-of-the-art DES methods and experimental DES shielding functions [124, 118] as well as proof-of-concept implementations of modern laminar-turbulent transition models [125, 116].

The time integration is carried out with a second-order implicit dual-time stepping method along with implicit residual smoothing and a three-level multigrid method for convergence acceleration. For spatial discretization, the second-order central differences Jameson-Schmidt-Turkel (JST) [126] scheme or up to sixth-order WENO schemes [127] are available. In all presented cases, the flow is assumed to be fully turbulent, thus, no transition modeling is applied. Note that additional code settings and details on the simulation setups as well as on the numerical grids are reported in the respective chapters of the dynamic stall cases of the RTG (Chapter 5) and the Bluecopter (Chapter 7).

4 Pre-Studies of Parameters Influencing Dynamic Stall and Rotor Aerodynamics

It is known from investigations of pitching airfoils that the manifestation and severity of dynamic stall depends on several case-dependent factors. Furthermore, studies on pitching wings and rotors showed that three-dimensional and rotational effects alter the dynamic stall process considerably, compare Sections 1.1 and 2.4. In this chapter, numerical pre-studies are presented in which the parameter variations classically associated with pitching airfoils, namely varying pitching motion and inflow Mach number, are applied to a rotor. In order to connect both scenarios, the results are then compared to the literature findings from pitching airfoils.

The simulations correspond to the RTG dynamic stall case, in which a two-bladed model rotor ($R = 0.65\,\mathrm{m}$) is operated in a hover-like condition and large cyclic pitch control is used to trigger dynamic stall. Anticipating Chapter 5, where a comprehensive flow field analysis of the dynamic stall process of this case and a validation with experimental data follows, the pre-studies here focus only on integral rotor blade loads (C_L, C_M). The rotor test rig is installed in front of a wind tunnel nozzle (see Fig. 5.1) to provide a low rotor-axial inflow, therefore, the influence of a wind tunnel environment is investigated in Section 4.3. The computations were carried out by Kozlowski [128] and Bußhardt [129], respectively, who used the CFD setups and post-processing methods of the author of the present thesis in a collaborative effort.

4.1 Numerical Setup

The CFD setup used here is a low-resolution version of those in Chapter 5. Beforehand, a grid- and time-step dependency study was carried out in Letzgus et al. [38] confirming that the key characteristics of dynamic stall are captured in any case. As shown in Fig. 4.1, besides the rotor blades, a simplified blade mount and a spinner were modeled to take the actual rotor hub and shaft geometry into account. The near-body grids were then embedded in a Cartesian off-body grid that extends to a distance of about $6R$ from the rotor origin. Roughly 8.5 million cells were used in each CH-type blade grid leading to about 22 million cells in total. For turbulence modeling and spatial discretization, the Menter-SST model and JST scheme, respectively, were used and the azimuthal time step size was $\Delta\psi = 1°$.

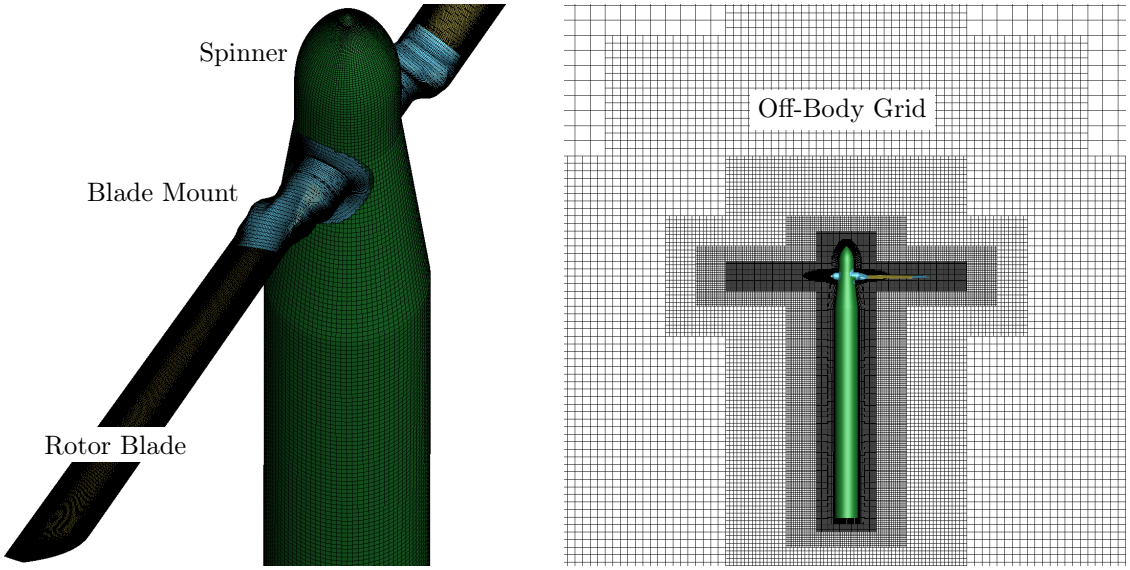

Figure 4.1: Surface grids of modeled rotor components (left) embedded in a Cartesian off-body grid (right), adapted from Letzgus et al. [38].

4.2 Pitching Motion and Mach Number

The cyclic pitch control transmitted by the swashplate leads to a 1/rev sinusoidal variation of the blade pitch angle θ that can be described as $\theta(t) = \bar{\theta} - \hat{\theta}\cos(2\pi\, f\, t)$ with $\bar{\theta}$ being the mean pitch angle, $\hat{\theta}$ the amplitude and f the rotational frequency.

First, the frequency and the mean pitch angle were kept constant with $f = 35.4\,\mathrm{Hz}$ (corresponding to a tip Mach number of $M_{\mathrm{tip}} = 0.42$) and $\bar{\theta} = 20°$ while the amplitude was varied with $\hat{\theta} = 5°, 10°, 12°$. Figure 4.2 shows the resulting polar plots of integral lift and pitching-moment coefficients of one dynamic stall cycle and, for comparison, the static pitch angle polars. Obviously, the lowest amplitude of $\hat{\theta} = 5°$ is too low to trigger dynamic stall, as the maximum pitch angle of $\theta = 25°$ is just below the static stall angle. However, choosing $\hat{\theta} = 10°$ or $\hat{\theta} = 12°$ is sufficiently high, indicated by the significant overshoot in lift and its final breakdown, the sudden and severe increase in nose-down pitching moment, and the strong hysteresis. Interestingly, the integral loads are qualitatively very similar to those of pitching airfoils (Fig. 2.4), although here the dynamic stall vortex is found to be rather three-dimensional and influenced by the tip vortex and the rotation, as revealed later in Chapter 5. Comparing the amplitudes, it shows that an increase leads to a delayed stall associated with a higher maximum lift and nose-down pitching moment, which is in accordance with findings from pitching airfoils [2, 7]. While the general flow typologies of the main dynamic stall events are very similar, it is found that the increase in pitch rate $^{\mathrm{d}\theta}/_{\mathrm{d}\psi}$ during the upstroke, which results

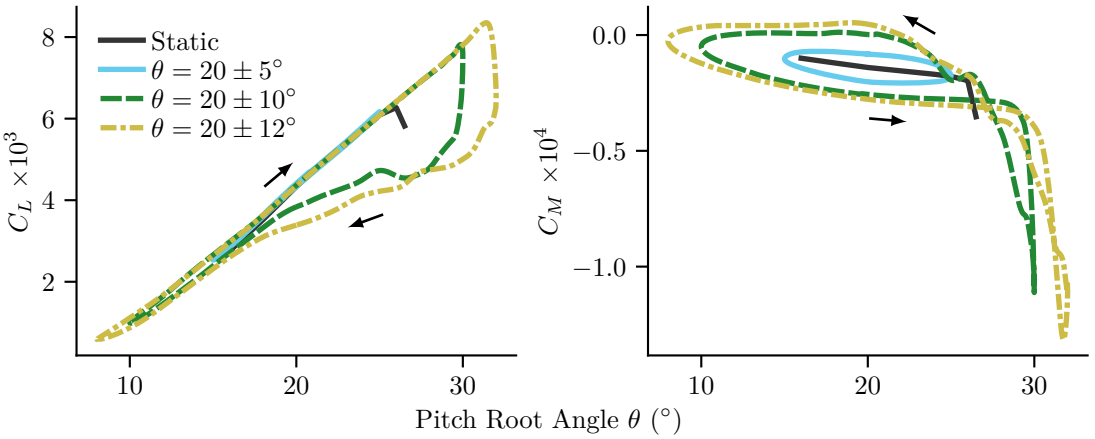

Figure 4.2: Comparison of integral lift and pitching-moment coefficients using different pitching motion amplitudes $\hat{\theta}$, $f = 35.4\,\mathrm{Hz}$. Adapted from Kozlowski [128].

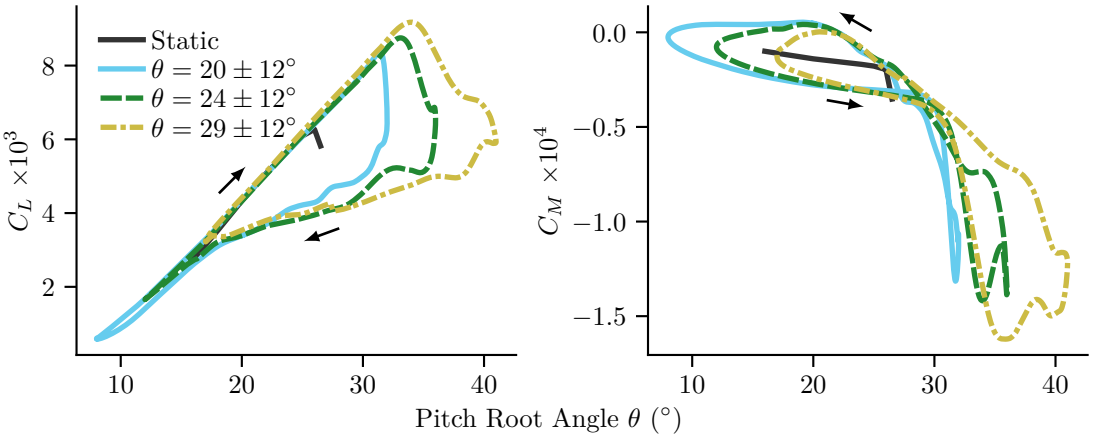

Figure 4.3: Comparison of integral lift and pitching-moment coefficients using different pitching motion mean angles $\bar{\theta}$, $f = 35.4\,\mathrm{Hz}$. Adapted from Kozlowski [128].

from an increase in the amplitude, leads to a weakened suction peak and later flow separation [128]. This is presumably due to the reduced effective angles of attack that are experienced by the rotor blade during its upstroke pitching motion, compare Section 2.4.

To study the variation of the mean pitch angle with $\bar{\theta} = 20°, 24°, 29°$, the frequency was kept at $f = 35.4\,\mathrm{Hz}$ and the amplitude was set to $\hat{\theta} = 12°$ to achieve the greatest effect. The resulting load coefficient polars plotted in Fig. 4.3 reveal that an increase of the mean pitch angle leads to higher stall angles and higher maximum values of lift and nose-down pitching moment, which was also observed for pitching airfoils [1]. Since the amplitude is identical in all three cases, so is the pitch rate. However, the pitch angle exceeds the static stall angle or rather the regime of very high pitch angles at different azimuthal positions and, thus, at different pitch

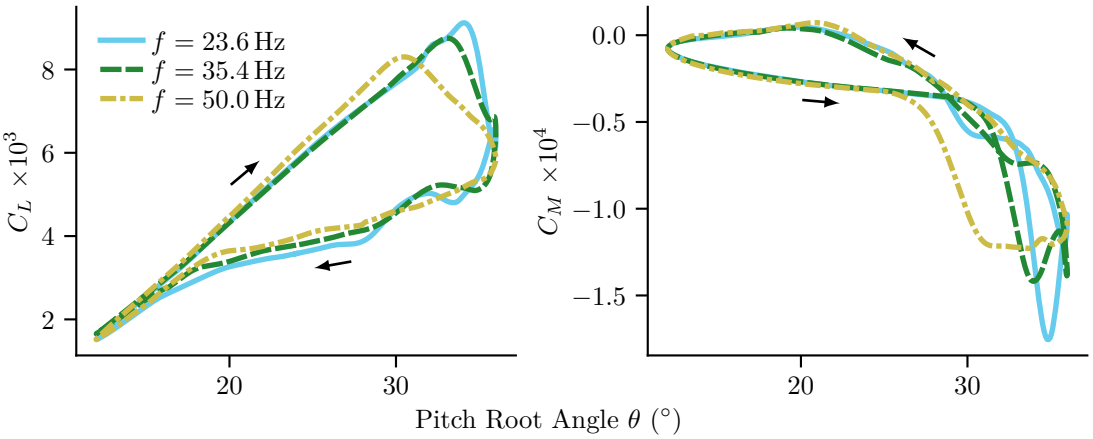

Figure 4.4: Comparison of integral lift and pitching-moment coefficients using different rotational frequencies or inflow Mach numbers, respectively, $\theta = 24° \pm 12°$. Adapted from Kozlowski [128].

rates, which alters the emergence of dynamic stall. Figure 4.3 also shows that the variants with $\bar{\theta} = 24°$ and $\bar{\theta} = 29°$ feature secondary dynamic stall events indicated by the smaller, local peaks in lift and pitching moment around the upper turning point.

Finally, the pitching motion was set to $\theta = 24° \pm 12°$ and the rotational frequency was varied with $f = 23.6\,\mathrm{Hz}, 35.4\,\mathrm{Hz}, 50.0\,\mathrm{Hz}$ and corresponding tip Mach numbers of $M_{\mathrm{tip}} = 0.28, 0.42, 0.60$, respectively. As depicted in Fig. 4.4, an increase in the rotational frequency leads to an earlier stall and an associated decrease of the lift and nose-down pitching-moment overshoot. Furthermore, the slope of the lift in the linear regime increases as well. These correlations, which are called the "Glauert effect", are well-known from static- and pitching airfoil aerodynamics and are caused by compressibility effects leading to shock-induced separation and an increase in effective angle of attack, respectively [1]. In the present investigation with $M_{\mathrm{tip}} = 0.60$, there actually is, in contrast to the two other cases, no upstream-moving trailing-edge separation but shock-induced leading-edge separation that appears to be related to the dynamic stall onset [128].

4.3 Wind Tunnel Environment

In the actual RTG experiment [37], the rotor was operated in an Eiffel-type wind tunnel that provided a low rotor-axial inflow of 2.2 $^{\mathrm{m}}/_{\mathrm{s}}$ to have defined inflow conditions for the PIV seeding and to prevent recirculation or ground effects. Unfortunately, the given circumstances only allowed for a $1.6\,\mathrm{m} \times 1.6\,\mathrm{m}$ square wind tunnel nozzle

one rotor radius in front of the rotor plane (Fig. 5.1). This gave rise to concern that the shear layer of the wind tunnel free-jet might interact with the rotor, which would lead to an even more complicated flow field. At IAG, great effort was put into simulating Eiffel-type wind tunnels using FLOWer, revealing that this is a surprisingly challenging task regarding meshing, boundary condition setup, turbulence modeling and numerical stability [129, 130, 131].

Eventually, Bußhardt [129] simulated the RTG rotor in a climb flight condition ($f = 23.6\,\mathrm{Hz}$, $\theta = 20°$) including the wind tunnel nozzle with a mean inflow velocity of $2.5\,{}^{\mathrm{m}}/_{\mathrm{s}}$ (the actual inflow velocity set in the experiment was not yet known at that time). While the outer contour of the wind tunnel was included to some extent, the actual flow in the wind tunnel was not modeled. Instead, a velocity distribution with a generic boundary-layer profile was enforced on the exit plane of the nozzle using a Dirichlet boundary condition.

Figure 4.5 shows contours of the axial flow velocity in the symmetry plane (side view) and the rotor plane (rotor-axial view) that indicate that the shear layer of the wind tunnel free-jet is significantly constricted and seems to merge with the inflow and wake of the rotor. As the nozzle shape is non-concentric, it is apparent that the interaction of the free-jet and a rotor blade is non-concentric as well and, thus, dependent on the azimuth. Consequently, the thrust generated by the rotor blade varies over one rotor revolution in the point-symmetric distribution plotted in Fig 4.6. It shows that there is a reduction in integral thrust of about five percent when the rotor blade is aligned with the diagonal of the nozzle. Considering the interaction of the shear layer of the free-jet and the rotor, this is quite plausible:

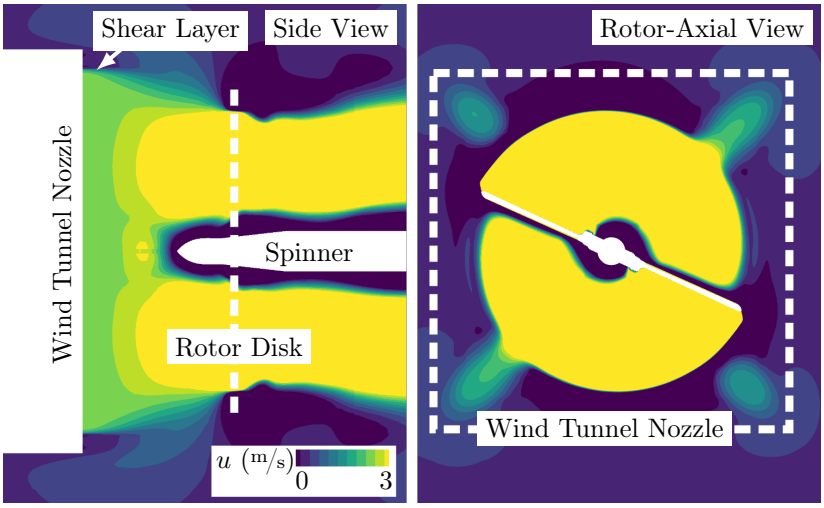

Figure 4.5: Contours of the axial velocity in the symmetry plane (side view) and the rotor plane (rotor-axial view) indicate the interaction of the shear layer of the wind tunnel free-jet and the inflow or the wake of the rotor. Adapted from Bußhardt [129].

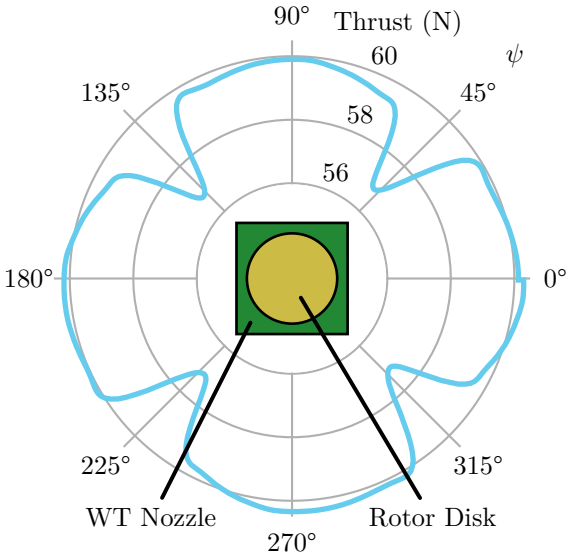

Figure 4.6: Azimuthal distribution of the thrust of one rotor blade when the wind tunnel is simulated. The orientation of the wind tunnel (WT) nozzle and the rotor disk are shown in the center, revealing a correlation of the rotor azimuth and the thrust due to the non-concentric nozzle shape. Adapted from Bußhardt [129].

The rotor-axial wind tunnel inflow reduces the effective angles of attack and by that the generated thrust of the rotor blade. However, except of the corner locations, where the rotor blade has the maximum distance to the nozzle and operates in the undisturbed jet core with a uniform inflow velocity, the outer part of the rotor blade interacts with the shear layer, in which the inflow velocity gradually drops to zero, thus the angle-of-attack-reducing effect vanishes.

Although the proof of concept was successful, the wind tunnel free-jet was not simulated in the RTG dynamic stall investigations presented in this thesis for several reasons: First, the impact of the interaction on the loads was found to be uncritical and was expected to be even weaker in the experiment where the inflow velocity was 12% lower. Then, matching the actual free-jet in CFD was believed to be almost impossible or at least subject to great uncertainty, as no measurements of the wind tunnel boundary and shear layer were available for validation. Furthermore, the significantly increased complexity of the CFD setup and reduced numerical stability and grid-wise flexibility would have made the high-fidelity dynamic stall computations even more challenging. Lastly, a comparison of numerical results between different approaches and flow solvers would have been aggravated by including the free-jet only in some cases. Instead of considering the free-jet shear layer, simply applying a uniform axial inflow resulted in good agreement with the experiment, as shown in Section 5.2.1.

4.4 Chapter Conclusions

Numerical pre-studies using a lower-resolution setup of the RTG rotor were carried out to investigate the influence of the rotor blade's pitching motion and inflow Mach number on dynamic stall. In addition, the RTG wind tunnel environment with the associated free-jet shear layer was simulated to study its interaction with the rotor. The main findings are as follows:

1. By applying large cyclic pitch control, dynamic stall, that is, a severe overshoot in lift and nose-down pitching moment and a strong hysteresis, can be triggered on a rotor in a hover-like flight condition.

2. Increasing the mean pitch angle or the amplitude of the sinusoidal pitching motion of the rotor blade leads to a delay of the dynamic stall onset and to a higher overshoot in integral lift and nose-down pitching moment due to unsteady boundary-layer effects.

3. Increasing the rotational frequency and thus also indirectly the pitch rate, leads to a higher slope of the lift polar in the linear regime and to an earlier dynamic stall onset due to compressibility effects.

4. The aforementioned findings are in accordance with reported observations made on pitching airfoils. In a way, this fact "justifies" the numerous investigations of "two-dimensional" dynamic stall, as the fundamental principles are applicable to rotor dynamic stall as well.

5. The shear layer of the RTG wind tunnel free-jet is constricted by the rotor and interacts with its inflow or wake, however, the impact on integral rotor thrust is not severe. Due to the overall significantly increased numerical complexity that comes with modeling the wind tunnel, applying a simple uniform axial inflow is recommended instead.

5 Simulation of Dynamic Stall on a Model Rotor in Axial Inflow

In this chapter, numerical computations of three-dimensional dynamic stall on a two-bladed model rotor ($R = 0.65\,m$, $M_{\text{tip}} = 0.28$, $Re_{\text{tip}} = 4.7 \times 10^5$) with 1/rev cyclic pitch control are presented and compared to experimental surface pressure and PIV data for validation. In addition to URANS simulations using the finite-volume flow solvers FLOWer and TAU[1], a DDES with Menter-SST as underlying RANS model was carried out with FLOWer to assess the general applicability and necessity of a hybrid RANS/LES approach in the field or rotor dynamic stall. The chapter is essentially based on Letzgus et al. [39] and has been expanded by a detailed study of the experimental cycle-to-cycle variation.

5.1 Setups and Flow Condition

First, the experimental and numerical FLOWer and TAU setups are described. Also, the flow conditions and the rotor blade pitching motion of the investigated dynamic stall case are introduced.

5.1.1 Experimental Setup

The experiments were conducted in the rotor test facility (RTG) at DLR in Göttingen. The rotor axis was horizontally mounted on a test bench that was integrated into an Eiffel-type wind tunnel with a rectangular nozzle, providing a well-defined inflow. Figure 5.1 shows the CAD model of this setup. The axial inflow leads to a climb-flight-like condition but ensures an undisturbed outflow preventing ground effect and flow recirculation. A swashplate was used to introduce a sufficiently large cyclic pitch variation which triggers dynamic stall. Since there was no edgewise inflow, the stationary part of the swashplate was rotated to investigate the flow field of the whole pitching cycle without costly repositioning of the PIV system. The rotor radius R is 0.65 m, the rotor

[1]The TAU computations were conducted by Anthony Gardner at DLR Göttingen. The solver output was provided to the author of the present thesis who carried out the post-processing and the analysis.

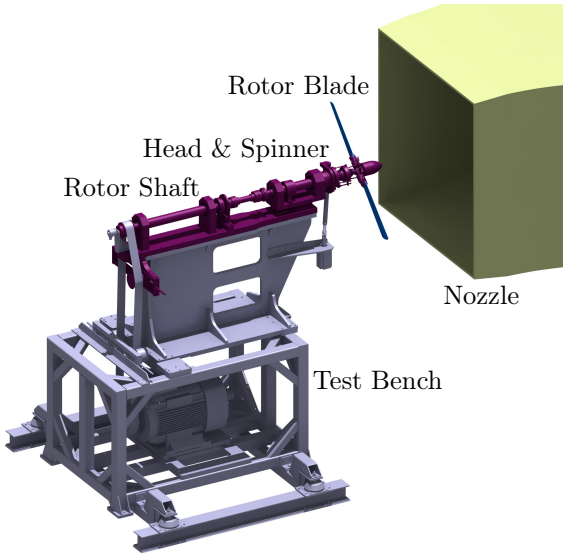

Figure 5.1: CAD model of the rotor test bench in front of the wind tunnel nozzle [39].

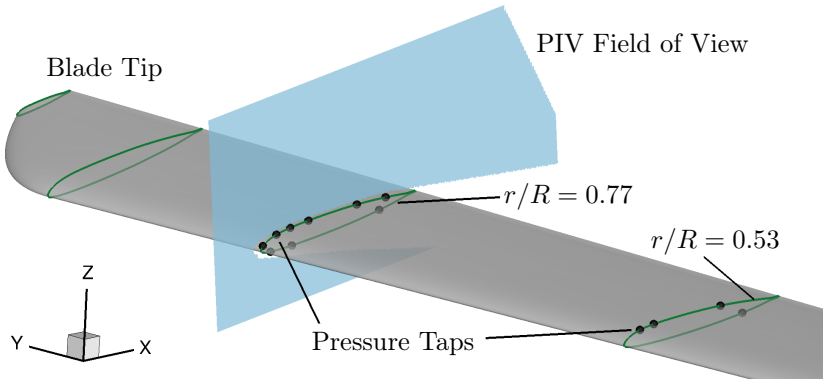

Figure 5.2: Sketch of the positions of the pressure taps and field of view of PIV in the experiment [39].

blade has a chord length c of 72 mm and uses a DSA-9A airfoil shape with a parabolically shaped SPP8 blade tip without anhedral. A linear negative twist of $-9.3°$ towards the tip is incorporated. Unsteady Kulite LQ-062 sealed gauge pressure transducers are installed in two radial stations at $r/R = 53\%$ and $r/R = 77\%$. Their chordwise positions and the field of view of the PIV measurement are sketched in Fig. 5.2. During one rotation of the stationary part of the swashplate, 8400 dynamic stall cycles were acquired and considered for phase averaging of the pressure data. Since at every third revolution a PIV image was taken, the dynamic stall cycle was covered by 2800 non-consecutive, instantaneous PIV images. Furthermore, PIV data at four other radial stations and tuft visualizations were obtained but are not evaluated here. A more detailed overview of the RTG is found in Schwermer et al. [132]. A detailed description of the experimental setup and a comprehensive analysis of the experimental data for the dynamic stall case were presented recently by Schwermer et al. [37].

5.1.2 Numerical Setup: FLOWer

The numerical investigations conducted at IAG used the flow solver FLOWer with the standard settings listed in Section 3.4. For spatial discretization, the second-order JST scheme with $k^{(4)} = 1/64$ (FLOWer's default value) was applied, since preliminary computations showed that the fifth-order WENO scheme introduces implausible high-frequency pressure fluctuations in the boundary layer while barely having an impact on the sectional loads. In the off-body grid, the very high spatial resolution was believed to sufficiently capture all relevant flow features. For turbulence modeling, the Menter-SST as well as the SA model were used (standard formulations, no curvature/rotation corrections). In general, a hybrid RANS/LES modeling approach is believed to improve numerical investigations of separated flow, since in the LES region of the computational domain the eddy viscosity introduced by a turbulence model is considerably reduced, and large-scale, energy-containing turbulent structures are resolved (Section 3.3). Therefore, in addition to the URANS simulations, a DDES was carried out with Menter-SST as underlying RANS model [110]. The maximum cell length $\Delta_{\max}$ in each index direction was taken as the LES filter width. Validation and first applications of DDES with the flow solver FLOWer were recently shown by Weihing et al. [124].

On the FLOWer side, two grids were investigated. The first one, denoted *baseline*, represents a typical high-resolution CH-type URANS grid and was taken from a previous investigation of the author [38]. There, a grid dependency study of the present configuration was carried out, although with somewhat different flow conditions ($f = 50\,\mathrm{Hz}$, $M_{\mathrm{tip}} = 0.6$). The results showed that a setup with roughly double the chordwise grid size at leading and trailing edge and double the grid size in the background grid ($\Delta s/c = 10\%$) give very similar lift and pitching moments during dynamic stall. However, only integral loads were compared. In general, resolution of the baseline grid are quite similar to those of other dynamic stall investigations [133, 81, 80]. The second grid, denoted *fine*, was optimized for a DES approach, as the spanwise spatial resolution was significantly increased. This grid was not only appropriate to resolve highly three-dimensional stalled flow, but the LES region inherently benefits from cubic cells, since, with the LES filter width, a refinement in only one or two directions would be wasteful and contradict the LES approach of filtering out isotropic turbulence [134]. Therefore, a dynamic stall focus region, based on results of preliminary URANS simulations, was specified, which covered the suction side of the rotor blade and the near wake with a grid size of 0.5% c, see Fig. 5.3. To enable this local refinement of a structured grid, a two-part blade grid of the CH-type was used. A fine near-wall grid with chordwise clustering near leading and trailing edge, based on gridding guidelines of AIAA's 6th Drag Prediction Workshop [135], covered the boundary layer. To reduce the number of

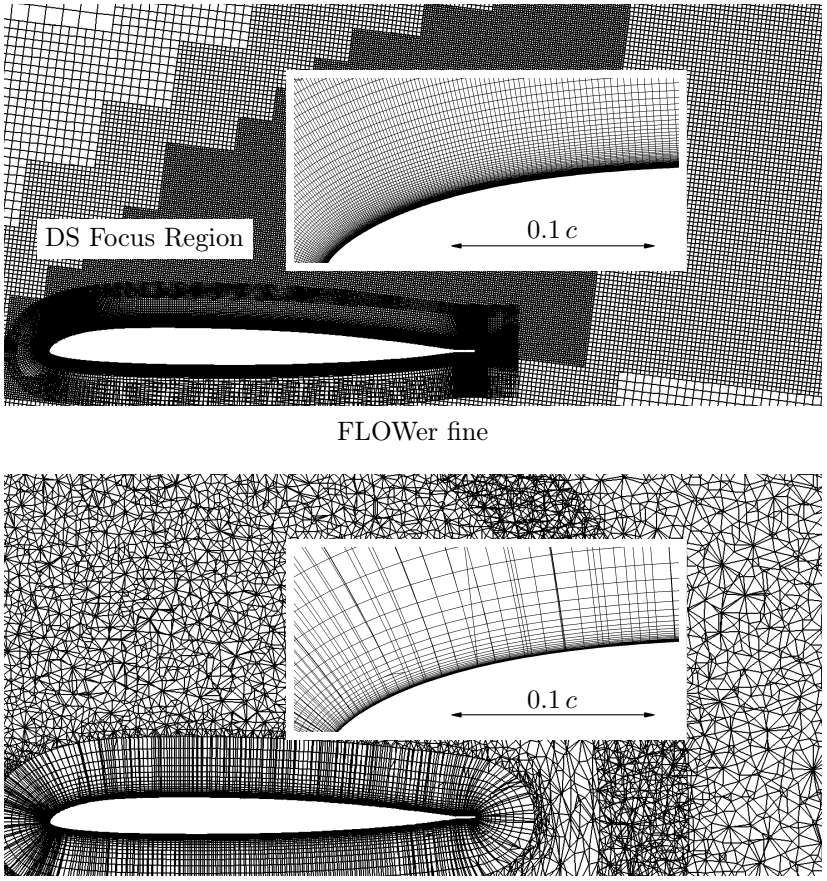

Figure 5.3: Spanwise slices at $r/R = 0.77$ through FLOWer fine and TAU grid and details of upper side of nose region [39].

grid cells, the chordwise resolution was coarsened on the lower side of the rotor blade. Also, a hanging grid-nodes interface was used to halve the spanwise resolution there. A Chimera interface then connected this grid with an auto-generated Cartesian far-wall blade grid with only cubic cells, which also used the hanging grid-nodes technique to refine or coarsen the grid. The interface between the two blade grids was located about 8% c above the surface, just outside the boundary layer in case of attached flow. For the fine setup, an additional Chimera C-type cap grid was required to mesh the parabolic tip of the rotor blade, as the pressure side had a lower spatial resolution than the suction side. Cell sizes and further grid data are shown in Table 5.1. The baseline as well as the fine rotor blade grids were embedded into a Cartesian background grid with $\Delta s_{\text{finest}}/c = 5\%$ and $\Delta s_{\text{finest}}/c = 4\%$, respectively, which extended to a distance of $6R$ and $10R$, respectively, from the rotor origin. A simplified blade mount and spinner were modeled as shown in Fig. 5.4. The boundary layer of the spinner was not resolved and an inviscid wall boundary condition (BC) was applied at the spinner surface.

Table 5.1: Cell sizes and grid data. Directions: x chordwise, y spanwise, z normal.

	TAU	FLOWer baseline	FLOWer fine
$\Delta x/c$ leading edge (%)	0.09	0.05	0.06
$\Delta x/c$ trailing edge (%)	0.15	0.05	0.06
$\Delta y/c$ blade tip (%)	0.11	0.90	0.08
Max. $\Delta x/c$ (upper side) (%)	1.15	0.80	0.50
Max. $\Delta y/c$ (upper side) (%)	3.00	6.00	0.50
Δz_1 (first cell height) (m)	3.4×10^{-6}	9.8×10^{-7}	8.0×10^{-7}
Growth rate boundary layer	1.25	1.15	1.10
Total grid nodes (million)	31.1	56.7	238.3

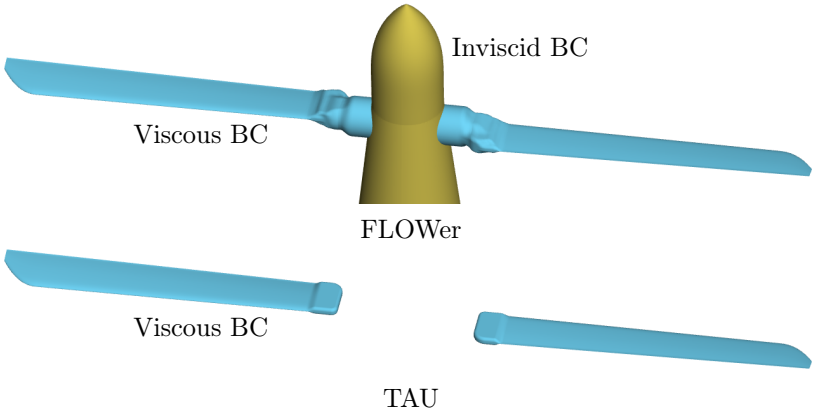

Figure 5.4: Modeled surfaces and boundary conditions (BC) of the numerical setups: FLOWer with rotor blades, simplified blade mount, spinner and shaft, TAU with isolated rotor blades [39].

Regarding the temporal resolution of simulations facing three-dimensional dynamic stall, recent URANS investigations [136, 48, 25] showed that an azimuthal time step of $\Delta\psi = 1/4°$ (1440 steps/cycle) or even larger is sufficient to reliably resolve the characteristic lift and nose-down pitching moment peaks. These findings are consistent with a time step dependency study carried out before [38] based on the RTG case that showed that a further reduction of the time step had no significant influence on integral lift and pitching moment. However, other numerical investigations of separated flow around airfoils or finite wings [134, 71, 94, 80] used much smaller time steps – especially if a DES was carried out – on the order of $\Delta t = \Delta_0/u_{max}$, with Δ_0 being the smallest grid size and u_{max} the largest flow velocity in the respective region.

Today, using $\Delta t = \Delta_0/u_{max}$ is computationally not feasible for rotor applications, since many revolutions must be simulated for the flow to reach a quasi-periodic state. Nevertheless, preliminary investigations showed that at least an azimuthal time step of $\Delta\psi = 1/12°$ (4320 steps/cycle) for the baseline setup and $\Delta\psi = 1/24°$ (8640 steps/cycle) for the fine setup was necessary to suppress numerical instabilities in

the form of high-frequency surface pressure fluctuations in the region of leading-edge flow separation. The dual-time stepping scheme used 20 to 65 inner iterations, depending on the drop of the global root mean square of the density residual. To save computational resources, a tolerance level was used to reduce the residuals by at least an order of magnitude, which was verified to be sufficient for reasonable inner-iterations convergence of sectional loads.

For the dynamic stall case, roughly 13 rotor revolutions were computed to bridge the initial transient, followed by four more rotor revolutions using the small time step. The FLOWer computations were carried out on the Cray XC40 cluster of the High Performance Computing Center Stuttgart (HLRS), where the baseline and fine grid were split into 3200 and 15900 blocks, respectively, and used 2280 and 13200 cores, respectively. For one rotor revolution with final settings, a wall time of approximately 16 and 37 hours was required for the baseline and fine grid cases, respectively.

Both the FLOWer and TAU setup used rigid rotor blades. In the experiment, a constant untwisting of the rotor blades of 0.8° and a maximum tip displacement of $0.4c$ in flap direction was measured in the dynamic stall case due to blade elasticity [37]. This introduces another discrepancy between the simulations and the experiment, which is not analyzed further in this work.

5.1.3 Numerical Setup: TAU

Additional computations were conducted at DLR Göttingen with DLR's second-order finite-volume URANS solver TAU [137], which uses unstructured hybrid grids, an implicit backward Euler time integration and four-level multigrid method. Again, both the Menter-SST and SA turbulence model were used (standard formulations, no curvature/rotation corrections) and the flow was considered fully turbulent. While the boundary-layer region used prism layers, tetrahedral cells were added to the surrounding region, which extended to conservatively chosen $920R$, see Fig. 5.3. The grid points were distributed according to Kaufmann et al. [79], who investigated static and dynamic stall on an OA209 finite wing using TAU and carried out a grid and time step dependency study. Further grid information is listed in Table 5.1. The pitching motion was resolved with 1800 azimuthal time steps per period ($\Delta\psi = 0.2°$) using 800 inner iterations, which reduced the residuals by three orders of magnitude. As Fig. 5.4 shows, the TAU setup only modeled the surface of the two rigid rotor blades.

For the dynamic stall case, ten rotor revolutions were computed using a coarse time step of $\Delta\psi = 3.6°$, followed by six revolutions using the smallest time step. The TAU computations, which were carried out on the SuperMUC cluster of the Leibniz Supercomputing Centre, required about 250,000 core hours per rotor revolution.

5.1.4 Flow Conditions and Pitching Motion

The rotor was operated at a rotational frequency of $f = 23.6\,\mathrm{Hz}$ (oscillation period $T = 0.042\,\mathrm{s}$), with a Mach number of 0.21 and a Reynolds number of 3.5×10^5 at 75% rotor radius. To trigger dynamic stall, the sinusoidal variation of the root pitch angle was $\theta(t) = 23.8° - 6.2°\cos(2\pi\, f\, t)$. The experiments were carried out with a wind tunnel exit velocity of $2.2\,\mathrm{m/s}$, the corresponding numerical investigations therefore used a uniform axial inflow velocity of $2.2\,\mathrm{m/s}$.

5.2 Numerical Results

Using FLOWer and TAU, both a static hover case and a dynamic stall case were computed and compared to measurements for validation.

5.2.1 Static Hover Case

To gain confidence in the numerical setups, the hover test case with 24° static root pitch angle was investigated first. This root pitch angle was about 2.7° below the static stall angle and lead to a highly loaded rotor with fully attached flow. Fig. 5.5 shows pressure distributions that exhibit an overall good agreement between URANS computations and experiment, also very good agreement is shown between FLOWer (baseline) and TAU, both using the Menter-SST turbulence model. The computations yield slightly higher lift at the leading part of the suction side, where free laminar-turbulent transition occurs in the experiment around $x/c = 0.1$ [37]. In this case, the rotor thrust measured via a dynamometer is 150.4 N compared to 150.9 N (+0.3%) computed by FLOWer.

Interestingly, the pressure distributions at $r/R = 0.31$ computed by both analyses agree well, although the modeled geometries strongly differ at the blade root, which begins at $r/R = 0.25$ (recall Fig. 5.4). The good numerical results of this static hover case suggest that influences of blade elasticity, test bench, rotor head and shear layer of the wind tunnel free-jet have a negligible influence on the blade pressure distributions, at least in hover.

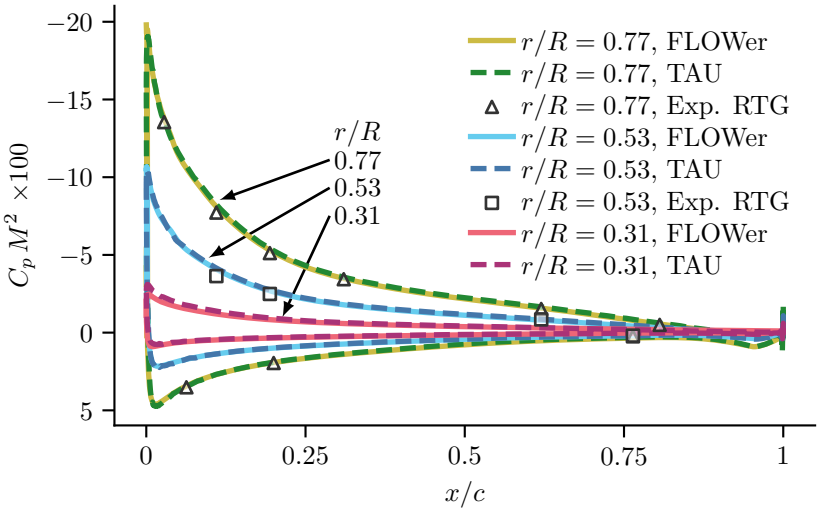

Figure 5.5: Pressure distributions of FLOWer baseline (SST URANS), TAU (SST URANS) and experiment for a highly loaded hover case with a static root pitch angle of $\theta = 24°$. Adapted from Letzgus et al. [39].

5.2.2 Dynamic Stall Case

FLOWer URANS and DDES Investigations

To introduce the general flow process of dynamic stall on the RTG rotor, a qualitative and brief overview by means of λ_2 isosurfaces [138] is given in Fig. 5.6 based on the URANS solution using the fine grid. At $t/T = 0.46$, the evolution of the dynamic stall vortex is visible near the leading edge, while the vortical structure further downstream is found to be a rollup of the separated shear layer, which is associated with trailing-edge separation. Moving on in time to $t/T = 0.48$, the typical Ω-shape of the vortex, which spreads outboard, lifts from the surface, convects downstream and grows, is more noticeable. This evolution continues beyond the upper turning point ($t/T = 0.5$) until the dynamic stall vortex passes the trailing edge around $t/T = 0.52$, where it has also almost reached its maximum spanwise extent. The λ_2 isosurfaces near the leading edge that are lifted from the surface indicate a separated shear layer and complete leading-edge separation, which typically follows the primary dynamic stall event.

A key aspect that is associated with the just mentioned vortex shedding is the overshoot of lift and nose-down pitching moment. Here, the sectional load coefficients at the radial station $r/R = 0.77$, where nine pressure sensors are available in the experiment, are compared. Unless otherwise stated, the numerical coefficients were integrated from surface pressures calculated at the nine experimental pressure tap positions (see Fig. 5.2) as well. All loads were obtained using a first-order trapezoidal integration scheme.

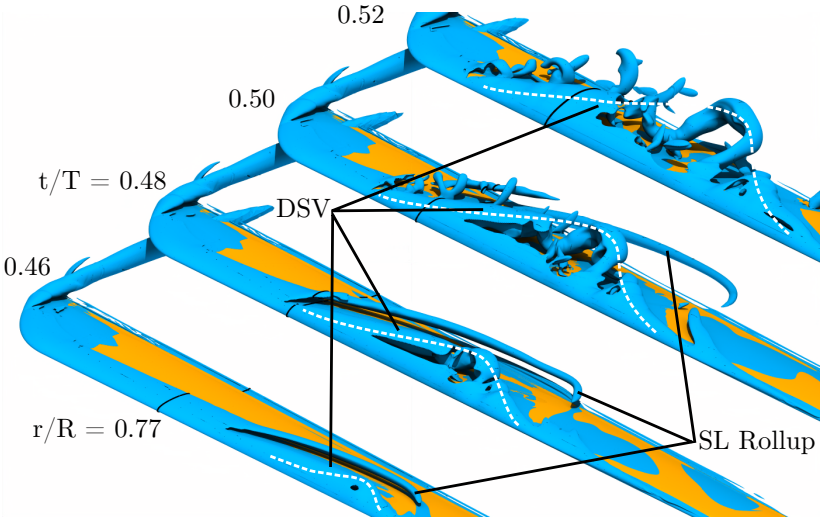

Figure 5.6: Evolution and convection of the dynamic stall vortex (DSV) and shear-layer (SL) rollup visualized by instantaneous λ_2 isosurfaces and estimated vortex core (dashed white line) at several points during the cycle using SST URANS fine.

In Fig. 5.7, the FLOWer load coefficients are compared to the measurements. The error bars represent the standard deviation of the phase-averaged experimental data, the numerical results are phase-averaged over the last two rotor revolutions, or four dynamic stall cycles. First, Fig. 5.7 shows that the URANS results using the baseline and the fine grid are very similar during the whole upstroke and minor differences are only found during the downstroke, when the polars exhibit a strong hysteresis due to complete flow separation. Secondly, URANS and DDES load coefficients are the same during most part of the upstroke until $\theta \approx 27° \uparrow$. During this linear phase, FLOWer yields a slightly higher lift and pitching moment than the experiment, especially at the lower turning point of the cycle. Here, laminar-turbulent transition occurs on the suction side around $x/c = 0.19$ in the experiment [37], which might explain the offset of the simulations, which were run fully turbulent. During the upstroke, the transition point moves upstream, its foremost measurable location is around $x/c = 0.11$ at $t/T = 0.23$. Although transition could never be detected at the foremost pressure sensor at $x/c = 0.03$, the transition point is expected to move further upstream until the onset of flow separation.

Continuing the upstroke until $\theta \approx 29° \uparrow$, the lift of DDES and experiment stops rising, while the slope of the lift of both URANS solutions remain constant. Then, with DDES, a strong peak in additional lift and (negative) nose-down pitching moment occurs more than 0.5° earlier than in the experiment or with URANS, which stalls last. This peculiarity of the DDES appears to be a modeling error that is studied later in more detail. Just before the upper turning point, the pitching moment rises to a pre-stall level and then drops rapidly again, as the blade starts to pitch down.

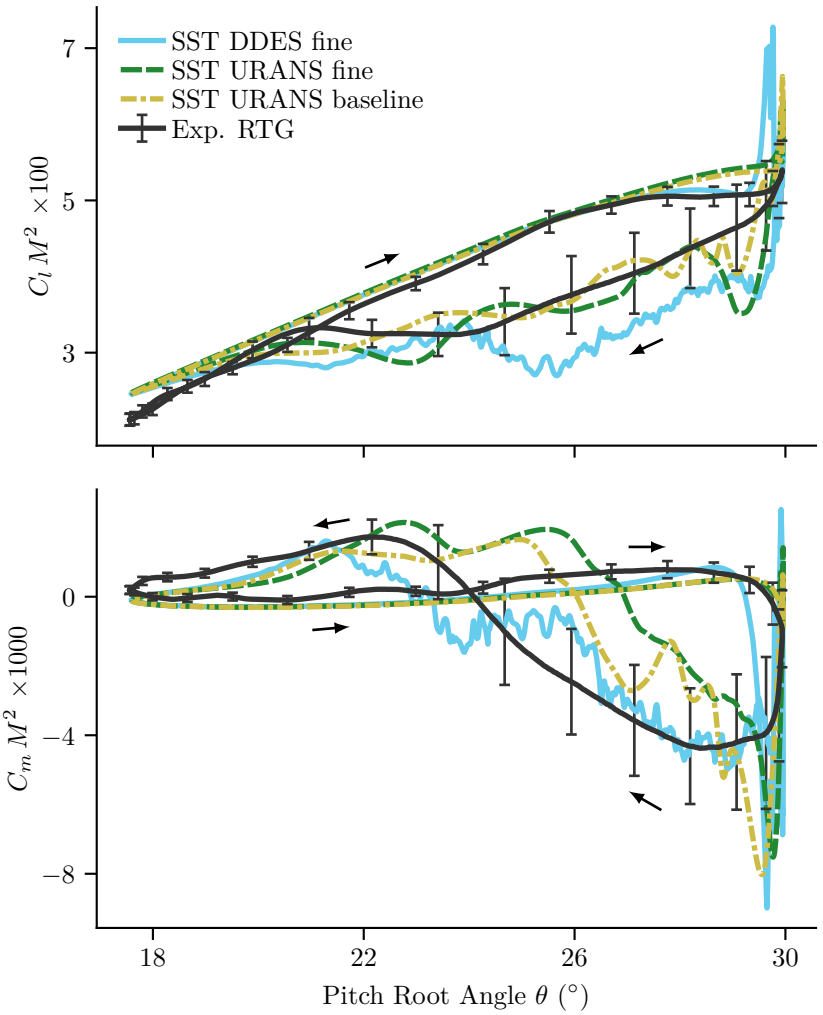

Figure 5.7: Comparison of experimental (phase-averaged) and numerical FLOWer (phase-averaged over four dynamic stall cycles, baseline and fine grid used) sectional lift and pitching-moment coefficients at $r/R = 0.77$. Adapted from Letzgus et al. [39].

During the downstroke, lift hysteresis of DDES is strongest and URANS agrees better with the experiment. Regarding the pitching moment, the URANS solutions show a somewhat earlier recovery and are in worse agreement than DDES.

Here, the computational maxima of lift and pitching moment exceed the phase-averaged maximum of the experiment significantly and occur as distinct peaks. However, phase-averaging of experimental pressure data can cancel out peak values, as stall onset and aerodynamic peak values change significantly from cycle to cycle [139, 81]. Therefore, non-phase-averaged load coefficients of four consecutive, arbitrarily chosen dynamic stall cycles are plotted in Fig. 5.8, revealing that the experimental lift as well as the pitching moment reach peak values comparable to those of the computations. Note that although evaluating only four

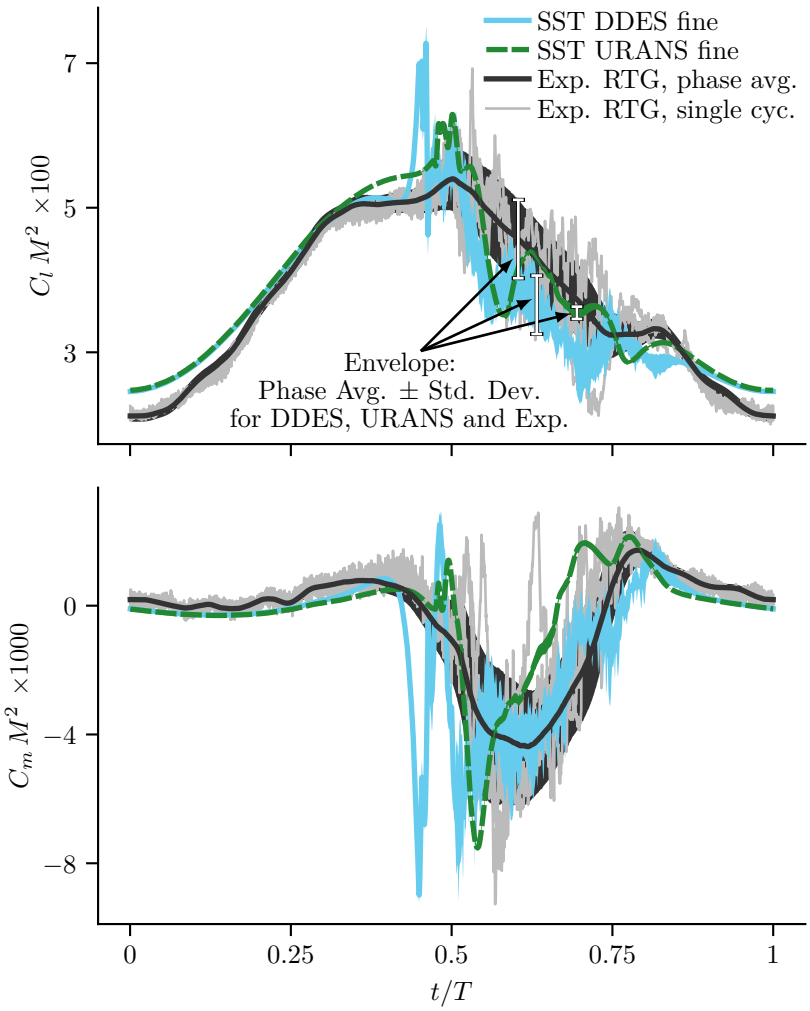

Figure 5.8: Phase-averaged lift and pitching-moment coefficients with envelopes of standard deviation at $r/R = 0.77$ to assess the cycle-to-cycle variations of experiment (8400 cycles) and FLOWer simulations (four cycles each). Additionally, experimental results of four randomly chosen single cycles are plotted.

random cycles, the experimental pitching moment of one cycle exhibits an extreme peak around $t/T = 0.63$, which illustrates the somewhat non-deterministic behavior of the flow in the stalled regime. A detailed study of the cycle-to-cycle variations of the measurement follows in Section 5.3. Concerning the computations, phase-averaged lift and pitching-moment coefficients and the envelopes of the standard deviation of four consecutive cycles using URANS and DDES are also depicted in Fig. 5.8. It shows that there is almost no cycle-to-cycle variation with URANS, even during the downstroke when flow is massively separated. In contrast, DDES yields increased standard deviations comparable to those of the experiment due to high-frequency fluctuations and cycle-to-cycle variations.

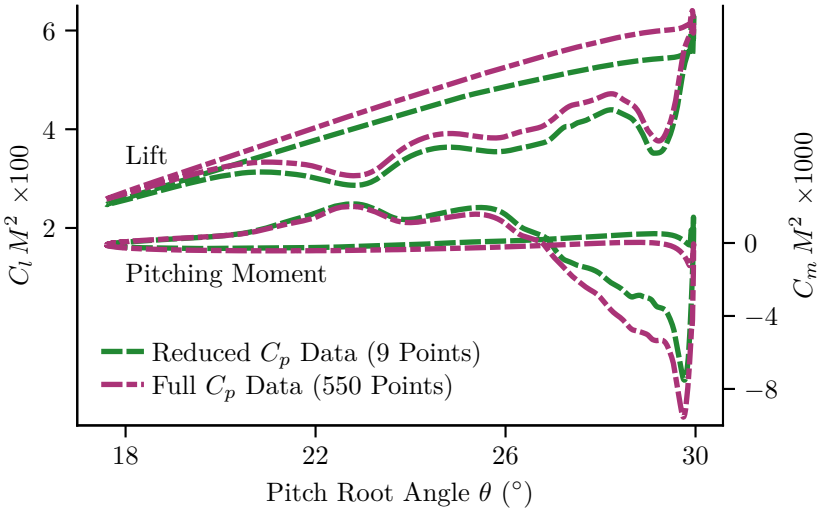

Figure 5.9: Comparison of sectional lift and pitching-moment coefficients of FLOWer URANS using all surface pressure data and sensor-reduced data, respectively, to assess the discretization error of using only nine pressure taps.

To assess the discretization error which is made by considering only nine pressure taps, the loads of the URANS simulation integrated from full-resolution and reduced surface pressure data are plotted in Fig. 5.9. It is apparent that the lift based on the nine tap locations is slightly lower basically at all times. The largest error of 9% is found between the linear regime and lift stall. Likewise, the nose-down pitching moment is higher using only reduced data, especially looking at the moment stall peak value, which is weakened by 20%. However, in general, the loads are qualitatively very similar and all load features are preserved despite the reduction of integration locations.

Judging only from Fig. 5.7 and 5.8, the characteristic dynamic stall event – a sudden peak in nose-down pitching moment and lift overshoot around the upper turning point – seems to simply occur earlier in the cycle of the DDES. Facing premature separation in combination with a DES approach, the well-known issue of modeled stress depletion causing grid-induced separation comes to mind, compare Section 3.3. Here, the LES region intrudes too far into the boundary layer, which reduces the Reynolds stresses and consequently the modeled transfer of momentum. Figure 5.10 shows vorticity contours and the RANS/LES interface ($f_d = 0.5$) of the DDES simulation at $r/R = 0.77$ at an early point during the upstroke. Also, boundary-layer calculations of DDES and URANS at a wall-normal extraction location (EL) at $x/c \approx 0.75$ are depicted. It becomes apparent that with DDES, the viscosity ratio ν_t/ν is in fact reduced in the outer part of the boundary layer, where the shielding function $1 - f_d$ drops from one to zero. In theory [96], $1 - f_d$ should not drop to zero until the edge of the boundary layer marked by δ, though the LES

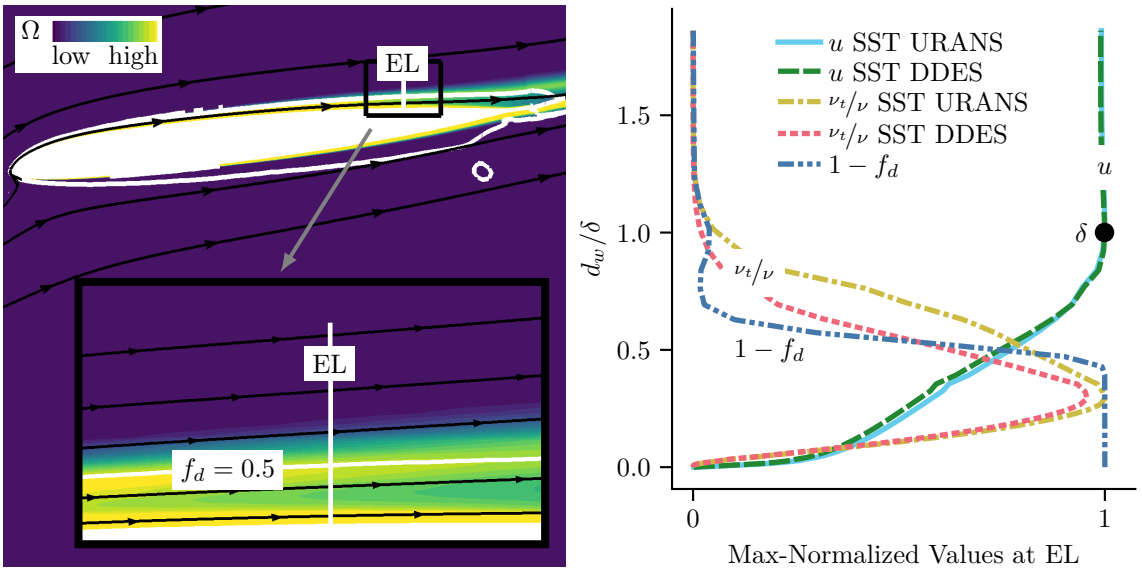

Figure 5.10: Boundary-layer calculations (right) of FLOWer fine SST URANS and DDES at $r/R = 0.77$, $x/c = 0.75$ and $t/T = 0.3$ ↑ at the wall-normal extraction location (EL) indicated by the white line on the spanwise slice (left) showing vorticity contours and the $f_d = 0.5$ isoline marking the RANS/LES interface. The ν_t/ν curves are normalized with $\max(\nu_t/\nu)$ of URANS.

mode in this case is activated at half of the boundary-layer height. Recently, similar observations with high-resolution DDES facing adverse pressure gradients were made by others [91, 113, 114, 115], who proposed some recalibrations of the model. In summary, it is assumed that grid-induced separation occurs in this DDES, although the flattening of the lift polar around $\theta = 27°$ ↑ agrees well with the experiment. This means that the earlier onset of trailing-edge separation predicted by the DDES might be physically correct but is caused by a modeling error, as the separation process should be – provided a correct boundary-layer shielding – governed by the underlying RANS model, which could then lead in fact to a worse agreement with the measurement. A detailed analysis and, eventually, a confirmation and a remedy of this issue is presented in the following Chapter 6.

Figure 5.11, showing surface streamlines on the suction side, reveals that with DDES, the upstream and outboard extent of trailing-edge flow separation is larger than with URANS at earlier stages of the cycle ($t/T = 0.37$, 0.40). Likewise, instantaneous in-plane streamlines at $r/R = 0.77$ indicate a distinct region of flow recirculation above the trailing edge only with DDES, see $t/T = 0.40$ in Fig. 5.12. The growing trailing-edge flow separation observed in all simulations resembles Leishman's definition [1] of the first stage of dynamic stall.

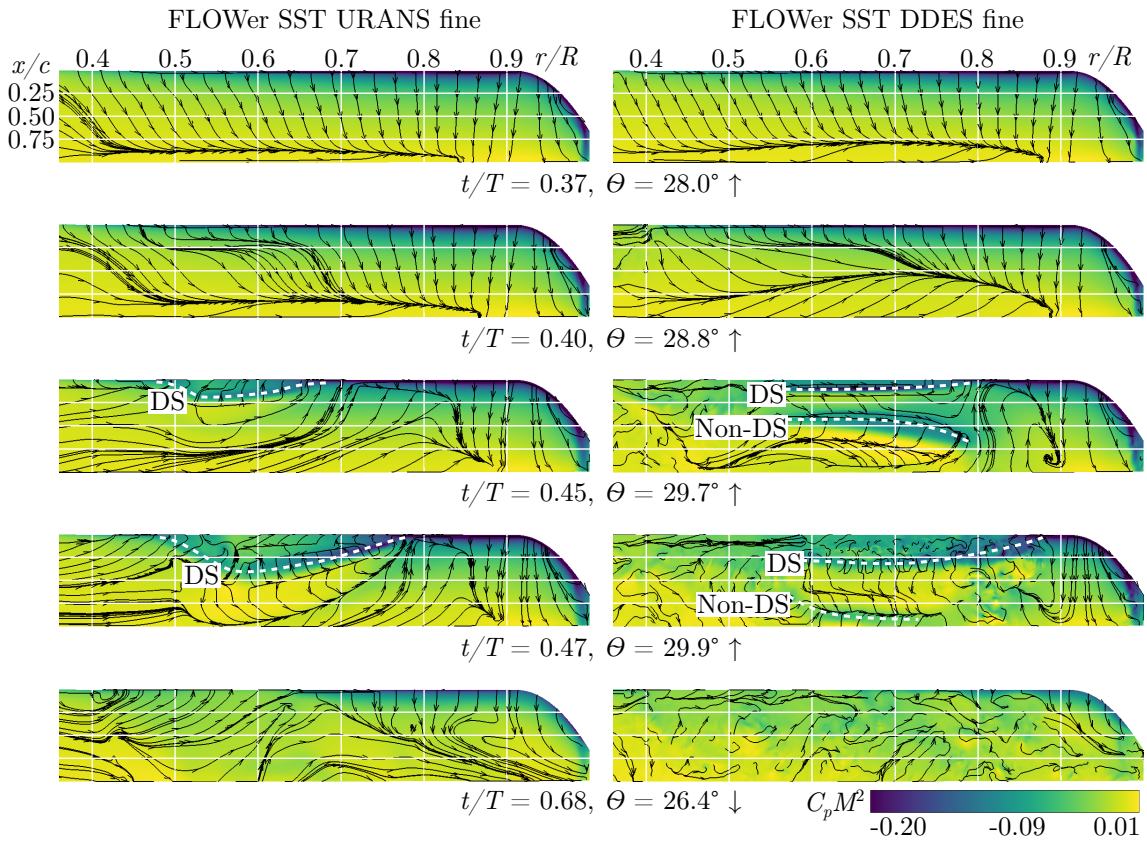

Figure 5.11: Comparison of instantaneous distributions of surface pressure and surface streamlines on the suction side between FLOWer URANS and DDES at several points during one cycle of dynamic stall. Adapted from Letzgus et al. [39].

As highlighted in Fig. 5.11 at $t/T = 0.45$, the DDES surface solution exhibits very low pressure around mid-chord between $0.55 < r/R < 0.83$. This region looks somewhat similar to the footprint of a dynamic stall vortex of a URANS simulation, and indeed, the recirculation zone evolving at the trailing edge has grown and moved upstream, forming a strong vortex around mid-chord that induces massive flow reversal (Fig. 5.12). This vortex evolves from the free shear layer at a fixed chordwise position and must not be confused with a dynamic stall vortex convecting from the leading edge and is therefore referred to as *non-DS*. Quite the contrary, the beginning of a dynamic stall event is seen just downstream of the leading edge between $0.55 < r/R < 0.75$ (Fig. 5.11). The event is more obvious in Fig. 5.13, where low pressure peaks in the pressure distributions near the leading edge indicate dynamic stall. Thus, the earlier peaks of nose-down pitching moment and lift observed in the DDES load polars are the result of short-term low pressure around mid-chord, which is neither present in the experiments nor in the URANS simulations. The low pressure peaks, which are not caused by dynamic stall, are believed to be related to the gray-area problem (Section 3.3). In this case, the free shear-layer breakup is non-physically delayed, which seems to allow the mentioned

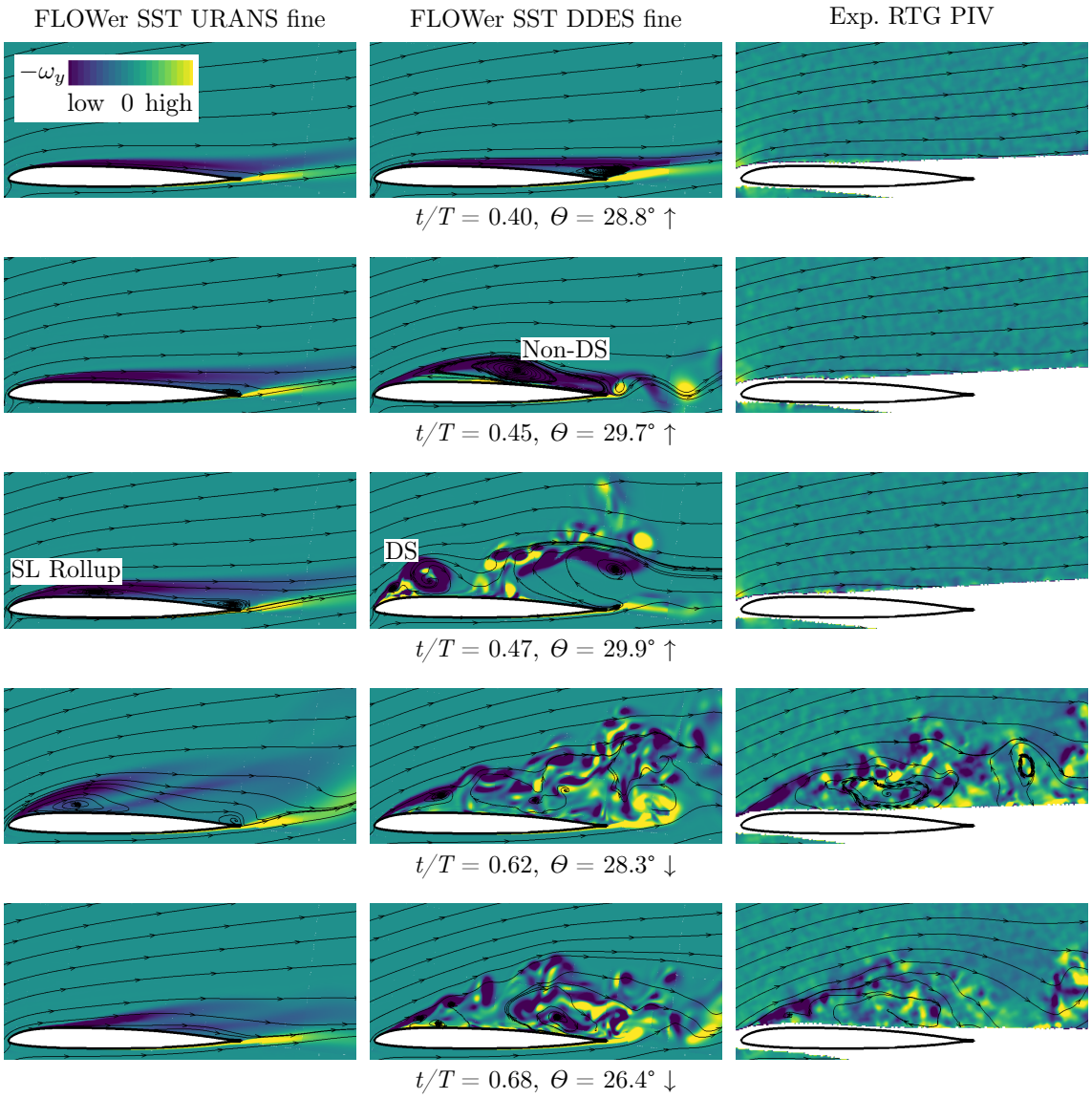

Figure 5.12: Comparison of contours of instantaneous in-plane vorticity and in-plane streamlines at $r/R = 0.77$ between FLOWer computations and experiment at several points during one cycle of dynamic stall. Adapted from Letzgus et al. [39].

non-dynamic-stall vortex to roll up and to gain such strength. According to high-fidelity LES investigations [74] and PIV measurements [13] of the dynamic stall onset on oscillating airfoils, the free shear layer resulting from trailing-edge separation should quickly develop downstream-convecting small-scale vortical structures due to the Kelvin-Helmholtz instability. For the present scenario, a possible gray-area mitigation by using the filter width Δ_{SLA} instead of $\Delta_{\max}$ is studied in Section 6.6.

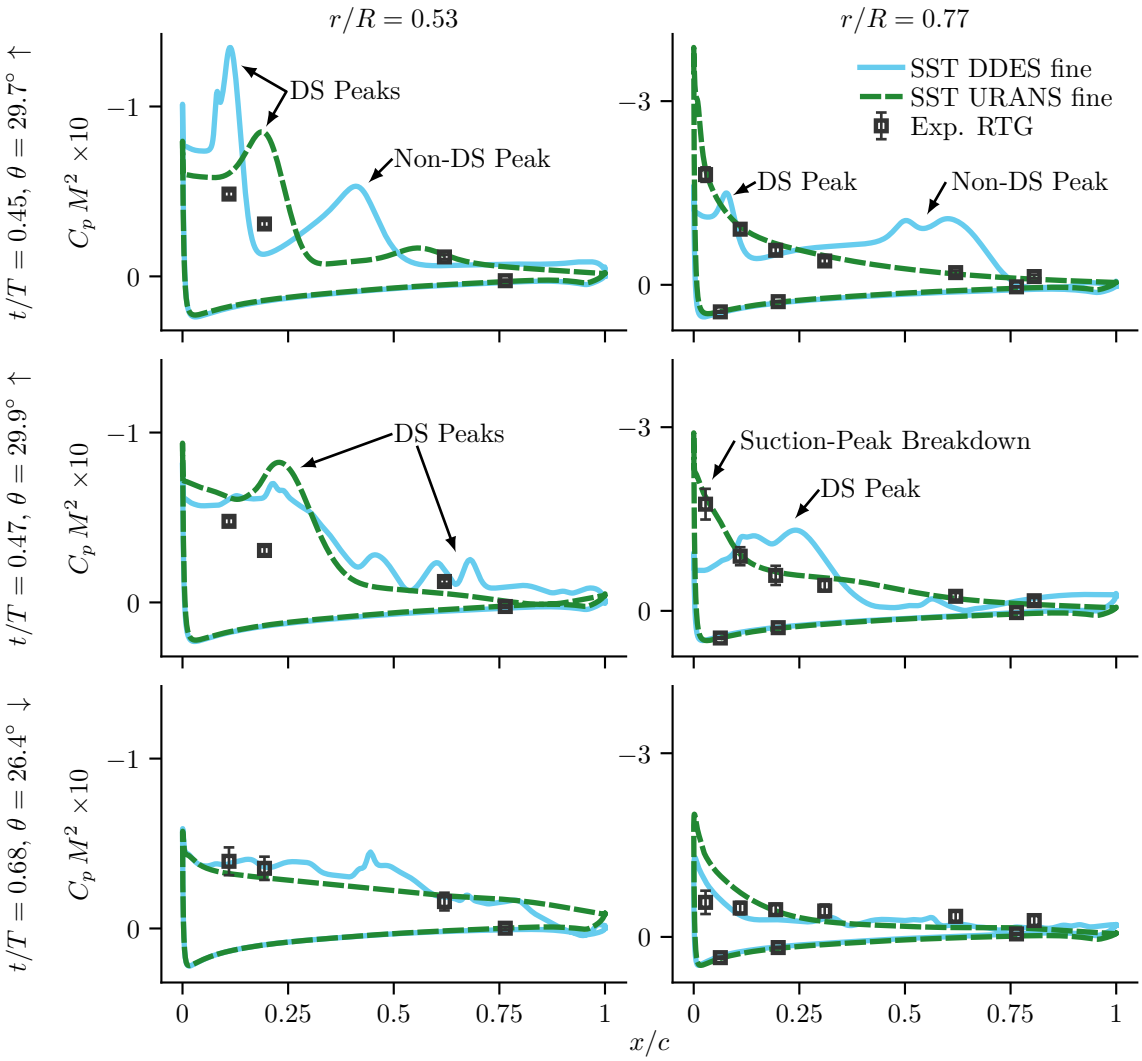

Figure 5.13: Comparison of pressure distributions of experiment (phase-averaged) and FLOWer fine URANS and DDES simulations (single phase) at several points during one cycle of dynamic stall. Adapted from Letzgus et al. [39].

Still at $t/T = 0.45$, both the surface solution and the pressure distribution of the URANS simulation already indicate dynamic stall more inboard, between $0.5 < r/R < 0.65$. In the experiment, the pressure distribution implies a conventional suction peak and the low standard deviation in phase-averaged pressures suggest that the flow is still attached (Fig. 5.13).

A moment later at $t/T = 0.47$, the free shear layer of DDES finally breaks up into smaller, incoherent vortical structures which quickly convect downstream, while at the leading edge, several dynamic stall vortices become visible (Fig. 5.12). The URANS solution exhibits shear-layer rollup in the leading half, but at the leading edge, a dynamic stall vortex is not yet visible. Basically no disturbance of the flow can

yet be seen in the instantaneous PIV image. As the URANS surface solution shows in Fig. 5.11, the Ω-shaped imprint of the dynamic stall vortex grows outboard and is about to reach $r/R = 0.77$, which is in accordance with the vortex visualization given in Fig. 5.6. At this point, the URANS pressure distribution matches the measurement very well (Fig. 5.13). The downstream convection of a pressure peak during dynamic stall cannot be observed in phase-averaged data. However, the significantly increased standard deviation of the experimental pressure sensor at $x/c = 0.03$ indicates the beginning of leading-edge stall, which correlates with the deformed URANS suction peak. The connection between stall and increasing standard deviation of pressure sensors is described by Gardner et al. [140]. Nevertheless, at $r/R = 0.53$ for $t/T = 0.47$, there is still no sign of dynamic stall in the experiment.

As soon as there is complete leading-edge flow separation, for instance at $t/T = 0.62$, DDES works as expected and is able to capture the flow field at $r/R = 0.77$ very well (Fig. 5.12). The instantaneous vorticity contours indicate chaotic, turbulent structures that agree well with the PIV data regarding size, shape and strength. Also, the vertical extent of the separated flow correlates well. In contrast, the URANS computation exhibits a coherent recirculation zone that is too small.

Finally, at $t/T = 0.68$, both the surface solutions (Fig. 5.11) and the in-plane flow field at $r/R = 0.77$ (Fig. 5.12) of the URANS simulation exhibit flow reattachment starting at the leading edge. The flow remains disturbed only close to the surface and at the aft part, where there is a strong near-wall flow directed towards the tip (Fig. 5.11). With DDES, the flow is still massively separated, indicated by rather chaotic surface streamlines. The dividing in-plane streamline of the DDES (Fig. 5.12) is similar to the corresponding experimental streamline and covers a region of flow separation with a vertical extent of one third of the chord. Again, the vortical structures of the DDES are quite comparable to those obtained from the PIV data. Recall that the integrated URANS sectional lift agrees remarkably better with the experiment compared to the DDES lift during this phase of the downstroke (Fig. 5.7). Considering the observations just drawn from the flow fields, this agreement is quite surprising. In fact, the pressure distributions at $t/T = 0.68$ (Fig. 5.13) reveal that this is accidental and misleading, as the URANS solution disagrees with the experiment; the underpredicted pressure at the leading part of the suction side is "compensated" for by overpredicted pressure at the trailing part. Consequently, the integrated URANS pitching-moment comparison with the experiment is, in fact, worse than the DDES comparison.

Comparison of FLOWer and TAU URANS Investigations

During much of the upstroke, when the root pitch angle is below the static stall angle ($\theta_{ss} \approx 26.7°$) and the flow is fully attached, all simulations are expected to yield very similar results. Figure 5.14 confirms that the calculations are similar for the lift and pitching-moment coefficients at $r/R = 0.77$. Then, between θ_{ss} and the upper turning point, all URANS simulations fail to capture the flattening of the experimental lift polar, and both TAU solutions yield slightly higher lift than FLOWer. At the upper turning point, neither the TAU simulations nor FLOWer SA show an additional sharp lift peak observed in the experiment and with FLOWer SST. These three simulations also do not have any moment stall at the turning point. At approximately $\theta = 28° \downarrow$ ($t/T = 0.63$) of the downstroke, the TAU SST solution

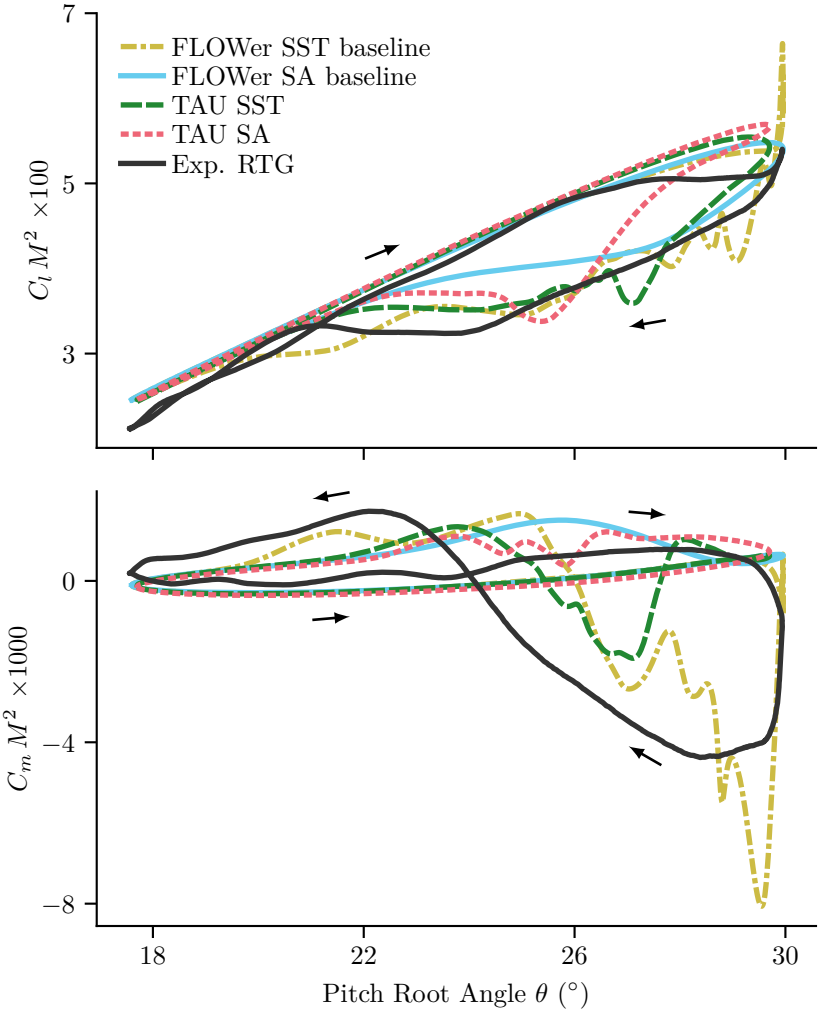

Figure 5.14: Comparison of sectional lift and pitching-moment coefficients at $r/R = 0.77$ of experiment (phase-averaged) and FLOWer and TAU simulations (single cycle). Adapted from Letzgus et al. [39].

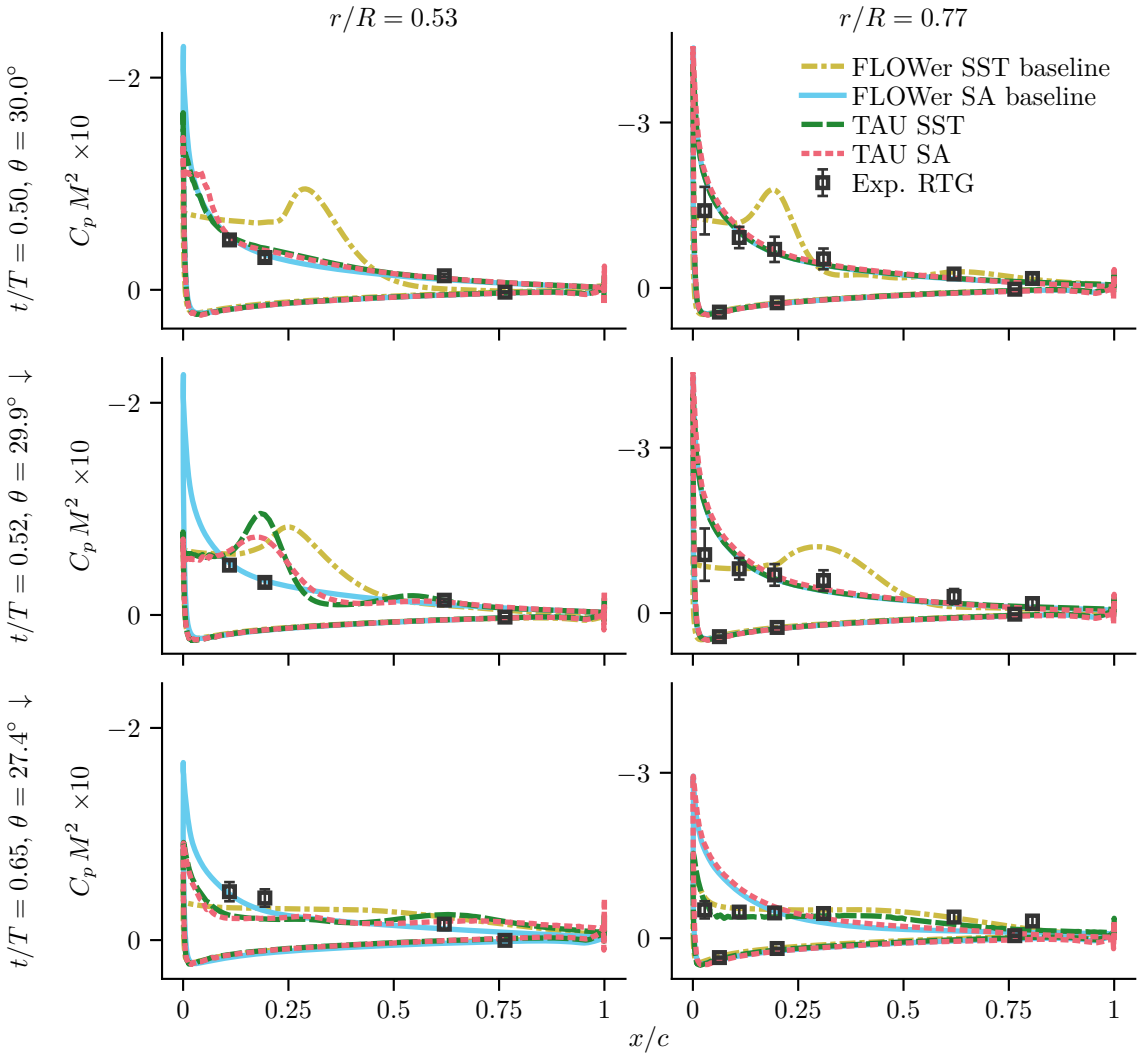

Figure 5.15: Comparison of FLOWer baseline and TAU (both URANS, single phase) and experimental (phase-averaged) pressure distributions at several points during one cycle of dynamic stall. Adapted from Letzgus et al. [39].

exhibits a steep but short rise in nose-down pitching moment, which indicates a delayed and weakened dynamic stall event. In general, both simulations using the SA turbulence model yield fairly similar pitching moments throughout the whole cycle, have weaker lift hysteresis and show no clear signs of dynamic stall in the loads at this radial station.

The pressure distributions in Fig. 5.15 reveal that at the upper turning point ($t/T = 0.50$), both TAU simulations and FLOWer SA retain a substantial suction peak. At $r/R = 0.53$, there is no pressure sensor near the leading edge, however, at $r/R = 0.77$, the strong suction peak is not observed in the measurements. Moving on in time to $t/T = 0.52$, the measured and computed surface pressure barely changes

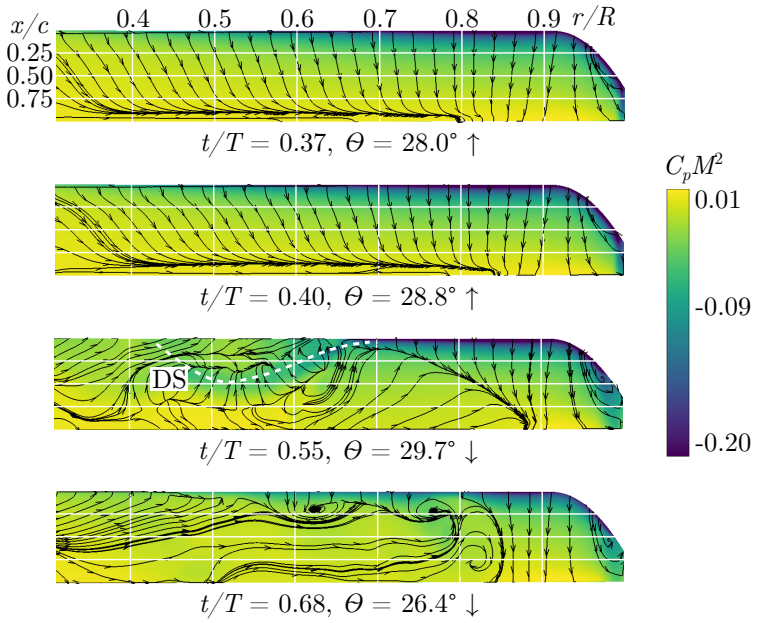

Figure 5.16: Instantaneous distributions of surface pressure and surface streamlines on the suction side of the TAU SST URANS simulation at several points during one cycle of dynamic stall. Adapted from Letzgus et al. [39].

at $r/R = 0.77$, but at $r/R = 0.53$ both TAU solutions show a breakdown of the leading-edge suction peak and the downstream convection of a low pressure peak, lagging behind the FLOWer SST solution. Finally, at $t/T = 0.65$, TAU SST is also mostly stalled at $r/R = 0.77$ and low pressure is shifted downstream of the quarter chord, inducing the nose-down pitching moment peak seen in Fig. 5.14, while both SA solutions keep their strong suction peak. At $r/R = 0.53$, only the FLOWer SA solution shows no dynamic stall event throughout the complete cycle. Regarding the experiment, the increased standard deviation of the two pressure sensors at $x/c = 0.11$ and $x/c = 0.19$ suggests that there is flow separation at the leading part of the suction side.

Comparing pressure distributions and surface streamlines of TAU SST in Fig. 5.16 with those of FLOWer SST URANS in Fig. 5.11 during the upstroke at $t/T = 0.37$, small differences are only found in the innermost region of the blade. These differences are most likely due to the different blade mount modeling (Fig. 5.4), which permits flow around the blade root and formation of a root vortex in case of the TAU setup. At $t/T = 0.40$, there is still only weak trailing-edge separation with TAU, while FLOWer already shows a second separation line around the quarter-chord line and strong spanwise flow inboard of $r/R \approx 0.7$. With TAU, a typical Ω-shaped footprint of a dynamic stall vortex is seen during the downstroke at $t/T = 0.55$, as highlighted in Fig. 5.16. Compared with FLOWer, where the footprint is seen much earlier at $t/T = 0.47$, induced pressure is not as low and the footprint is more inboard.

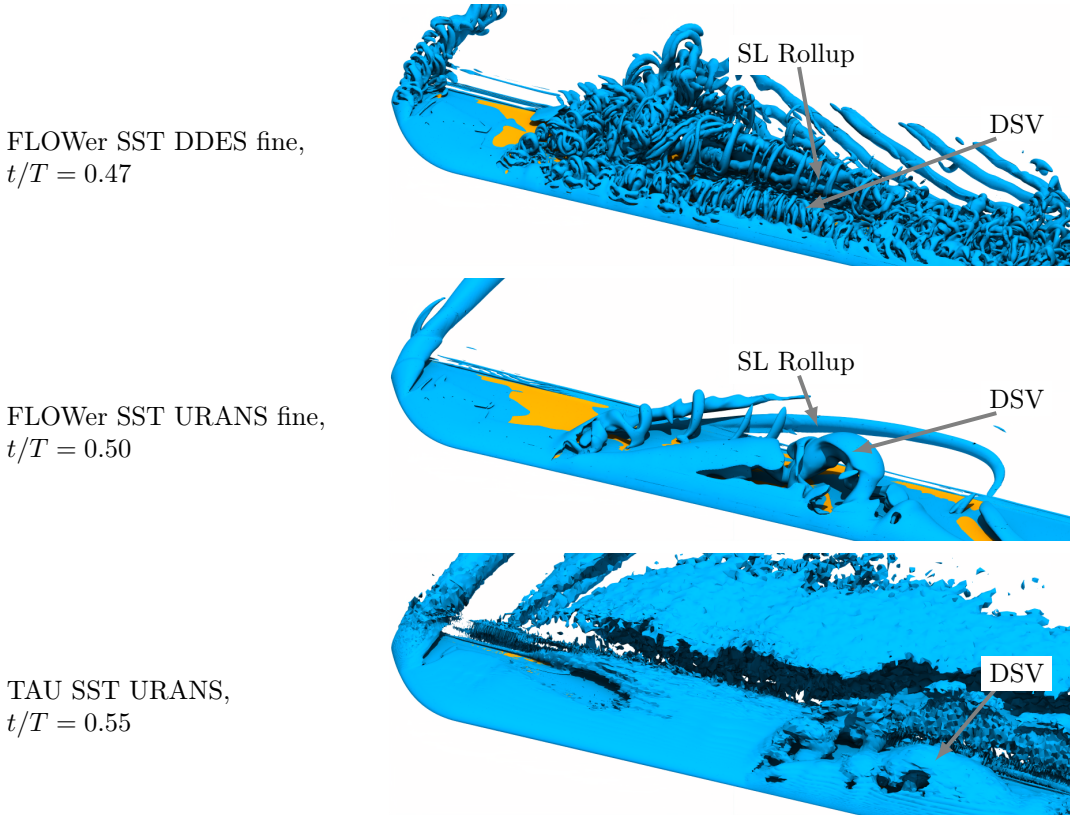

Figure 5.17: Visualization of dynamic stall vortices (DSV) and shear-layer (SL) rollup by means of instantaneous isosurfaces of the λ_2-criterion. Adapted from Letzgus et al. [39].

Since the dynamic stall event of TAU is delayed beyond the upper turning point of the pitching motion, the vortical structure may have a different strength and spread. Finally, at $t/T = 0.68$, flow reattachment is already more advanced with TAU, especially in the blade tip region.

Figure 5.17 visualizes the main dynamic stall vortices and shear-layer rollups of all simulations that use the SST turbulence model by means of instantaneous isosurfaces of the λ_2-criterion. Since the dynamic stall events do not happen simultaneously, different points in time are chosen. DDES has mostly small-scale, incoherent vortical structures, except in the wake, where tube-shaped structures indicate typical URANS flow separation resembling a Kármán vortex street. These structures evolved early in the cycle, when the LES mode was either not yet active or suffered from the gray-area problem. DDES also exhibits smaller, secondary vortex filaments orbiting the main blade-tip vortex. Regarding the URANS simulations, the dynamic stall vortex of FLOWer convects more outboard and is more distinct compared to the TAU vortex, as assumed before.

In summary, satisfactory agreement between FLOWer and TAU is only achieved in the linear regime where the flow is fully attached. While both SA computations essentially fail to capture dynamic stall, TAU SST predicts delayed and weakened dynamic stall in comparison to FLOWer SST and the experiment. As no single reason for the discrepancies in CFD results could be found, a combination of differences in grids and numerical schemes is assumed to be the issue. Interestingly, there is another TAU investigation using URANS Menter-SST of basically the same dynamic stall case by Goerttler et al. [40], who focused on the analysis of the tip vortices. In their simulation, the dynamic stall onset is predicted similar to FLOWer SST, however, the hysteresis of the sectional loads differs. These observations underscore the difficulties of current turbulence models in predicting the onset of flow separation correctly or even consistently.

5.3 Cycle-to-Cycle Variations in Experiment

It is well known from experimental investigations of dynamic stall, for example on a model rotor in forward flight condition [33] or on pitching airfoils [139], that cycle-to-cycle variations occur. This means that the dynamic stall onset, the maximum lift and pitching-moment coefficients, the appearance of secondary dynamic stall events and the flow reattachment process can significantly vary from one cycle to another [139]. Ramasamy et al. [90] showed that on pitching airfoils, the variation can even go so far that dynamic stall occurs in some cycles but not in others, which means that there is a physical bifurcation in the flow processes. Thus, there is a growing concern among researchers that applying the common phase-averaging not only smears the peaks of the loads, which is somewhat compensated for by evaluating the standard deviation, but also "blends" two fundamentally different flow processes, which is not quite appropriate and questions the suitability of a respective dataset for CFD validation.

As an alternative to phase-averaging, Ramasamy and Sanayei et al. [139, 141, 90] proposed an innovative concept that tries to cluster individual cycles that are phenomenologically similar based on proper orthogonal decomposition (POD). To assess the cycle-to-cycle variation of the present experimental data [37], this approach was applied to the measurements in the following way: First, one has to choose the quantity the clustering relies on, which could be for example the lift coefficient, the data of all pressure sensors combined or, as it was done here, the data of a single pressure sensor. Since dynamic stall is associated with a strong leading-edge vortex, the foremost sensor on the upper side at $x/c = 0.03$ was chosen. Then, a weak low-pass filtering was applied to remove very high-frequency fluctuations

that were considered to be measurement noise, and the 4560 samples per cycle or rotor revolution were downsampled to $m = 360$ samples per cycle, which completely preserved the major characteristics. Next, the $C_p\,M^2$ data of the leading-edge sensor was mean-centered and arranged in a matrix A of shape $(m \times n)$ with n being the number of cycles, that is, $n = 8400$. According to Ramasamy et al. [90], the POD decomposes the matrix A into three matrices

$$A_{m\times n} = C_{p_{m\times n}} = U_{m\times m}\, S_{m\times n}\, V^T_{n\times n} \tag{5.1}$$

where U represents eigenmodes, S the energy contained in each mode and V^T the time coefficients, respectively. By analyzing the matrix S, it shows that most energy is contained in the first two modes, thus, all others were discarded, which reduces the dimension of V^T to (2×8400). With this, there is a two-dimensional time coefficient for every single cycle that is emerged from the course of $C_p\,M^2$ over one rotor revolution, thus, it is shaped by the dominant flow features. Finally, for detecting phenomenologically similar dynamic stall cycles, a clustering algorithm of choice must be applied to the reduced V^T dataset, which is, however, a complicated topic of its own [90]. Here, for simplicity and after some trial and error, the number of clusters (CL) was fixed at five and an iterative, hierarchical agglomerative clustering provided by the Python library *scikit-learn* [142] was carried out.

In preliminary tests, which are not presented here, the clustering analysis was also carried out using other quantities, namely different pressure sensors, all sensors altogether as well as the integrated lift or pitching-moment coefficients. Furthermore, the number of clusters was slightly varied and different clustering algorithms were investigated. All in all, the differences were found to be small and the qualitative findings were the same.

Figure 5.18 depicts the clustered envelopes of mean-centered pressure coefficients of the leading-edge pressure sensor plotted against the moment in time during one cycle. For the first part of the upstroke ($t/T < 0.4$) and the last part of the downstroke ($t/T > 0.85$), the variation of $C_p\,M^2$ between the cycles is small, which is plausible, as flow is fully attached in these phases. Around the upper turning point ($t/T = 0.5$), where dynamic stall and flow separation set in, the cycles exhibit either a sudden increase (clusters 2,3) or decrease (clusters 1,4,5) in $C_p\,M^2$, which is the physical foundation of the clustering. It also shows that some clusters overlap, indicating that there is a very broad spectrum of $C_p\,M^2$ courses. This is especially true for the $C_p\,M^2$ range of cluster 5 that overlaps with cluster 4 for the most part, except of around $t/T = 0.65$, where cluster 4 returns earlier to the phase average. In other words, the assignment of a cycle to one cluster or another and, in the first place, the exact number of clusters is less distinct.

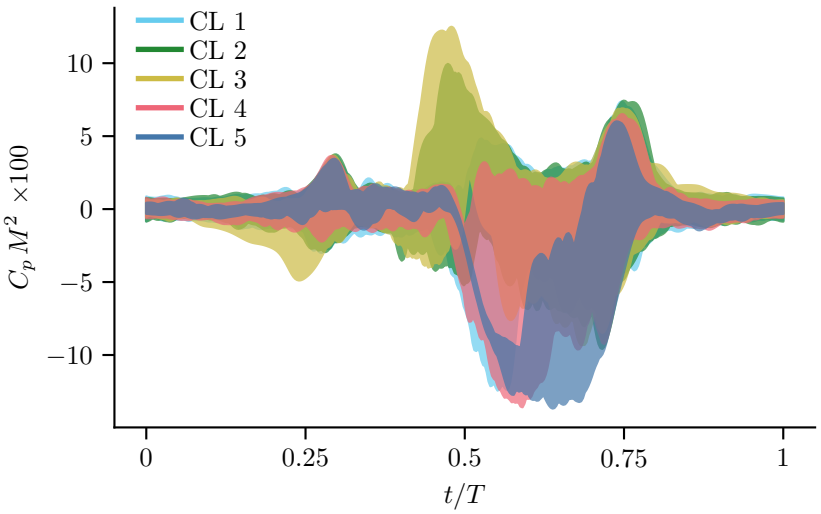

Figure 5.18: Clustered envelopes of pressure coefficients (phase average subtracted) of leading-edge pressure sensor located at $x/c = 0.03$ of RTG experiment.

As every individual cycle is assigned to a cluster, phase-averaging of lift and pitching moments can now be carried out only over the cycles of a respective cluster instead of over all cycles available. Therefore, there is no longer the risk of "blending" fundamentally different flow processes. Looking at Fig. 5.19, the sectional loads of clusters 1,2 and 3 are very similar regarding their peak values of lift and nose-down pitching moment. However, there is a slight temporal offset in the prediction of final lift overshoot and stall as well as the point of maximum negative pitching moment, suggesting that dynamic stall occurs first in cluster 3 followed by the clusters 2 and 1. Also, it becomes apparent that the phase average computed over all available cycles, denoted *Total* in Fig. 5.19, represents the loads of clusters 1,2 and 3 fairly well, as they all lie within the total standard deviation. By contrast, the loads of clusters 4 and 5 do not agree with the total phase average between $0.25 < t/T < 0.75$ and also differ from each other especially in pitching moment during the first part of the downstroke. Interestingly, they exhibit lower lift starting around $t/T = 0.25$, where the flow is expected to be still fully attached, and also a lower overshoot in lift. Regarding the pitching moment, a severe breakdown is absent from both curves, which indicates very delayed (cluster 4) or even no dynamic stall (cluster 5).

Further insight is provided by Fig. 5.20, showing cluster-based phase-averaged pressure distributions at different points during the cycle. At $t/T = 0.28$, the suction peak of clusters 4 and 5 is lower, explaining the reduced lift coefficients that were observed before. Moving on to $t/T = 0.48$, cluster 3 exhibits a breakdown of the suction peak and lower pressure further downstream, which is a clear sign of dynamic stall. This correlates well with the course of the loads (Fig. 5.19), where cluster 3 showed the first lift and moment stall. Then, at $t/T = 0.50$, the pressure

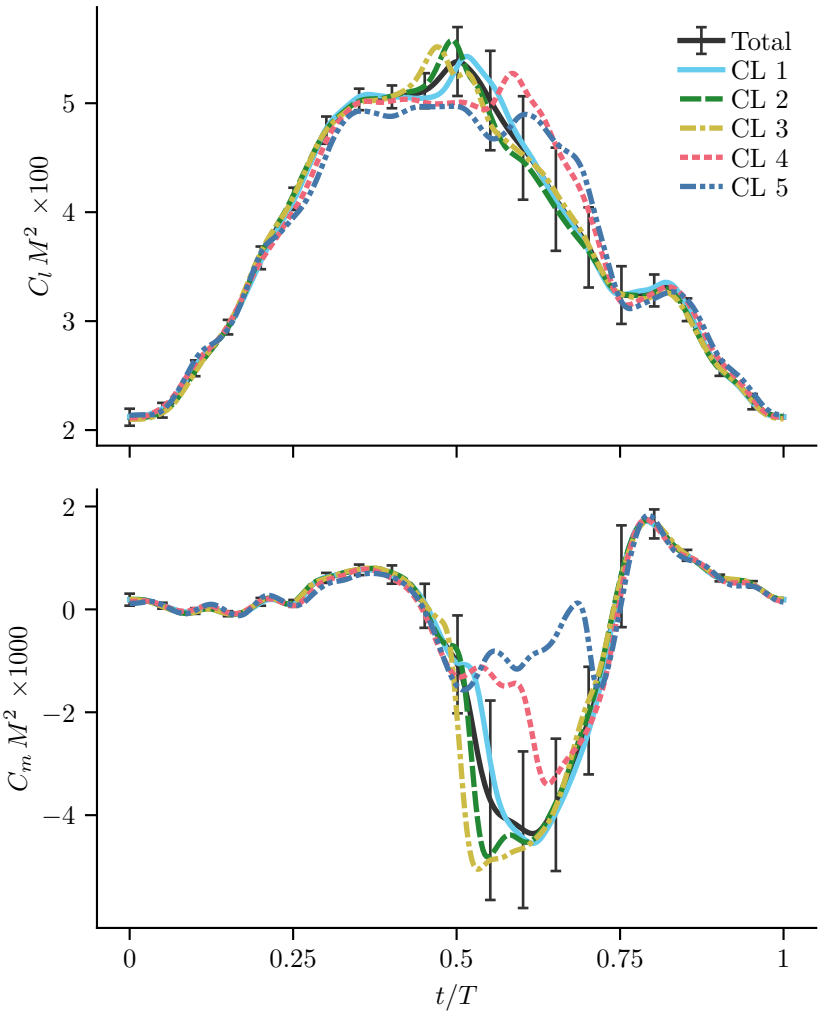

Figure 5.19: Cluster-based phase-averaged local sectional lift and pitching moment coefficients at $r/R = 0.77$. Averaging over all cycles yields the curve denoted *Total*.

distributions indicate ongoing dynamic stall for cluster 2 and yet no stall for cluster 1, which is again in good agreement with the order found in the loads. Eventually at $t/T = 0.60$, the suction peak of cluster 4 also breaks down and lower pressure further downstream suggests delayed dynamic stall. Cluster 5, however, retains its suction peak throughout the whole cycle, which, in combination with the course of its loads, indicates the complete absence of dynamic stall, at least at the examined radial station of $r/R = 0.77$.

So far, it has not yet been discussed how the cycles are distributed among the clusters, that is, which cycles are in which cluster. Figure 5.21 visualizes the assignment of all 8400 consecutive cycles of the experiment to the respective clusters. Also, the cluster probability is listed, which simply is the number of cycles in a cluster divided by the total number of cycles. Obviously, the vast majority of the cycles is assigned to

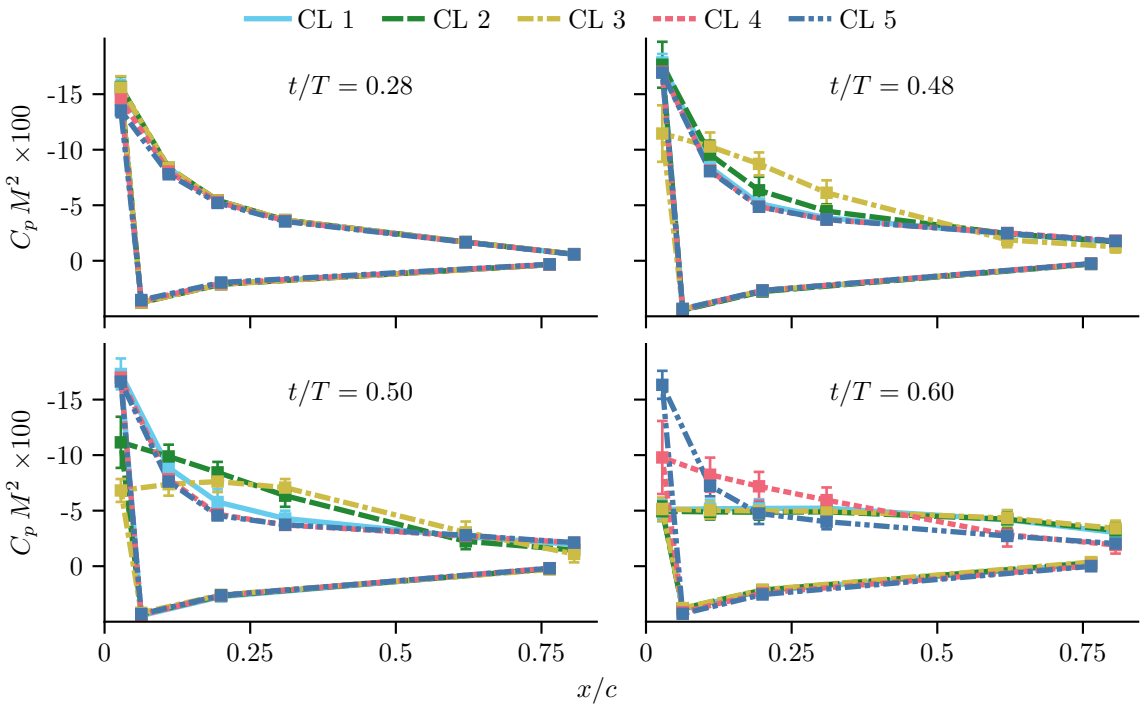

Figure 5.20: Cluster-based phase-averaged pressure distributions at $r/R = 0.77$.

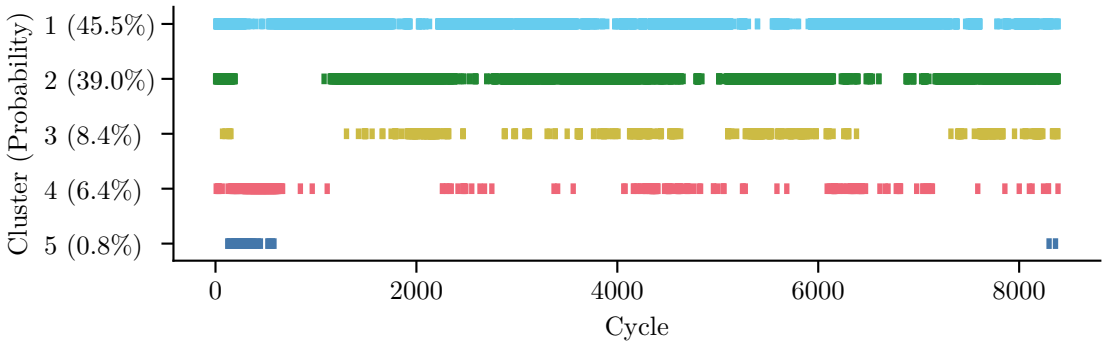

Figure 5.21: Cluster assignment for all 8400 consecutive experimental cycles. The cluster probability (number of cycles in a cluster divided by the total number of cycles) is in brackets.

either cluster 1 (45.5%) or cluster 2 (39%). Furthermore, with few exceptions, cycles are repeatedly assigned to those two clusters throughout the whole measurement period. Cluster 4, which represents delayed and weakened dynamic stall cycles, also occurs repeatedly, but only with a probability of 6.4%. Finally, cycles that exhibit no dynamic stall at all are extremely rare and, for some reason, only appear at the beginning and the end of the measurement (cluster 5, 0.8% probability). Combining clusters 1,2 and 3 – which showed a comparable dynamic stall characteristic with some minor variations in stall onset and which are very well represented by the total phase average – roughly 93% of the cycles are covered. Hence, it can be concluded

that the present RTG dataset is not dominated by physical bifurcation, thus, the total or common phase average and standard deviation are well suited for representing the measurement and, consequently, for CFD validation.

A detailed discussion of the causes of these very cycle-to-cycle variations is, at this point, somewhat speculative. Besides variations triggered by the chaotic nature of separated flow and the strong hysteresis, fluctuations of the wind tunnel inflow or structural dynamic responses of the rotor test rig might play a role. Further insight could be provided by a Markov chain that analyses the cluster assignment and switching as a sequence of events to find out if and how the cycles are connected.

5.4 Chapter Conclusions

Numerical investigations of three-dimensional dynamic stall on a two-bladed model rotor in axial flow with 1/rev cyclic pitch control were carried out and compared to experimental surface pressure and PIV data. In addition to URANS simulations using the finite-volume flow solvers FLOWer (structured) and TAU (hybrid unstructured), a high-resolution DDES with Menter-SST as the underlying RANS model was performed using FLOWer. The URANS simulations were carried out with both the Menter-SST and SA turbulence model. Furthermore, the cycle-to-cycle variations of the experiment were assessed using a clustering approach. The main findings are as follows:

1. Good agreement between experimental results, FLOWer and TAU simulations of a static, highly loaded hover case has been achieved. Influences of blade elasticity, rotor hub geometry and test bench components as well as shear-layer effects of the wind tunnel jet seem negligible.

2. In case of dynamic stall, only the DDES captures the flattening of the lift polar beyond the static stall angle observed in the experiment and associated with trailing-edge separation, but most likely due to the unwanted numerical artifact of grid-induced separation. DDES is also able to reproduce realistic high-frequency load fluctuations and cycle-to-cycle variations when the flow is separated, which is not possible with URANS. In the case of complete flow separation, only the DDES flow field agrees well with the PIV data regarding size and shape of incoherent vortical structures and the form of dividing streamlines.

3. The main issues of a hybrid RANS/LES approach – modeled stress depletion causing grid-induced separation and the gray-area problem – are also very likely to exist in this DDES case. During the complex transition from attached to completely separated flow, grid-induced separation promotes excessive trailing-edge separation, while the gray-area problem prevents flow instabilities and, thus, supports the rollup of a strong vortex from the free shear layer at mid-chord. This rollup event, which must not be confused with premature dynamic stall, severely influences lift and nose-down pitching moment during a short period of time and is not seen in URANS and experimental results.

4. During the downstroke, when the flow is massively separated, the integrated sectional lift of the URANS simulation seems to agree better with the experiment than the lift of the DDES; for the pitching moment, however, the opposite is true. The pressure distributions reveal that, accidentally, compensating deviations result in the misleadingly good URANS lift correlation.

5. For the majority of the upstroke, as long as the flow is attached, all simulations yield the same sectional loads at $r/R = 0.77$ that match the experimental loads fairly well. Load peaks of the FLOWer SST simulations are of the same magnitude as of non-phase-averaged measurements. However, phase-averaging of experimental data reduces peak values significantly.

6. The TAU SST simulation exhibits a dynamic stall occurrence that is delayed and much weaker than in the FLOWer SST calculation. A combination of differences in grids and usage of numerical schemes is assumed to be the cause of the differences, since the implementation of the turbulence model is extensively validated for both codes and attention is paid to time convergence. Note that the investigated case exhibits light dynamic stall, which suggests an even more sensitive stall event. The SA solutions of FLOWer and TAU are comparable and show the same non-stall behavior outboard at $r/R = 0.77$. Consequently, both SA solutions completely fail to capture dynamic stall there. Further inboard at $r/R = 0.53$, TAU SA shows only weak dynamic stall while FLOWer SA shows no leading-edge stall throughout the complete cycle. This underscores the sensitivity to numerical methods and the difficulties of current CFD in predicting the onset of flow separation consistently.

7. The cycle-to-cycle variations of the present RTG dataset are mostly limited to small variations of the point in time of dynamic stall onset. Thus, the phase-average and the standard deviation are representative of the dynamic stall event and well suited for CFD validation.

6 Assessment and Improvement of Delayed Detached-Eddy Simulations (DDES) of Rotor Dynamic Stall

In the previous chapter, where results of a high-fidelity DDES of dynamic stall on a model rotor were presented, it was shown that before the dynamic stall event, the DDES suffers from modeled-stress depletion leading to grid-induced separation due to a breakdown of the boundary-layer shielding function f_d. Combined with the gray-area problem (Section 3.3), this has a severe and erroneous impact on sectional loads. Therefore, in the present chapter, several approaches to eliminate grid-induced separation – proposed by others and self-developed – are presented and investigated. For testing, the already discussed RTG case (Chapter 5) as well as the Bluecopter case, which will be described in greater detail in Chapter 7, are selected. Both cases feature dynamic stall, which renders them especially challenging for any DES, since there is a highly unsteady movement of the point of flow separation, that is, a complex transition from fully attached to partly to completely separated flow in a very short physical time. Note that although a DES can be coupled with various underlying RANS turbulence models, here, only the DDES version using Menter-SST [110] is considered. The chapter is loosely based on Letzgus et al. [143], but has been largely expanded by the inclusion of the Bluecopter test case, the development of the wall-normal flow analysis (WNFA) shielding, the assessment of the BDES and ZDES19 boundary-layer shieldings as well as of the gray-area mitigation approach using the Δ_{SLA} filter width.

6.1 Modifications to the DDES Shielding Function f_d to Prevent Grid-Induced Separation

Recall from Section 3.3 that DDES was designed as an advancement of the original DES to eliminate grid-induced separation and that it was shown by several studies, including the one presented in the previous chapter, that the issue still persists with DDES if "fine enough" grids are used. By now, there are a couple of approaches to improve or replace the original shielding function f_d, which handles the transition from RANS to LES mode, that are investigated in the following.

6.1.1 Increase of Empirical Constant C_{d1}

According to Equation 3.3, the DDES boundary-layer shielding function f_d reads as

$$f_d = 1 - \tanh\left[(C_{d1} \cdot r_d)^{C_{d2}}\right].$$

To ensure sufficient boundary-layer shielding, some researchers successfully increased the empirical constant C_{d1}, from 8 to 16 [91] or to 14 [114] for the SA version and from 20 to 25 [113] for the Menter-SST version, respectively. By increasing C_{d1}, the hyperbolic-tangent term stays somewhat longer close to one and f_d close to zero, thus, the RANS mode is promoted. Here, the effect of setting $C_{d1} = 25, 30$ was investigated for the RTG case (Section 6.2) and $C_{d1} = 30$ for the Bluecopter case (Section 6.5), respectively.

6.1.2 Bernoulli-Based Boundary-Layer Shielding (BDES)

A different, more sophisticated approach, in which the author of the present thesis was supportively involved, was proposed by Weihing [118, 116]. The idea of this Bernoulli-equation-based boundary-layer shielding (BDES) is to obtain the boundary-layer edge-velocity u_e from the compressible Bernoulli equation [144], assuming constant pressure in wall-normal direction and isentropic outer flow:

$$\begin{aligned} u_e &= \sqrt{\frac{2\gamma}{\gamma - 1}\left(\frac{p_\infty}{\rho_\infty} - \frac{p}{\rho_e}\right) + u_\infty^2}, \\ \rho_e &= \rho_\infty \left(\frac{p}{p_\infty}\right)^{\frac{1}{\gamma}}, \end{aligned} \tag{6.1}$$

where the subscripts e and ∞ denote quantities at the boundary-layer edge and the free stream, respectively, and $\gamma = 1.4$ is the isentropic exponent. Now, at every point, the local velocity magnitude u is compared to the edge-velocity u_e, with a threshold $t_{\mathrm{BL}} = 0.99$ to decide whether a point lies inside the boundary layer ($u \leq t_{\mathrm{BL}}\, u_e$, $f_{\mathrm{BL}} = 1$, RANS mode) or outside ($u > t_{\mathrm{BL}}\, u_e$, $f_{\mathrm{BL}} = 0$, LES mode). However, evaluating only this sensor, regions of separated flow are also declared to lie inside the boundary layer and to be in RANS mode, respectively, which contradicts the DES principle, recall Fig. 3.1. Therefore, three additional sensors are defined that locally enforce the LES mode: f_{3dturb} aims at detecting three-dimensional turbulence by analyzing velocity gradients, f_{SL} tries to detect free shear layers based on the vorticity magnitude and the wall distance, and f_{inv} uses a ratio of laminar to turbulent viscosity to clip essentially inviscid flow regions. To always retain RANS mode very

close to the surface, the f_b function from IDDES [111] is borrowed that enforces RANS mode in near-wall cells with high aspect ratios. Then, the final shielding function of BDES reads

$$f_d = 1 - \max(f_{\mathrm{BL}} \cdot f_{\mathrm{3dturb}} \cdot f_{\mathrm{SL}} \cdot f_{\mathrm{inv}},\, f_b). \tag{6.2}$$

A validation of the model with canonical test cases and the application to a wind turbine was carried out by Weihing [118, 116]. In the present thesis, BDES was tested both with the RTG case (Section 6.2) and the Bluecopter case (Section 6.5).

6.1.3 Vorticity-Integrated Algebraic DES (VIADES)

The vorticity-integrated algebraic DES (VIADES) approach was developed in a joint work of Weihing [118, 116] and the author of the present thesis, who implemented it into FLOWer [143]. It is a non-local concept and requires a wall-normal evaluation of the flow field, similar to ADDES developed by Probst et al. [117]. The basic idea is to use a pseudo-velocity u_{ps} based on the piecewise wall-normal (here z-direction) integration of the vorticity magnitude Ω, as for example done in Spalart and Strelets [145]. This pseudo-velocity converges very fast outside the boundary-layer if the outer flow is essentially inviscid, even in case of, for example, accelerated flow on the suction side, thus, the determination of an edge-velocity u_{ps_∞} is relatively robust.

$$\begin{aligned} u_{\mathrm{ps}}(z) &= \int_0^z \Omega \, d\tilde{z}, \\ u_{\mathrm{ps}_\infty} &= \int_0^\infty \Omega \, d\tilde{z}. \end{aligned} \tag{6.3}$$

The subscript ∞ denotes the far-field condition that is reached at the border of the computational domain. The transition from RANS to LES mode is then determined by the δ_{99} criterion [100], that is, as soon as $u_{\mathrm{ps}}(z) > 0.99\, u_{\mathrm{ps}_\infty}$, the LES mode is activated by setting $f_d = 1$, otherwise it is $f_d = 0$.

Since this criterion alone would keep regions of separated flow in RANS mode, similar to the f_{BL} sensor of BDES and contradicting the DES principle, a novel, locally defined sensor is proposed that is based on the comparison of the projections of the vorticity. The idea here is that with fully attached, mostly two-dimensional flow, the vorticity vector $\vec{\omega}$ is primarily governed by the wall-normal velocity gradient, which means that only the spanwise component of $\vec{\omega}$ is large. Since the spanwise direction or "span vector" $\vec{s}$ is not obvious in three-dimensional flow, it is defined to be perpendicular to the wall-normal vector $\vec{n}$ and the velocity vector $\vec{u}$ as sketched in Fig. 6.1, thus, $\vec{s} = \vec{n} \times \vec{u}$. Now, the vorticity is projected onto each of these

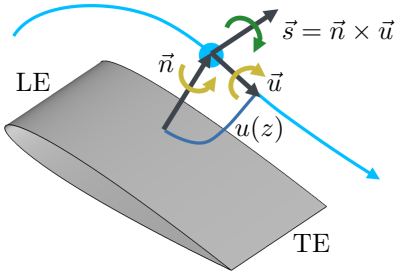

Figure 6.1: Sketch of wall-normal vector $\vec{n}$, velocity vector $\vec{u}$ and resulting "span" vector $\vec{s} = \vec{n} \times \vec{u}$ onto which the local vorticity $\vec{\omega}$ is projected for the flow separation criterion in VIADES. Adapted from Letzgus et al. [143].

three vectors by simply computing the respective dot product. In terms of flow physics, the projected vorticity component describes the tendency of a fluid particle to rotate around the respective vector. With separated flow, the vorticity distribution becomes more isotropic and is no longer dominated by the spanwise component, thus, flow is declared to be separated ($f_{\text{sep}} = 1$) when the wall-normal and flow direction components $\omega_{n+u} = \sqrt{(\vec{\omega} \cdot \vec{n})^2 + (\vec{\omega} \cdot \vec{u})^2}$ are of the order of the spanwise component Ω_s:

$$f_{\text{sep}} = \begin{cases} 1, & \text{if} \quad \sqrt{(\vec{\omega} \cdot \vec{n})^2 + (\vec{\omega} \cdot \vec{u})^2} \geq t_{\text{sep}}\, \vec{\omega} \cdot \vec{s} \\ 0, & \text{otherwise} \end{cases} . \tag{6.4}$$

In purely two-dimensional flow, the square root of Equation 6.4 becomes zero and separation is detected ($f_{\text{sep}} = 1$) if the vorticity becomes negative, which is the case for reversed flow or, more generally, for a negative wall-normal velocity gradient. In the original version [143], the threshold was set to $t_{\text{sep}} = 0.99$ to somewhat mimic the δ_{99} criterion. However, it turned out that more consistent results are achieved when ω_{n+u} is noticeably larger than the spanwise component, therefore, $t_{\text{sep}} = 1.25$ is recommended, although this is a rather "cosmetic" issue.

Figure 6.2 illustrates the components and functionality of VIADES for a typical airfoil trailing-edge separation that is indicated by the vorticity contours and the in-plane streamlines on the left-hand side. At the wall-normal extraction location (EL), shear-layer data is extracted and plotted on the right-hand side, where the local minimum in the velocity magnitude and the negative spanwise vorticity Ω_s indicate recirculating flow. Consequently, $f_{\text{sep}} = 1$ is set there. Note that in the free shear layer, which connects the recirculation zone and the outer flow, the sensor does not detect separation, as this region behaves like an attached boundary layer, that is, a large positive wall-normal velocity gradient leads to a dominating Ω_s component. To enforce the LES mode everywhere downstream the point of separation and not only

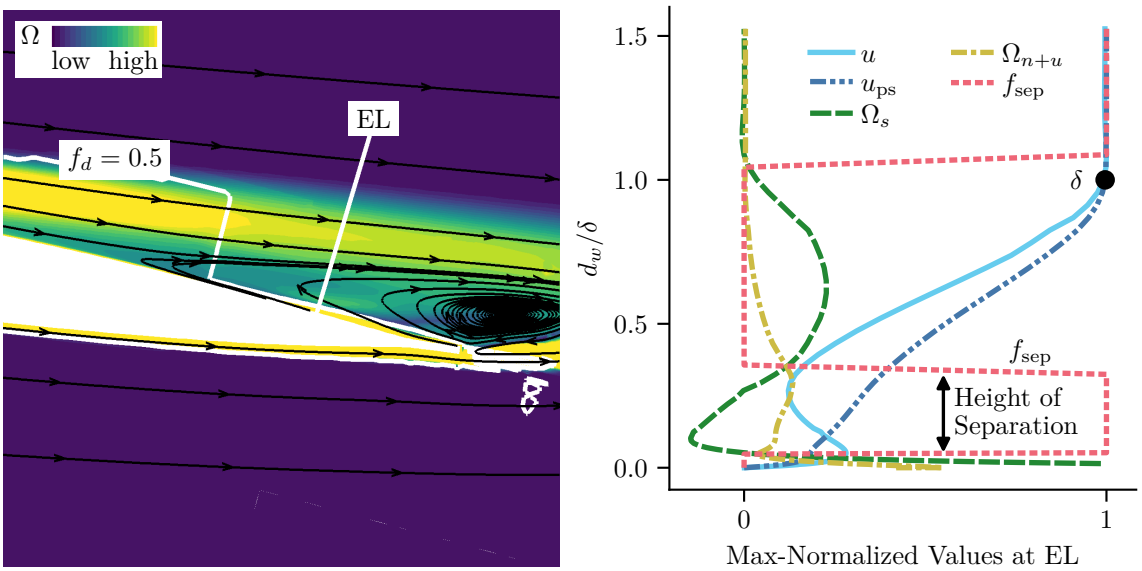

Figure 6.2: Shear-layer calculations (right) of VIADES at the wall-normal extraction location (EL) indicated by the white line on the spanwise slice (left) showing vorticity contours and in-plane streamlines that indicate trailing-edge separation. The RANS/LES interface is indicated by the white line where $f_d = 0.5$.

in the recirculation zone to fulfill Fig. 3.1, the LES mode is activated at the first, wall-nearest occurrence of $f_{sep} = 1$ and is then enforced in wall-normal direction on all cells above until the end of the computational domain is reached. However, without constraining this destruction of the shielding, the smallest recirculation, for example occurring in a shallow, near-wall separation bubble, would trigger the LES mode in the entire boundary layer above, which dramatically increases the risk of erroneous, premature separation [116]. Therefore, the total height of detected flow separation ($f_{sep} = 1$) is compared to the boundary-layer or shear-layer thickness δ and the destruction is only allowed if at least 25% of δ are marked as separated, as highlighted in Fig. 6.2. The effect of this thresholding becomes evident on the left-hand side of Fig. 6.2, where the isoline of $f_d = 0.5$ indicates the final RANS/LES interface and it shows that a small region downstream of the point of separation is still kept in RANS mode. In the present work, VIADES was tested both with the RTG case (Section 6.2) and the Bluecopter case (Section 6.5), while a validation with canonical test cases was carried out by Weihing [118, 116].

With VIADES being a non-local approach, information must be distributed in wall-normal direction for the integration of the pseudo velocity u_{ps}, the evaluation of the separation flag f_{sep} and for the deliberate destruction of the shielding, which is not an easy task in a multi-block, parallel flow solver. Fortunately, in FLOWer, the already existing ghost- or dummy-layer and block-exchange code infrastructure can be exploited: At first, each process computes the required values for the blocks it

owns and stores the results in the boundary cells. Then, several block exchanges are carried out that distribute the single-block values throughout all relevant blocks. Given n blocks that cover the whole computational domain in wall-normal direction (typically, $n = 2 - 5$), $n - 1$ exchanges are needed. Furthermore, the structured grid and the fact that it is always generated by wall-normal extrusion is utilized, in that the computation is not carried out in the actual wall-normal direction but in the index direction of the grid that is approximately wall-normal. This significantly reduces the complexity and the computational effort of the approach without losing too much accuracy. Since the algorithm is carried out only once per physical time step, its impact on the overall performance is negligible.

6.1.4 Shielding Based on Eddy-Viscosity Gradient (ZDES19)

Most recently, Deck and Renard [119] proposed an advancement of their zonal DES method (ZDES) that features a modification of the f_d shielding function based on the wall-normal gradient of the eddy viscosity, which is here referred to as ZDES19[1]. The new shielding reads as

$$f_d = f_{d_{\mathrm{DDES}}}(1 - (1 - f_{P2})f_R) \tag{6.5}$$

where $f_{d_{\mathrm{DDES}}}$ is the original DDES shielding, f_{P2} a second shielding function and f_R an inhibition function to switch off the second shielding when flow separation is detected. f_{P2} is very similar to the original f_d function (compare Equation 3.3) as it reads as

$$\begin{aligned} f_{P2} &= 1 - \tanh\left[(C_{d1} \cdot r_{\mathrm{ZDES}})^{C_{d2}}\right], \\ r_{\mathrm{ZDES}} &= \frac{C_3 \max(0, -\partial\nu_t/\partial n)}{\kappa d_w \sqrt{\frac{\partial u_i}{\partial x_j}\frac{\partial u_i}{\partial x_j}}}. \end{aligned} \tag{6.6}$$

The crucial part is the introduction of the wall-normal gradient of the eddy viscosity $\partial\nu_t/\partial n$ that aims at restoring the shielding at the outer part of the boundary layer where the eddy viscosity typically rapidly decreases ($\partial\nu_t/\partial n \ll 0$). The inhibition function f_R evaluates the wall-normal gradient of the vorticity magnitude $\partial\Omega/\partial n$ that becomes positive in a separated shear layer, but it is only allowed to disable the additional shielding. As a consequence, ZDES19 cannot promote the LES mode more aggressively than DDES. In the course of the present thesis, ZDES19 was implemented into FLOWer and tested both with the RTG case (Section 6.2) and the Bluecopter case (Section 6.5).

[1]The notation *zonal* refers to the whole framework proposed by Deck and Renard [119], but the here investigated shielding mechanism is purely local.

6.2 Application of Alternative Shieldings to Model-Rotor Dynamic Stall (RTG Case)

In this section, the aforementioned alternative shielding approaches are applied to the dynamic stall case of Chapter 5. All computations were carried out using the *FLOWer fine* setup and were restarted from the same converged DDES run. In Fig. 5.10, it has been shown that DDES switches from RANS to LES mode at half of the boundary-layer height, and, thus, modeled-stress depletion and, consequently, grid-induced separation is very likely. This assumption is supported by the fact that at the extraction location of Fig. 5.10 the maximum grid cell size $\Delta_{\max}$ is only 9% of the boundary-layer thickness δ, while according to Menter [112], a ratio of $\Delta_{\max}/\delta < 0.3$ makes DDES prone to grid-induced separation. To investigate the effectiveness of the new shieldings, boundary-layer calculations are presented in Fig. 6.3 corresponding to the very wall-normal extraction location of Fig. 5.10 (attached flow, $r/R = 0.77$, $x/c = 0.75$, $t/T = 0.3$ ↑). First, it shows that increasing the constant C_{d1} moves the transition from RANS to LES mode away from the surface as intended. However, with $C_{d1} = 25$, the LES mode is still fully activated ($1 - f_d = 0$) inside the boundary layer, which yields a deficient viscosity ratio ν_t/ν. Using $C_{d1} = 30$, the mode transition

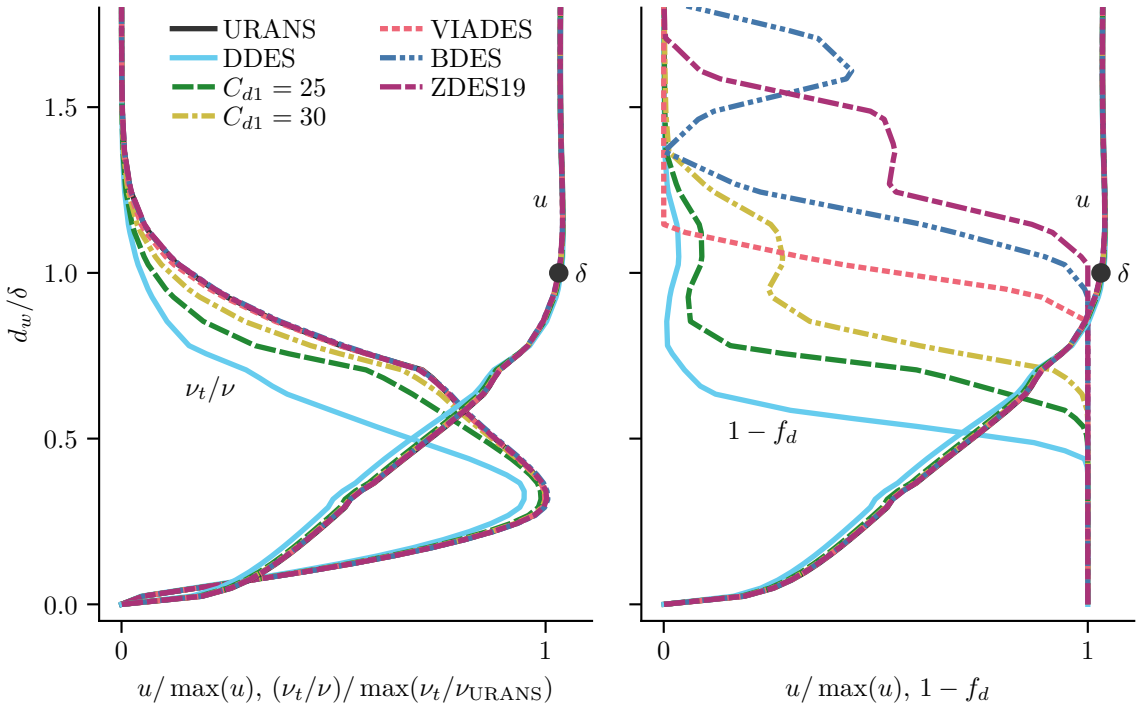

Figure 6.3: Comparison of viscosity ratios ν_t/ν (left) and boundary-layer shielding functions $1 - f_d$ (right) at $r/R = 0.77$, $x/c = 0.75$ and $t/T = 0.3$ ↑ corresponding to wall-normal extraction location of Fig. 5.10. Adapted from Letzgus et al. [143].

also starts early but is not completed within the boundary layer, thus, the viscosity ratio is almost completely restored. Secondly, VIADES, BDES and ZDES19 yield viscosity ratios that coincide with the one of URANS, indicating perfect boundary-layer shielding. Indeed, with those three methods, the transitions from RANS to LES mode occur around the approximate boundary-layer thickness δ with VIADES being the most aggressive and ZDES19 the most conservative.

Comparing the instantaneous flow fields by means of in-plane vorticity and streamlines in Fig. 6.4, it is apparent that the strong trailing-edge separation found in DDES at $t/T = 0.42$ is widely reduced with all methods, although the $C_{d1} = 25$ solution

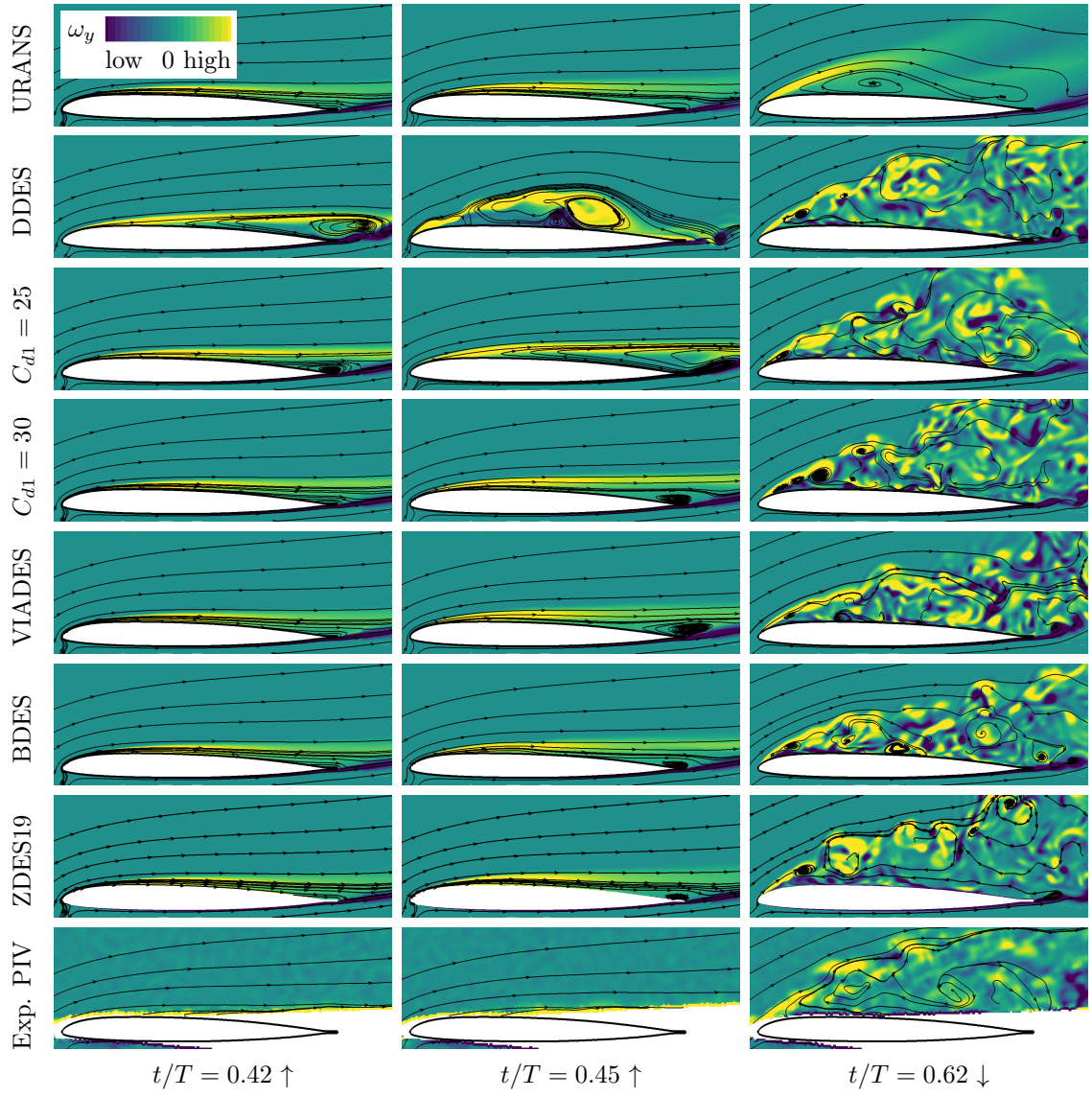

Figure 6.4: Comparison of contours of instantaneous in-plane vorticity and in-plane streamlines at $r/R = 0.77$ at three points during the dynamic stall cycle. Adapted from Letzgus et al. [143].

is somewhere in-between. At $t/T = 0.45$, the massive shear-layer rollup of DDES is absent from all other computations and, again except of the $C_{d1} = 25$ variant, all new shielding approaches exhibit a quite comparable trailing-edge separation. Then, at $t/T = 0.62$, when there is complete leading-edge flow separation, all DDES-based computations show very similar flow fields that agree very well with the PIV measurement, indicating that all variants are correctly operating in the LES mode.

Looking at the sectional lift and pitching-moment coefficients plotted in Fig. 6.5, the proper functioning of the new shieldings is confirmed: Recall that the non-plausible premature peaks in lift and nose-down pitching moment of DDES were caused by the dramatic shear-layer rollup resulting from the strong trailing-edge separation and were not related to dynamic stall. None of $C_{d1} = 30$, VIADES, BDES or ZDES19

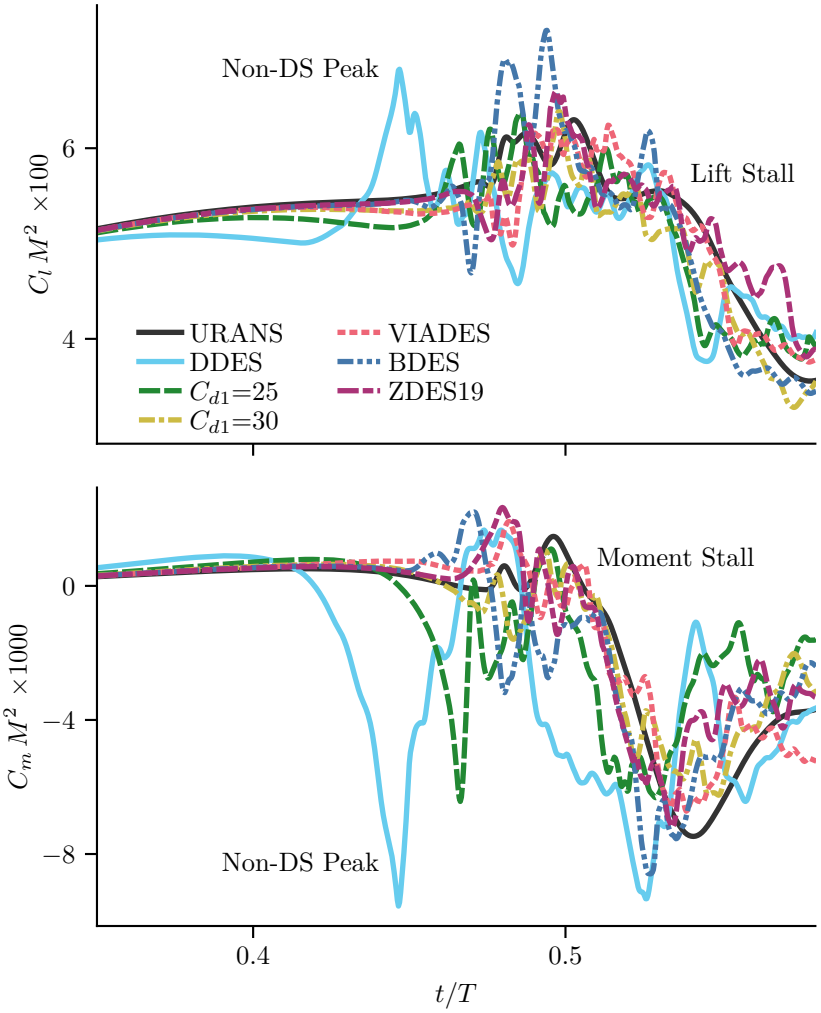

Figure 6.5: Computed sectional lift (top) and pitching moment (bottom) coefficients (reduced data, single cycle, slightly low-pass filtered) at $r/R = 0.77$ around upper turning point show influence of different boundary-layer shielding approaches.

exhibits this artifact, but have their dynamic-stall-related lift and moment stall quite simultaneously with URANS. This fact is a strong indication of a sufficient boundary-layer shielding, as the point of separation in space and time should be determined by the underlying RANS turbulence model that governs the relevant boundary-layer processes. Since the trailing-edge separation is reduced with the new shieldings, the associated flattening of the lift curve around $t/T = 0.4$ is no longer present, too. Furthermore, Fig. 6.5 finally confirms that setting $C_{d1} = 25$ does not provide sufficient shielding, as a premature, although smaller, peak in nose-down pitching moment still occurs.

The overall shieldings or the final RANS/LES regions of VIADES, BDES and ZDES19 are depicted in Fig. 6.6 by means of contours of $f_d = 0.5$ at three points during the dynamic stall cycle. At $t/T = 0.46$, with VIADES, the shallow separation bubble at the leading part of the suction side is treated in RANS mode, but the trailing-edge separation is almost entirely in LES mode, which is in accordance with the DES concept (compare Fig. 3.1). Using BDES, the separation bubble dominates the flow field and only its upper part is in LES mode, perhaps due to the very weak trailing-edge separation that is still in RANS mode. The shielding provided by ZDES19 is rather conservative, as the RANS mode is retained over a large distance from the surface, which was already visible in Fig. 6.3 for another boundary layer. Only a small part of the separation bubble is already in LES mode, presumably due to the inhibition function f_R that detects a positive wall-normal gradient of the vorticity there. Moving on in time to $t/T = 0.49$, where the flow is completely separated on the upper side, both VIADES and BDES have the RANS mode only in the immediate vicinity of the surface. With BDES, some shielding artifacts are noticeable, however, they are believed to have only a minor impact on the overall solution [116]. Again, ZDES19 exhibits a more conservative shielding, which is especially relevant at the beginning of the free shear layer forming at the leading

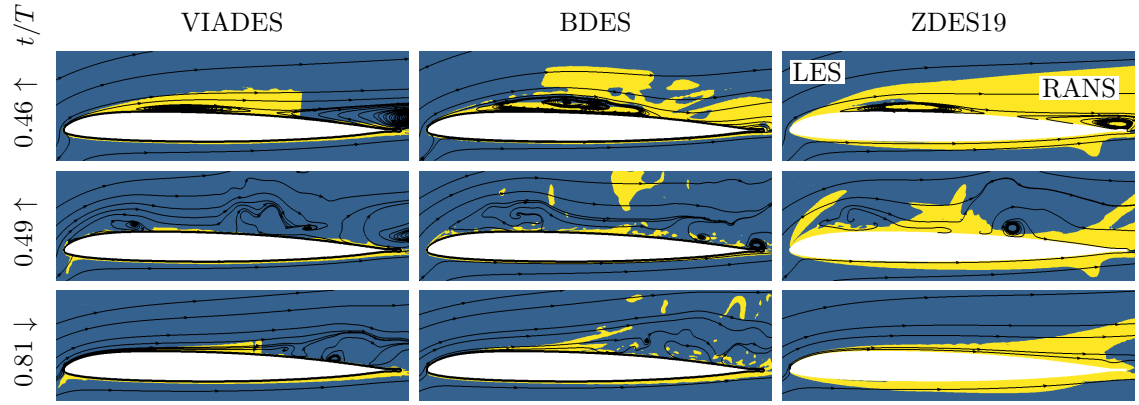

Figure 6.6: Contours of $f_d = 0.5$ of VIADES, BDES and ZDES19 indicating LES mode and RANS mode at $r/R = 0.77$ at three points during the dynamic stall cycle.

edge, as this suppresses actually desired flow instabilities (see gray-area problem in Section 3.3). Finally, at $t/T = 0.81$, with both VIADES and BDES, the flow reattachment starting at the leading edge is treated in RANS mode while the ongoing separation at the aft part is still in LES mode. At this point, reattachment is already completed with ZDES19 and the RANS mode dominates.

Overall, except of setting $C_{d1} = 25$, all investigated alternative shielding approaches provide a sufficient boundary-layer shielding to prevent grid-induced separation for the RTG dynamic stall case. They slightly vary in how vigorously they promote the LES mode, which leads to small differences in the overall flow field, but the resulting aerodynamic loads agree well and are free of non-physical, premature peaks.

6.3 Shortcomings of VIADES and BDES in Case of Rotational Inflows

In the previous section, the proper functioning of VIADES and BDES was demonstrated for a complex case of rotor dynamic stall. Nonetheless, both approaches have conceptual shortcomings in the specific scenario of having a wing or rotor blade experiencing a non-uniform, rotational inflow. This may be the natural case, for example, with staggered rotors like contra-rotating open rotors, wind farms, deliberate inflow turbulence or complex helicopter rotor flows where a rotor blade impinges on the tip vortex or wake of a preceding blade. Also, disturbances especially in the vorticity distribution in the outer flow may arise from numerical errors at hanging grid nodes or Chimera interfaces and from convergence deficits. Concerning VIADES, small fragments of vorticity found in the outer flow hinder the pseudo velocity introduced in Equation 6.3 from converging and, consequently, the δ_{99} criterion fails. With BDES, having a non-potential, that is, rotational inflow, the requirements for the Bernoulli equation are no longer completely met. Furthermore, the assumption of a negligible wall-normal pressure gradient may become problematic.

Based on the Bluecopter case that is described in great detail in Chapter 7, where strong flow separation as well as blade-vortex and blade-wake interaction occurs all over the retreating side of the rotor, two examples of the shortcomings of VIADES and BDES are given in Fig. 6.7. With VIADES, the flow separation on the suction side is correctly treated in LES mode, however, at the leading part of the pressure side the RANS mode reaches far into the outer flow. The boundary-layer calculation at the marked extraction location reveals that after the primary drop of vorticity very close to the surface, where the actual boundary-layer edge is judging from the velocity profile, there is still low vorticity which decreases only

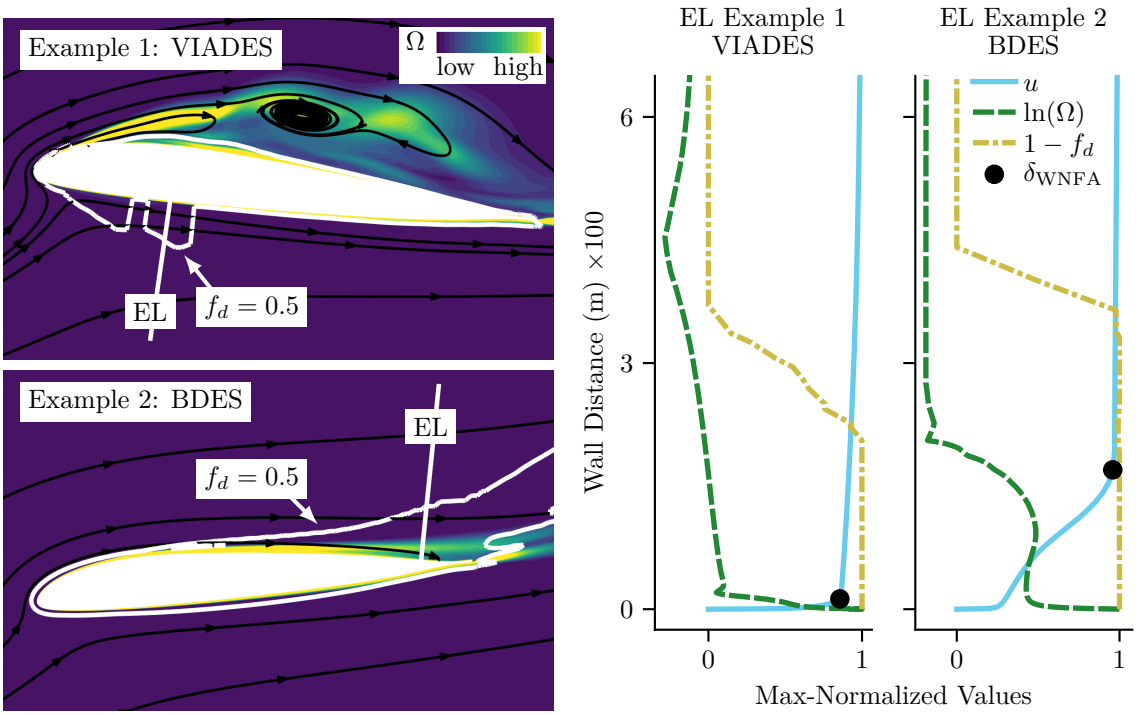

Figure 6.7: Shortcomings of VIADES ($\psi = 315°$) and BDES ($\psi = 180°$) on a helicopter rotor blade. The RANS/LES interface is indicated by the white line where $f_d = 0.5$, which partially disagrees with the boundary-layer edge highlighted by the vorticity contours. The profiles on the right show data of the marked extraction locations (EL), Ω is plotted logarithmically for clarity. The black dots indicate the correct boundary-layer edge found by the WNFA shielding introduced in Section 6.4.

gradually. This causes VIADES to determine the boundary-layer edge and the transition from RANS to LES mode, respectively, way too far from the surface. With BDES, a shielding artifact occurs at $\psi = 180°$, where the flow is about to separate at the trailing edge. In the whole aft part of the suction side, the detection of the boundary-layer edge fails and the RANS mode reaches far into the outer flow.

Arguably, it is conservative and by that noncritical to treat parts of the outer flow in RANS mode. However, at least with VIADES, there is a potentially dangerous mechanism that could unintentionally destroy the shielding: The flow separation sensor (Equation 6.4) should only be active in the viscous inner flow, but when VIADES detects the boundary-layer edge somewhere far off in the outer flow, inflow disturbances may also be counted as separated flow, thus, the ratio of "separated to attached flow" might exceed the threshold of 25%, and, consequently, the LES mode would be activated prematurely. Furthermore, concerning both VIADES and BDES, the named issues sometimes also trigger the RANS mode in regions of massively separated flow leading to an inconsistent

RANS/LES interface contradicting the DES principle. Although the successful application of both approaches to the mentioned helicopter dynamic stall case will be demonstrated in Section 6.5, a somewhat careless use of VIADES and BDES is not recommended given the circumstances of disturbed, rotational inflow.

6.4 Wall-Normal Flow Analysis Shielding (WNFA)

As just shown, even the newly developed RANS/LES shieldings BDES and VIADES struggle with complex helicopter rotor flows. Therefore, yet another method is presented that is based – as the VIADES shielding – on the instantaneous wall-normal flow analysis (WNFA). The primary goal of this method is to not only detect the boundary-layer edge in case of attached flow but also to consistently and robustly detect the outer edge of the separated shear layer, even in case of non-uniform, rotational inflow. At first glance, this is counter-intuitive because in the context of a DES the ultimate objective is to define the transition from RANS to LES mode, which does not necessarily have to happen at said edge. Recall that, on the contrary, the fundamental principle of a DES is to treat separated flow in LES mode to enable more realistic flow instabilities (Fig. 3.1).

However, knowing the correct outer edge of the separation zone is very important for two reasons: First, it allows to evaluate the height and by that the strength of the separation zone, which can be used to decide if the shielding is to be partially destroyed for an early switch to LES mode or not (compare VIADES in Section 6.1.3). Secondly, detecting only the primary drop of vorticity or primary increase of velocity close to the surface yields an error-prone shielding, because a shielding-worthy boundary-layer profile may feature local extrema well inside the boundary layer that would prematurely trigger the LES mode. In sum, detecting the outermost edge that separates the viscous inner and inviscid outer flow significantly increases the chance of making the right choice between RANS and LES mode, as demonstrated in this section.

6.4.1 Algorithm of WNFA Shielding

The proposed method is divided into five steps: The first step is to compute the moving average of the velocity from the outer flow towards the surface to establish a local far-field condition. In the second step, the actual and the just computed averaged velocity are compared in order to identify and blank near-wall regions of

separated flow, which significantly eases the detection of the outermost boundary-layer or shear-layer edge. This detection is carried out in steps three and four by means of a sophisticated analysis of the wall-normal vorticity distribution. Finally, in step five, the strength of a possible flow separation can safely be evaluated and, if appropriate, an early transition to LES mode is allowed.

As for VIADES, the structured grid topology is utilized to "move along" grid indices instead of the actual wall-normal direction and the existing dummy-layer and block-exchange code infrastructure is used to distribute data. Thus, for each surface cell, the shielding is determined individually by applying the following algorithm to the "pillar" of cells that are stacked on top of it. The subscript 0 denotes the cell that is closest to the surface, the subscript ∞ denotes the cell that is the farthest away from it (often at the end of the computational domain) and is expected to be in the far field, and the subscript i denotes the current cell when marching across a wall-normal "pillar". To be independent of the grid, all averages that are computed throughout the WNFA shielding are weighted with the wall-normal cell height.

Step 1: Moving-Averaged Velocity and Projected Velocity ($\vec{u}_{\mathrm{MA}_{\infty\to 0}}$, $\vec{u}_{\mathrm{PoMA}}$)

The purpose of the steps 1 and 2 is to detect near-wall regions of flow separation and to blank or exclude them from the following detection of the boundary-layer or shear-layer edge, which substantially increases the robustness and consistency of the method when facing non-uniform, rotational inflow. The blanking is based on a comparison of the actual flow velocity vector to an averaged velocity vector that is supposed to represent the far field, since in case of separation, the near-wall flow no longer follows the general direction of the outer flow.

Due to the complexity of the helicopter rotor flow field, it is impossible to globally find a single flow vector that represents the *true* far field. Nevertheless, if far enough above a particular spot on the rotor blade surface, the influence of the viscous surface vanishes and the flow becomes basically inviscid, thus, a "local far field" is reached. However, as discussed in Section 6.3, typically there are still some small disturbances and gradients in that far field that render an easy determination of the boundary-layer edge impossible. The first step of the presented shielding therefore is to smooth out small fluctuations while preserving the far-field condition. This is achieved by a cumulative moving average (MA) of the velocity, starting farthest away from and ending at the surface, denoted $\vec{u}_{\mathrm{MA}_{\infty\to 0}}$. By using a cumulative moving average instead of a moving average with a sample window, a data point has less impact the closer it is to the surface, which preserves the far-field condition sufficiently well. Using the velocity instead of the vorticity at this point is advantageous, because velocity

fluctuations in the far field are rather small compared to the velocity magnitude, while the vorticity magnitude approaches zero in the far field, which makes even small vorticity fluctuations to appear large.

Next, the local velocity vector $\vec{u}$ is projected on that moving-averaged vector $\vec{u}_{\mathrm{MA}_{\infty\to0}}$ yielding a new vector

$$\vec{u}_{\mathrm{PoMA}} = \frac{\vec{u}\cdot\vec{u}_{\mathrm{MA}_{\infty\to0}}}{|\vec{u}_{\mathrm{MA}_{\infty\to0}}|^2}\vec{u}_{\mathrm{MA}_{\infty\to0}} \tag{6.7}$$

that is parallel to $\vec{u}_{\mathrm{MA}_{\infty\to0}}$. Figure 6.8 illustrates these three velocities in case of massively separated flow at the extraction location (EL). A two-dimensional analysis of the flow at a spanwise slice (Fig. 6.8 left) already indicates strong flow separation, which is confirmed by the three-dimensional view (Fig. 6.8 center). Far above the rotor blade surface, there is almost uniform chordwise flow, thus, $\vec{u}$ and $\vec{u}_{\mathrm{PoMA}}$ basically coincide. However, near the surface, $\vec{u}$ has a high spanwise component and the streamlines indicate recirculating flow, which is – as intended – not the case with the moving-averaged velocity $\vec{u}_{\mathrm{MA}_{\infty\to0}}$. Consequently, the magnitudes of the real velocity u and the projected velocity u_{PoMA} differ greatly (Fig. 6.8 right) in the region of flow separation, which lays the foundation of the following blanking.

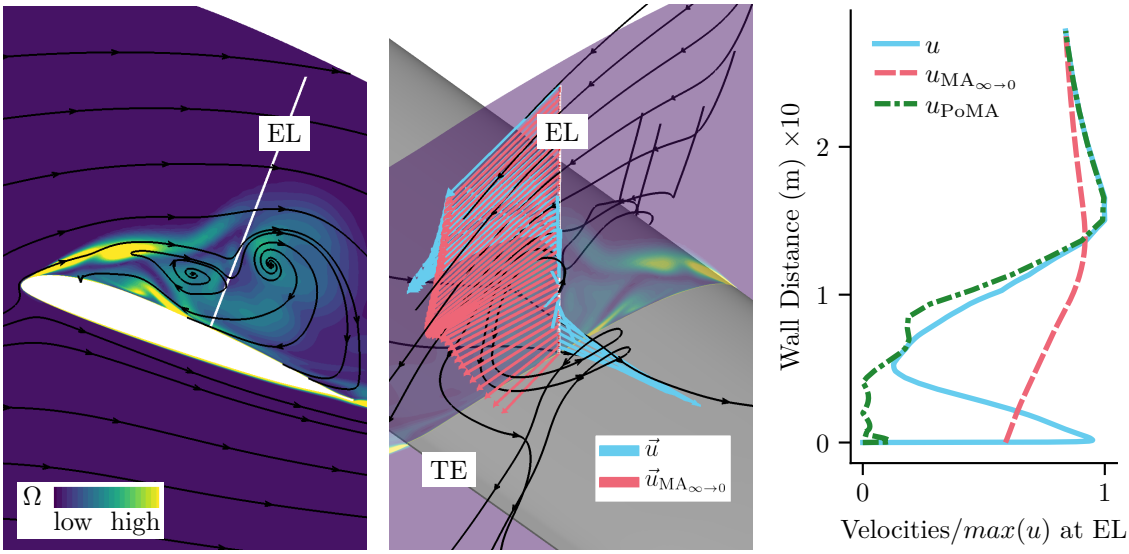

Figure 6.8: Exemplary computation of the projected velocity u_{PoMA} in case of massively separated flow on a rotor blade at the wall-normal extraction location (EL) indicated by the white line. The real velocity $\vec{u}$ has a high spanwise component near the blade surface, which is not the case for the cumulatively moving-averaged velocity $\vec{u}_{\mathrm{MA}_{\infty\to0}}$. The vector projection of $\vec{u}$ on $\vec{u}_{\mathrm{MA}_{\infty\to0}}$ yields the final value u_{PoMA}. (Left) In-plane streamlines and vorticity. (Center) 3D streamlines and velocity vectors. (Right) Velocity magnitudes extracted at EL.

Step 2: Blanking of the Projected Velocity ($u_{\mathrm{PoMA}_{\mathrm{blanked}}}$)

In this step, the real velocity u and the projected velocity u_{PoMA} from step 1 are compared and analyzed to identify and blank regions of separated flow, which allows the robust detection of the outer boundary-layer or shear-layer edge in the following steps 3 and 4. The first modification is to only keep positive values ($u_{\mathrm{PoMA}} = \max(u_{\mathrm{PoMA}}, 0)$), because if u_{PoMA} is negative, the angle between the velocity vector $\vec{u}$ and the moving-averaged velocity $\vec{u}_{\mathrm{MA}_{\infty\to 0}}$ exceeds 90°, which is a strong indication of flow separation. In many cases of three-dimensional separation, however, this condition is not fully met. Therefore, additional criteria are required.

For the next modification, consider moving along the wall-normal "pillar" from the outer far field towards the surface. When "entering" the viscous inner flow, be it in form of an attached boundary layer or separated shear layer, both the real velocity u and the projected velocity u_{PoMA} are expected to decrease substantially. Thus, to meet the necessary condition to be inside the inner region and not, by mistake, in the outer region, it is looked for a significant drop of the projected velocity u_{PoMA}. For that purpose, it is checked if the current value $u_{\mathrm{PoMA}}(i)$ becomes zero or is at a local minimum where the value is well below (threshold t_1) the continuously updated maximum value.

Of course, this criterion alone is not enough, as the projected velocity u_{PoMA} significantly decreases and reaches zero at the surface also in case of attached flow. Therefore, two sufficient conditions are introduced that allow to differentiate between attached (no blanking allowed) and separated flow (blanking allowed). The first one is that u_{PoMA} significantly increases (threshold t_2) again approaching the surface. This occurs when there is strong attached, near-wall flow below a separation zone that is somewhat aligned with the outer flow direction. The second sufficient condition is that the projected velocity u_{PoMA} increases a bit but is significantly smaller (threshold t_3) than the velocity u, which is the case when the near-wall flow direction below a separation zone noticeably deviates from the general direction of the outer flow. In many cases, both sufficient conditions are met simultaneously.

The threshold factors are set to $t_1 = 2/3$, $t_2 = 4/3$ and $t_3 = t_1 = 2/3$. Note that the thresholding here aims for robustness instead of exact separation, that is, allowing for various shapes of velocity profiles and for small velocity disturbances, for example unexpected local extrema, in the boundary layer.

To summarize, the pseudo code for a loop over the cells in wall-normal direction starting at the far field and moving towards the surface is:

for $i = \infty$ **to** 0

$u_{\mathrm{PoMA}}(i) = \max(u_{\mathrm{PoMA}}(i), 0)$

$u_{\mathrm{PoMA_{max}}} = \max(u_{\mathrm{PoMA_{max}}}, u_{\mathrm{PoMA}}(i))$

if $u_{\mathrm{PoMA}}(i) = 0$ **or** $\big(u_{\mathrm{PoMA}}(i) < t_1\, u_{\mathrm{PoMA_{max}}}$ **and** $u_{\mathrm{PoMA}}(i) \geq u_{\mathrm{PoMA}}(i+1)\big)$

  blankingPossible = True

  $u_{\mathrm{PoMA_{min}}} = u_{\mathrm{PoMA}}(i)$

if *blankingPossible* **and** $\Big(u_{\mathrm{PoMA}}(i) > t_2\, u_{\mathrm{PoMA_{min}}}$ **or** $\big(u_{\mathrm{PoMA}}(i) < t_3\, u(i)$ **and** $u_{\mathrm{PoMA}}(i) \geq u_{\mathrm{PoMA}}(i+1)\big)\Big)$

  blankingActivated = True

The blanking of the projected velocity is demonstrated in Fig. 6.9. In both example cases, there is massively separated flow at the respective extraction location and there is a local minimum of u_{PoMA} that is well below $^2/_3\, u_{\mathrm{PoMA_{max}}}$, thus, blanking might be appropriate. Marching towards the surface, in example 1, the projected velocity then increases well beyond $^4/_3\, u_{\mathrm{PoMA_{min}}}$, which finally activates the blanking starting at the location of $u_{\mathrm{PoMA_{min}}}$. In example 2, the other sufficient condition of the blanking is met, since u_{PoMA} stays below $^4/_3\, u_{\mathrm{PoMA_{min}}}$ but is lower than $^2/_3\, u$.

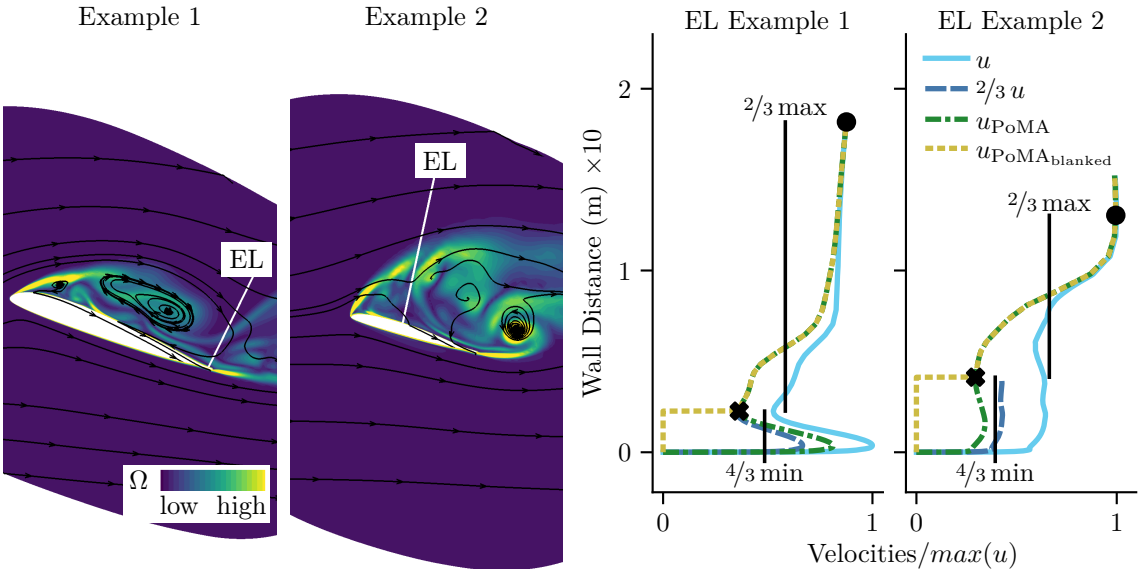

Figure 6.9: Blanking of the projected velocity u_{PoMA} at the extraction location (EL) in case of massively separated flow. Starting from the far-field, the maximum of u_{PoMA} is marked by ●. The following local minimum (necessary condition) that is below $^2/_3\, \max(u_{\mathrm{PoMA}})$ is marked by ✖. In example 1, the sufficient condition activating the blanking is $u_{\mathrm{PoMA}} > {}^4/_3\, \min(u_{\mathrm{PoMA}})$. In example 2, it is $u_{\mathrm{PoMA}} < {}^2/_3\, u$.

Step 3: Coefficient of Variation of the Vorticity ($\mathrm{CV} = {}^{\sigma_\Omega}/_{\mu_\Omega}$)

So far, the projected and blanked velocity (step 1 and step 2, respectively) enables to roughly differentiate between inviscid outer and viscous inner flow in case of separation. Recall, however, that the goal is to determine the edge of the boundary layer or shear layer. Unfortunately, it is impossible to solely rely on the convergence of the velocity in the far field since, often enough, the velocity simply does not converge at a reasonable distance from the rotor blade, compare Figs. 6.8–6.12. Detecting a vanishing of the vorticity in the far field is also prone to failure for basically the same reason.

Nevertheless, analyzing the wall-normal vorticity distribution in one way or another is fundamentally important, as it is a direct indication of wall-bound shear flow. Here, this is done by computing the so-called coefficient of variation (CV) [146], which is the ratio of standard deviation σ to the mean μ. It is computed locally at every grid cell starting from the surface and moving towards the far field, in other words, the mean $\mu_{\Omega,0\to\infty}$ is simply the cumulative moving average and $\sigma_{\Omega,0\to\infty}$ the cumulative standard deviation of the vorticity.

The typical course of these quantities is illustrated in Fig. 6.10. Since most of the vorticity is found in close proximity to the surface, the moving average $\mu_{\Omega,0\to\infty}$ yields a smoothed vorticity distribution that slowly approaches zero marching towards the

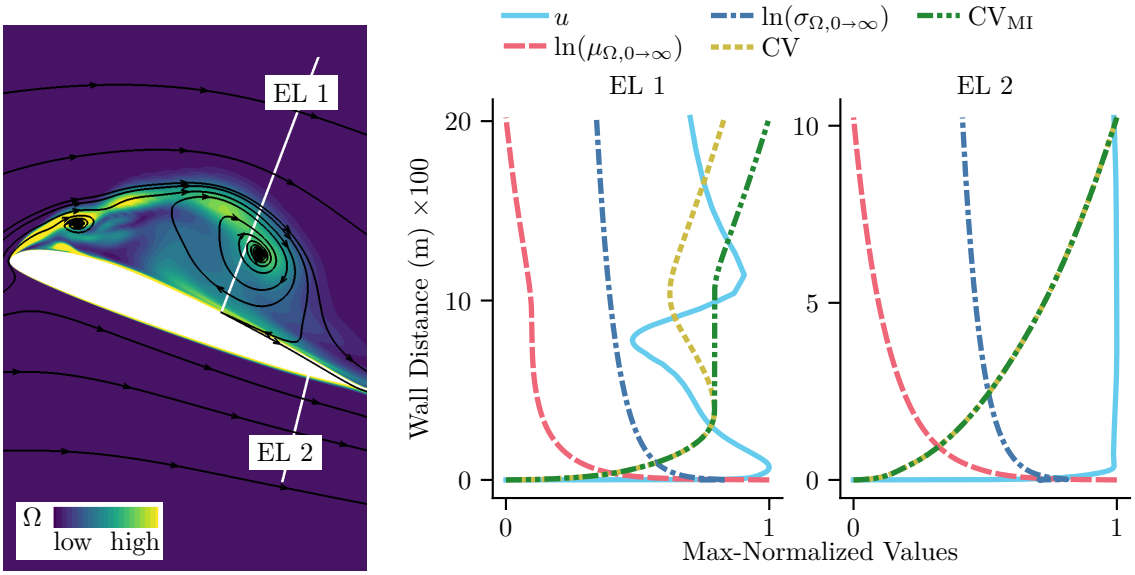

Figure 6.10: Example of the coefficient of variation ($\mathrm{CV} = {}^{\sigma}/_{\mu}$) and its monotonically increasing variant ($\mathrm{CV_{MI}}$) at the two extraction locations EL 1 and EL 2. The cumulatively moving-averaged (starting at the surface) vorticity $\mu_{\Omega,0\to\infty}$ and its standard deviation $\sigma_{\Omega,0\to\infty}$ are plotted logarithmically for clarity.

far field. The cumulative standard deviation $\sigma_{\Omega,0\to\infty}$ is, naturally, zero at the first cell but immediately reaches its maximum near the surface due to the strong vorticity gradients. It then decreases, but at a slower rate than the moving average. As a consequence, the coefficient of variation is zero at the surface and gradually increases towards the far field. In between, the course of the coefficient basically results from the vorticity distribution, in that it increases quickly when the vorticity drops significantly, which leads to a rather sudden increase of the standard deviation $\sigma_{\Omega,0\to\infty}$ and a decrease of the moving average $\mu_{\Omega,0\to\infty}$. In most cases, the coefficient of variation increases monotonically throughout the whole wall-normal "pillar" (EL 2 in Fig. 6.10), but sometimes, in case of flow separation, it does not (EL 1 in Fig. 6.10). It was found that the robustness of this part of the shielding is greatly improved by enforcing a monotonic increase (MI) of the coefficient of variation, see course of the additional quantity $\mathrm{CV}_{\mathrm{MI}}$.

Step 4: Shielding Functions for BL/SL-Edge Detection (f_{CV}, f_{d_w}, f_δ)

Finally, all components are available to assemble shielding functions that allow the determination of the boundary-layer or shear-layer edge. The first function uses the coefficient of variation computed in step 3, as every local value $\mathrm{CV}_{\mathrm{MI}_i}$ is normalized by the "global" maximum value that is identical to the value at the far field $\mathrm{CV}_{\mathrm{MI}_\infty}$:

$$f_{\mathrm{CV}} = 1 - \frac{\mathrm{CV}_{\mathrm{MI}_i}}{\max(\mathrm{CV}_{\mathrm{MI}})} = 1 - \frac{\mathrm{CV}_{\mathrm{MI}_i}}{\mathrm{CV}_{\mathrm{MI}_\infty}}. \tag{6.8}$$

Due to the nature of $\mathrm{CV}_{\mathrm{MI}}$, the function f_{CV} is one at the surface and zero at the far field, as shown in Fig. 6.11. The second function f_{d_w} is a simple weighting that reduces the influence of a point the farther it is away from the surface:

$$f_{d_w} = \sqrt{1 - \frac{d_{w_i}}{d_{w_\infty}}}. \tag{6.9}$$

This function is supposed to further increase the robustness of the shielding, as data in the far-field region, which is potentially "noisy", is damped. However, the influence of f_{d_w} turned out to be only minor. Eventually, the projected, blanked velocity $u_{\mathrm{PoMA}_{\mathrm{blanked}}}$ is multiplied with f_{CV} and f_{d_w} yielding the ultimate shielding function f_δ:

$$f_\delta = u_{\mathrm{PoMA}_{\mathrm{blanked}}} \cdot f_{\mathrm{CV}} \cdot f_{d_w}. \tag{6.10}$$

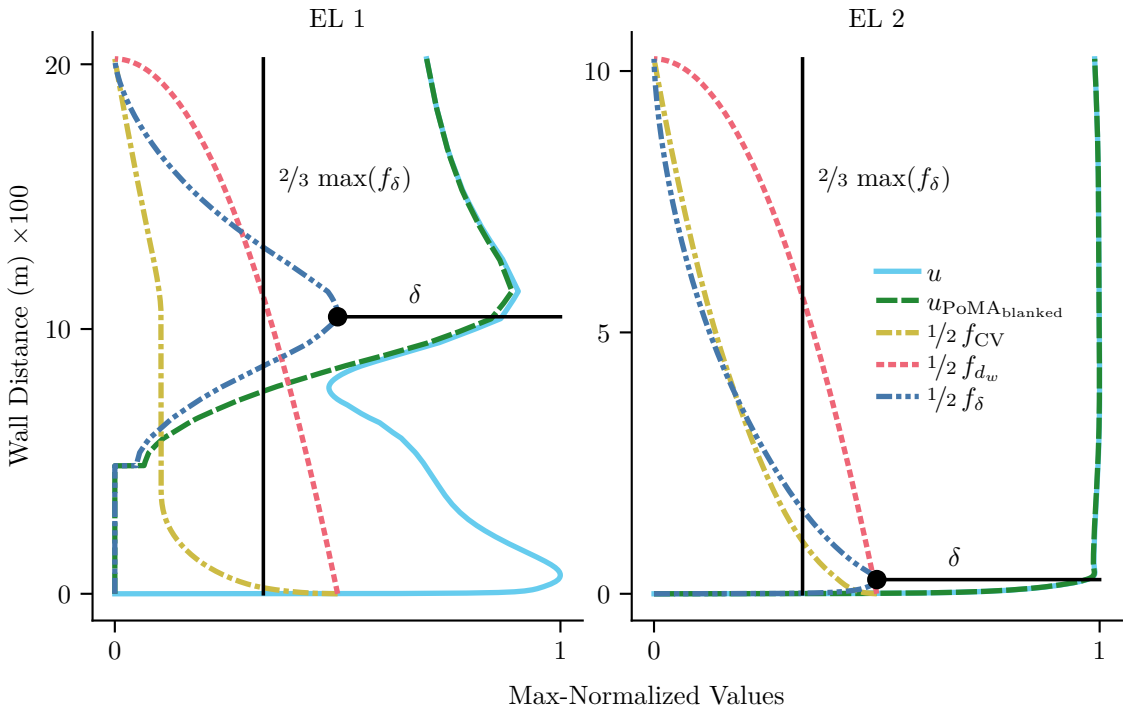

Figure 6.11: Example of the shielding functions f_{CV}, f_{d_w} and f_δ and velocity profiles related to the extraction locations (EL) in Fig. 6.10. The shear-layer (EL 1) or boundary-layer (EL 2) thickness δ corresponds to the location of the outermost maximum of the final shielding function f_δ. Shielding functions are scaled with ½ for clarity.

Now, the edge of the boundary layer or shear layer is found at the position δ of the local maximum of f_δ that is the farthest away from the surface, see Fig. 6.11. As for the blanking of the projected velocity, a simple but robust threshold is applied to avoid false-positive results in the far field, where small local maxima of f_δ might occur: A local maximum at f_{δ_i} is only considered if $f_{\delta_i} > t_4 \max(f_\delta)$ with $t_4 = ⅔$.

In Fig. 6.12, the edge detection is demonstrated on a rotor blade experiencing flow separation and highly turbulent inflow in the fourth quadrant, where it impinges on the chaotic wake and tip vortices of the preceding blades. At the outer spanwise slices, where the extraction locations EL 1–3 are, the large separation zones on the suction side are well detected. On the pressure side, the vorticity contours indicate an undisturbed far field, thus, the edge detection there is relatively easy. At the innermost slice containing EL 4, however, there clearly are vortical structures both above the suction and the pressure side that do not originate from flow separation at the slice, but are part of the turbulent inflow. Arguably, a flow situation like this is the most challenging because knowing for example only the flow data at EL 4, it is not obvious if there is a narrow boundary layer or a thick shear layer. Looking at the vorticity distributions, there is no clear indication why the one of

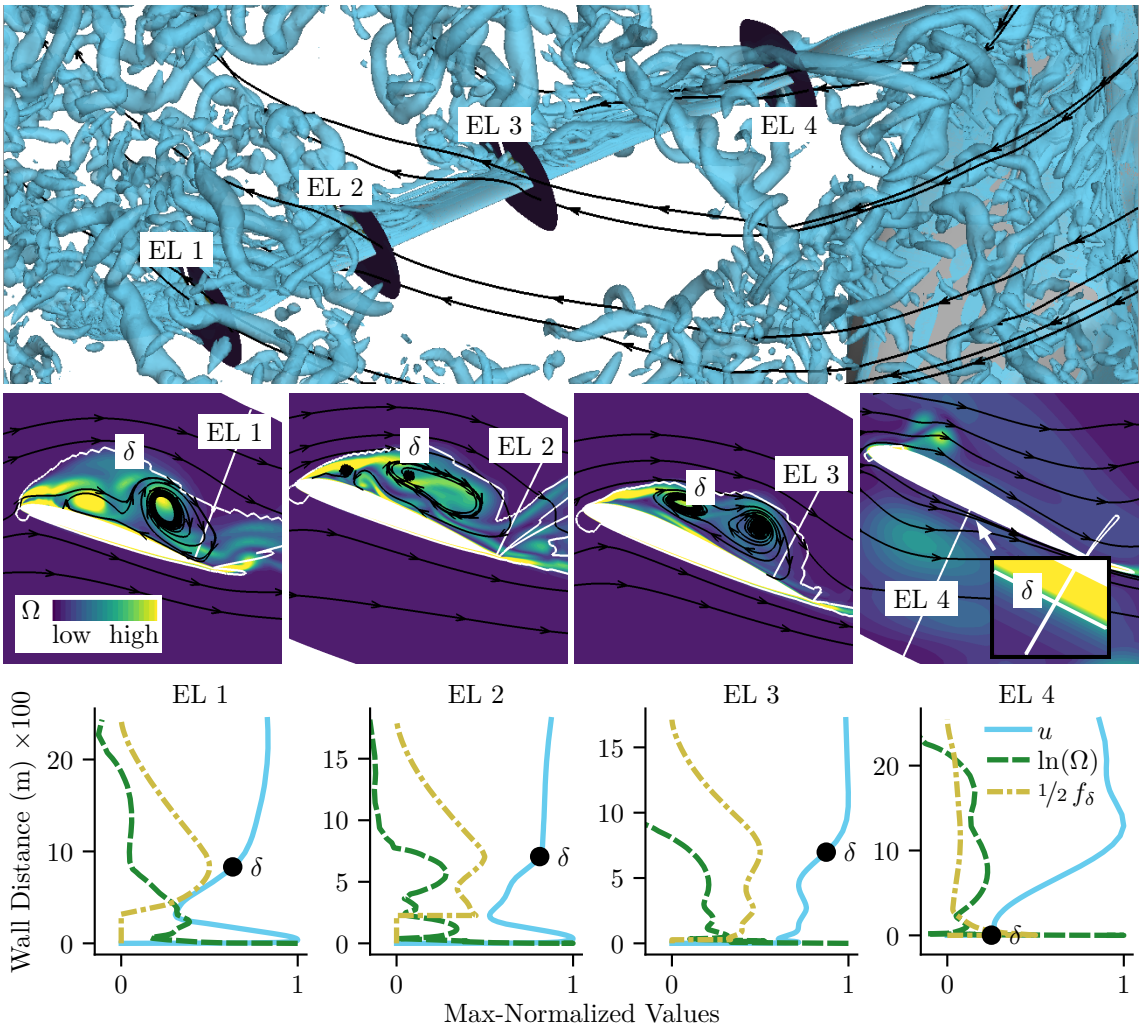

Figure 6.12: Detection of boundary-layer or shear-layer edge on rotor blade experiencing turbulent inflow in forth quadrant. A detailed analysis is provided at the spanwise slices and the extraction locations EL 1 to EL 4. (Top) λ_2 isosurfaces visualizing complex inflow. (Center) In-plane streamlines and vorticity with extraction location (white wall-normal line) and detected boundary-layer (EL4) or shear-layer edge (EL 1–3) labeled with δ. (Bottom) Corresponding profiles of velocity, vorticity (plotted logarithmically for clarity) and shielding function f_δ (scaled with $1/2$ for clarity).

EL 1 should represent separated and the one of EL 4 attached flow. Also, when comparing the velocity distributions of EL 3 and EL 4, it is obvious that they are ambiguous regarding the condition of the flow. Nevertheless, the proposed algorithm manages to detect the correct edge, judging from the "whole picture" that is provided by the spanwise slices.

Note that for less complex flows, for example in case of an irrotational inflow providing an undisturbed far field, a smooth boundary layer or even a separated flow featuring a distinct recirculation zone, it would be sufficient but much simpler and threshold-

free to only consider the velocity magnitude u and the non-modified coefficient of variation CV to compute

$$f_{\delta_{\text{simple}}} = u \left(1 - \frac{\text{CV}_i}{\text{CV}_\infty}\right) \tag{6.11}$$

and search for the outermost local maximum of $f_{\delta_{\text{simple}}}$ to get the location of the boundary-layer or shear-layer edge. For complex flows, however, only the combination of all the proposed steps promotes the crucial features and allows for tolerant yet robust thresholds, which significantly reduces the number of faulty results and provides a very consistent edge detection as demonstrated in Fig. 6.12.

Step 5: Partial Destruction of the SL Shielding if Flow is Separated

With the previous steps, the outer edge of a boundary layer in case of attached flow or of a shear layer in case of separated flow is determined. Now, a transition point must be defined that allows a quick transition from RANS to LES mode in case of strong flow separation. For this, the approach of the VIADES shielding (Section 6.1.3) is applied again: A projection of the vorticity vector is used to locally decide whether the flow is attached or separated (Equation 6.4). In addition, flow is also declared to be separated if $u_{\text{PoMA}} \leq 0$. Then, the summed-up height of separated flow is compared to the shear-layer thickness found in step 4. Since it is very important to keep narrow separation bubbles in RANS mode, the shielding is, analogous to VIADES, only destroyed if the separation height is at least 25% of the shear-layer thickness.

Lastly, if there is substantial flow separation allowing a partial destruction of the shielding, the near-wall region, featuring a thin boundary layer of the recirculation zone, must still be defined to be treated in RANS mode, as illustrated in Fig. 3.1. For this purpose, a signal processing algorithm [147] is applied to detect the end point or "knee" of the primary drop of vorticity that occurs near the surface. The algorithm is simple: First, the point of the global maximum of the vorticity profile, denoted P_S, is connected to its endpoint at the far field, denoted P_E, yielding a line $\vec{b}$. Then, for each point $P(i)$ of the vorticity profile, the minimum distance vector $\vec{s}$ to that connecting line is computed and the searched-for "knee" point, denoted d_{w_Ω}, is found where this distance is the largest. For increased robustness and since already computed in step 3, the profile of the cumulative moving average $\mu_{\Omega,0\to\infty}$ is used

instead of the real vorticity. With basic vector analysis, one has

$$\begin{aligned}
\vec{b} &= P_E - P_S = \big(\mu_{\Omega,0\to\infty}(\infty) \approx 0, d_w(\infty)\big) - \big(\max(\mu_{\Omega,0\to\infty}), d_w(\max(\mu_{\Omega,0\to\infty}))\big),\\
\hat{b} &= \frac{\vec{b}}{|\vec{b}|},\\
\vec{p} &= P(i) - P_S = \big(\mu_{\Omega,0\to\infty}(i), d_w(i)\big) - P_S,\\
\vec{s} &= \vec{p} - (\vec{p}\cdot\hat{b})\,\hat{b}.
\end{aligned} \tag{6.12}$$

In Fig. 6.13, the partial destruction of the shielding is visualized for a case of leading-edge separation. The outer edge of the shear layer, labeled δ, is correctly detected judging from the vorticity contours and the velocity profile. At the marked extraction location, the separation criterion f_{sep} is met for about 75% of the shear-layer height, thus the shielding is to be partially destructed in this region. On the right-hand side of the figure, the described vector analysis is depicted that leads to the final shielding or RANS/LES transition point at d_{w_Ω}. Looking at the vorticity contours or the velocity profile again, it shows that the edge of the boundary layer of the recirculation zone is conservatively, due to the use of $\mu_{\Omega,0\to\infty}$ instead of Ω, yet properly detected.

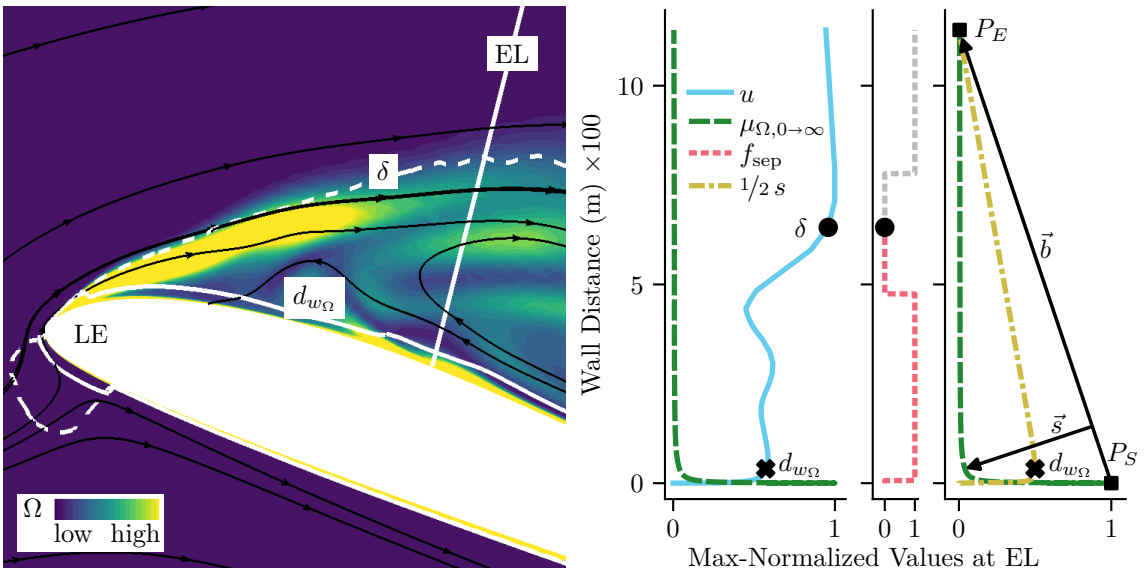

Figure 6.13: Example of the partial destruction of the shielding in case of leading-edge separation. The determined edge of the shear layer is at δ, indicated by the dashed white line in the spanwise slice (left) or by ● in the profile (right), which represents the data taken at the marked extraction location. The actual shielding or transition from RANS to LES mode occurs at d_{w_Ω}, indicated by the white line in the spanwise slice or by ✖ in the profile. The determination of d_{w_Ω} is visualized by the profiles of s (scaled with 1/2 for clarity) and $\mu_{\Omega,0\to\infty}$ and the vectors $\vec{s}$ and $\vec{b}$.

6.4.2 Assessment of Other Boundary-Layer- or Shear-Layer-Edge Detection Methods

One might state that the here presented algorithm for the WNFA shielding is unnecessarily complicated, as there are several known boundary-layer-edge detection methods that have proven to work well in multiple test cases. However, it showed that for helicopter rotor flows, they are prone to failure at some point or the other because, put simply, they do not anticipate and incorporate the complexity or sometimes rather oddity of these flows (compare velocity profiles in Figs. 6.8–6.13). Note that in the following assessment, there is no strict differentiation between attached boundary-layer and separated shear-layer edge, as it is believed that a method that only works for one or the other is of no real use anyway.

- **99% criterion or the like**: Generally, the boundary-layer edge is defined as the point above the surface where the velocity equals 99% of the free-stream velocity [100, 148]. Obviously, this criterion is only applicable to simple, idealized flows and would already fail in case of an accelerated flow. Using the vorticity-integrated pseudo velocity u_{ps} as in the proposed VIADES shielding mitigates that problem to a great extent. Alternatively, as done in the TAU [149] or elsA [150] CFD code, one can define a threshold value of the vorticity or shear stress, for example $\Omega/\max(\Omega) < 0.001$, that indicates the boundary-layer edge. However, specifying the correct far-field threshold value is very sensitive and case-dependent. Moreover, all these variants fail as soon as the vorticity does not gradually reach zero, that is, has plateaus or local extrema, which is common for separated flows. For elsA, these limitations are recognized and several restraints and exceptions are proposed, however, the fundamental flaw of relying on one velocity or vorticity value that represents the condition at the edge of the shear or boundary layer remains. This fact leads Cliquet et al. [150] to also provide a backup criterion that declares the boundary-layer edge at the point where the velocity stops increasing in wall-normal direction, which is even more prone to failure.

- **Bernoulli criterion**: The boundary-layer edge can also be detected using the compressible Bernoulli equation, as done in the BDES shielding [118], the TAU code [149] or in laminar-turbulent transition methods [151]. However, the fundamental requirements of the Bernoulli criterion are often not met for complex helicopter rotor flows, compare Section 6.3. Even if the flow allows the application of the approach, a crucial threshold must be defined [116], since the local flow velocity is compared to the edge velocity returned by the Bernoulli equation, leading to the described problems of a "99% criterion" approach.

- **Stock-Haase criterion**: Stock and Haase [152] proposed a wall-normal analysis of the flow by a diagnostic function $F_{\mathrm{SH}} = n\,{}^{\partial u}/_{\partial n} \approx n\,\Omega$ with n being the wall-normal coordinate. This diagnostic functions usually has its maximum somewhere in the boundary layer and the authors proposed $\delta = \epsilon\, n_{\max(F_{\mathrm{SH}})}$ and $\epsilon = 1.936$ for turbulent boundary layers, while Probst et al. [117] showed that ϵ has to be calibrated depending on the turbulence model. The function F_{SH} is also used for blanking the near-wall region, for example by Cliquet et al. [150]. Unfortunately, it turned out that the diagnostic function behaves very inconsistently for rotor flows and is very sensitive to small disturbances occurring outside the boundary layer, which makes it useless for a robust shielding.

- **Vorticity-integration method**: The method of integrating the vorticity to get a pseudo velocity, as used in the VIADES shielding or in Lovely [153], is promising, as it is simple, physics-based and this new quantity usually converges very quickly outside the boundary layer, allowing for a "99% criterion" approach that is less ambiguous than most others. However, it is not robust enough for cases with vortical inflow, as shown in Section 6.3.

- **Curvature or "Knee"-detection methods**: In step 5 of the proposed WNFA shielding, a signal processing algorithm [147] is used to detect the endpoint of the primary drop of the vorticity. In the same manner, one could try to detect the characteristic kink or "knee" in the wall-normal profiles of the (pseudo) velocity or vorticity that correlates very well with the edge of the boundary layer. Alike, the curvature [154] of a profile could be computed and the location of the maximum used as the boundary-layer edge, as done in a NASA code [155] based on the total-enthalpy profile. Although this approach mimics the astonishing human ability of determining the primary kink in a wall-normal profile very well, it is very sensitive to small disturbances like local extrema, which frequently occur very close to the surface, and is thus too error-prone. Applying massive curve smoothing would mitigate the numerical instability, but the results would still be ambiguous, since, for example in case of flow separation, one could not differentiate between the outer edge of a separated shear layer and the edge of the inner boundary layer.

- **Shape factor** H: The shape factor $H = {}^{\delta^*}/_{\theta}$ with δ^* being the displacement thickness and θ the momentum thickness, both obtained by wall-normal integration of the velocity, is often used to quantify the condition of a boundary layer [100, 148]. In the field of DES shieldings, it is used to decide whether a flow is attached or not, for example by Probst et al. [117], based on Castillo et al. [156] who proposed that separation is present if the shape factor becomes large and exceeds a certain value in the range of $H > 3$. Besides the fact that the computation of δ^* and θ is a "vicious circle" problem since a

meaningful value of the far-field velocity is required, it showed that for some flow separations on rotor blades, H is in the range of one, erroneously indicating fully attached flow. Consequently, the shape factor is no reliable criterion in the present context.

6.4.3 Concluding Remarks on the Wall-Normal Flow Analysis Shielding (WNFA) Approach

The here presented non-local shielding approach aims specifically at rotor applications where a non-uniform, rotational inflow is encountered, as disturbances in the generally inviscid outer flow are anticipated. The goal is to robustly detect the outer edge of a boundary layer or of a separated shear layer, afterwards to evaluate the strength of flow separation and, finally, allow a fast transition from RANS to LES mode as appropriate. Moving-averaging the velocity yields a far-field condition that is compared to the local velocity to get a sound knowledge of the condition of the flow. By computing the coefficient of variation of the vorticity, which is based on the moving average and standard deviation of the vorticity, the boundary- or shear-layer edge can be located. The employed thresholds are used only where they are considered less sensitive and edgy.

It is acknowledged that the WNFA shielding is somewhat cumbersome and cannot be implemented into a flow solver in a straight-forward manner. However, the intention of the proposal – besides providing a sufficient boundary-layer shielding – is twofold: First, it is believed that some ideas and methods – for example, the flow field averaging, the coefficient of variation or the identification of distinctive points in a boundary-layer profile – could be used as a standalone concept or initiate improvements in further shielding developments. Secondly, revealing the complexity and accepting numerical oddities and imperfections of boundary-layer or shear-layer flows in a helicopter rotor environment is found to be important for a thorough analysis of RANS/LES shieldings, or any boundary-layer evaluation for that matter.

6.5 Application of Alternative Shieldings to Helicopter-Rotor Dynamic Stall (Bluecopter Case)

In the previous Sections 6.3 and 6.4, it has been discussed that a helicopter rotor environment is particularly challenging for a boundary-layer shielding because of the non-uniform, rotational inflow due to tip vortex or wake interactions. Therefore, the presented alternative approaches were applied to the Bluecopter helicopter rotor case that is described in the following Chapter 7, where further details on the numerical setup and the flow conditions can be found. In short, the helicopter is in a highly loaded, high-speed turn flight associated with strong flow separations, multiple dynamic stall events and tip vortex and wake interactions over most parts of the retreating side. The resolution of the rotor blade grid is lower than that of the RTG grid and the cell-size/boundary-layer-thickness ratio is found to be $\Delta_{\max}/\delta \approx 0.6$, which is above the critical value of 0.3 determined by Menter [112]. Thus, the case is not really expected to suffer from grid-induced separation even when using the original DDES.

In Fig. 6.14, vorticity contours in the airfoil's aft region at an outboard spanwise slice are shown that indicate fully attached flow at $\psi = 180°$ (Fig. 6.14a) and strong trailing-edge separation at $\psi = 225°$ (Fig. 6.14b). Also, the respective RANS/LES interfaces are indicated by white isolines of $f_d = 0.5$. Additionally, wall-normal extraction locations (EL) of boundary- or shear-layer data are highlighted, which are more precisely analyzed in Fig. 6.15. First, with the attached flow, it is apparent that all shielding approaches keep the boundary layer on both sides sufficiently in RANS mode. Judging from the vorticity contours, WNFA and VIADES meet the boundary-layer edge the best, while the RANS mode of BDES and ZDES19 is too conservative. Furthermore, as already suspected, the shielding of the original DDES seems acceptable, but can be extended by setting $C_{d1} = 30$. Basically the same conclusions can be drawn from the boundary-layer profiles in Fig. 6.15a, where it is also confirmed that DDES has a too early beginning of the switching to LES mode, however, it is not fully activated ($f_d = 1$) within the boundary layer.

Then, with trailing-edge separation, both WNFA and VIADES – using the same shielding destruction mechanism – activate the LES mode shortly downstream the point of separation, which is in accordance with the DES concept (Fig. 3.1). Using standard DDES, the upper part of the shear layer already is in LES mode, while with $C_{d1} = 30$, BDES and ZDES19, this is the case only in a wedge-shaped region in the aft part of the shear layer, thus, the transition to LES mode seems delayed. Again, the shear-layer computations in Fig. 6.15b confirm these findings. It shows that WNFA and VIADES only shield the thin boundary layer of the recirculation

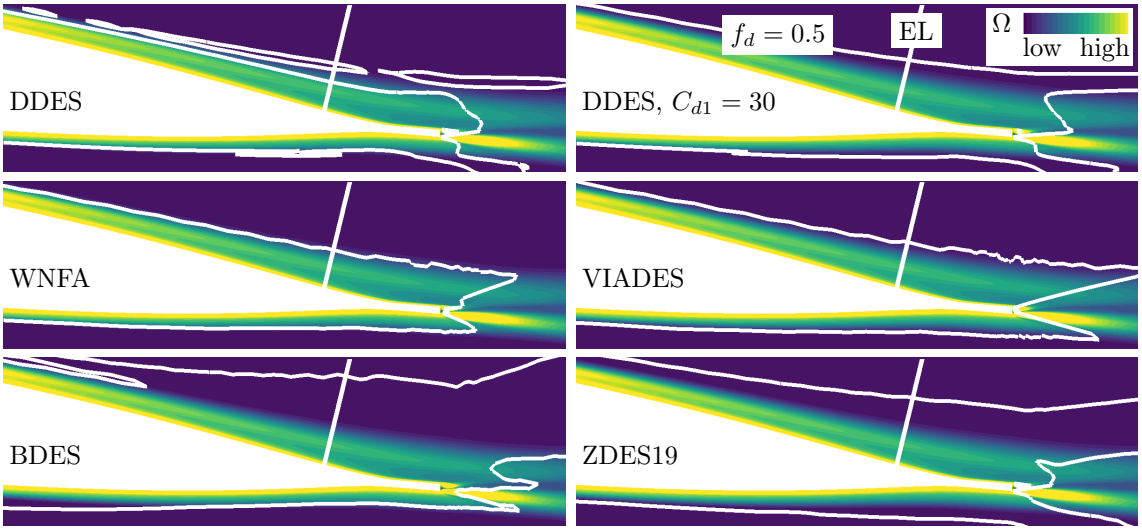

(a) Attached flow, $\psi = 180°$

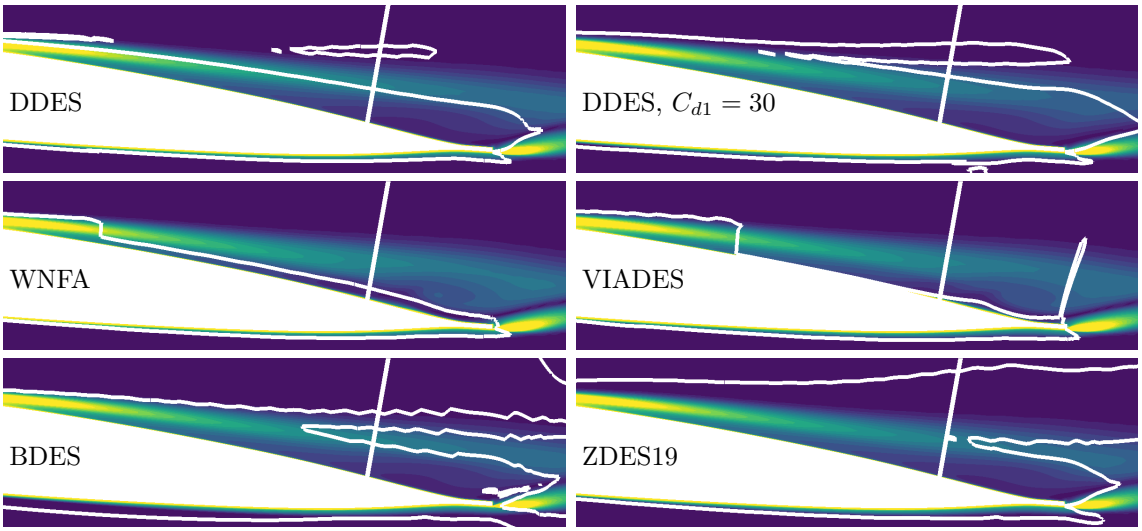

(b) Trailing-edge separation, $\psi = 225°$

Figure 6.14: Contours of vorticity magnitude indicating attached boundary layer (top) and trailing-edge boundary-layer separation (bottom) and white isolines of $f_d = 0.5$ indicating RANS/LES interface. Wall-normal lines show extraction locations (EL) for Fig. 6.15.

zone, DDES and BDES reach full LES mode in the middle of the shear layer but then switch back to RANS, and $C_{d1} = 30$ as well as ZDES19 only switch to LES mode well beyond the shear-layer edge.

The same analysis is given in Fig. 6.16 for the flow condition of leading-edge separation at $\psi = 270°$. Here, in general, all shielding approaches allow LES mode for the separated flow, but only WNFA and VIADES limit the RANS mode to a thin

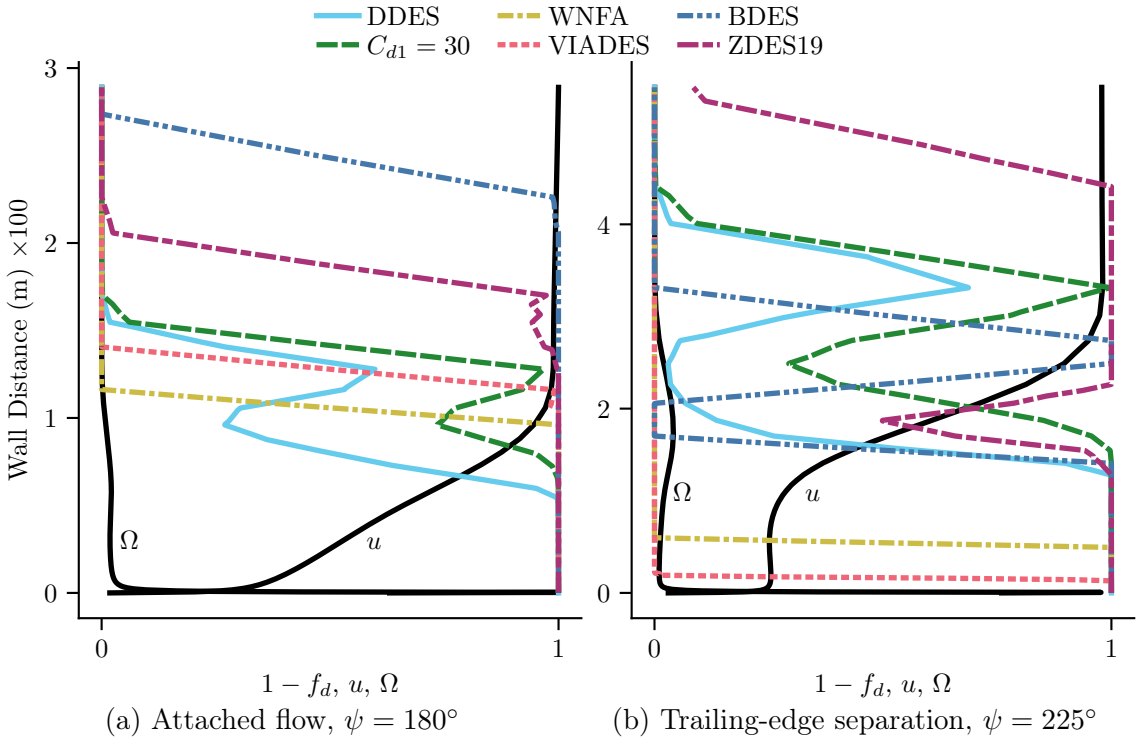

Figure 6.15: Max-normalized profiles of shielding function f_d and magnitudes of velocity and vorticity taken from the extraction locations (EL) indicated in Fig. 6.14.

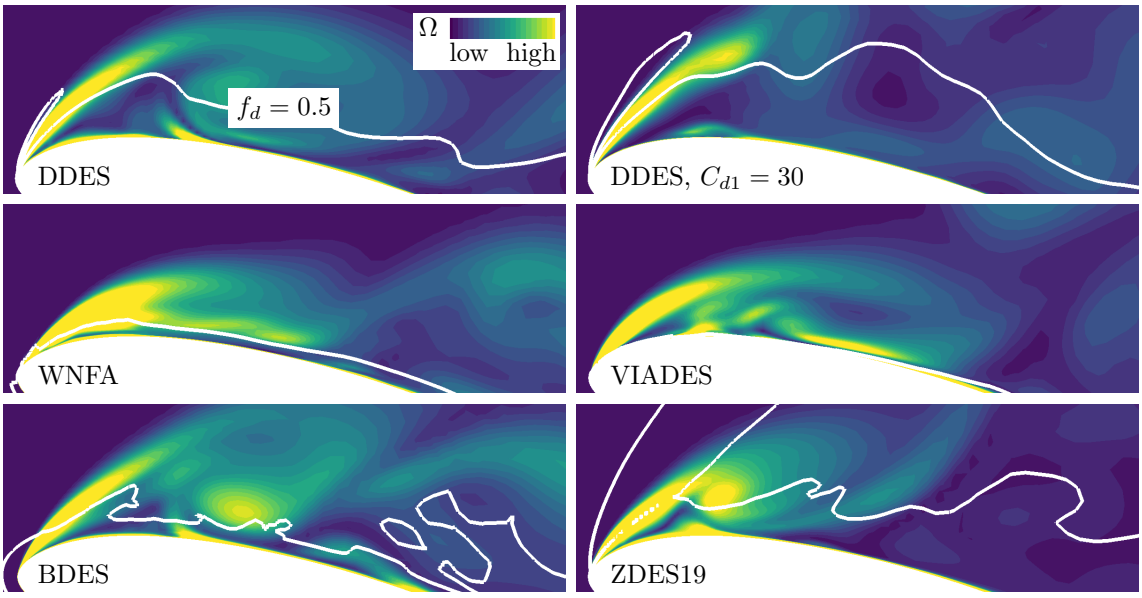

Figure 6.16: Contours of vorticity magnitude indicating leading-edge boundary-layer separation and white isolines of $f_d = 0.5$ indicating RANS/LES interface at $\psi = 270°$.

near-wall region, while the others keep substantial parts of the separation zone in RANS mode. Furthermore, WNFA and VIADES show the most and $C_{d1} = 30$ and ZDES19 the least aggressive switching at the formation of the shear layer.

To assess the influence of the various shielding methods on the actual rotor loads, a rotor map of the sectional pitching-moment $C_m\,M^2$, which is the key characteristic of dynamic stall, is given in Fig. 6.17. On the retreating side, several dynamic stall and flow separation events occur that are analyzed in great detail in Chapter 7, thus, only an introductory overview of the distinct overshoots in nose-down pitching moment is given here: The labels ①–⑤ mark distinct overshoots in nose-down pitching moment that are, first, associated with BVI-induced, outboard-moving dynamic stall. Secondly, there is a second dynamic stall event near the blade tip, followed by, thirdly, formation of an apex vortex and, fourthly, another dynamic stall event. Fifthly, there is massively separated flow for a large portion of the azimuth.

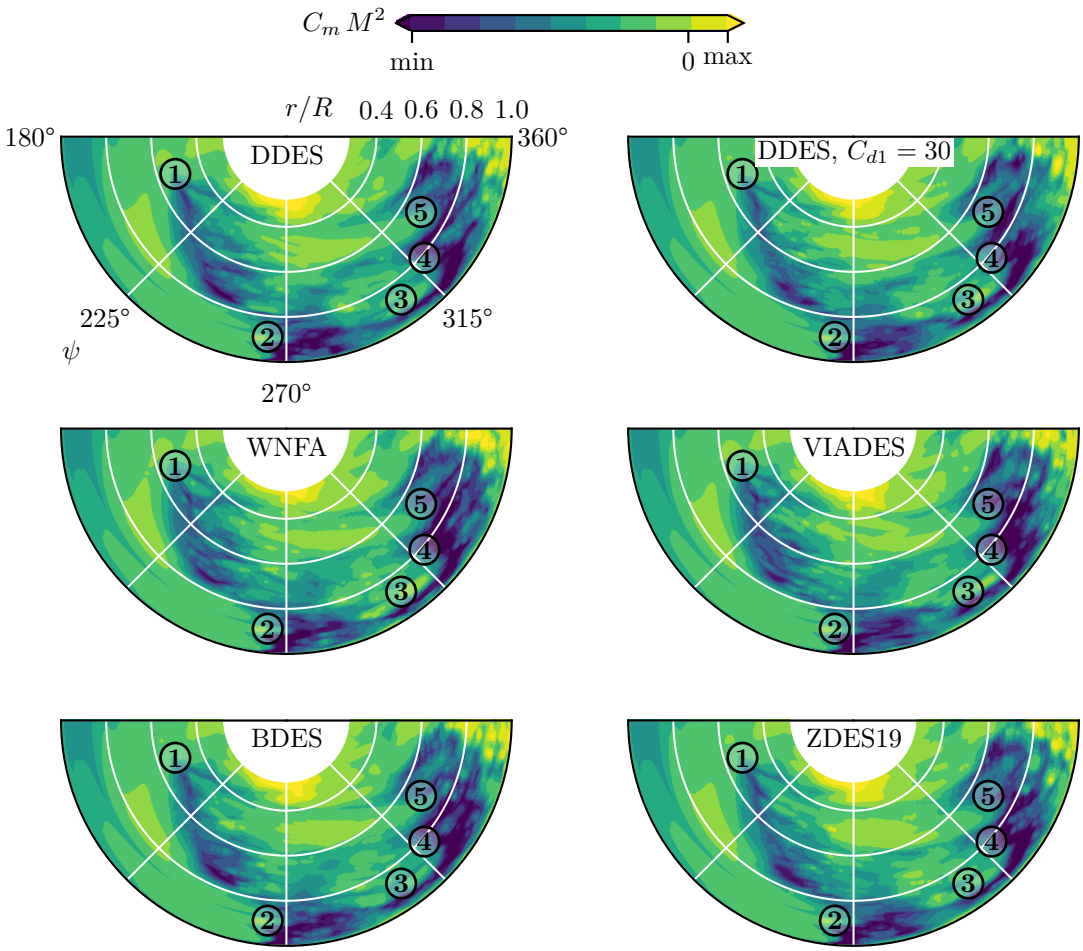

Figure 6.17: Rotor map of sectional pitching-moment coefficient $C_m\,M^2$ of investigated RANS/LES shielding approaches on retreating side with marked dynamic stall and flow separation events (①–⑤).

Overall, the pitching moments correspond well between all shielding variants, and the point in time, the location as well as the strength of the mentioned events barely differ. A similar observation was made before for the RTG case (Section 6.2) and is found plausible for two reasons: First, if the boundary-layer shielding is correct – which appears to be the case judging from Fig. 6.14 – the separation process is primarily governed by the underlying RANS model. Secondly, all investigated methods manage to treat the separated flow mostly in LES mode (Fig. 6.16). Also, the observed differences (Figs. 6.15b and 6.16) between the variants in allowing the LES mode to intrude deep into the separation zone are assumed to have only a weak impact due to the damping that is associated with the gray-area problem.

In conclusion, all investigated alternative approaches provide a sufficient boundary-layer shielding for the Bluecopter dynamic stall case and it appears that the mentioned shortcomings of VIADES and BDES for helicopter rotor flows (Section 6.3) play only a minor role in this particular setup. Furthermore, VIADES, BDES and ZDES19 behave very similar to the RTG case, that is, VIADES (and thereby WNFA, too) shows a rather aggressive transition from RANS to LES compared to BDES or ZDES19. Recall that in the present case, the near-body grids are not fine enough to cause serious problems using the original DDES, thus, it is expected that the alternative shieldings become more important in future setups.

6.6 Gray-Area Mitigation

A promising approach to mitigate the gray-area problem, which is a delayed transition from modeled to resolved turbulence, is to replace the standard filter width $\Delta_{\max}$ with the shear-layer-adaptive filter width Δ_{SLA} [120] (Section 3.3). The underlying idea is that by employing a filter width that decreases in regions of mostly two-dimensional shear flow, the damping eddy viscosity is significantly reduced outside the RANS mode, which speeds-up the transition to three-dimensional, turbulent flow structures. Arguably, a reduction of the gray area is particularly important for dynamic stall scenarios, since they show a transition from fully attached to fully separated flow and back in a very short physical period of time. In contrast to static stall cases, where an initial transient can be bridged from a simulation point-of-view, one cannot rely on or rather wait for the inherent instability of a shear layer to amplify and take over. In the present thesis, the Δ_{SLA} approach was investigated both in the RTG case (Section 6.6.1) and the Bluecopter case (Section 6.6.2).

6.6.1 Application of Alternative Filter Width Δ_{SLA} to Model-Rotor Dynamic Stall (RTG Case)

Recall from Chapter 5 that the issue with DDES is twofold in this case: First, there is strong trailing-edge separation that leads to a flattening of the lift curve, which is in good agreement with the experiment but was found to be a grid-induced, numerical artifact (Section 6.2). Then, while the rotor blade is still pitching up, the separated shear layer rolls up into a strong, coherent vortex around mid-chord that induces a severe premature nose-down pitching moment and lift overshoot that disagrees both with the experiment and other CFD simulations. It is suspected that the gray-area problem is involved in this process, allowing the coherent shear-layer vortex to evolve in the first place.

The situation of interest is exhibited in Fig. 6.18 at the spanwise station $r/R = 0.77$ at $t/T = 0.41 \uparrow$, showing the RANS/LES interface and massive trailing-edge separation when using the standard filter width Δ_{max}. Obviously, a substantial part of the separated shear layer already is in LES mode, yet, instead of flow instabilities, which are expected in actuality [102], there only is a coherent recirculation zone. Now, when applying the filter width Δ_{SLA} to the RTG case using standard DDES boundary-layer shielding, it is important to note that the results cannot be compared straightforward for the following reason: With Δ_{SLA}, the eddy viscosity is greatly reduced in the LES region, however, as discussed, the LES region intrudes too far into the boundary layer. Thus, even more modeled-stress depletion leading to premature, grid-induced separation and, consequently, a time shift of the flow separation events is to be expected.

Figure 6.19 shows vorticity contours at three points during the upstroke using Δ_{SLA}. At $t/T = 0.33$, there clearly is trailing-edge separation indicated by the wedge-shaped region of low vorticity in the aft part of the suction side. In this instance, the separated shear layer appears to be stable, as observed with standard DDES or

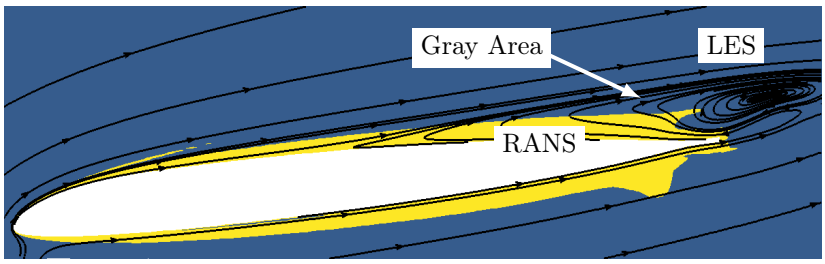

Figure 6.18: Contours of the f_d function of DDES indicating LES mode and RANS mode reveal a potential gray-area problem at $r/R = 0.77$ and $t/T = 0.41 \uparrow$ using the standard filter width Δ_{max}.

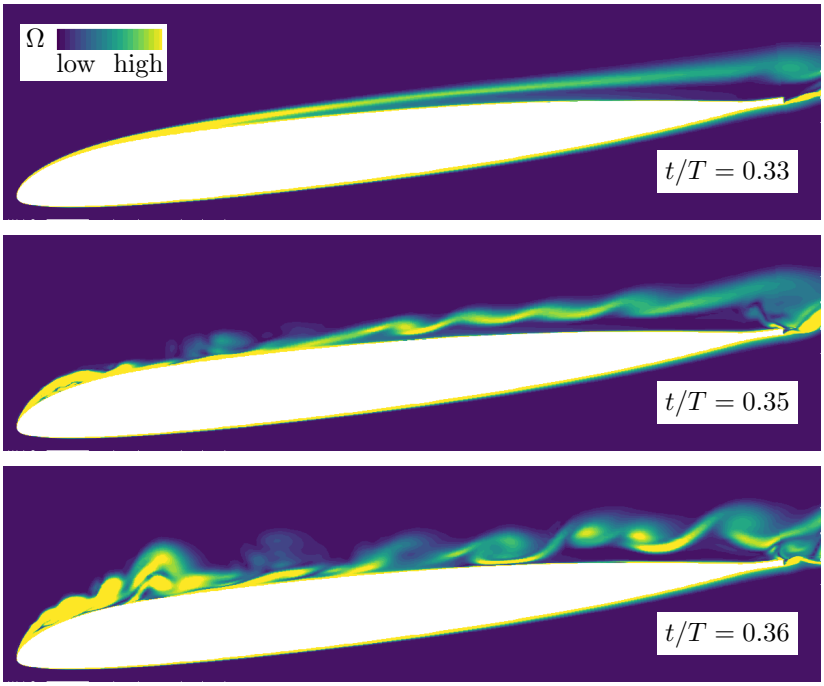

Figure 6.19: Vorticity contours at $r/R = 0.77$ at three points during upstroke of dynamic stall cycle indicating early instabilities and breakup of separated shear layer when using shear-layer-adaptive filter width Δ_{SLA}.

URANS (compare Fig. 5.12). However, a moment later at $t/T = 0.35$, the shear layer is already wavily distorted. Then, only shortly after at $t/T = 0.36$, the shear layer exhibits classical Kelvin-Helmholtz instabilities. Unfortunately, the relevant near-wall aft part of the spanwise slice was outside the RTG PIV field of view (compare Fig. 5.2), nevertheless, the here observed flow process is qualitatively in accordance with high-fidelity LES simulations [74] and PIV measurements [13] of the dynamic stall onset on pitching airfoils at comparable Reynolds numbers. Thus, in contrast to using the standard filter width Δ_{max} (Fig. 5.12, $t/T = 0.45$), there is no formation of a single, strong vortex around mid-chord.

The effect of the different flow processes (Δ_{max} vs. Δ_{SLA}) of the upstream moving trailing-edge separation on the pressure distributions is presented in Fig. 6.20. As discussed in Chapter 5, beneath the shear-layer vortex that forms around $t/T = 0.4$ with standard Δ_{max}, the surface pressure around $x/c = 0.7$ is very low, which causes the problematic premature peak in nose-down pitching moment. Using Δ_{SLA}, however, this characteristic is absent and only the effects of the actual dynamic stall event are present, that is, the breakdown of the suction peak and the following downstream convection of a low-pressure peak. Consequently, it is not surprising that the Δ_{SLA} pitching moment does not feature the seeming "double stall" of Δ_{max} that does not agree with the experiment, see Fig. 6.21.

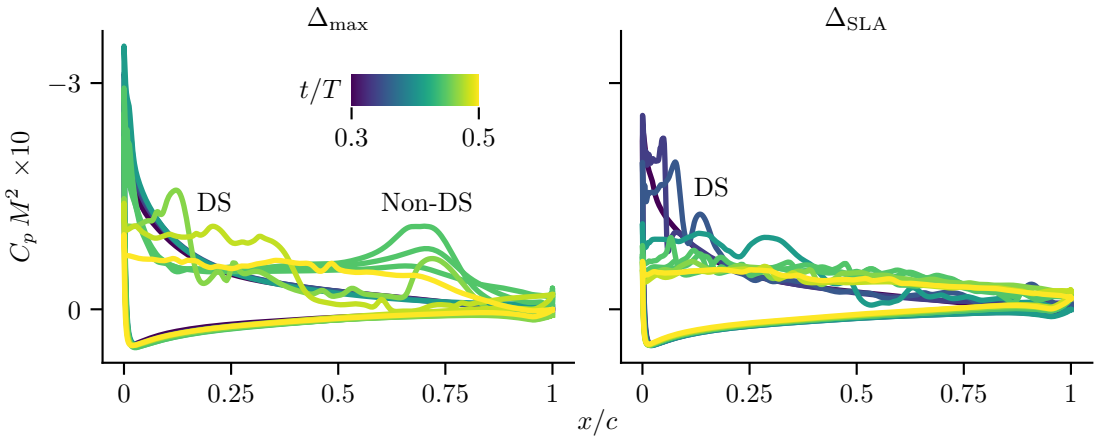

Figure 6.20: Pressure distributions at $r/R = 0.77$ at several points during the upstroke of a dynamic stall cycle using DES filter widths Δ_{max} and Δ_{SLA}.

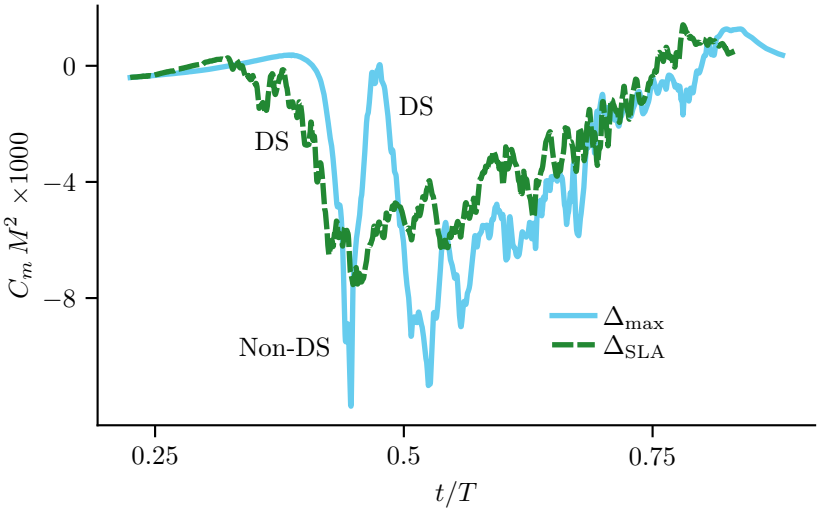

Figure 6.21: Pitching-moment coefficients (single cycle, full CFD data) at $r/R = 0.77$ using DES filter widths Δ_{max} (standard) and Δ_{SLA}.

Recall that, due to the insufficient boundary-layer shielding, the Δ_{SLA} variant predicts the moment stall way too early in the cycle. Nevertheless, it is concluded that the comparison of the Δ_{max} and Δ_{SLA} results is an impressive demonstration of the gray-area problem. Furthermore, it shows that the alternative filter width produces more realistic shear-layer flows featuring an early formation of Kelvin-Helmholtz instabilities.

6.6.2 Application of Alternative Filter Width Δ_{SLA} to Helicopter Rotor Dynamic Stall (Bluecopter Case)

Here, the influence of the alternative shear-layer-adaptive filter width Δ_{SLA} is assessed qualitatively for the Bluecopter dynamic stall case, where strong flow separation occurs on the retreating side, as analyzed in detail in Chapter 7. Note that, in contrast to the RTG case, sufficient boundary-layer shielding is ensured, thus, no premature separation is expected when using the alternative filter width, and both variants (Δ_{max} vs. Δ_{SLA}) can be examined at the same points in time. Also, for fair comparison, no re-trimming was carried out to ensure an identical rotor blade movement.

The effect of Δ_{SLA} at an outboard spanwise slice is shown in Fig. 6.22. At $\psi = 243°$, the vorticity contours indicate separation at the leading part of the airfoil. While with Δ_{max}, the shear layer is stable over the whole chord, a breakup into several

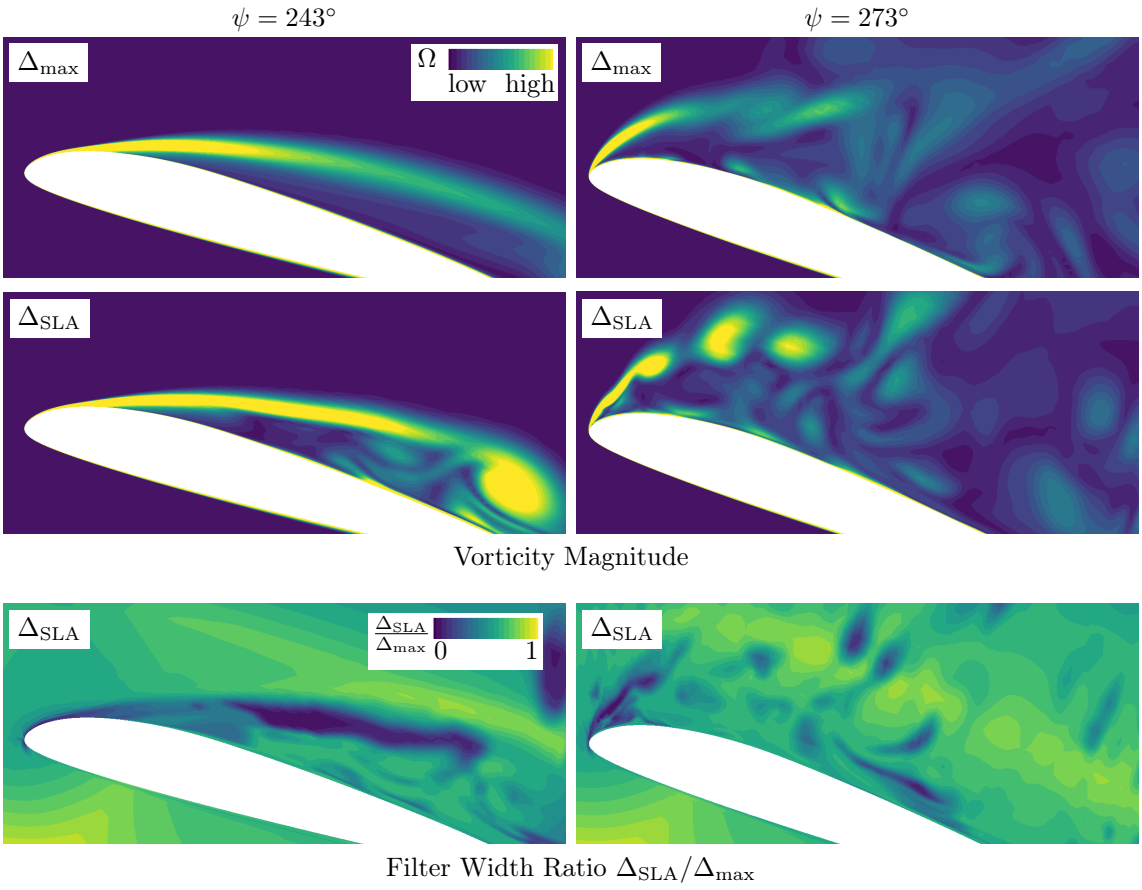

Figure 6.22: Contours of instantaneous vorticity magnitude and filter width ratio $\Delta_{SLA}/\Delta_{max}$ at $r/R = 0.75$ for $\psi = 243°$ and $\psi = 273°$.

vortical structures is observable in the aft part of the Δ_{SLA} simulation. Then, at $\psi = 273°$, there is complete leading-edge separation and chaotic vortical structures are found in both cases, which indicates the proper functioning of the LES mode. However, it is apparent that there is an earlier shear-layer breakup using Δ_{SLA}. The underlying mechanism of the alternative filter width is revealed by the filter width ratio $\Delta_{\mathrm{SLA}}/\Delta_{\mathrm{max}}$ depicted in the lower part of Fig. 6.22. In those regions where $\Delta_{\mathrm{SLA}}/\Delta_{\mathrm{max}} \ll 1$, a very small filter width is computed that could have been achieved with Δ_{max} only on a much finer grid. It also shows that the Δ_{SLA} variant seems to operate as intended, as it differs from Δ_{max} primarily in the separated shear layer, where it is supposed to reduce the eddy viscosity (recall that $\nu_t \propto S\,\Delta^2$).

The observations from the spanwise slice hold true for the whole separated flow around the rotor blade, as visualized in Fig. 6.23 by means of λ_2 isosurfaces colored by the viscosity ratio μ_t/μ. First, it is obvious that the eddy viscosity is drastically reduced throughout the flow field using Δ_{SLA}, indicating its proper functioning. Secondly, it shows that the shear-layer breakup occurs earlier or more upstream, forming smaller vortical structures in case of Δ_{SLA}, which is considered to be physically more accurate [97].

A more quantitative analysis of the influence of the filter width is given in Fig. 6.24, where the sectional pitching-moment coefficients at $r/R = 0.75$ and 0.90 of the two investigated variants are plotted. In general, the onset of moment stall is captured similarly, which is plausible, as it should be primarily governed by the underlying RANS turbulence model. At $r/R = 0.75$, using Δ_{SLA} yields a noticeably higher peak value in negative pitching moment for the first dynamic stall event around $\psi = 250°$.

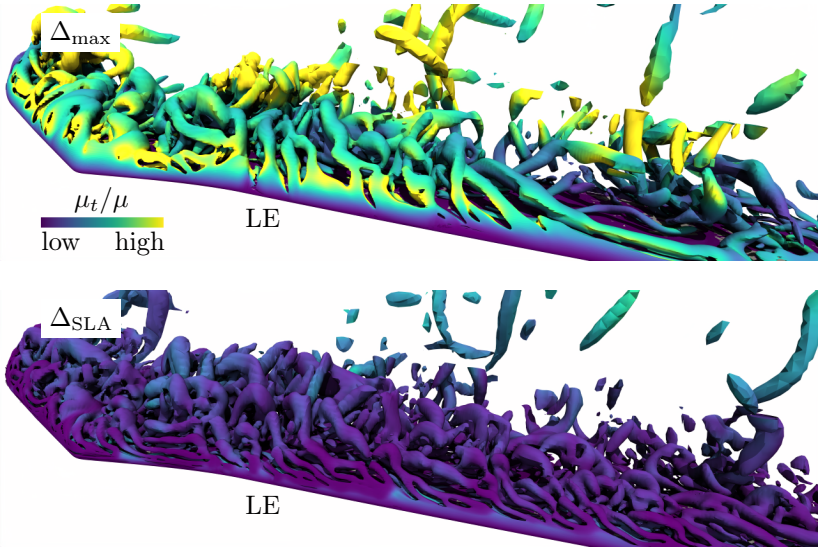

Figure 6.23: Flow visualization by means of λ_2 isosurfaces colored by the viscosity ratio μ_t/μ in the outboard region at $\psi = 278°$ using filter widths Δ_{max} and Δ_{SLA}.

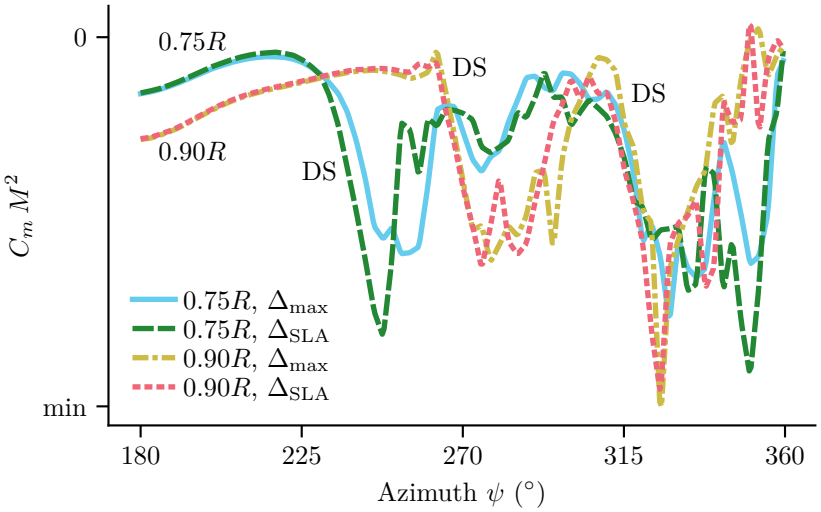

Figure 6.24: Comparison of sectional pitching-moment coefficients $C_m M^2$ at $r/R = 0.75$ and 0.90 indicate multiple dynamic stall (DS) events on the retreating side using filter widths $\Delta_{\max}$ and Δ_{SLA}.

Also, towards the end of the fourth quadrant, where several smaller flow separation events occur, Δ_{SLA} exhibits another more severe overshoot in pitching moment. More outboard at $r/R = 0.90$, the differences are smaller overall, in particular regarding the peak values induced by the dynamic stall events. Although not done in this thesis, but judging from the present results, it seems worthwhile to further explore the effects of the alternative filter width on a larger scale, that is, considering re-trimming of the rotor.

6.7 Chapter Conclusions

To eliminate one common issue of DDES, namely modeled-stress depletion that can cause grid-induced separation, several modifications to the boundary-layer shielding function f_d were investigated based on the RTG and Bluecopter dynamic stall cases. In detail, three purely local methods from literature were presented (increase of model constant C_{d1}, BDES, ZDES19) and two non-local, grid-independent approaches (VIADES, WNFA) were developed. With VIADES, the vorticity is integrated in wall-normal direction to get a pseudo velocity, which allows to apply the δ_{99} criterion to detect the boundary-layer edge. With WNFA, a complex wall-normal analysis and averaging of the flow is conducted to distinguish between viscous inner and inviscid outer flow. Both VIADES and WNFA incorporate a novel approach, which is based on a projection of the local vorticity, to quickly activate the LES mode in case of strong flow separation. Furthermore, the influence of the alternative filter width Δ_{SLA} and its capability to mitigate the well-known gray-area problem was investigated in both dynamic stall cases as well. The following conclusions can be drawn:

1. All investigated f_d modifications, except of setting DDES's empirical constant C_{d1} only to 25 instead of 30, significantly improve the boundary-layer shielding and eliminate grid-induced separation.

2. The shielding variants differ in complexity and applicability: Increasing DDES's empirical constant C_{d1} is trivial, but requires calibrating and lacks a physical foundation. ZDES19 is a promising approach that integrates well into the DDES framework, but still depends on quantities of the turbulence model. The Bernoulli-based BDES is more flow-physics-based, however, requires essentially irrotational inflow, which also holds true for VIADES that is more difficult to implement into a flow solver. Finally, the most complex wall-normal analysis of the flow is carried out with WNFA that is designed for non-uniform, vortical inflow.

3. The shielding variants also differ in how aggressive or early they initiate the transition from RANS to LES mode: While VIADES and WNFA have an abrupt mode switching as soon as the vorticity in the boundary layer vanishes, $C_{d1} = 30$, BDES and ZDES19 have a rather conservative shielding that sometimes reaches into the outer flow. Furthermore, VIADES and WNFA aggressively activate the LES mode in vicinity of the surface for the entire region of separated flow, while the other methods still exhibit RANS mode in the lower part of the recirculation zone.

4. With helicopter rotor flows or any scenario that features disturbed, rotational inflow and unusual boundary layers, be it due to numerical artifacts or caused by flow physics, common methods to analyze the boundary layer or estimate its thickness are prone to error, as they rely on disturbance-free boundary-layer profiles and a uniform, inviscid outer flow.

5. Applying the alternative shear-layer-adaptive filter width Δ_{SLA} to the test cases promotes the more realistic early evolution of Kelvin-Helmholtz instabilities in a separated shear layer by significantly reducing the eddy viscosity in regions of rather two-dimensional shear flow. Thus, it is a promising gray-area mitigation approach; however, a sufficient boundary-layer shielding is strictly required.

6. Concerning the RTG case, it is confirmed that grid-induced separation in combination with the gray-area problem causes a severe, premature overshoot in nose-down pitching moment that is not related to dynamic stall and does not agree with the experiment and other URANS simulations. When applying the modified shieldings or the alternative filter width, this modeling error disappears.

7. Concerning the Bluecopter case, the alternative filter width Δ_{SLA} also has an impact on the severity of the dynamic stall events. However, a deeper analysis would require re-trimming.

8. For future investigations of separated flows including dynamic stall, the best results are expected only by a combination of a suitable RANS model, ideal boundary-layer shielding in the DES part and effective gray-area mitigation.

7 Simulation of Dynamic Stall on a Rotor in High-Speed Turn Flight

In this chapter, simulations of a highly loaded, high-speed turn flight of Airbus Helicopters' *Bluecopter* demonstrator helicopter are presented, based on a loose CFD/CSD coupling of the flow solver FLOWer and the rotorcraft comprehensive code CAMRAD II. The rotor aerodynamics is computed using a high-fidelity DDES, and on CSD side, a three-degree-of-freedom trim of an isolated rotor is carried out. Besides a detailed analysis of the dynamic stall and flow separation events, the computed pitch-link loads and rotor control angles are compared to flight-test measurements. Also, the influence of the target rotor thrust of the trim, the consideration of the rotor hub and the fuselage in CFD, the turbulence modeling as well as the rotor blade elasticity are assessed. The chapter is essentially based on Letzgus et al. [157].

Although advanced boundary-layer shielding methods and a gray-area mitigation approach were investigated in the previous chapter for the Bluecopter case, they are not applied here, since most of the approaches were not yet available at the time of the computations, and since the here used grids are too coarse to really suffer from grid-induced separation in the first place. Furthermore, the focus of this investigation is on the flow physics and not on DES methods.

7.1 Flight-Test Case

The flight test investigated here was conducted with Airbus Helicopters' light/medium twin-engine demonstrator helicopter Bluecopter (Fig. 7.1), which incorporates innovative technologies that aim to reduce fuel consumption and acoustic emission [158]. A key feature is its five-bladed bearingless main rotor whose rotor blades use an advanced planform with double-swept blade tips [159].

A highly loaded, high-speed coordinated left-turn flight, which was classified as dynamic stall relevant, was selected from the flight-test campaign and formed the basis of the loosely coupled CFD/CSD simulation. In this flight condition, the rotor advance ratio μ was 0.35, the helicopter was heavily rolled to the left and had

Figure 7.1: The Bluecopter. Courtesy of Airbus Helicopters Deutschland [157].

Table 7.1: Overview of the flight-test conditions.

Maneuver	Left turn
Advance ratio μ	0.35
Descent angle	9°
Rotor thrust coef. C_T/σ	0.145 ± 0.007

a descent angle of 9°. While main rotor hub moments and pitch-link loads were measured using strain gauges, the rotor blades were not instrumented with pressure transducers. Based on the available instrumentation and sensor data, a rotor blade loading C_T/σ of 0.145 with 5 % accuracy was derived. Furthermore, the inflow angle of attack and sideslip angle were measured at the nose boom of the helicopter. An overview of the flight-test conditions is given in Table 7.1.

In such a demanding flight condition, fluctuations of control inputs, aircraft orientation and velocities occur naturally. However, for the CFD/CSD simulation of this dynamic stall case, the flight condition was assumed to be stationary and the measured data that was used for the numerical inputs was time-averaged over about 4.5 s.

7.2 Numerical Approach

To mimic the flight condition of the experiment realistically with reasonable computational effort, a loose CFD/CSD coupling of an isolated rotor between the flow solver FLOWer and the rotorcraft comprehensive code CAMRAD II was carried out. Thus, high-fidelity aerodynamic rotor blade loads computed by FLOWer, which are assumed to be periodic, are used to gradually improve or replace the low-fidelity

aerodynamic loads obtained by CAMRAD II. In return, CAMRAD II provides the structural rotor blade dynamics and rotor control angles that are required to trim the rotor.

Controlling and automatizing of the coupling process requires additional in-house scripts and tools. The procedure is well established and was recently successfully applied to less critical flight conditions as the simulation of a complete H145 helicopter in descent flight [160] or light tail shake on the Bluecopter helicopter [161].

7.2.1 CFD Setup

On the CFD side, besides the standard settings described in Section 3.4, the JST scheme with a dissipation coefficient $\kappa^{(4)}$ of 1/128 was used in all near-body grids to sustain numerical stability, whereas a fifth-order WENO scheme [127] was applied to the off-body grids.

In accordance with previous dynamic stall investigations [48, 28, 27], an azimuthal step size of $\Delta\psi = 1/4°$ (1440 steps per rotor revolution) with 40 sub-iterations was chosen. After the initial transient was bridged, the CFD/CSD exchange was done every 1152 time steps (4/5 of a revolution or four blade passings). That time span, which is roughly the time it takes the flow to convect across the rotor disk, was chosen to save computational time, as it is long enough to obtain a basically periodic flow. The chaotic nature of separated flow introduced some cycle-to-cycle variations of the aerodynamic loads. However, it is believed that this did not influence the coupling and trim procedure significantly.

For closure of the RANS equations, the DDES versions of the SA [96] and Menter-SST [110] turbulence models were investigated. Although in the present case, the resolution of the near-body grids is not fine enough to really be at risk of grid-induced separation (Section 6.5), the empirical constant C_{d1} of the f_d shielding function was increased from 20 to 30 for the SST-DDES model and from 8 to 16 for the SA-DDES model, respectively (compare Section 6.1.1). Additionally, it was verified that the boundary-layer flows were treated in RANS mode. In LES mode, the maximum cell length in each index direction was taken as the filter width ($\Delta_{\max}$). Simplified rotation corrections were applied to both turbulence models as well. For all simulations, the flow was modeled as fully turbulent.

The rotor blade grid consists of three grids that share an overset or Chimera interface: An O-type cap grid for the blade root, a C-type cap grid for the blade tip and an O-type grid for the main section of the blade, see Fig. 7.2. Its grid spacings are based

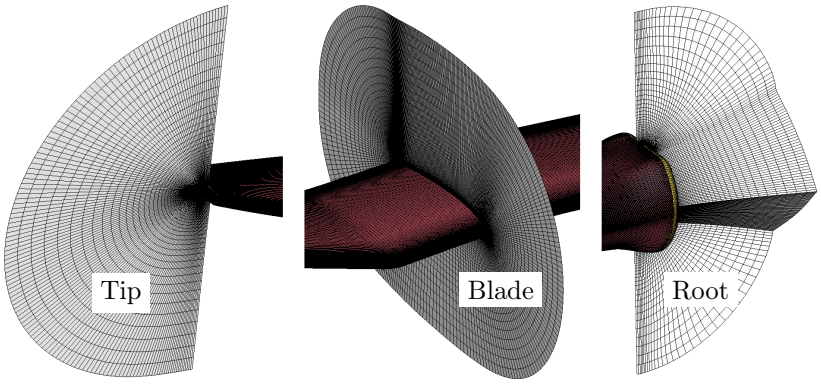

Figure 7.2: Near-body rotor blade grids at tip (left), main section (center) and root (right) [157].

Table 7.2: Cell spacings and grid information.

Leading-edge spacing	0.07% c_{local}
Trailing-edge spacing	0.02% c_{local}
Finest off-body spacing	6% c_{mean}
$y+$ value	0.6
Chordwise points	345
Radial points	721
Normal (BL) points	113
Tip + blade + root cells (M)	2.5 + 23.4 + 0.8 = 26.7
Off-body cells (M)	24.9 (B) or 25.5 (BHF)
Hub-cap & mast cells (M)	2.7
Fuselage & tail boom cells (M)	3.0
Grid cells in total (M)	158.4 (B) or 164.7 (BHF)

on gridding guidelines of AIAA's 6th Drag Prediction Workshop [135] and results of previous dynamic stall investigations [48, 28, 27, 39]. Further grid information is listed in Table 7.2. As shown in Fig. 7.3, the near-body grids are embedded in a Cartesian off-body grid that has several levels of refinement adapted to the near-body grids, utilizing the hanging-grid-nodes technique. The finest spacing of the off-body grid is 6% of the mean chord length c_{mean} and it extends to a distance of $5.5R$ from the rotor origin. To assess the influence and necessity of modeling other helicopter components, two near-body grid variants were investigated: The first variant – denoted *B* – contains only isolated rotor blades (B), the second variant – denoted *BHF* – additionally contains a hub cap (H) and a simplified rotor mast without control components, the fuselage (F) with the mast fairing and the tail boom, see Fig. 7.4 and Table 7.3.

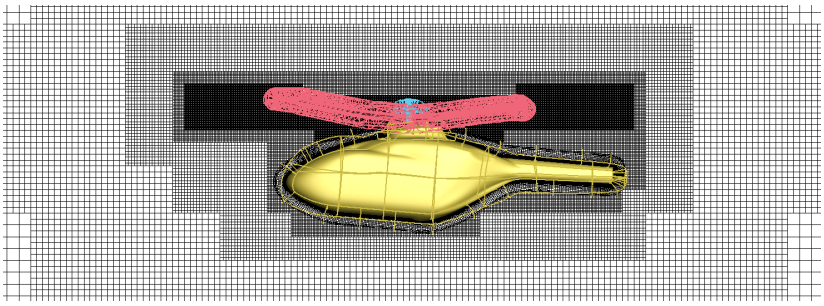

Figure 7.3: Section of the Cartesian off-body grid with levels of refinement adapted to the near-body grids (BHF variant) [157].

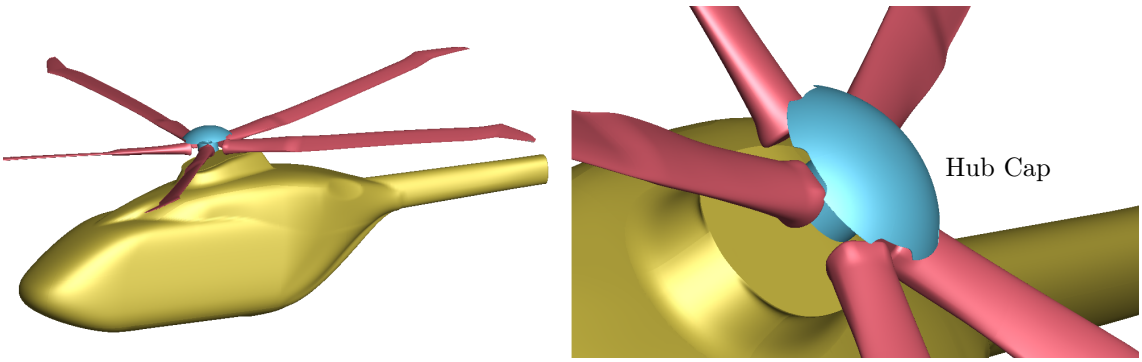

Figure 7.4: In case of the BHF variant, the modeled helicopter components are rotor blades, simplified hub cap and mast, fuselage with mast fairing and tail boom [157].

Table 7.3: Investigated variants of modeled helicopter components in CFD.

Variant	Modeled components
B	Rotor blades (B) only
BHF	Rotor blades (B), simplified hub cap (H) and rotor mast, fuselage (F) with mast fairing and tail boom

As proposed by Dietz et al. [162], a kinematic chain of rigid-body motions was used to simulate the actual turn flight and to take inertial forces into account: First, a yaw motion is applied that corresponds to the turn rate, secondly, there is a radial translation of the turn radius, thirdly, a vertical translation represents the descent rate and, finally, the yaw, pitch and roll rotation of the helicopter is added. While the pitch and roll angle were set to the averaged measurements of the flight test, the yaw angle was beforehand iterated manually until both angle of attack and sideslip angle of CFD and flight test agreed within 0.5°.

The FLOWer computations were carried out on the Cray XC40 cluster of the HLRS, where the grids, split into 7700 blocks, were computed on 7000 cores. For one trim step, a wall time of roughly 6.5 hours was required.

7.2.2 CSD and Trim: CAMRAD II

The rotorcraft comprehensive code CAMRAD II [57] incorporates multibody dynamics, nonlinear finite elements, structural dynamics, and low-fidelity rotorcraft aerodynamics. On the CAMRAD II side, only the isolated rotor was considered using a structural dynamics model that was provided by Airbus Helicopters.

For the initial trim, the rotor aerodynamics is computed by a rotor wake analysis based on blade element theory using two-dimensional, steady airfoil tables. To increase the robustness of CAMRAD II's internal aerodynamics against unsteady effects that occur in a dynamic stall case, the airfoil tables were modified, that is, the lift stall was removed from the polars and replaced by a linear increase. However, as the CAMRAD II loads get corrected by CFD loads trim step by trim step, CAMRAD II's internal aerodynamics becomes less important over time and is not a factor in the final converged solution. The azimuthal step size of the CSD code was $\Delta\psi = 5°$. To ease trim convergence, the stiffness property of the swashplate and the pitch links was set to rigid. This is a simplification that changes the dynamic response of the rotor blade and can have a significant impact on the pitch-link loads [163].

Since an isolated rotor was modeled, a three-degree-of-freedom trim was carried out, with the rotor thrust and the hub pitch and roll moment as trim targets that were set to match the flight-test measurements. As trim variables the rotor control angles, that is collective, lateral cyclic and longitudinal cyclic pitch angle, were chosen.

7.2.3 Investigated Target Rotor Thrusts

Preliminary investigations of the present dynamic stall case and results of others [27] revealed that the aerodynamic loads and the coupling procedure are sensitive to small changes of the target rotor thrust. Since an uncertainty remained in the rotor thrust derived from the flight-test measurements, the target rotor thrust was varied and three C_T/σ cases were investigated, as listed in Table 7.4.

Table 7.4: Investigated cases of target rotor thrust in loose FLOWer/CII coupling.

Case Identifier	C_T/σ
T_{high}	0.147
T_{mid}	0.145
T_{low}	0.142
Flight Test	0.145 ± 0.007

7.3 Numerical Results

In the present case, the flow field is found to be quite complex, as visualized by the vortical structures in Fig. 7.5. Known rotor flow phenomena occur, that is, growing trailing-edge flow separation on the suction side of the rotor blade beginning in the third quadrant of the rotor disk, where blade-vortex interaction is observed as well. Then, several dynamic stall events happen in the third and fourth quadrant and the flow is massively separated for a large portion of the azimuth. Also, shock-induced separation is found in the first quadrant in the outboard region of the rotor blade. These general observations of the flow field apply regardless the three slightly different rotor thrusts, the two turbulence models and the two variants of modeled components that were investigated (Tables 7.3 and 7.4).

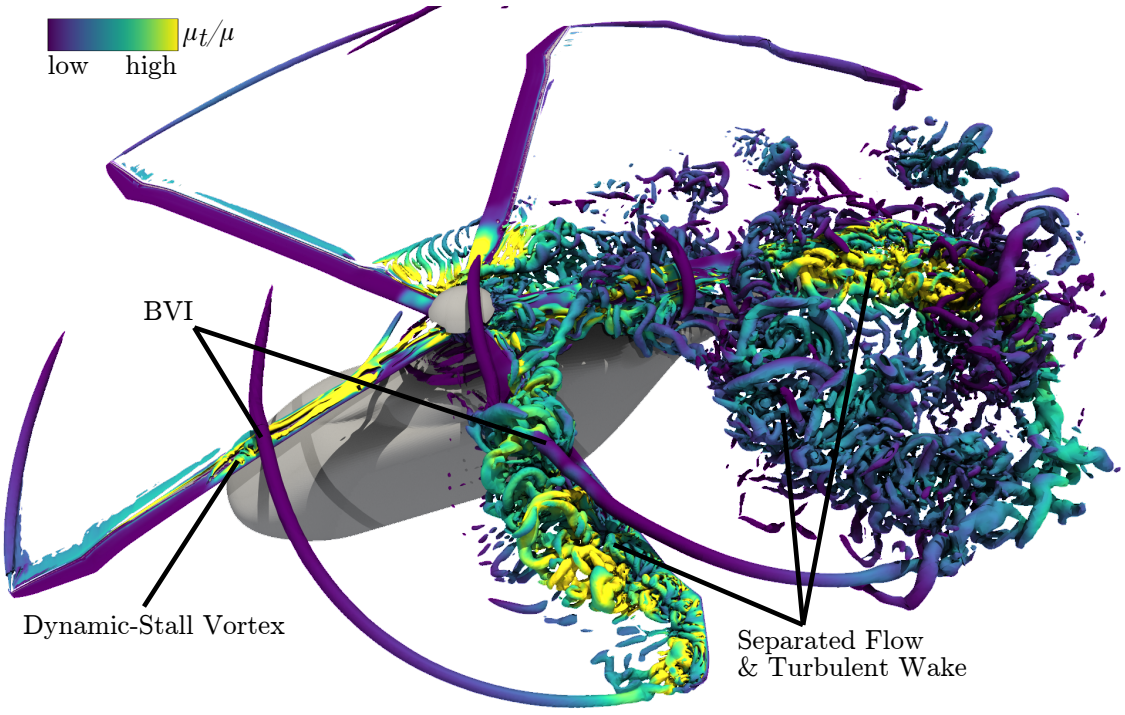

Figure 7.5: Visualization of the instantaneous flow field by means of isosurfaces of the λ_2 criterion colored by the viscosity ratio μ_t/μ, case: T_{mid}, BHF. Adapted from Letzgus et al. [157].

7.3.1 Analysis of Dynamic Stall and Flow Separation

Since the rotor aerodynamics of all computed cases is similar, the following detailed analysis of dynamic stall events and flow separation is based on the mid thrust case with modeled rotor hub and fuselage using the SST-DDES turbulence model (T_{mid}, BHF, SST), which has the best overall agreement with the flight test, as shown later in detail.

Instantaneous distributions of surface pressure and surface streamlines on the suction side of the rotor blade are depicted in Fig. 7.6 for different azimuthal positions. At $\psi = 183°$, there already is substantial trailing-edge flow separation that propagates upstream and towards the blade root.

Moving on in time to $\psi = 196°$, the first dynamic stall event, marked by ①, occurs at the leading edge, which can be identified by the Ω-shaped low-pressure region around $r/R = 0.5$. Also, a sudden change in sectional thrust and pitching moment sets in at this azimuthal and radial position, see Fig. 7.7, which is characteristic of dynamic stall. Interestingly, the start of this first event coincides in space and time with the blade-vortex interaction shown on the left-hand side of Fig. 7.5, where the rotor blade is perpendicular to and – due to the descent of the helicopter – about one chord length below the blade-tip vortex of the preceding blade. Recent

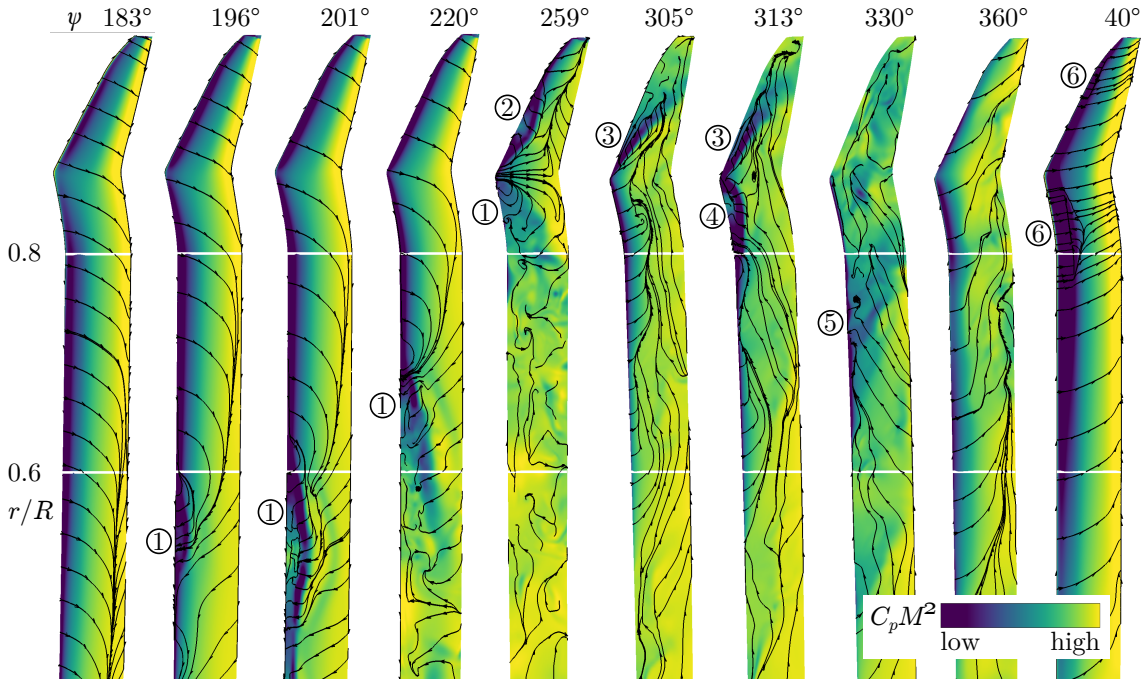

Figure 7.6: Instantaneous distributions of pressure and surface streamlines on the suction side of the rotor blade indicate dynamic stall events and flow separation [157].

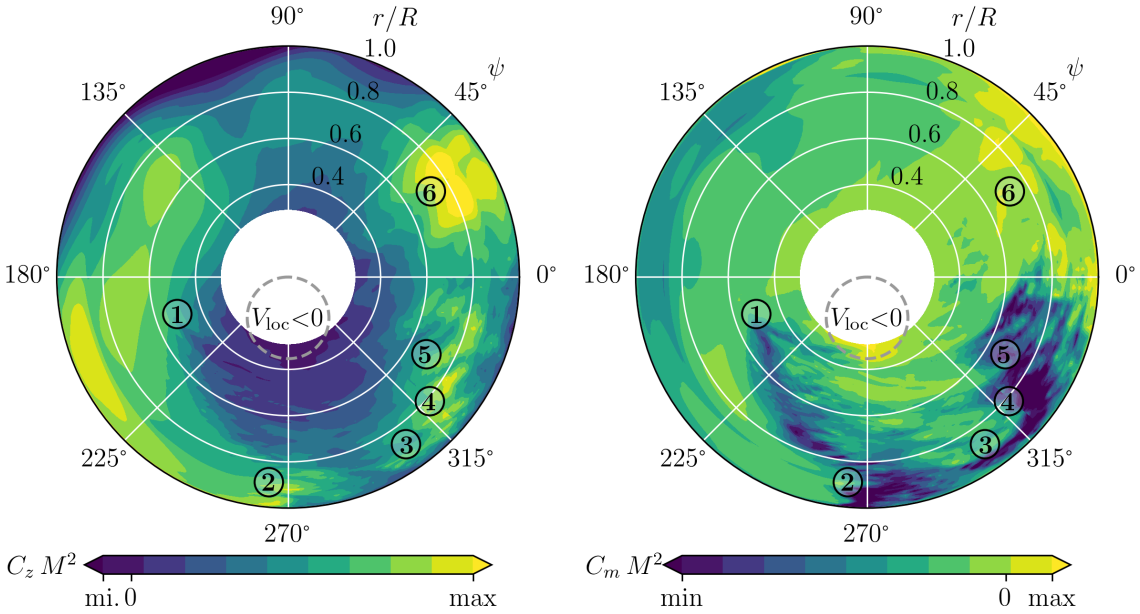

Figure 7.7: Rotor map of sectional thrust coefficient $C_z\,M^2$ (left) and sectional pitching-moment coefficient $C_m\,M^2$ (right) [157].

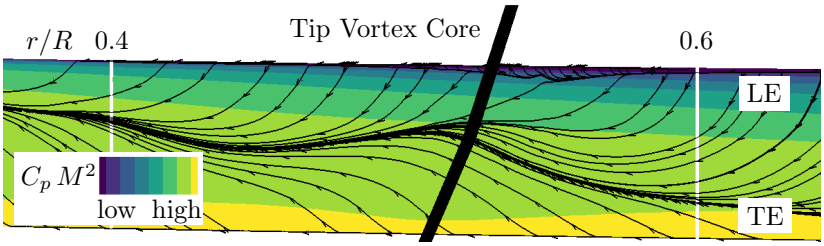

Figure 7.8: Radial position of tip vortex of preceding rotor blade at BVI event at $\psi = 193°$ and pressure and surface streamlines on suction side [157].

numerical investigations of dynamic stall on a UH-60A rotor by Chaderjian [48] and on ONERA's 7A rotor by Richez [28] showed that dynamic stall can be triggered by blade-vortex interaction, so it might be the case here as well. Figure 7.8 shows the vertically projected position of the core of the preceding tip vortex, revealing an influence of the tip vortex on the rotor blade flow. Outboard of its position, leading-edge flow separation is stronger, which might be due to the fact that the tip vortex increases the effective angle of attack outboard of its core. At the trailing-edge, the tip vortex seems to intensify the separation both inboard and outboard of its core.

Then, at $\psi = 201°$, the low pressure region convected downstream and spread in inboard and outboard directions (Fig. 7.6). The isosurfaces of the λ_2 criterion in Fig. 7.9 visualize the dynamic stall vortex, whose imprint is seen in the pressure distribution. Note that for clarity of the dynamic stall vortices, a very low value

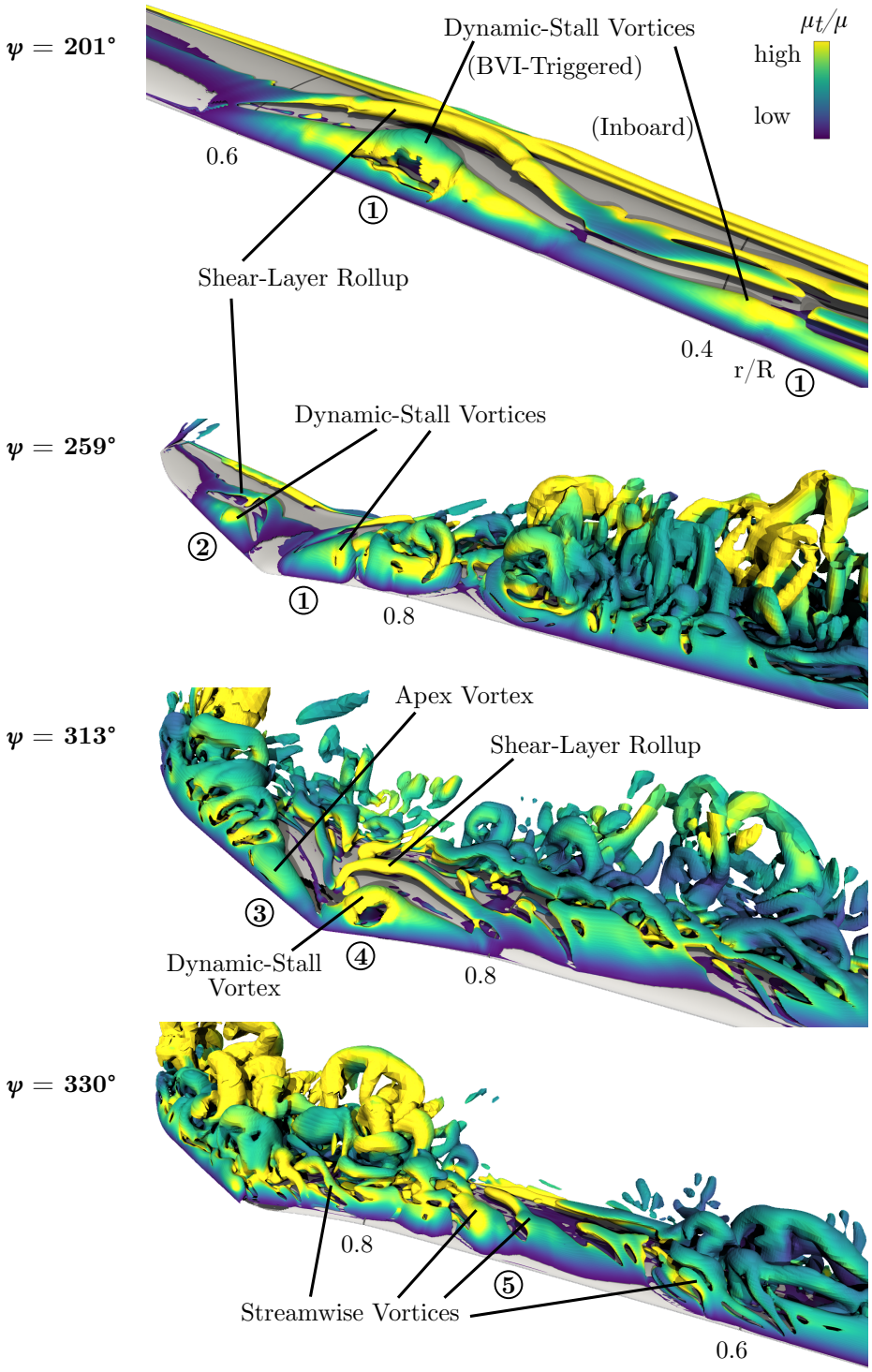

Figure 7.9: Visualization of dynamic stall vortices and flow separation by means of isosurfaces of the λ_2 criterion colored by the viscosity ratio μ_t/μ [157].

of λ_2 was chosen, which causes the tip vortex to vanish in Fig. 7.9, while it is visible in Fig. 7.5. Inboard of $r/R = 0.5$, the dynamic stall vortex is parallel to the leading

edge and seems to merge with the Ω-shaped vortex. Interestingly, this inboard dynamic stall vortex evolves at roughly the same azimuthal position as the vortex at $r/R = 0.5$, but far inboard of the sphere of influence of the BVI event. Instead, the inboard vortex appears to be triggered by the progressing trailing-edge separation reaching the leading edge, which corresponds to a known type of dynamic stall [164]. Furthermore, Fig. 7.9 reveals a rollup of the separated shear layer just downstream the dynamic stall vortex, which is also associated with a region of low surface pressure, see Fig. 7.6 again. Such a strong shear-layer rollup was also observed numerically by Benton and Visbal [75] and experimentally by Mulleners and Raffel [13] on pitching airfoils.

Moving on in time, the dynamic stall vortex mainly spreads in outboard direction, see azimuth positions $\psi = 220°$ and $\psi = 259°$ in Fig. 7.6 and the progression of the nose-down pitching moment region in Fig. 7.7. Then, the kink in the rotor blade planform, where the forward sweep changes to a backward sweep, seems to stop the outboard spreading of the dynamic stall vortex. This flow-stabilizing effect of the forward-backward-swept section was also observed by Lütke et al. [21], who investigated a pitching finite wing version of the present blade tip. Instead, at $\psi = 259°$, a new dynamic stall vortex, marked by ②, evolves outboard of the apex, see Fig. 7.9 again. Its dynamic-stall-typical influence on the pressure distribution and, consequently, on sectional thrusts and pitching moments is clearly visible in Fig. 7.6 and 7.7, respectively.

Then, in the outboard region of the rotor blade, the flow starts to reattach substantially, most likely due to the angle-of-attack-reducing influence of the tip vortex of the preceding blade that passes by almost parallel to the following blade, see blade-vortex interaction in the lower center of Fig. 7.5. Around $\psi = 305°$, a new event appears marked by ③. A vortex that behaves like a common blade-tip vortex forms at the apex of the planform. Beneath this apex vortex, surface pressure is very low (Fig. 7.6), thus, sectional thrusts and nose-down pitching moments rise again (Fig. 7.7).

At $\psi = 313°$, the apex vortex is still present, but yet another dynamic stall event takes place just inboard of the apex, marked by ④. This vortex quickly convects downstream and pulls the apex vortex along. Then, for the remaining forth quadrant, for example at $\psi = 330°$, the flow stays massively separated, but several rather streamwise vortices, marked by ⑤, form at the leading edge (Fig. 7.9), travel outboard and vanish, while new vortices evolve more inboard again. This phenomenon was observed before for dynamic stall cases on rotor blades, both numerically by the author [38] and experimentally by DiOttavio et al. [165], who proposed that it could correspond to the rollup of the separated shear layer. Just like with the typical

dynamic stall vortices and the apex vortex, the surface pressure beneath these vortices is very low, almost up to the trailing edge, see Fig. 7.6 again. As a result, sectional thrusts and nose-down pitching moments remain high in the outboard region of the blade throughout the remaining forth quadrant, compare Fig. 7.7.

Finally, at $\psi = 360°$, the flow is reattached in the leading part of the rotor blade. However, as observed in other high-speed dynamic stall relevant flight conditions [28, 27], there is also another kind of flow separation around $\psi = 40°$, marked by ⑥. As depicted in Fig. 7.10a, a narrow shock-induced separation occurs in the outboard part of the rotor blade for a small portion of the azimuth.

Table 7.5 summarizes the previous analysis of the given flow field and aerodynamic loads with regard to the flow separation and dynamic stall events. Comparing these findings to experimental and numerical investigations of forward flight dynamic stall on ONERA's 7A rotor and on the UH-60A helicopter (see Table 1.1), the regions of trailing-edge and shock-induced flow separation and of dynamic stall events are qualitatively similar, although the cases differ in flight conditions and rotor geometries. Also, the evolution and the streamwise and spanwise propagation of the dynamic stall vortices is comparable. Furthermore, the basic characteristics of dynamic stall in high-speed forward and turn flight closely resemble those of dynamic stall on pitching finite wings [79, 80, 20, 81, 21, 82] or on a rotor without edgewise inflow [37, 38, 39]. However, the blade-vortex interactions (events ① and ③) and the shock-induced separation (event ⑥) are not present in these cases due to the simplified configurations or lower inflow Mach numbers, respectively.

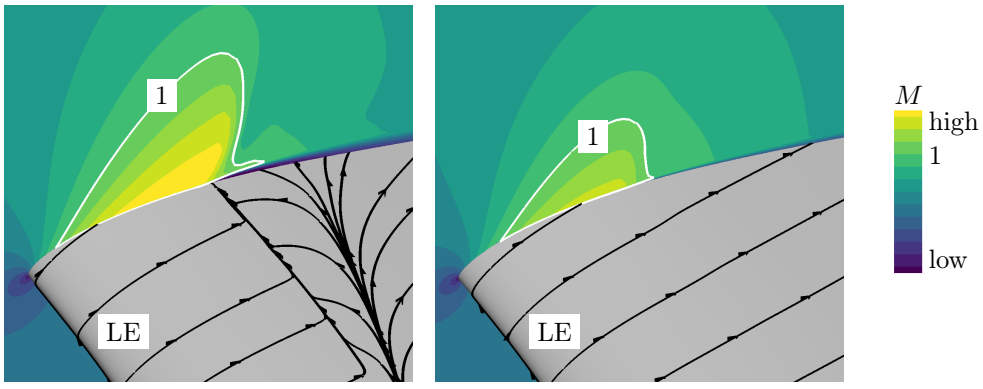

(a) With elastic twist (standard) (b) Without elastic twist

Figure 7.10: Close-up at $\psi = 40°$ of Mach number contours at $r/R = 0.81$ and surface streamlines indicating shock-induced separation (⑥) when elastic twist is allowed. Adapted from Letzgus et al. [157].

Table 7.5: Overview of flow separation and dynamic stall events and corresponding labeling. The radial and azimuthal values represent the approximate starting point of the respective event.

Label	Event	r/R	ψ
①	First DS, triggered by BVI and TE separation, outboard spreading	$0.25 - 0.55$	195°
②	Second DS, outboard of apex	0.9	255°
③	Second BVI, flow reattachment, apex vortex with DS-like effect	$0.6 - 0.95$	290°
④	Third DS, inboard of apex	0.85	310°
⑤	Massively separated flow, streamwise vortices form at LE with DS-like effect	$0.5 - 0.9$	320°
⑥	Shock-induced separation	0.85	20°

7.3.2 Influence of Elastic Twist

It was found before that the elastic twist of a rotor blade plays a role in the characteristics of shock-induced separation [28] and dynamic stall [46]. To investigate its influence in the standard case (T_{mid}, BHF, SST), which is considered in the flow field analysis in the previous section, the elastic twist was suppressed for test purposes by simply removing the elastic torsional deformation from the CFD blade movement. Note that no re-trimming or other setup changes were carried out.

The sectional blade pitch angles and the sectional pitching moment coefficients in Fig. 7.11 for the case with and without elastic twist are taken at $r/R = 0.81$ for example. It shows that there is substantial high-frequency elastic twist throughout a rotor revolution, supposedly due to the large unsteady aerodynamic loads in the present flight condition. It is tempting to analyze the correlation of local extrema in blade pitch and moment-stall events, however, this is inappropriate as one would neglect the complex interaction of aerodynamics and structural dynamics of the entire rotor blade. Nevertheless, it is apparent that the elastic twist has only a small influence on both major dynamic stall events (①, ④), as they agree well qualitatively and only differ somewhat in the peak values of the pitching moments. While the first event (①) is – as discussed earlier – assumed to be triggered by BVI and trailing-edge separation, the moment stall in the fourth quadrant (④) is supposed to be related to the high control angle and the global maximum of the blade pitch angle, respectively, and is virtually independent of elastic twist. The biggest effect of neglecting the elastic twist is found in the first quadrant, where the shock-induced separation (⑥) is no longer present, see Fig. 7.10b. As the overshoot in blade pitch angle – due to elastic twist – around $\psi = 20°$ is removed, the effective angle of attack

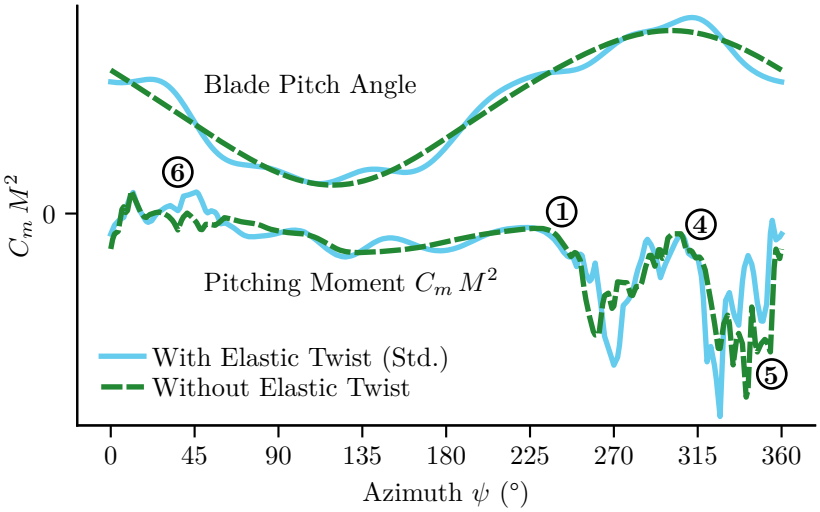

Figure 7.11: Influence of elastic twist on sectional blade pitch angles and sectional pitching moment coefficients at $r/R = 0.81$. Adapted from Letzgus et al. [157].

is expected to also be reduced, leading to lower flow velocities near the leading edge and a weaker shock that does not cause separation, compare Figs. 7.10a and 7.10b. This correlation of torsional excitation on the retreating side and shock-induced separation on the advancing side was also observed by Castells et al. [29] on the 7A rotor.

7.3.3 Influence of Turbulence Model

The SA-DDES and SST-DDES turbulence models are compared using the lower target thrust T_{low}. As discussed later in detail, the convergence of the trim control angles of these two cases differ, thus the untrimmed CFD results using initial controls and deformations provided by CAMRAD II are compared in order to have identical rotor blade movements. Figure 7.12 reveals that the two models yield very similar integral single-blade thrusts except around $\psi = 40°$ and between $\psi = 290°$ and 350°, where the SA-DDES values are higher. At these azimuthal positions, shock-induced and leading-edge separation occurs, respectively (Fig. 7.6). However, Fig. 7.13 exemplarily confirms at $\psi = 320°$ that the flow separation is less pronounced and that the suction peaks are stronger with SA-DDES, which explains the differences in thrust. Other simulations of two- and three-dimensional dynamic stall showed that the SA-URANS model predicts higher stall and reattachment angles than SST-URANS or does not capture a dynamic stall event at all [68, 69, 39]. As the prediction of stall onset is mostly determined by the underlying RANS turbulence model if the RANS-LES interface is placed correctly at the boundary-layer edge [106], a similar behavior is found for the SA-DDES model [80].

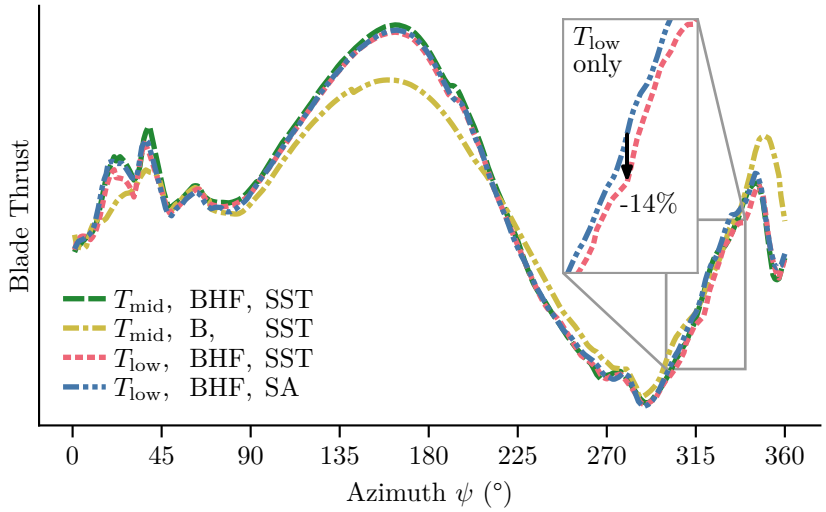

Figure 7.12: Single-blade integral thrusts using control angles of trim zero show influence of fuselage and turbulence modeling. Adapted from Letzgus et al. [157].

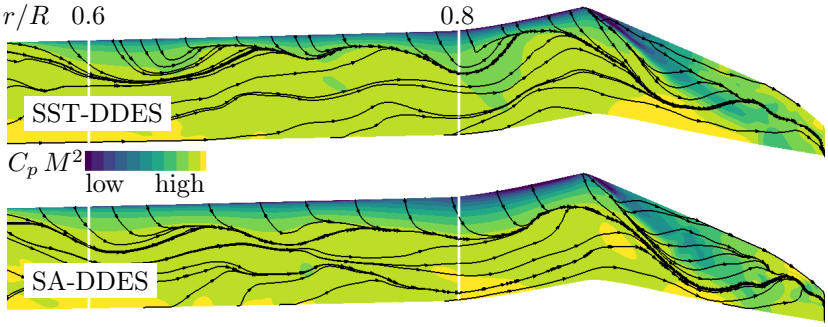

Figure 7.13: Instantaneous distributions of pressure and surface streamlines on the suction side at $\psi = 320°$ using control angles of trim zero [157].

7.3.4 Influence of Hub and Fuselage Modeling

It was shown before by other researchers [44, 24, 166] that the fuselage and rotor hub components can have a noticeable influence on the main rotor aerodynamics, as they deflect the inflow and induce an upwash around $\psi = 180°$ and a downwash on the rear side. Figure 7.14, which compares the rotor inflow of the two investigated variants – namely only isolated rotor blades (B) and the configuration with additionally modeled hub cap, fuselage with mast fairing and tail boom (BHF) – shows that this applies in the present case as well. Consequently, when considering identical blade movements, the isolated rotor variant (B) yields significantly lower thrust in the front area and higher thrust in the rear area of the rotor disk (Fig. 7.12). Besides, smaller deviations in thrust are noticeable over the entire azimuth. The following sections show that the additional consideration of the named helicopter components improves the overall agreement with the flight-test measurements.

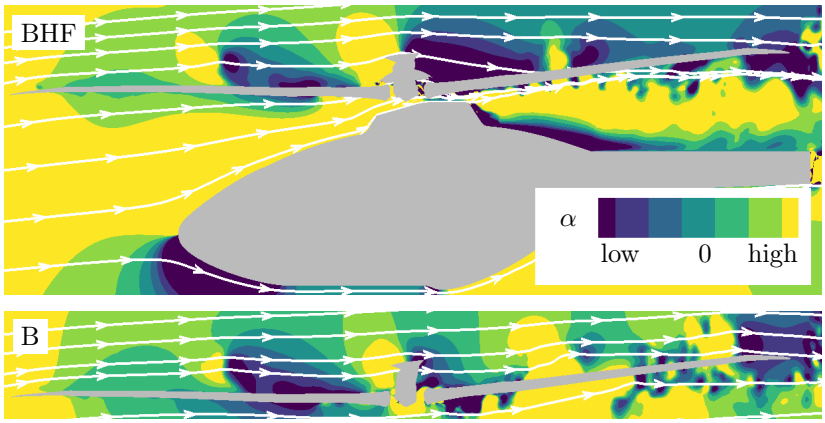

Figure 7.14: Comparison of instantaneous angles of attack α and vertical flow deflections in the plane of symmetry, left rotor blade is at $\psi = 198°$, cases: T_{mid}, BHF (top) and T_{mid}, B (bottom) [157].

7.3.5 Rotor Trim

In the course of the loose CFD/CSD coupling, the rotor controls change from trim iteration to trim iteration until changes in the rotor structural dynamics and aerodynamics ideally vanish. Figure 7.15 shows the convergence history of the collective, lateral cyclic and longitudinal cyclic pitch angles. In all computed cases, all controls converge reasonably, considering the unsteadiness and cycle-to-cycle variations introduced by the flow separation.

With increasing target rotor thrust, the initial jump from iteration zero to iteration one of all control angles becomes higher and the converged controls differ more from the initial solution, reflecting the natural limitations of the blade-element-theory-based aerodynamics of CAMRAD II. Concerning the measured collective pitch, the lower target thrust T_{low} cases yield too low angles. Using the higher thrust T_{high}, the collective is somewhat overpredicted, using the mid thrust T_{mid}, it is only slightly underpredicted. The computed lateral cyclic pitch angles of the lower and mid thrust cases lie within the range of the flight-test measurements, for the higher thrust the lateral cyclic is somewhat overpredicted. The longitudinal cyclic pitch angle is slightly underpredicted by the lower thrust cases, while the higher thrust and mid thrust with modeled helicopter components case (BHF) yields results that are within the flight-test range.

Regarding the two variants of modeled components, that is, only isolated rotor blades (B) versus blades with rotor hub, fuselage and tail boom (BHF), the collective and lateral cyclic pitch of variant B seems to converge slower and settles to a 0.5 ° lower value. The longitudinal cyclic pitch is even 1 ° lower than the one of variant BHF. Compared to the flight-test data, collective and longitudinal cyclic pitch angles of

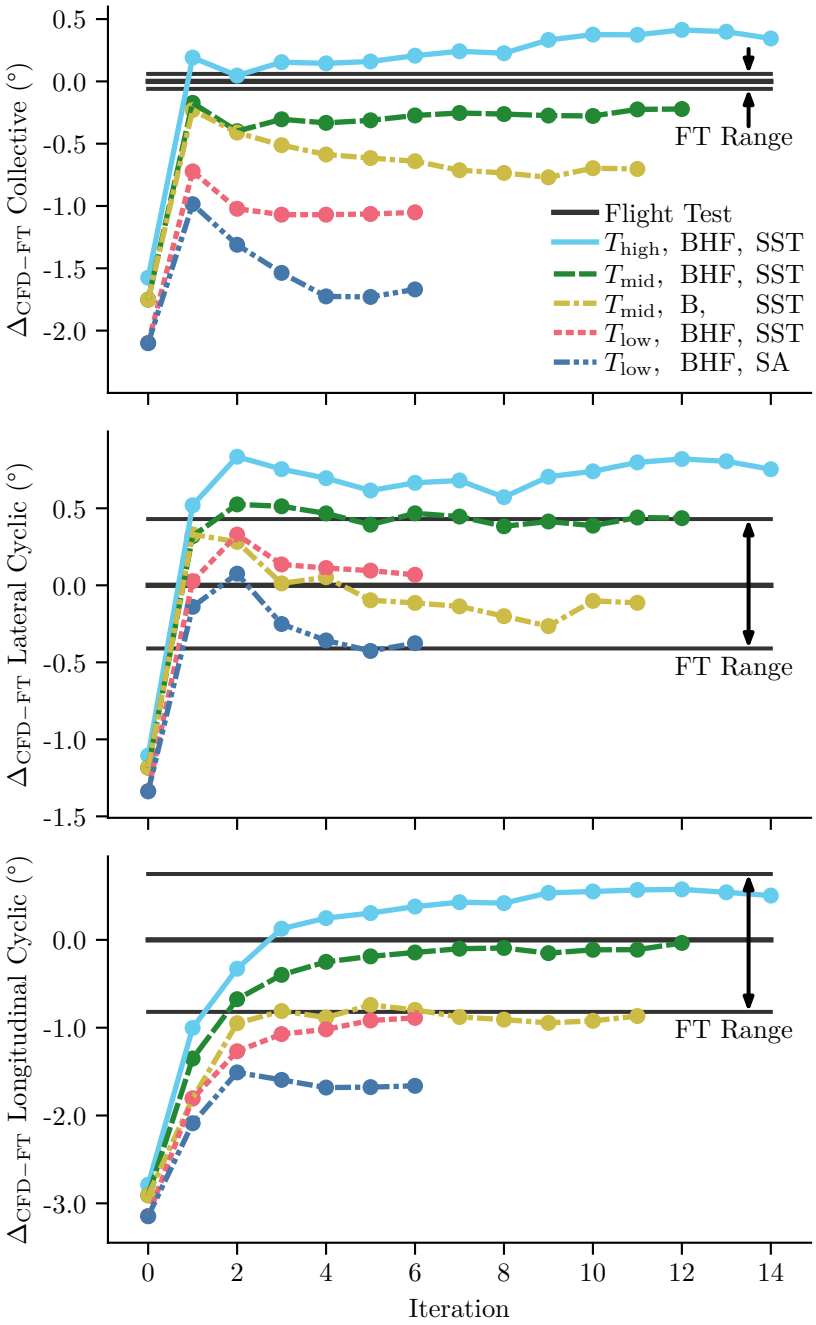

Figure 7.15: Convergence history of trim control angles relative to flight-test (FT) mean values during loose CFD/CSD coupling. Adapted from Letzgus et al. [157].

variant BHF agree better than variant B, but for the lateral cyclic pitch variant B lies closer to the measured mean. The variation of the turbulence models shows a clear trend, as the SA-DDES model consistently yields 0.5 ° to 1 ° lower control angles than SST-DDES. As discussed before, the SA-DDES model predicts less flow separation, which in the present case seems to lead to a worse agreement with the flight test.

Overall, very good agreement of rotor control angles is achieved with the mid target thrust in combination with also considering the rotor hub and fuselage in CFD (T_{mid}, BHF), especially keeping the challenging flight condition in mind. Comparing variant B with BHF, the additional effort in grid generation and slightly increased computational costs (4% more grid cells) seems to be worthwhile.

7.3.6 Measured and Computed Pitch-Link Loads

The pitch-link loads of the investigated CFD/CSD cases were computed by CAMRAD II based on the aerodynamic CFD loads of the respective final trim iteration. In Fig. 7.16 the computed and measured pitch-link loads are plotted in the time domain. The error bars denote the standard deviation of the measurement, indicating rather low cycle-to-cycle variations.

It is apparent that all CFD/CSD cases yield similar oscillations of the pitch-link loads, where mainly the amplitudes of the peaks differ. With increasing target rotor thrust the amplitudes increase as well. Using the SA turbulence model yields the smallest amplitudes. Larger deviations are found for the case using only isolated rotor blades (B), as it shows noticeably larger amplitudes at $\psi = 200°$ and $\psi = 250°$ and smaller ones elsewhere. However, it should be kept in mind that the final trim control angles and blade dynamics differ between the computed cases, which plays a key role for the pitch-link loads.

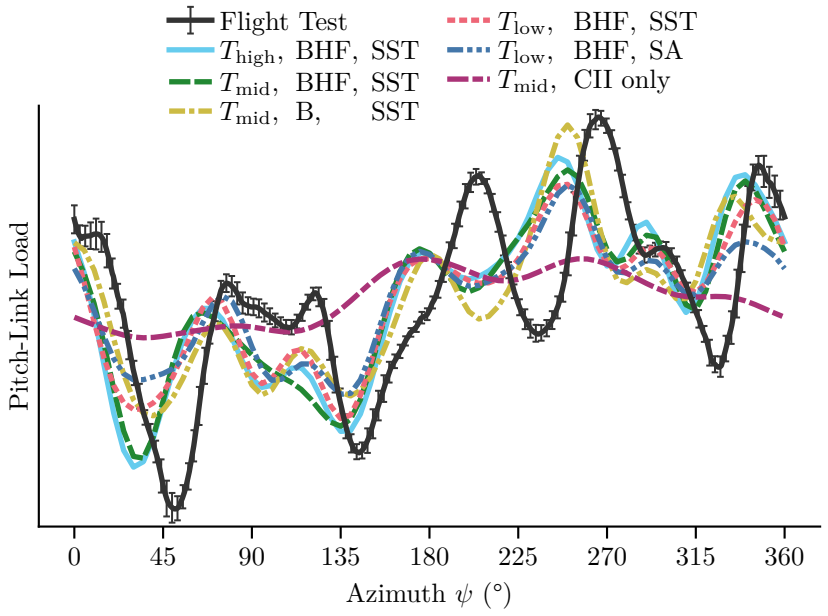

Figure 7.16: Comparison of measured and computed pitch-link loads in the time domain. Adapted from Letzgus et al. [157].

Compared to the flight-test measurements, all amplitudes are underpredicted and there seems to be a phase shift between the computed and measured data that somewhat varies across the azimuth. However, the CFD/CSD results show similar trends as the flight-test data. The benefits of the CFD/CSD coupling and trimming become evident when compared to standalone CAMRAD II results that completely misses the peaks of the pitch-link loads.

The analysis of the pitch-link loads in the time domain is confirmed by an analysis in the frequency domain obtained by a fast Fourier transform (FFT), see Fig. 7.17. The half peak-to-peak (p2p) amplitude is underpredicted by the computations by 20 % to 45 %. Regarding the four most dominant frequencies, the 1/rev content is captured fairly well in amplitude and phasing. Then, the amplitude of the 4/rev content is underpredicted by at least 30 %, along with a substantial azimuthal phase shift. The amplitude of the third-most dominant 3/rev content is captured better again, while for the 8/rev content the agreement is the worst.

As the stiffness of the swashplate and pitch links were defined as rigid to ease trim convergence, which, of course, is not the case in reality, a change in the dynamic response of the rotor is most likely and, consequently, an impact on both pitch-link-load amplitudes and phasing is expected, as already observed in other CFD/CSD studies [86, 45, 88]. Beyond deficiencies in the structural dynamic modeling of the rotor, it is known that especially the point in space and time of flow separation and reattachment is often incorrectly predicted by CFD, which might also contribute to the differences between computed and measured pitch-link loads.

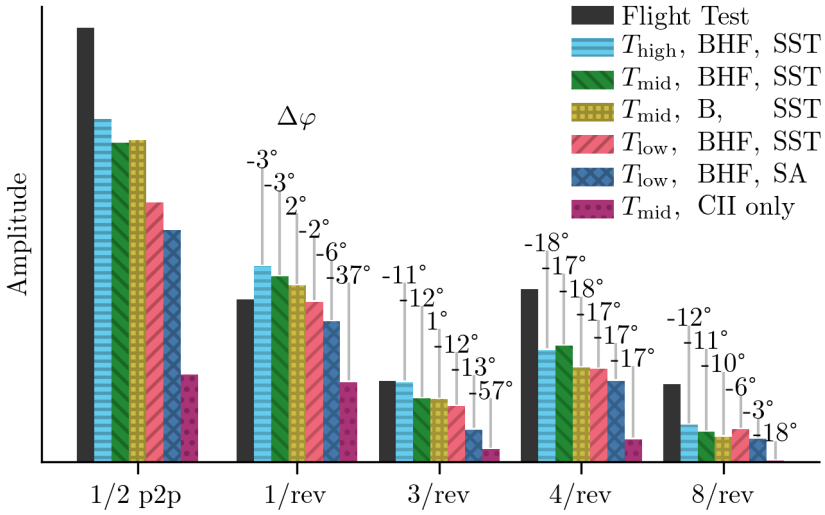

Figure 7.17: Half peak-to-peak (p2p) magnitude and amplitudes and phase shift $\Delta\varphi$ of dominant frequencies of measured and computed pitch-link-load time signals. Adapted from Letzgus et al. [157].

7.4 Chapter Conclusions

In this chapter, a highly loaded, high-speed turn flight – which was classified as dynamic stall relevant – of Airbus Helicopters' Bluecopter demonstrator helicopter was numerically investigated with a loose coupling of the CFD code FLOWer and the rotorcraft comprehensive code CAMRAD II, performing a three-degree-of-freedom trim of the isolated rotor. On the CFD side, a high-fidelity DDES was carried out. Differences between the SA-DDES and SST-DDES turbulence model as well as the influence of elastic twist (elastic versus torsionally rigid rotor), of additionally modeled helicopter components (hub, fuselage and tail boom) and of a variation of the target rotor thrust (low, mid and high) were investigated. Computed rotor control angles and pitch-link loads were then compared to flight-test measurements. The main findings are as follows:

1. The rotor flow field in the present flight condition is highly unsteady and complex, as the flow phenomena of trailing-edge separation, blade-vortex interaction, several different dynamic stall events and shock-induced separation occur throughout a large portion of the azimuth.

2. The first dynamic stall event happens in the third quadrant of the rotor disk and might be triggered by blade-vortex interaction and more inboard by progressing trailing-edge separation. The dynamic stall vortex quickly spreads in- and outboards, inducing overshoots of sectional thrusts and pitching moments. Then, the kink in the planform of the rotor blade seems to delay the outboard spreading of dynamic stall and is the origin of a tip-vortex-like apex vortex. Several other typical dynamic stall events and streamwise vortices appear in the outboard region of the blade in the fourth quadrant, which sustain overshoots of sectional thrust and pitching moments.

3. Phenomenologically, the results show great similarities with other experimental and numerical dynamic stall investigations that considered different rotor geometries and flight conditions.

4. Although there is substantial high-frequency elastic twist of the rotor blade, the additional changes in blade pitch angles play only a minor role in the characteristics of the dynamic stall events. However, in the present case, shock-induced separation does not occur when elastic twist is suppressed.

5. With the SA-DDES turbulence model, the flow separation in the fourth quadrant of the rotor disk is less pronounced than with SST-DDES, leading to an overall worse agreement with the flight test.

6. The additional consideration of the hub cap, fuselage with mast fairing and the tail boom in CFD alters the rotor inflow, which improves the agreement with both flight-test control angles and pitch-link loads.

7. The trim control angles of all cases converge reasonably within at least six loosely coupled CFD/CSD iterations. While the lower target thrust cases underpredict and the higher target thrust case overpredicts the flight-test control angles, the control angles of the mid target thrust agree very well with the measurements.

8. All computed CFD/CSD cases underpredict the amplitudes of the flight-test pitch-link loads and phase shifts are apparent. However, overall trends agree reasonably and it becomes clear that CFD/CSD coupling and trimming yields better results than a standalone CAMRAD II analysis. Most likely causes for the remaining deviations are deficiencies in meeting the free-flight trim conditions or in the structural dynamic modeling of the main rotor, therefore, as a next step, the elasticity of the rotor controls needs to be considered.

8 Conclusion and Outlook

In the course of this work, high-fidelity CFD simulations using the flow solver FLOWer were carried out to investigate dynamic stall, which is an unsteady flow phenomenon that occurs when a lifting surface temporarily experiences angles of attack beyond its static stall angle. The characteristic formation and shedding of a coherent leading-edge vortex is associated with large overshoots in lift, pitching moment and vibrations that limit the performance of a helicopter, where dynamic stall appears in high-speed or maneuvering flight. Investigations of dynamic stall in a rotating environment are very rare and limited to only a few rotors. For this thesis, two novel experimental cases of rotor dynamic stall were chosen to assess and improve CFD methods and to numerically study the phenomenon in greater detail. In the first experiment, conducted in the Rotor Test Facility (RTG) at DLR Göttingen, dynamic stall was triggered by high cyclic pitch control on a two-bladed model rotor operating in a climb-flight-like condition. In the second case, it was observed on Airbus Helicopters' Bluecopter demonstrator in turn flight.

At first, based on the RTG case and in analogy to fundamental pitching airfoil investigations, parameter studies were conducted using a lower-resolution CFD setup. Although the dynamic stall vortex was found to be in the typical three-dimensional Ω-shape known from pitching finite wings and affected by the tip vortex and the rotation, the characteristics of lift and pitching-moment overshoot, stall onset and hysteresis are very similar to rather two-dimensional dynamic stall. Furthermore, it showed that an increase in pitching amplitude, mean pitch angle and inflow Mach number have qualitatively the same influence on rotor dynamic stall as on pitching airfoil dynamic stall. Thus, the sound knowledge of the flow physics of the phenomenon, which has been gained from much simpler test cases, is in general applicable to the rotor environment as well.

Based on the comprehensive RTG measurements provided by DLR, a validation of high-resolution URANS and delayed detached-eddy simulations (DDES) was carried out. Overall, the onset of dynamic stall and the associated peak values of lift and pitching-moment overshoot are matched well. However, an unprecedented comparison of instantaneous PIV and CFD results of rotor dynamic stall revealed that after stall onset, the flow field of URANS resembles a phase average of the reality – at best. In contrast, using a DDES, the chaotic nature of the separated flow is captured throughout the hysteresis part of the cycle, where the size, shape

and strength of incoherent vortical structures as well as the extent of the separated region correlate very well with PIV. Also, only DDES is able to reproduce the experimental cycle-to-cycle variation to some extent. Concerning the latter, it was shown by flow-feature-based cycle clustering that the measured surface pressure data is represented well by its phase average and the corresponding standard deviation. Moreover, a comparison of FLOWer and provided TAU data as well as a variation of the RANS turbulence model demonstrated the noticeable dependence of the results on the specific numerics in case of massive flow separation. While all simulations yield very similar loads during attached flow, discrepancies are evident in the prediction of the onset and severity of dynamic stall.

Closer inspection of the RTG DDES results showed that, before the actual dynamic stall event, the simulation suffers from an unfortunate and complex combination of both major issues of a DES. Due to the very fine near-body grid, the DDES allows an unintended intrusion of the LES mode into the boundary layer, causing modeled-stress depletion and, eventually, grid-induced trailing-edge separation. In addition, the delayed transition from modeled to resolved turbulence at the RANS/LES interface, described as the gray-area problem, damps shear-layer instabilities, enabling the nonphysical rollup of a strong, coherent vortex around mid-chord that causes dynamic-stall-like overshoots in lift and pitching moment, which do not agree with the experiment or other simulations. Before, these deficits of DES were reported for much simpler test cases, however, only in the DES community, and are unprecedented for dynamic stall or rotor scenarios where DES is becoming increasingly popular.

To eliminate grid-induced separation, several available (C_{d1}, BDES, ZDES19) and self-developed (VIADES, WNFA) modifications to the DDES boundary-layer shielding function f_d were tested and assessed based on the RTG and Bluecopter dynamic stall cases. All methods were found to work properly, but differ in complexity, physical foundation and transition behavior from RANS to LES mode. The two developed approaches perform a wall-normal analysis of the vorticity and velocity distribution to determine the boundary-layer edge, and incorporate a vorticity-based sensor to detect separated flow, allowing a rapid and consistent switching to LES mode downstream of the point of separation. Furthermore, an alternative shear-layer-adaptive subgrid filter width Δ_{SLA} was assessed, again for both dynamic stall cases. It showed that this modification leads to a significant reduction of the damping eddy viscosity in a separated shear layer, which promotes the early formation of Kelvin-Helmholtz instabilities and, thus, effectively mitigates the gray-area problem. Since this alternative filter width was found to enable a more realistic simulation of separated flow and to impact the load peaks of dynamic stall, further investigations are recommended.

Lastly, a loose computational fluid dynamics/structural dynamics (CFD/CSD) coupling of a FLOWer DDES and the rotorcraft comprehensive code CAMRAD II of the Bluecopter helicopter in an unprecedented high-speed, highly loaded turn flight was carried out. The three-degree-of-freedom trim of an isolated rotor yielded main rotor control angles that agree very well with the flight-test measurements. A comparison of computed and in-flight measured pitch-link loads, which so far has only been done for the UH-60A flight-test campaign, showed a good correlation regarding the overall trends and a significant improvement over a stand-alone CAMRAD II analysis, but the pitch-link-load amplitudes are underpredicted and somewhat phase-shifted. The flow field was found to be highly unsteady and complex throughout a large portion of the azimuth, exhibiting strong trailing-edge, leading-edge and shock-induced separation as well as multiple dynamic stall events that are partly triggered by blade-vortex interaction. Interestingly, these findings are phenomenologically very similar to other experimental and numerical dynamic stall investigations that considered different rotor geometries and flight conditions.

The present thesis demonstrates that it is possible to simulate rotor dynamic stall in overall good agreement with experiments. However, it showed once more that current CFD methods still have difficulties in accurately predicting the onset of flow separation and (dynamic) stall. Although the ever-increasing computational power allows for higher spatial and temporal resolutions, decades-old turbulence models are used that were designed for attached flows. In fact, more advanced nonlinear eddy-viscosity or Reynolds-stress models barely play a role in complex CFD simulations, be it due to numerical effort, stability issues or the lack of clear superiority. Thus, it is necessary to further improve RANS turbulence models and promote the implementation and investigation of already existing enhancements, as it is believed that turbulence modeling of boundary-layer flows will stay relevant for years to come.

Although the hybrid RANS/LES approach of a detached-eddy simulation cannot solve the aforementioned modeling issue, it was shown to be far superior in simulating separated flow and preserving flow features in the wake and, thus, it is assumed to become even more popular. Today, there is no widely accepted solution to the issue of modeled-stress depletion or the gray-area problem. However, as presented in this thesis, there are promising, multifaceted concepts on the rise. Of course, there is a need for more testing and validation, which undoubtedly holds true for the methods developed in this work. Moreover, for the use in everyday CFD simulations in research and industry, a further increase in robustness, universality and user-friendliness is important.

Regarding the accuracy of rotor dynamic stall simulations, the mentioned possible advances in turbulence and hybrid RANS/LES modeling would surely be beneficial, however, it is believed that improvements in structural dynamics modeling and rotor trim are essential. Several helicopter CFD/CSD investigations, including the present one, revealed the noticeable influence of the CSD model, for example, the stiffness of the rotor controls or blade elasticity, on trim convergence, pitch-link loads and, due to the coupling process, also on the aerodynamics. On CSD side, deficits are likely to be found in incorrect material properties, oversimplified modeling or discretization errors and, consequently, topics outside the main subject area of aerodynamicists must be addressed. Furthermore, with the present turn flight condition, difficulties regarding the rotor trim convergence appeared, perhaps due to the decoupling of thrust and collective control input on the heavily stalled rotor, that are assumed to become critical when even more challenging stall-relevant flight conditions, like high-g maneuvers, come into focus. Consequently, advanced trim strategies or coupling procedures are of interest as well.

References

[1] Leishman, J. G., *Principles of helicopter aerodynamics*, Cambridge University Press, second edition, 2006.
doi: 10.1017/S0001924000087352 (Pages 1, 1, 2, 7, 17, 18, 19, 20, 20, 20, 21, 31, 32, 49)

[2] McCroskey, W. J., "The phenomenon of dynamic stall." Technical memorandum 81264, NASA Ames Research Center, Moffett Field, CA, 1981. (Pages 2, 3, 16, 20, 30)

[3] Kufeld, R. M. and Bousman, W. G., "High load conditions measured on a UH-60A in maneuvering flight," *Journal of the American Helicopter Society*, Vol. 43, (3), 1998.
doi: 10.4050/JAHS.43.202 (Pages 2, 2, 6)

[4] Kufeld, R., Balough, D. L., Cross, J. L., Studebaker, K. F., Jennison, C. D., and Bousman, W. G., "Flight testing the UH-60A airloads aircraft," Proceedings of the 50th Annual Forum of the American Helicopter Society, Washington, DC, May 11–13, 1994. (Pages 2, 5, 5, 10)

[5] McHugh, F. J., "What are the lift and propulsive force limits at high speed for the conventional rotor?" Proceedings of the 34th Annual Forum of the American Helicopter Society, Washington, DC, May 15–17, 1978. (Page 2)

[6] Bousman, W. G., "A qualitative examination of dynamic stall from flight test data," *Journal of the American Helicopter Society*, Vol. 43, (4), 1998.
doi: 10.4050/JAHS.43.279 (Pages 2, 5, 19)

[7] Carr, L. W., "Progress in analysis and prediction of dynamic stall," *Journal of Aircraft*, Vol. 25, (1), 1988.
doi: 10.2514/3.45534 (Pages 3, 3, 7, 20, 30)

[8] Bailey, F. J. and Gustafon, F. B., "Observations in flight of the region of stalled flow over the blades of an autogiro rotor," Technical note 741, NACA, Langley Field, VA, 1939. (Page 3)

[9] Ham, N. D. and Garelick, M. S., "Dynamic stall considerations in helicopter rotors," *Journal of the American Helicopter Society*, Vol. 13, (2), 1968.
doi: 10.4050/JAHS.13.49 (Page 3)

[10] Carr, L. W., McAlister, K. W., and McCroskey, W. J., "Analysis of the development of dynamic stall based on oscillating airfoil experiments," Technical note 8382, NASA Ames Research Center, Moffett Field, CA, 1977. (Pages 3, 12, 20)

[11] Le Pape, A., Pailhas, G., David, F., and Deluc, J.-M., "Extensive wind tunnel tests measurements of dynamic stall phenomenon for the OA209 airfoil including 3D effects," Proceedings of the 33rd European Rotorcraft Forum, Kasan, Russia, September 11–13, 2007.
doi: 20.500.11881/204 (Pages 4, 4, 8)

[12] Gardner, A. D., Richter, K., Mai, H., Altmikus, A. R. M., Klein, A., and Rohardt, C.-H., "Experimental investigation of dynamic stall performance for the EDI-M109 and EDI-M112 airfoils," *Journal of the American Helicopter Society*, Vol. 58, (1), 2013.
doi: 10.4050/JAHS.58.012005 (Page 4)

[13] Mulleners, K. and Raffel, M., "Dynamic stall development," *Experiments in Fluids*, Vol. 54, (2), 2013.
doi: 10.1007/s00348-013-1469-7 (Pages 4, 51, 97, 115)

[14] Gupta, R. and Ansell, P. J., "Unsteady flow physics of airfoil dynamic stall," *AIAA Journal*, Vol. 57, (1), 2019.
doi: 10.2514/1.J057257 (Page 4)

[15] Corke, T. C. and Thomas, F. O., "Dynamic stall in pitching airfoils: Aerodynamic damping and compressibility effects," *Annual Review of Fluid Mechanics*, Vol. 47, (1), 2015.
doi: 10.1146/annurev-fluid-010814-013632 (Page 4)

[16] Lind, A. H. and Jones, A. R., "Unsteady aerodynamics of reverse flow dynamic stall on an oscillating blade section," *Physics of Fluids*, Vol. 28, (7), 2016.
doi: 10.1063/1.4958334 (Page 4)

[17] Lorber, P. F., Carta, F. O., and Covino, A. F., "An oscillating three-dimensional wing experiment: Compressibility, sweep, rate, waveform, and geometry effects on unsteady separation and dynamic stall," UTRO report R92-958325-6, United Technologies Research Center, East Hartford, CT, 1992. (Page 4)

[18] Schreck, S. J. and Hellin, H. E., "Unsteady vortex dynamics and surface pressure topologies on a finite pitching wing," *Journal of Aircraft*, Vol. 31, (4), 1994.
doi: 10.2514/3.46577 (Page 4)

[19] Piziali, R. A., "2-D and 3-D oscillating wing aerodynamics for a range of angles of attack including stall," Technical memorandum 4632, NASA Ames Research Center, Moffett Field, CA, 1994. (Pages 4, 7, 25)

[20] Merz, C. B., Wolf, C. C., Richter, K., Kaufmann, K., Mielke, A., and Raffel, M., "Spanwise differences in static and dynamic stall on a pitching rotor blade tip model," *Journal of the American Helicopter Society*, Vol. 62, (1), 2017. doi: 10.4050/JAHS.62.012002 (Pages 4, 9, 116)

[21] Lütke, B., Nuhn, J., Govers, Y., and Schmidt, M., "Design of a rotor blade tip for the investigation of dynamic stall in the transonic wind-tunnel Göttingen," *The Aeronautical Journal*, Vol. 120, (1232), 2016. doi: 10.1017/aer.2016.74 (Pages 4, 115, 116)

[22] McCroskey, W. J. and Fisher, R. K., "Detailed aerodynamic measurements on a model rotor in the blade stall regime," *Journal of the American Helicopter Society*, Vol. 17, (1), 1972. doi: 10.4050/JAHS.17.1.20 (Page 4)

[23] Crozier, P., "Recent improvements in rotor testing capabilities in the ONERA S1MA wind tunnel," Proceedings of the 20th European Rotorcraft Forum, Amsterdam, The Netherlands, October 4–7, 1994. doi: 20.500.11881/2216 (Pages 4, 10)

[24] Ortun, B., Potsdam, M., Yeo, H., and Van Truong, K., "Rotor loads prediction on the ONERA 7A rotor using loose fluid/structure coupling," *Journal of the American Helicopter Society*, Vol. 62, (3), 2017. doi: 10.4050/JAHS.62.032005 (Pages 4, 5, 9, 9, 10, 13, 119)

[25] Richez, F., "Numerical analysis of dynamic stall for different helicopter rotor flight conditions," Proceedings of the 73rd Annual Forum of the American Helicopter Society, Fort Worth, TX, May 9–11, 2017. (Pages 4, 10, 11, 41)

[26] Yeo, H., Potsdam, M., Ortun, B., and Truong, K. V., "High-fidelity structural loads analysis of the ONERA 7A rotor," *Journal of Aircraft*, Vol. 54, (5), 2017. doi: 10.2514/1.C034286 (Pages 4, 10, 11)

[27] Grubb, A., Castells, C., Jain, R., Richez, F., and Smith, M., "High fidelity CFD analyses of dynamic stall on a four-bladed fully articulated rotor system," Proceedings of the 74th Annual Forum of the American Helicopter Society, Phoenix, AZ, May 14–17, 2018. (Pages 4, 9, 10, 11, 13, 107, 108, 110, 116)

[28] Richez, F., "Analysis of dynamic stall mechanisms in helicopter rotor environment," *Journal of the American Helicopter Society*, Vol. 63, (2), 2018. doi: 10.4050/JAHS.63.022006 (Pages 4, 10, 11, 107, 108, 113, 116, 117)

[29] Castells, C., Richez, F., and Costes, M., "A numerical analysis of the dynamic stall mechanisms on a helicopter rotor from light to deep stall," *Journal of the American Helicopter Society*, Vol. 65, (3), 2020.
doi: 10.4050/JAHS.65.032005 (Pages 4, 10, 11, 118)

[30] Pahlke, K., "The GOAHEAD project," Proceedings of the 33rd European Rotorcraft Forum, Kasan, Russia, September 11–13, 2007.
doi: 20.500.11881/213 (Pages 4, 10)

[31] Mulleners, K., Kindler, K., and Raffel, M., "Dynamic stall on a fully equipped helicopter model," *Aerospace Science and Technology*, Vol. 19, (1), 2012.
doi: 10.1016/j.ast.2011.03.013 (Page 4)

[32] Raghav, V. and Komerath, N., "Velocity measurements on a retreating blade in dynamic stall," *Experiments in Fluids*, Vol. 55, (2), 2014.
doi: 10.1007/s00348-014-1669-9 (Page 4)

[33] Raghav, V. and Komerath, N., "Dynamic stall life cycle on a rotating blade in steady forward flight," *Journal of the American Helicopter Society*, Vol. 60, (3), 2015.
doi: 10.4050/JAHS.60.032007 (Pages 4, 58)

[34] Norman, T. R., Shinoda, P., Peterson, R. L., and Datta, A., "Full-scale wind tunnel test of the UH-60A airloads rotor," Proceedings of the 67th Annual Forum of the American Helicopter Society, Virginia Beach, VA, May 3–5, 2011. (Pages 5, 5, 10)

[35] Datta, A., Yeo, H., and Norman, T. R., "Experimental investigation and fundamental understanding of a full-scale slowed rotor at high advance ratios," *Journal of the American Helicopter Society*, Vol. 58, (2), 2013.
doi: 10.4050/JAHS.58.022004 (Page 5)

[36] Le Pape, A., Pailhas, G., David, F., and Deluc, J.-M., "Slowed rotor wind tunnel testing of an instrumented rotor at high advance ratio," Proceedings of the 40th European Rotorcraft Forum, Southampton, England, September 2–5, 2014.
doi: 20.500.11881/3463 (Page 5)

[37] Schwermer, T., Gardner, A. D., and Raffel, M., "A novel experiment to understand the dynamic stall phenomenon in rotor axial flight," *Journal of the American Helicopter Society*, Vol. 64, (1), 2019.
doi: 10.4050/JAHS.64.012004 (Pages 5, 12, 32, 38, 42, 43, 45, 58, 116)

[38] Letzgus, J., Keßler, M., and Krämer, E., "CFD-simulation of three-dimensional dynamic stall on a rotor with cyclic pitch control," Proceedings of the 41th European Rotorcraft Forum, Munich, Germany, September 1–4, 2015. doi: 20.500.11881/3604 (Pages 5, 29, 30, 39, 41, 115, 116)

[39] Letzgus, J., Gardner, A. D., Schwermer, T., Keßler, M., and Krämer, E., "Numerical investigations of dynamic stall on a rotor with cyclic pitch control," *Journal of the American Helicopter Society*, Vol. 64, (1), 2019. doi: 10.4050/JAHS.64.012007 (Pages 5, 37, 38, 38, 40, 41, 44, 46, 50, 51, 52, 54, 55, 56, 57, 108, 116, 118)

[40] Goerttler, A., Braukmann, J. N., Schwermer, T., Gardner, A. D., and Raffel, M., "Tip-vortex investigation on a rotating and pitching rotor blade," *Journal of Aircraft*, Vol. 55, (5), 2018. doi: 10.2514/1.C034693 (Pages 5, 58)

[41] Kaufmann, K., Müller, M. M., and Gardner, A. D., "Dynamic stall computations of double-swept rotor blades," New Results in Numerical and Experimental Fluid Mechanics XII, edited by Dillmann, A., Heller, G., Krämer, E., Wagner, C., Tropea, C., and Jakirlić, S., 2020. (Page 5)

[42] Müller, M. M., Schwermer, T., Mai, H., and Stieg, C., "Development of an innovative double-swept rotor blade tip for the rotor test facility Göttingen," Deutscher Luft- und Raumfahrtkongress, Friedrichshafen, Germany, September 4–6, 2018. (Page 5)

[43] Isaacs, N. and Harrison, R., "Identification of retreating blade stall mechanisms using flight test pressure measurements," Proceedings of the 45th Annual Forum of the American Helicopter Society, Boston, MA, May 22–24, 1989. (Page 5)

[44] Potsdam, M., Yeo, H., and Johnson, W., "Rotor airloads prediction using loose aerodynamic/structural coupling," *Journal of Aircraft*, Vol. 43, (3), 2006. doi: 10.2514/1.14006 (Pages 6, 10, 11, 11, 119)

[45] Bhagwat, M., Ormiston, R., Saberi, H., and Xin, H., "Application of CFD/CSD coupling for analysis of rotorcraft airloads and blade loads in maneuvering flight," Proceedings of the 63rd Annual Forum of the American Helicopter Society, Virginia Beach, VA, May 1–3, 2007. (Pages 6, 10, 11, 123)

[46] Datta, A. and Chopra, I., "Prediction of the UH-60A main rotor structural loads using computational fluid dynamics/comprehensive analysis coupling," *Journal of the American Helicopter Society*, Vol. 53, (4), 2008. doi: 10.4050/JAHS.53.351 (Pages 6, 10, 11, 117)

[47] Roget, B., Sitaraman, J., and Wissink, A. M., "Maneuvering rotorcraft simulations using HPCMP CREATE-AV Helios," 54th AIAA Aerospace Sciences Meeting, San Diego, CA, January 4–8, 2016.
doi: 10.2514/6.2016-1057 (Page 6)

[48] Chaderjian, N. M., "Navier-Stokes simulation of UH-60A rotor/wake interaction using adaptive mesh refinement," Proceedings of the 73rd Annual Forum of the American Helicopter Society, Fort Worth, TX, May 9–11, 2017. (Pages 6, 10, 11, 11, 13, 41, 107, 108, 113)

[49] Yu, Y. H., Lee, S., McAlister, K. W., Tung, C., and Wang, C. M., "Dynamic stall control for advanced rotorcraft application," *AIAA Journal*, Vol. 33, (2), 1995.
doi: 10.2514/3.12496 (Page 6)

[50] Greenblatt, D. and Wygnanski, I., "Dynamic stall control by periodic excitation, part 1: NACA0015 parametric study," *Journal of Aircraft*, Vol. 38, (3), 2001.
doi: 10.2514/2.2810 (Page 6)

[51] Gardner, A. D., Richter, K., Mai, H., and Neuhaus, D., "Experimental investigation of air jets for the control of compressible dynamic stall," *Journal of the American Helicopter Society*, Vol. 58, (4), 2013.
doi: 10.4050/JAHS.58.042001 (Page 6)

[52] Post, M. L. and Corke, T. C., "Separation control using plasma actuators: Dynamic stall vortex control on oscillating airfoil," *AIAA Journal*, Vol. 44, (12), 2006.
doi: 10.2514/1.22716 (Page 6)

[53] Mai, H., Dietz, G., Geißler, W., Richter, K., Bosbach, J., Richard, H., and de Groot, K., "Dynamic stall control by leading edge vortex generators," *Journal of the American Helicopter Society*, Vol. 53, (1), 2008.
doi: 10.4050/JAHS.53.26 (Page 6)

[54] Heine, B., Mulleners, K., Joubert, G., and Raffel, M., "Dynamic stall control by passive disturbance generators," *AIAA Journal*, Vol. 51, (9), 2013.
doi: 10.2514/1.J051525 (Page 6)

[55] Gerontakos, P. and Lee, T., "Dynamic stall flow control via a trailing-edge flap," *AIAA Journal*, Vol. 44, (3), 2006.
doi: 10.2514/1.17263 (Page 6)

[56] Gardner, A. D., Opitz, S., Wolf, C. C., and Merz, C. B., "Influence of a back-flow flap on the dynamic stall flow topology," *CEAS Aeronautical Journal*, Vol. 9, (1), 2018.
doi: 10.1007/s13272-017-0274-z (Page 6)

[57] Johnson, W., "Rotorcraft aerodynamics models for a comprehensive analysis," Proceedings of the 54th Annual Forum of the American Helicopter Society, Washington, D.C., May 20, 1998. (Pages 6, 110)

[58] Gormont, R. E., "A mathematical model of unsteady aerodynamics and radial flow for application to helicopter rotors," USAAMRDL technical report 72-67, The Boeing Company, Philadelphia PA, 1973. (Page 7)

[59] Leishman, J. G. and Beddoes, T. S., "A semi-empirical model for dynamic stall," *Journal of the American Helicopter Society*, Vol. 34, (3), 1989.
doi: 10.4050/JAHS.34.3.3 (Page 7)

[60] Petot, D., "Differential equation modeling of dynamic stall," *La Recherche Aerospatiale*, Vol. 5, 1989. (Page 7)

[61] Ramesh, K., Gopalarathnam, A., Granlund, K., Ol, M., and Edwards, J., "Discrete-vortex method with novel shedding criterion for unsteady aerofoil flows with intermittent leading-edge vortex shedding," *Journal of Fluid Mechanics*, Vol. 751, 2014.
doi: 10.1017/jfm.2014.297 (Page 7)

[62] Modarres, R., Peters, D. A., and Gaskill, J., "Dynamic stall model with circulation pulse and static hysteresis for NACA0012 and VR-12 airfoils," *Journal of the American Helicopter Society*, Vol. 61, (3), 2016.
doi: 10.4050/JAHS.61.032004 (Page 7)

[63] Lui, H. F. S. and Wolf, W. R., "Construction of reduced-order models for fluid flows using deep feedforward neural networks," *Journal of Fluid Mechanics*, Vol. 872, 2019.
doi: 10.1017/jfm.2019.358 (Page 7)

[64] Ekaterinaris, J. A. and Menter, F. R., "Computation of oscillating airfoil flows with one- and two-equation turbulence models," *AIAA Journal*, Vol. 32, (12), 1994.
doi: 10.2514/3.12300 (Page 7)

[65] Spalart, P. R. and Allmaras, S. R., "A one-equation turbulence model for aerodynamic flows," *Recherche Aerospatiale*, 1994. (Pages 7, 24)

[66] Menter, F. R., "Two-equation eddy-viscosity turbulence models for engineering applications," *AIAA Journal*, Vol. 32, (8), 1994.
doi: 10.2514/3.12149 (Pages 7, 24)

[67] Costes, M., Gleize, V., Szydlowski, J., Sankar, L., Guzel, G., and Rhee, M., "Grid sensitivity study for the turbulent viscous flow around a NACA0015 airfoil at stall," Proceedings of the 31st European Rotorcraft Forum, Florence, Italy, September 13–15, 2005.
doi: 20.500.11881/1261 (Page 8)

[68] Richter, K., Le Pape, A., Knopp, T., Costes, M., Gleize, V., and Gardner, A. D., "Improved two-dimensional dynamic stall prediction with structured and hybrid numerical methods," *Journal of the American Helicopter Society*, Vol. 56, (4), 2011.
doi: 10.4050/JAHS.56.042007 (Pages 8, 118)

[69] Klein, A., Lutz, T., Krämer, E., Richter, K., Gardner, A. D., and Altmikus, A., "Numerical comparison of dynamic stall for two-dimensional airfoils and an airfoil model in the DNW–TWG," *Journal of the American Helicopter Society*, Vol. 57, (4), 2012.
doi: 10.4050/JAHS.57.042007 (Pages 8, 118)

[70] Zanotti, A., Nilifard, R., Gibertini, G., Guardone, A., and Quaranta, G., "Assessment of 2D/3D numerical modeling for deep dynamic stall experiments," *Journal of Fluids and Structures*, Vol. 51, 2014.
doi: 10.1016/j.jfluidstructs.2014.08.004 (Page 8)

[71] Liggett, N. D. and Smith, M. J., "Temporal convergence criteria for time-accurate viscous simulations of separated flows," *Computers & Fluids*, Vol. 66, 2012.
doi: 10.1016/j.compfluid.2012.06.010 (Pages 8, 41)

[72] Hodara, J., Lind, A. H., Jones, A. R., and Smith, M. J., "Collaborative investigation of the aerodynamic behavior of airfoils in reverse flow," *Journal of the American Helicopter Society*, Vol. 61, (3), 2016.
doi: 10.4050/JAHS.61.032001 (Page 8)

[73] Sánchez-Rocha, M. and Menon, S., "The compressible hybrid RANS/LES formulation using an additive operator," *Journal of Computational Physics*, Vol. 228, (6), 2009.
doi: 10.1016/j.jcp.2008.11.021 (Page 8)

[74] Visbal, M. R. and Garmann, D. J., "Analysis of dynamic stall on a pitching airfoil using high-fidelity large-eddy simulations," *AIAA Journal*, Vol. 56, (1), 2018.
doi: 10.2514/1.J056108 (Pages 8, 24, 51, 97)

[75] Benton, S. I. and Visbal, M. R., "The onset of dynamic stall at a high, transitional Reynolds number," *Journal of Fluid Mechanics*, Vol. 861, 2019.
doi: 10.1017/jfm.2018.939 (Pages 8, 115)

[76] Spentzos, A., Barakos, G., Badcock, K., Richards, B., Wernert, P., Schreck, S., and Raffel, M., "Investigation of three-dimensional dynamic stall using computational fluid dynamics," *AIAA Journal*, Vol. 43, (5), 2005.
doi: 10.2514/1.8830 (Page 8)

[77] Spentzos, A., Barakos, G. N., Badcock, K. J., Richards, B. E., Coton, F. N., Galbraith, R. A. M., Berton, E., and Favier, D., "Computational fluid dynamics study of three-dimensional dynamic stall of various planform shapes," *Journal of Aircraft*, Vol. 44, (4), 2007.
doi: 10.2514/1.24331 (Page 8)

[78] Costes, M., Richez, F., Le Pape, A., and Gavériaux, R., "Numerical investigation of three-dimensional effects during dynamic stall," *Aerospace Science and Technology*, Vol. 47, 2015.
doi: 10.1016/j.ast.2015.09.025 (Page 8)

[79] Kaufmann, K., Costes, M., Richez, F., Gardner, A. D., and Le Pape, A., "Numerical investigation of three-dimensional static and dynamic stall on a finite wing," *Journal of the American Helicopter Society*, Vol. 60, (3), 2015.
doi: 10.4050/JAHS.60.032004 (Pages 9, 42, 116)

[80] Jain, R., Le Pape, A., Grubb, A., Costes, M., Richez, F., and Smith, M., "High-resolution computational fluid dynamics predictions for the static and dynamic stall of a finite-span OA209 wing," *Journal of Fluids and Structures*, Vol. 78, 2018.
doi: 10.1016/j.jfluidstructs.2017.12.012 (Pages 9, 13, 39, 41, 116, 118)

[81] Kaufmann, K., Merz, C. B., and Gardner, A. D., "Dynamic stall simulations on a pitching finite wing," *Journal of Aircraft*, Vol. 54, (4), 2017.
doi: 10.2514/1.C034020 (Pages 9, 39, 46, 116)

[82] Visbal, M. R. and Garmann, D. J., "Dynamic stall of a finite-aspect-ratio wing," *AIAA Journal*, Vol. 57, (3), 2018.
doi: 10.2514/1.J057457 (Pages 9, 24, 116)

[83] Gardner, A. D. and Richter, K., "Influence of rotation on dynamic stall," *Journal of the American Helicopter Society*, Vol. 58, (3), 2013.
doi: 10.4050/JAHS.58.032001 (Page 9)

[84] Dietz, M., Khier, W., Knutzen, B., Wagner, S., and Krämer, E., "Numerical simulation of a full helicopter configuration using weak fluid-structure coupling," 46th AIAA Aerospace Sciences Meeting and Exhibit, 2008.
doi: 10.2514/6.2008-401 (Pages 9, 10)

[85] Antoniadis, A., Drikakis, D., Zhong, B., Barakos, G., Steijl, R., Biava, M., Vigevano, L., Brocklehurst, A., Boelens, O., Dietz, M., Embacher, M., and Khier, W., "Assessment of CFD methods against experimental flow measurements for helicopter flows," *Aerospace Science and Technology*, Vol. 19, (1), 2012.
doi: 10.1016/j.ast.2011.09.003 (Pages 9, 10)

[86] Sitaram, J., Datta, A., Baeder, J., and Chopra, I., "Coupled CFD/CSD prediction of rotor aerodynamic and structural dynamic loads for three critical flight conditions," Proceedings of the 31th European Rotorcraft Forum, Florence, Italy, September 13–15, 2005. (Pages 10, 11, 123)

[87] Yeo, H. and Potsdam, M., "Rotor structural loads analysis using coupled computational fluid dynamics/computational structural dynamics," *Journal of Aircraft*, Vol. 53, (1), 2016.
doi: 10.2514/1.C033194 (Pages 10, 11, 13)

[88] Yeo, H. and Romander, E. A., "Loads correlation of a full-scale UH-60A airloads rotor in a wind tunnel," *Journal of the American Helicopter Society*, Vol. 58, (2), 2013.
doi: 10.4050/JAHS.58.022003 (Pages 10, 11, 123)

[89] Potsdam, M., Datta, A., and Jayaraman, B., "Computational investigation and fundamental understanding of a slowed UH-60A rotor at high advance ratios," *Journal of the American Helicopter Society*, Vol. 61, (2), 2016.
doi: 10.4050/JAHS.61.022002 (Pages 10, 12)

[90] Ramasamy, M., Sanayei, A., Wilson, J., Martin, P., Harms, T., Nikoueeyan, P., and Naughton, J., "Data-driven optimal basis clustering to characterize cycle-to-cycle variations in dynamic stall measurements," Proceedings of the 75th Annual Forum of the American Helicopter Society, Philadelphia, PA, May 13–16, 2019. (Pages 12, 58, 58, 59, 59)

[91] Probst, A., Radespiel, R., Wolf, C., Knopp, T., and Schwamborn, D., "A comparison of detached-eddy simulation and Reynolds-stress modelling applied to the flow over a backward-facing step and an airfoil at stall," Paper 2010–0920, Proceedings of the 48th AIAA Aerospace Sciences Meeting, Orlando, FL, January 4–7, 2010.
doi: 10.2514/6.2010-920 (Pages 13, 27, 49, 66)

[92] Medida, S. and Baeder, J. D., "Numerical investigation of 3-D dynamic stall using delayed detached eddy simulation," Paper 2012–0099, Proceedings of the 50th AIAA Aerospace Sciences Meeting Including the New Horizons Forum and Aerospace Exposition, Nashville, TN, January 9–12, 2012.
doi: 10.2514/6.2012-99 (Page 13)

[93] Le Pape, A., Richez, F., and Deck, S., "Zonal detached-eddy simulation of an airfoil in poststall condition," *AIAA Journal*, Vol. 51, (8), 2013.
doi: 10.2514/1.J052235 (Page 13)

[94] Richez, F., Le Pape, A., and Costes, M., "Zonal detached-eddy simulation of separated flow around a finite-span wing," *AIAA Journal*, Vol. 53, (11), 2015. (Pages 13, 41)

[95] Menter, F. R., Kuntz, M., and Langtry, R., "Ten years of industrial experience with the SST turbulence model," *Turbulence, heat and mass transfer*, Vol. 4, (1), 2003. (Pages 13, 26)

[96] Spalart, P. R., Deck, S., Shur, M. L., Squires, K. D., Strelets, M. K., and Travin, A., "A new version of detached-eddy simulation, resistant to ambiguous grid densities," *Theoretical and computational fluid dynamics*, Vol. 20, (3), 2006.
doi: 10.1007/s00162-006-0015-0 (Pages 13, 26, 48, 107)

[97] Mockett, C., Haase, W., and Schwamborn, D., *Go4Hybrid: Grey area mitigation for hybrid RANS-LES methods: Results of the 7th framework research project Go4Hybrid, funded by the European Union, 2013-2015*, Vol. 134, Springer, 2017. (Pages 13, 27, 100)

[98] Anderson, J., *Fundamentals of aerodynamics*, McGraw-Hill Education, 6th edition, 2017. (Pages 15, 17)

[99] Oertel, H., editor, *Prandtl's essentials of fluid mechanics*, Springer-Verlag, 2004.
doi: 10.1007/b97538 (Page 16)

[100] Schlichting, H. and Gersten, K., *Boundary-layer theory*, Springer Berlin Heidelberg, 2017.
doi: 10.1007/978-3-662-52919-5 (Pages 16, 16, 17, 67, 88, 89)

[101] McLean, D., *Understanding aerodynamics: Arguing from the real physics*, John Wiley & Sons, Ltd, 2012.
doi: 10.1002/9781118454190 (Pages 16, 17, 24)

[102] Simpson, R. L., "Turbulent boundary-layer separation," *Annual Review of Fluid Mechanics*, Vol. 21, (1), 1989.
doi: 10.1146/annurev.fl.21.010189.001225 (Pages 17, 96)

[103] Johnson, W., *Rotorcraft aeromechanics*, Cambridge Aerospace Series, Cambridge University Press, 2013.
doi: 10.1017/CBO9781139235655 (Pages 19, 20)

[104] Blazek, J., *Computational fluid dynamics: Principles and applications*, Elsevier, third edition, 2015.
doi: 10.1016/c2013-0-19038-1 (Pages 23, 24, 25)

[105] Deardorff, J. W., "A numerical study of three-dimensional turbulent channel flow at large Reynolds numbers," *Journal of Fluid Mechanics*, Vol. 41, (2), 1970.
doi: 10.1017/S0022112070000691 (Page 24)

[106] Mockett, C., *A comprehensive study of detached-eddy simulation*, Ph.D. thesis, Technische Universität Berlin, 2009.
doi: 10.14279/depositonce-2305 (Pages 24, 25, 27, 118)

[107] Matyushenko, A. A. and Garbaruk, A. V., "Adjustment of the k-ω SST turbulence model for prediction of airfoil characteristics near stall," *Journal of Physics: Conference Series*, Vol. 769, 2016.
doi: 10.1088/1742-6596/769/1/012082 (Page 25)

[108] Spalart, P. R., Jou, W., Strelets, M., and Allmaras, S. R., "Comments on the feasibility of LES for wings, and on a hybrid RANS/LES approach," *Advances in DNS/LES*, Vol. 1, 1997. (Pages 25, 25, 27)

[109] Fröhlich, J. and von Terzi, D., "Hybrid LES/RANS methods for the simulation of turbulent flows," *Progress in Aerospace Sciences*, Vol. 44, (5), 2008.
doi: 10.1016/j.paerosci.2008.05.001 (Page 25)

[110] Gritskevich, M. S., Garbaruk, A. V., and Menter, F. R., "Fine-tuning of DDES and IDDES formulations to the k-ω shear stress transport model," *Progress in Flight Physics*, Vol. 5, 2013.
doi: 10.1051/eucass/201305023 (Pages 26, 39, 65, 107)

[111] Shur, M. L., Spalart, P. R., Strelets, M. K., and Travin, A. K., "A hybrid RANS-LES approach with delayed-DES and wall-modelled LES capabilities," *International Journal of Heat and Fluid Flow*, Vol. 29, (6), 2008. (Pages 26, 67)

[112] Menter, F., "Stress-blended eddy simulation (SBES)–a new paradigm in hybrid RANS-LES modeling," Progress in Hybrid RANS-LES Modelling, edited by Hoarau, Y., Peng, S.-H., Schwamborn, D., and Revell, A., 2018.
doi: 10.1007/978-3-319-70031-1_3 (Pages 27, 27, 71, 91)

[113] Ashton, N., "Recalibrating detached-eddy simulation to eliminate modelled-stress depletion," Paper 2017–4281, Proceedings of the 23rd AIAA Computational Fluid Dynamics Conference, Denver, CO, June 5–9, 2017.
doi: 10.2514/6.2017-4281 (Pages 27, 49, 66)

[114] Jain, N., Lee, B., and Baeder, J. D., "Assessment of shielding parameters in conventional DDES method under the presence of alternative turbulence length scales," Paper 2017–4282, Proceedings of the 23rd AIAA Computational Fluid Dynamics Conference, Denver, CO, June 5–9, 2017. (Pages 27, 49, 66)

[115] Vatsa, V. N., Lockard, D. P., and Spalart, P. R., "Grid sensitivity of SA-based delayed-detached-eddy-simulation model for blunt-body flows," *AIAA Journal*, Vol. 55, (8), 2017. (Pages 27, 49)

[116] Weihing, P., *Numerical study of transition, flow separation and wake phenomena of wind turbines with enhanced hybrid RANS/LES methods*, Ph.D. thesis, University of Stuttgart, 2021. (Pages 27, 27, 28, 66, 67, 67, 69, 69, 74, 88)

[117] Probst, A., Radespiel, R., and Knopp, T., "Detached-eddy simulation of aerodynamic flows using a Reynolds-stress background model and algebraic RANS/LES sensors," 20th AIAA computational fluid dynamics conference, 2011. (Pages 27, 67, 89, 89)

[118] Weihing, P., Letzgus, J., Lutz, T., and Krämer, E., "Development of alternative shielding functions for detached-eddy simulations," Progress in Hybrid RANS-LES Modelling, edited by Hoarau, Y., Peng, S.-H., Schwamborn, D., Revell, A., and Mockett, C., 2020. (Pages 27, 28, 66, 67, 67, 69, 88)

[119] Deck, S. and Renard, N., "Towards an enhanced protection of attached boundary layers in hybrid RANS/LES methods," *Journal of Computational Physics*, Vol. 400, 2020.
doi: 10.1016/j.jcp.2019.108970 (Pages 27, 70, 70)

[120] Shur, M. L., Spalart, P. R., Strelets, M. K., and Travin, A. K., "An enhanced version of DES with rapid transition from RANS to LES in separated flows," *Flow, Turbulence and Combustion*, Vol. 95, (4), 2015.
doi: 10.1007/s10494-015-9618-0 (Pages 27, 95)

[121] Raddatz, J. and Fassbender, J. K., "Block structured Navier-Stokes solver FLOWer," *MEGAFLOW-Numerical Flow Simulation for Aircraft Design*, Vol. 89, Springer, 2005, pp. 27–44.
doi: 10.1007/3-540-32382-1_2 (Page 28)

[122] Kranzinger, P. P., Kowarsch, U., Schuff, M., Keßler, M., and Krämer, E., "Advances in parallelization and high-fidelity simulation of helicopter phenomena," High Performance Computing in Science and Engineering '15, edited by Nagel, W. E., Kröner, D. H., and Resch, M. M., 2016. (Page 28)

[123] Letzgus, J., Dürrwächter, L., Schäferlein, U., Keßler, M., and Krämer, E., "Optimization and HPC-applications of the flow solver FLOWer," High Performance Computing in Science and Engineering '17, edited by Nagel, W. E., Kröner, D. H., and Resch, M. M., 2018. (Page 28)

[124] Weihing, P., Letzgus, J., Bangga, G., Lutz, T., and Krämer, E., "Hybrid RANS/LES capabilities of the flow solver FLOWer–application to flow around wind turbines," Progress in Hybrid RANS-LES Modelling, edited by Hoarau, Y., Peng, S.-H., Schwamborn, D., and Revell, A., 2018.
doi: 10.1007/978-3-319-70031-1_31 (Pages 28, 39)

[125] Frey, F., Herb, J., Letzgus, J., Weihing, P., Keßler, M., and Krämer, E., "Enhancement and application of the flow solver FLOWer," High Performance Computing in Science and Engineering ' 18, edited by Nagel, W. E., Kröner, D. H., and Resch, M. M., 2019. (Page 28)

[126] Jameson, A., Schmidt, W., and Turkel, E., "Numerical solution of the Euler equations by finite volume methods using Runge Kutta time stepping schemes," AIAA 14th Fluid and Plasma Dynamics Conference, Palo Alto, CA, June 23–25, 1981.
doi: 10.2514/6.1981-1259 (Page 28)

[127] Jiang, G.-S. and Shu, C.-W., "Efficient implementation of weighted ENO schemes," *Journal of Computational Physics*, Vol. 126, (1), 1996.
doi: 10.1006/jcph.1996.0130 (Pages 28, 107)

[128] Kozlowski, D., *CFD-Untersuchung der Einflüsse verschiedener Testparameter auf dynamische Strömungsablösung (Dynamic Stall) am Rotorblatt*, Diploma thesis, Institute of Aerodynamics and Gas Dynamics, University of Stuttgart, 2016. (Pages 29, 31, 31, 31, 32, 32)

[129] Bußhardt, F., *URANS-Simulationen von Windkanalfreistrahlen zur Untersuchung von Rotorprüfständen*, Bachelor's thesis, Institute of Aerodynamics and Gas Dynamics, University of Stuttgart, 2017. (Pages 29, 33, 33, 33, 34)

[130] Siring, M., *URANS-Strömungssimulation eines runden Windkanal-Freistrahls*, Bachelor's thesis, Institute of Aerodynamics and Gas Dynamics, University of Stuttgart, 2016. (Page 33)

[131] Stein, A., *Simulation eines windkanalfreistrahls*, Bachelor's thesis, Institute of Aerodynamics and Gas Dynamics, University of Stuttgart, 2017. (Page 33)

[132] Schwermer, T., Richter, K., and Raffel, M., "Development of a rotor test facility for the investigation of dynamic stall," *New Results in Numerical and Experimental Fluid Mechanics X*, Springer, 2016, pp. 663–673. (Page 38)

[133] Richez, F. and Ortun, B., "Numerical investigation of the flow separation on a helicopter rotor in dynamic stall configuration," Proceedings of the 42nd European Rotorcraft Forum, Lille, France, September 5–8, 2016. (Page 39)

[134] Spalart, P. R., "Young-person's guide to detached-eddy simulation grids," NASA/CR-2001-211032, July 2001. (Pages 39, 41)

[135] Tinoco, E. N., Brodersen, O. P., Keye, S., Laflin, K. R., Feltrop, E., Vassberg, J. C., Mani, M., Rider, B., Wahls, R. A., Morrison, J. H., *et al.*, "Summary of data from the sixth AIAA CFD drag prediction workshop: CRM cases 2 to 5," Proceedings of the 55th AIAA Aerospace Sciences Meeting, Grapevine, TX, January 9–13, 2017.
doi: 10.2514/1.C034409 (Pages 39, 108)

[136] Nilifard, R., Zanotti, A., Gibertini, G., Guardone, A., and Quaranta, G., "Numerical investigation of three-dimensional effects on deep dynamic stall experiments," Proceedings of the 71st Annual Forum of the American Helicopter Society, Virginia Beach, VA, May 5–7, 2015. (Page 41)

[137] Schwamborn, D., Gardner, A. D., von Geyr, H., Krumbein, A., Lüdeke, H., and Stürmer, A., "Development of the DLR TAU-code for aerospace applications," Proceedings of the International Conference on Aerospace Science and Technology, Bangalore, India, June 26–28, 2008. (Page 42)

[138] Jeong, J. and Hussain, F., "On the identification of a vortex," *Journal of Fluid Mechanics*, Vol. 285, 1995. (Page 44)

[139] Ramasamy, M., Wilson, J. S., McCroskey, W. J., and Martin, P. B., "Characterizing cycle-to-cycle variations in dynamic stall measurements," *Journal of the American Helicopter Society*, Vol. 63, (2), 2018.
doi: 10.4050/JAHS.63.022002 (Pages 46, 58, 58, 58)

[140] Gardner, A. D., Wolf, C. C., and Raffel, M., "A new method of dynamic and static stall detection using infrared thermography," *Experiments in Fluids*, Vol. 57, (9), 2016. (Page 53)

[141] Sanayei, A., Ramasamy, M., Wilson, J., and Martin, P., "Development of modal analysis based clustering technique using pitching airfoil measurements," AIAA Scitech 2019 Forum, San Diego, CA, January 7–11, 2019.
doi: 10.2514/6.2019-1828 (Page 58)

[142] Pedregosa, F., Varoquaux, G., Gramfort, A., Michel, V., Thirion, B., Grisel, O., Blondel, M., Prettenhofer, P., Weiss, R., Dubourg, V., Vanderplas, J., Passos, A., Cournapeau, D., Brucher, M., Perrot, M., and Duchesnay, E., "Scikit-learn: Machine learning in Python," *Journal of Machine Learning Research*, Vol. 12, 2011. (Page 59)

[143] Letzgus, J., Weihing, P., Keßler, M., and Krämer, E., "Assessment of delayed detached-eddy simulation of dynamic stall on a rotor," Progress in Hybrid RANS-LES Modelling, edited by Hoarau, Y., Peng, S.-H., Schwamborn, D., Revell, A., and Mockett, C., 2020.
doi: 10.1007/978-3-030-27607-2_25 (Pages 65, 67, 68, 68, 71, 72)

[144] Ames Research Staff, "Equations, tables, and charts for compressible flow," Report 1135, NACA Ames Aeronautical Laboratory, Moffett Field, CA, 1953. (Page 66)

[145] Spalart, P. R. and Strelets, M. K., "Mechanisms of transition and heat transfer in a separation bubble," *Journal of Fluid Mechanics*, Vol. 403, 2000. (Page 67)

[146] Everitt, B. and Skrondal, A., *The Cambridge dictionary of statistics*, Cambridge University Press Cambridge, fourth edition, 2010. (Page 82)

[147] Satopaa, V., Albrecht, J., Irwin, D., and Raghavan, B., "Finding a "kneedle" in a haystack: Detecting knee points in system behavior," 31st International Conference on Distributed Computing Systems Workshops, 2011. (Pages 86, 89)

[148] Pope, S. B., *Turbulent flows*, Cambridge University Press, 2000.
doi: 10.1017/CBO9780511840531 (Pages 88, 89)

[149] Institute of Aerodynamics and Flow Technology, *TAU-code user guide*, DLR, 2018. (Page 88, 88)

[150] Cliquet, J., Houdeville, R., and Arnal, D., "Application of laminar-turbulent transition criteria in Navier-Stokes computations," *AIAA Journal*, Vol. 46, (5), 2008.
doi: 10.2514/1.30215 (Pages 88, 88, 89)

[151] Heister, C. C., "A method for approximate prediction of laminar turbulent-transition on helicopter rotors," *Journal of the American Helicopter Society*, Vol. 63, (3), 2018.
doi: 10.4050/JAHS.63.032008 (Page 88)

[152] Stock, H. W. and Haase, W., "Feasibility study of e^n transition prediction in Navier-Stokes methods for airfoils," *AIAA Journal*, Vol. 37, (10), 1999.
doi: 10.2514/2.612 (Page 89)

[153] Lovely, D., *Boundary layer and shock detection in CFD solutions*, Master's thesis, Department of Aeronautics and Astronautics, Massachusetts Institute of Technology, 1999. (Page 89)

[154] Hazewinkel, M., editor, *Encyclopaedia of mathematics*, Springer Netherlands, 1989.
doi: 10.1007/978-94-009-5983-5 (Page 89)

[155] Saunders, D. A. and Prabhu, D. K., "BLAYER user guide," Tm-2018-219749, NASA Ames Research Center, Moffett Field, CA, 2018. (Page 89)

[156] Castillo, L., Wang, X., and George, W. K., "Separation criterion for turbulent boundary layers via similarity analysis," *Journal of Fluids Engineering*, Vol. 126, (3), 2004.
doi: 10.1115/1.1758262 (Page 89)

[157] Letzgus, J., Keßler, M., and Krämer, E., "Simulation of dynamic stall on an elastic rotor in high-speed turn flight," *Journal of the American Helicopter Society*, Vol. 65, (2), 2020.
doi: 10.4050/JAHS.65.022002 (Pages 105, 106, 108, 109, 109, 111, 112, 113, 113, 114, 116, 118, 119, 119, 120, 121, 122, 123)

[158] Bebesel, M., D'Alascio, A., Schneider, S., Guenther, S., Vogel, F., Wehle, C., and Schimke, D., "Bluecopter demonstrator – an approach to eco-efficient helicopter design," Proceedings of the 41th European Rotorcraft Forum, Munich, Germany, September 1–4, 2015.
doi: 20.500.11881/3574 (Page 105)

[159] Schimke, D., Link, S., and Schneider, S., "Noise and performance improved rotor blade for a helicopter," Patent EP 2 505 500 A1, 2011. (Page 105)

[160] Kowarsch, U., Öhrle, C., Keßler, M., and Krämer, E., "Aeroacoustic simulation of a complete H145 helicopter in descent flight," *Journal of the American Helicopter Society*, Vol. 61, (4), 2016.
doi: 10.4050/JAHS.61.042001 (Page 107)

[161] Schäferlein (né Kowarsch), U., Keßler, M., and Krämer, E., "Aeroelastic simulation of the tail shake phenomenon," *Journal of the American Helicopter Society*, Vol. 63, (3), 2018.
doi: 10.4050/JAHS.63.032003 (Page 107)

[162] Dietz, M., Schimke, D., and Embacher, M., "Advanced industrial application of CFD for helicopter development," Proceedings of the 36th European Rotorcraft Forum, Paris, France, September 7–9, 2010.
doi: 20.500.11881/932 (Page 109)

[163] Kufeld, R. M. and Johnson, W., "The effects of control system stiffness models on the dynamic stall behavior of a helicopter," *Journal of the American Helicopter Society*, Vol. 45, (4), 2000.
doi: 10.4050/JAHS.45.263 (Page 110)

[164] Carr, L. W., Mcalister, K. W., and Mccroskey, W. J., "Analysis of the development of dynamic stall based on oscillating airfoil experiments," Technical note d-8382, NASA Ames Research Center, Moffett Field, CA, 1977. (Page 115)

[165] DiOttavio, J., Watson, K., Cormey, J., Kondor, S., and Komerath, N., "Discrete structures in the radial flow over a rotor blade in dynamic stall," 26th AIAA Applied Aerodynamics Conference, Guidance, Navigation, and Control, Honolulu, HI, August 18–21, 2008. (Page 115)

[166] Steijl, R. and Barakos, G. N., "Computational study of helicopter rotor-fuselage aerodynamic interactions," *AIAA Journal*, Vol. 47, (9), 2009.
doi: 10.2514/1.41287 (Page 119)